THE UNIVERSITY OF CHICAGO

FLUORESCENCE-ENCODED INFRARED VIBRATIONAL SPECTROSCOPIES

A DISSERTATION SUBMITTED TO

THE FACULTY OF THE DIVISION OF THE PHYSICAL SCIENCES

IN CANDIDACY FOR THE DEGREE OF

DOCTOR OF PHILOSOPHY

DEPARTMENT OF CHEMISTRY

BY

JOSEPH NATHANAEL MASTRON

CHICAGO, ILLINOIS

MARCH 2019

I dedicate this work to my grandfather, John Ryan, and grandmother, Delores Ryan. May I one day live up to your legacy. To my parents, David and Holly Mastron. May I collect a library to rival yours.

To my siblings, Johnathan, Jesse, Joy, and Joanna Mastron.

To my first nibling, Elizabeth: “My brother had a daughter – The beauty that she brings, illumination”

To my educators and mentors, academic institutions and leadership opportunities.

To my good friends and ba’sibs.

"I wish to preach, not the doctrine of ignoble ease, but the doctrine of the strenuous life, the life of toil and effort, of labor and strife; to preach that highest form of success which comes, not to the [person] who desires mere easy peace, but to the [person] who does not shrink from danger, from hardship, or from bitter toil, and who out of these wins the splendid ultimate triumph."[1]

[1] Theodore Roosevelt, "The Strenuous Life, Essays and Addresses"

Table of Contents

List of Figures

Appendix 4: Supplementary Figures to Chapter 7

List of Tables

Acknowledgements

Graduate education is fundamentally based on a juxtaposition of contradictory ideas within the academy, whether in its goals (the education of doctoral students versus the creation of new knowledge), the form of education (didactic in early stages versus dialectic in later stages), or even the nature of the academy (collective versus individual). It is in the dialectic synthesis of these concepts that a well-trained graduate student is formed into a doctor. The first president of the University of Chicago wrote that "individualism, in education, as distinguished from collectivism, is the greatest contribution of the nineteenth century to the cause of college education."[I] Indeed, the hard-earned individual contribution to the development of knowledge is a vital component of doctoral education. According to William James, "Our higher degrees were instituted for the laudable purpose of stimulating scholarship, especially in the form of 'original research.' . . . [and] there are [those]. . . who nevertheless rise to the challenge, get a stimulus from the difficulty, and become doctors, not without some baleful nervous wear and tear. . . but on the whole successfully, and with advantage."[II] However, as poetically mused almost 300 years prior, "No man is an island entire of itself; every man is a piece of the continent, a part of the main."[III] While seemingly contradictory, these statements can be synthesized to describe a properly-functioning academic process. Even the most independent, individual researcher cannot be successful in a vacuum - academic interactions with colleagues and peers are vital to produce and polish one's best work, and social interactions with supportive friends are necessary to maintain one's health and sanity. I would like to acknowledge those individuals who have filled these roles during my doctoral education.

Firstly, I would like to acknowledge Andrei Tokmakoff for serving in the most valuable academic role as my advisor and mentor. I would like to thank him for our many meetings and critical feedback, which came more often in the form of a question or a conversation than a direct counterpoint.

I would like to acknowledge those professors who have contributed to my graduate education, with special thanks to Gregory Engel and David Mazziotti for serving on my committee.

I would like to acknowledge the members of the Tokmakoff group and my cohort for countless discussions. I would like to give special thanks to Samuel Penwell and Lukas Whaley-Mayda for conversations and feedback on this project, including the publications that were expanded upon in Chapters 3 and 4 of this document. I would like to thank Chi-Jui Feng and Anthony Schlimgen for feedback and discussion on Chapter 2, Sam and Lukas for additional feedback on Chapters 5 and 7, and Nick Lewis for feedback and discussion on Chapters 6 and 7.

I would like to acknowledge Xinxing Zhang for *ad hoc* mentorship and extensive conversations ranging from academic research to personal well-being.

This work was supported by a grant from the National Science Foundation (CHE-1561888).

[I] Harper, William Rainey. "The Trend in Higher Education." The University of Chicago Press. (1905)
[II] James, William. “The PhD Octopus.” Harvard Monthly. (March 1903)
[III] Donne, John. "Donne's Devotions." Cambridge University Press. (1923)

I would also like to thank my peers and colleagues who have become dear friends and provided endless opportunities for rest and relaxation after long days in the laser lab, without which I might have burned out. Thank you for recharging my strength to go on.

I thank those peers within my cohort that have been valuable in support and friendship, who are too many to list but include Michael the Punctual, Tony, Darren, Becca, and Tom.

I would like to thank the core Beyonder group for our mutual enjoyment in our forays in destroying a fictional world: Preston, Tamara, Tim, Michael the Bold, and Michael the Punctual

I would like to thank previously-unlisted members of the Palmer-Schiller 'bash and affiliates for dinners, theatre, games of all kinds, and many other fun experiences: Ada, Lauren, Jonathan, Allie

Special thanks to all those who have gone with me many times to Costco and Chinatown and have kept me nourished, and to the Coffee Club, Denise Schach, Rajib Biswas, and Xinxing, for keeping me alert.

I would like to thank the many friends that I have made across the university through service to the Graduate Council, the Student Health Advisory Board, and the Committee on Graduate Education.

I would like to thank my family for love and encouragement, despite my abstract discussions on the arcana of spectroscopy and al-chemistry.

To the unnamed friends, peers, and colleagues, I proclaim: though I do not have time nor space to list you all individually, you are not far from my thoughts and appreciation. Thank you.

Chapter 1
Introduction

Dissertation Abstract

While ultrafast Infrared spectroscopies are valuable tools to study condensed phase structural dynamics, they are limited in terms of accessible concentrations. In order to develop a more sensitive Infrared vibrational spectroscopy, I have developed a set of multidimensional mixed-infrared-visible techniques in which a vibrational excitation modulates the resonance of an electronic transition with an initially off-resonance encoding field. The resulting electronic excited state population can relax radiatively and the incoherently-emitted fluorescence can be detected with high sensitivity as the experimental observable. This class of fluorescence-encoded Infrared (FEIR) vibrational spectroscopies was demonstrated to be sensitive to vibrational coherences that result from an excited superposition of coupled modes in the encoding time delay between the respective vibrational and electronic excitations. In the case of FEIR that is linear in IR intensity, condensed-phase solvation measurements can report on the same processes as FTIR absorption at the lower concentrations accessible to fluorescence-detection, and higher orders of FEIR that are analogous to 2D IR can be predicted from a response function formalism. By demonstrating that coupled-vibrational information can be encoded into a fluorescence observable, this research lays the groundwork for high-sensitivity vibrational measurements at the dilute concentrations accessible with the detection of fluorescence.

1.1 The Aim of this Present Research

As part of a wider toolbox of structural techniques, vibrational spectroscopies are widely used in Chemistry to characterize molecular structures due to the correlation between functional moieties and vibrational frequencies. Ultrafast vibrational multidimensional spectroscopies extend this concept into the time domain to observe the evolution of correlated structural features in the form of coupled nuclear coordinates on an ultrafast (femtosecond to picosecond) timescale that is inaccessible to other structural techniques. While ultrafast Infrared (IR) vibrational spectroscopies can be used to sufficiently resolve condensed-phase structural dynamics on the electronic ground state, these techniques are often limited to much higher concentrations than can be accessed with optical spectroscopies. In this work, I will discuss the development of ultrafast IR vibrational spectroscopies that encode a vibrational excitation into a more sensitive experimental observable to enable the measurement of structural dynamics at lower concentrations.

1.2 Optical Spectroscopy as a Light-Matter interaction

1.2.1 Matter

Optical spectroscopies have been described in great detail elsewhere,[1] but in the simplest sense, are used to observe transitions between energy levels of a system by the detection of electromagnetic radiation, i.e. light. In Chemistry, the system of interest is a collection of charged particles, electrons and nuclei, that are held together by the electrostatic force, and can be treated as a single, collective object. The

quantized levels of this system are described quantum mechanically with eigenvectors $|\varphi\rangle$ of the Schrodinger equation, with energies that are the eigenvalues of the same. The state of the quantum system can be described in Hilbert space with a wavefunction $|\psi\rangle$ expanded in the eigenvector basis $|\psi\rangle = \sum_n c_n |\varphi_n\rangle$.

However, in time-dependent spectroscopy it is more convenient to describe the state of the system in Liouville space with the density matrix ρ expanded in the basis as $\rho = \sum_{n,m} c_n c_m^* |\varphi_n\rangle\langle\varphi_m|$. The expectation value of an operator $\hat{A}$ can be written as in Liouville space using a trace over the density matrix upon applying the operator $\langle \hat{A} \rangle = Tr\left[\hat{A}\rho\right]$. The time evolution of the density matrix can be described with a commutator between the density matrix and the Hamiltonian operator $\hat{H}$ in the Liouville-Von Neumann equation $\frac{\partial \rho}{\partial t} = -\frac{i}{\hbar}\left[\hat{H}, \rho\right]$.

1.2.2 Light

The experimental observable, electromagnetic radiation, can be treated classically for most purposes as a time-dependent electric field. For a number $n-1$ oscillating electric fields at the sample, the average electric field $E(\vec{r},t)$ can be described as a function of frequency ω and momentum $\vec{k}$ of the incoming light fields $E(\vec{r},t) = \sum_{j=1}^{n-1}\left[E_j(\vec{r},t)e^{(i\vec{k}_j\vec{r}-i\omega_j t)} + E_j^*(\vec{r},t)e^{(i\vec{k}_j\vec{r}+i\omega_j t)}\right]$.

1.2.3 Light-Matter Interaction

The time evolution of the density matrix upon interaction with the electromagnetic field can be described using the time-dependent dipole operator $\hat{\mu}(t) = e^{\left(\frac{i}{\hbar}\hat{H}t\right)}\hat{\mu}e^{\left(-\frac{i}{\hbar}\hat{H}t\right)}$ as an interaction term $\frac{\partial\rho}{\partial t} = -\frac{i}{\hbar}\left[\hat{H},\rho\right] - \frac{i}{\hbar}\left[-E(t)\hat{\mu}(t),\rho\right]$. A time-dependent polarization $P(\vec{r},t)$ that will emit a signal field can then be defined as a function of the time-dependent density matrix $P(\vec{r},t) = \left\langle \mu\rho(t)\right\rangle$.

This polarization can be expanded in orders of the electric field $P(\vec{r},t) = \sum_{n=1}^{\infty} P^{(n)}(\vec{r},t)$. The n[th]-order $P^{(n)}(\vec{r},t)$ polarization can be described as the multidimensional integral of an n[th]-order response function $S^{(n)}$, which itself can be recast as a n[th]-order nested commutator of optical dipole operators $\hat{\mu}(\tau)$, enforcing causality with Heaviside step functions $\theta(\tau)$.

$$P^{(n)} = \int_0^\infty dt_n \int_0^\infty dt_{n-1} \cdots \int_0^\infty dt_1 S^{(n)}(t_n, t_{n-1}, \cdots, t_1) \prod_{\alpha=1}^{n} E\left(\vec{r}, t - \left(\sum_{\beta=1}^{n} t_\beta - \sum_{\beta=1}^{\alpha-1} t_\beta\right)\right)$$

$$S^{(n)}(t_n, t_{n-1}, \cdots, t_1) \equiv \left(\frac{i}{\hbar}\right)^n \left(\prod_{\alpha=1}^{n} \theta(t_\alpha)\right) \left\langle \left[\left[\left[\cdots\left[\hat{\mu}\left(\sum_{\beta=1}^{n} t_\beta\right), \hat{\mu}\left(\sum_{\beta=1}^{n-1} t_\beta\right)\right], \cdots\right], \hat{\mu}(t_1)\right], \hat{\mu}(0)\right] \rho_0 \right\rangle$$

In centrosymmetric systems such as an isotropic solution or a centrosymmetric molecule, the even-order terms of the polarization vanish, and thus even-order coherent spectroscopies are only allowed when centrosymmetry is broken, e.g. at an interface.

1.3 Mixed IR/Vis Ground State Vibrational Techniques

In a vibronic transition, vibrational modes are coupled to electronic states, and a transition from the ground electronic state to the electronic excited state will result in a superposition of vibrational modes. Under the Born-Oppenheimer approximation, the prepared nuclear wavefunction of the electronic excited state will be the result of a projection of the ground state nuclear wavefunction from the ground state basis to the excited state basis, with Franck-Condon factors as coefficients of this projection.

1.3.1 2D VE

The Franck-Condon factors can be measured as a function of the initial vibrational state using a third order spectroscopy. In two-dimensional vibrational electronic (2D VE) spectroscopy, a pair of IR interactions is used to interferometrically resolve a vibrational frequency axis, and an interaction with an optical pulse prepares an electronic coherence that emits.[2,3] For Franck-Condon-active modes, 2D VE can be used to measure Liouville pathways that are linear in the IR though the coherent detection of a visible observable.

1.3.2 VIPERS

If the IR and electronic interactions are interleaved, that is, the first IR interaction is followed by an optical interaction, the system will be prepared in a long-lived coherence between the electronic excited state and a vibrational mode on the ground state.[4,5] This technique, VIPER, increases the time that a vibrational mode can be observed, and exchange can be observed. However, the signal observed depends on both ground and electronic excited state structural dynamics.

1.4 Motivations for FEIR

1.4.1 Incoherently-Detected Electronic Spectroscopies

Incoherently-detected nonlinear electronic spectroscopy has been described previously, as a quasi-third-order process wherein an additional interaction prepares an electronic population that can relax incoherently.[6–13] This process is described by taking the trace of the resulting density matrix over the electronic excited states. The terms of the quasi-third order response function can be related to those observed in coherently-detected 2D electronic spectroscopy, with ground state bleach features and excited state absorption features; however the signs of the terms are different, and there are 14 (out of 16 for the fourth-order coherent response) terms, with both positively and negatively signed excited state absorption pathways.

1.4.2 FEIR

It has already been shown in two-pulse measurements that a vibrational excitation can modulate an electronic transition resulting in a change in a fluorescence observable.[14–18] Fluorescence-encoded IR (FEIR) vibrational spectroscopy was initially investigated in the 1970s by Kaiser and co-workers as a picosecond IR spectroscopy[14,15,19,20]. However, few investigations have followed up on this concept using modern ultrafast laser technology[17,18,21–23]. More recently, fluorescence encoding has also been used as a strategy for super-resolution IR vibrational imaging[24,25].

1.4.3 An Incoherently-Detected Quasi-2D VE Analogue

By analogy to incoherently-detected electronic spectroscopies, the two-pulse FEIR experiment pioneered by Kaiser can be described as an incoherently-detected analogue to 2D VE, collected at zero waiting time between the IR interactions. This suggests that the FEIR measurement can be expanded in more time delays to resolve a signal that is linear in the IR intensity.

Chapter Bibliography

(1) Mukamel, S. *Principles of nonlinear optical spectroscopy*; 1995; Vol. 6.

(2) Courtney, T. L.; Fox, Z. W.; Slenkamp, K. M.; Khalil, M.; Courtney, T. L.; Fox, Z. W.; Slenkamp, K. M.; Khalil, M. Two-Dimensional Vibrational-Electronic Spectroscopy Two-Dimensional Vibrational-Electronic Spectroscopy *J. Chem. Phys.* **2015**, *143* (154201).

(3) Gaynor, J. D.; Khalil, M. Signatures of Vibronic Coupling in Two-Dimensional Electronic-Vibrational and Vibrational-Electronic Spectroscopies *J. Chem. Phys.* **2017**, *147* (9).

(4) Wilderen, L. J. G. W. Van; Messmer, A. T.; Bredenbeck, J. Mixed IR / Vis Two-Dimensional Spectroscopy : Chemical Exchange beyond the Vibrational Lifetime and Sub-Ensemble Selective Photochemistry** *Angew. Chem. Int. Ed.* **2014**, *53*, 2667–2672.

(5) Wilderen, L. J. G. W. van; Messmer, A. T.; Bredenbeck, J. VIPER 2D-IR: Novel Pulse Sequence to Track Exchange Beyond the Vibrational Lifetime *Springer Proc. Phys.* **2015**, *162*, 572–575.

(6) De, A. K.; Monahan, D.; Dawlaty, J. M.; Fleming, G. R. Two-Dimensional Fluorescence-Detected Coherent Spectroscopy with Absolute Phasing by Confocal Imaging of a Dynamic Grating and 27-Step Phase-Cycling *J. Chem. Phys.* **2014**, *140* (19), 0–8.

(7) Wagner, W.; Li, C.; Semmlow, J.; Warren, W. Rapid Phase-Cycled Two-Dimensional Optical Spectroscopy in Fluorescence and Transmission Mode. *Opt. Express* **2005**, *13* (10), 3697–3706.

(8) Li, C.; Wagner, W.; Ciocca, M.; Warren, W. S. Multiphoton Femtosecond Phase-Coherent Two-Dimensional Electronic Spectroscopy *J. Chem. Phys.* **2007**, *126* (16).

(9) Tekavec, P. F.; Lott, G. A.; Marcus, A. H. Fluorescence-Detected Two-Dimensional Electronic Coherence Spectroscopy by Acousto-Optic Phase Modulation *J. Chem. Phys.* **2007**, *127* (21).

(10) Widom, J. R.; Johnson, N. P.; Von Hippel, P. H.; Marcus, A. H. Solution Conformation of 2-Aminopurine Dinucleotide Determined by Ultraviolet Two-Dimensional Fluorescence Spectroscopy *New J. Phys.* **2013**, *15*.

(11) Perdomo-Ortiz, A.; Widom, J. R.; Lott, G. A.; Aspuru-Guzik, A.; Marcus, A. H. Conformation and Electronic Population Transfer in Membrane-Supported Self-Assembled Porphyrin Dimers by 2D Fluorescence Spectroscopy *J. Phys. Chem. B* **2012**, *116* (35), 10757–10770.

(12) Grégoire, P.; Kandada, A. R. S.; Vella, E.; Leonelli, R.; Silva, C. Incoherent Population Mixing Contributions to Phase-Modulation Two-Dimensional Coherent Excitation Spectra *J. Chem. Phys.* **2017**, *147* (114201).

(13) Tiwari, V.; Matutes, Y. A.; Gardiner, A. T.; Jansen, T. L. C.; Cogdell, R. J.; Ogilvie, J. P. Spatially-Resolved Fluorescence-Detected Two-Dimensional Electronic Spectroscopy Probes Varying Excitonic Structure in Photosynthetic Bacteria *Nat Comm* **2018**, *9* (4219).

(14) Seilmeier, A.; Kaiser, W.; Laubereau, A. Vibrational Combination States of Polyatomic Molecules Investigated by Ultrashort Two-Pulse Spectroscopy *Opt. Comm.* **1978**, *26* (3), 441–445.

(15) Laubereau, A.; Seilmeier, A.; Kaiser, W. A New Technique to Measure Ultrashort Vibrational Relaxation Times in Liquid Systems *Chem. Phys. Let.* **1975**, *36* (2), 232–237.

(16) Graener, H.; Seifert, G.; Laubereau, A. New Spectroscopy of Water Using Tunable Picosecond Pulses in the Infrared *Phys. Rev. Lett.* **1991**, *66* (16), 2092–2095.

(17) Emmerling, F.; Lettenberger, M.; Laubereau, A. Vibrational Dynamics of Anthracene in Liquid Solution Studied by Picosecond IR/UV Spectroscopy with Polarization Resolution *J. Phys. Chem.* **1996**, *100* (50), 19251–19256.

(18) Lettenberger, M.; Emmerling, F.; Gottfried, N. H.; Laubereau, A. Orientational Motion of Anthracene in Liquid Solution Studied by IR/UV Double-Resonance Spectroscopy *Chem. Phys. Lett.* **1995**, *240* (4), 324–329.

(19) Seilmeier, A.; Kaiser, W.; Laubereau, A.; Fischer, S. F. A Novel Spectroscopy Using Ultrafast Two-Pulse Excitation of Large Polyatomic Molecules *Chem. Phys. Lett.* **1978**, *58* (2), 225–229.

(20) Ding, K.; Kranitzky, W.; Fischer, S. F.; Kaiser, W. Structured UV-Spectrum of Naphthalene Obtained by Ultrafast Two-Pulse Excitation *Chem. Phys. Lett.* **1980**, *72* (1), 39–42.

(21) Gottfried, N. H.; Emmerling, F. High-Resolution Two-Pulse Spectroscopy of Anthracene in Solution *J. Lumin.* **1999**, *81* (2), 143–147.

(22) Sakai, M.; Fujii, M. Vibrational Energy Relaxation of the 7-Azaindole Dimer in CCl 4 Solution Studied by Picosecond Time-Resolved Transient Fluorescence Detected IR Spectroscopy *Chem. Phys. Lett.* **2004**, *396* (4–6), 298–302.

(23) Sakai, M. Vibrational Energy Relaxation Process of the 7-Azaindole Dimer in Gas Phase and Solution *J. Spectrosc. Soc. Japan* **2005**, *54* (3), 163–169.

(24) Bokor, N.; Inoue, K.; Kogure, S.; Fujii, M.; Sakai, M. Visible-Super-Resolution Infrared Microscopy Using Saturated Transient Fluorescence Detected Infrared Spectroscopy *Opt. Commun.* **2010**, *283* (3), 509–514.

(25) Sakai, M.; Kawashima, Y.; Takeda, A.; Ohmori, T.; Fujii, M. Far-Field Infrared Super-Resolution Microscopy Using Picosecond Time-Resolved Transient Fluorescence Detected IR Spectroscopy *Chem. Phys. Lett.* **2007**, *439* (1–3), 171–176.

Chapter 2
An Aminocoumarin Molecular Rotor

Chapter Abstract

For the development of mixed electronic and vibrational spectroscopies, a model system must be chosen in which coupled nuclear and electronic degrees of freedom contribute to the observation. In this chapter, I will explore the behavior of Coumarin 466, an aminocoumarin molecular rotor, through a series of DFT calculations. In Coumarin 466, the first electronic excited state should have a change in transition energy upon a vibrational excitation. Further, the molecular rotor moiety should be "locked" to the Coumarin core in the electronic ground state. Thus, Coumarin 466 (and other aminocoumarins with similar behavior) should be a good choice of model system for the development of new detection methods for IR spectroscopies.

2.1 Introduction

The class of aminocoumarin dyes such as Coumarin 466 (Figure 2.1) contains several good selections for model systems for the Fluorescence-Encoded Infrared (FEIR) class of experiments. Consisting of an aromatic core formed with a lactone ring moiety (formally a chromen-2-one), the coumarins have strong electronic transitions. An aminocoumarin functionalizes this coumarin core at the 7 position with a diarylamino group that can act as a molecular rotor. Coumarin 466 is a simple aminocoumarin, consisting of an unmodified coumarin core with a diethylamino molecular rotor, with strong electronic absorption and emission such that it can be used as a laser dye. In this chapter, I will characterize the Coumarin 466 model system both in the ground state equilibrium geometry as well as a function of

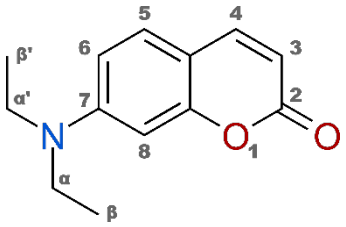

Figure 2.1) Coumarin 466 Structure. The structure of Coumarin 466 (IUPAC: 7,7-diethylaminochromen-2-one) contains several functional moieties. The aromatic Coumarin core is formed with a lactone ring connectivity, and Coumarin 466 has a diethylamino group attached at the 7 position, which acts as a molecular rotor.

molecular rotor angle and nuclear displacements through a series of DFT calculations to build a qualitative picture of the behavior and structural degrees of freedom of this model dye molecule.

2.2 Methods

Vibrational modes, electronic transitions, and molecular orbitals were calculated using Gaussian 09d using Density Functional Theory (DFT) methods with the B3LYP/STO6-31GD functional and Polarizable-Continuum-Modelled (PCM) Cyclohexane solvent.[1–3] For ground state calculations, the structure was optimized before running separate vibrational mode analysis and time-dependent DFT (for electronic transitions and Kohn-Sham molecular orbitals[4]) calculations. Kohn-Sham molecular orbitals were plotted in Chemcraft. Frequencies were then scaled by an empirically-determined scaling factor of 0.963 for this functional.[5,6] The energy eigenvalue calculated for the Kohn-Sham Highest-Occupied Molecular Orbital will correspond to the first ionization potential with a self-interaction error.[7,8] The other energy eigenvalues of the molecular orbitals will have a significant error in magnitude, but as this error is linear in the Hartree-Fock energies,[7] the KS energies can still be used for a qualitative description of relative changes in orbital energies.

For non-equilibrium rotor geometry calculations, as the algorithm used in DFT is valid only at stationary states, the following method was used to generate pseudo-stationary states in order to scan the potential energy surface. Starting from the optimized equilibrium geometry, the coumarin diethylamino rotor angle was set by rotating the plane formed by the C_{α}-N-$C_{\alpha'}$ vectors around the N-Core bond to a fixed angle relative to the plane of the aromatic core. The positions of the coumarin core Carbon atoms, the rotor nitrogen, and the rotor α-Carbon atoms were fixed, and the frequency reoptimized to allow rearrangement of the rotor β-Carbon atoms and Hydrogen atoms. Normal mode analyses and time-dependent DFT calculations were then run on these geometries as pseudo-stationary states on the

potential energy surface. This process is computationally much less expensive for a qualitative calculation than an MD trajectory that uses umbrella sampling of the nuclear potential as a function of twist angle, which would yield more quantitative results.

For non-equilibrium nuclear displacement calculations, the normalized displacement vectors for select vibrational modes were calculated for the ground state optimized geometry. These displacement vectors were then used as nuclear coordinates, along which atoms in the optimized geometry were displaced and then fixed. Time-Dependent DFT calculations were then run on these geometries as pseudo-stationary states to sample the nuclear potential as a function of nuclear displacement in a vibrational coordinate.

2.3 Results

2.3.1 The Ground State Aminocoumarin

The optimized geometry of Coumarin 466 shows, as previously reported, that the diethylamino moiety acts as a hindered molecular rotor[9,10] that is sterically hindered from rotation in the ground electronic state (Figure 2.2A). In the ground state, the C_{α}-N-$C_{\alpha'}$ rotor plane is twisted 6° out of the plane of the aromatic core due to steric hindrance between the rotor and the core Hydrogen atoms. These Hydrogen atoms appear to "lock" the rotor in place, and sit in between the rotor ethylamine α and β-Carbon atoms. Further, this induces a conformational chirality in the molecule which breaks the symmetry of the aromatic core, as the α and β'-Carbon atoms will be positioned on the opposite side of the core as the α' and β-Carbon atoms.

Five vibrational modes were calculated to be present in the mid-Infrared (mid-IR) ring-stretch region from 1500 cm^{-1} to 1800 cm^{-1} (Figure 2.2B), four of which are IR-active. These are assigned from atomic displacement vectors (Figure 2.3) as two lower-energy ring stretch modes that contain displacement of the rotor nitrogen, $\nu_{ArN\text{-}s}$ and $\nu_{ArN\text{-}a}$, two higher-energy ring stretch modes that contain slight carbonyl displacement, $\nu_{Ar\text{-}s}$ and $\nu_{Ar\text{-}a}$, and the lactone carbonyl stretch motion, ν_{CO}. Although this molecule is fairly

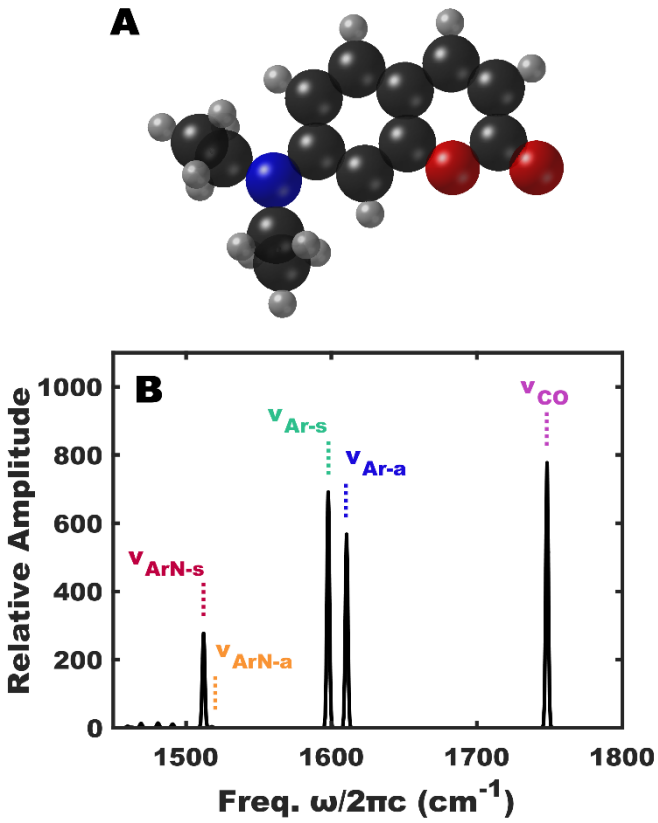

Figure 2.2) Coumarin 466 DFT Vibrational Modes. A.) The optimized geometry of C466 shows that the aromatic core is planar while the diethylamino group sticks out of this plane. The C_{α}-N-$C_{\alpha'}$ diethylamino plane in the optimized geometry is rotated 6° due to steric hindrance between the core Hydrogens and the ethyl groups. **B.)** DFT can be used to assign vibrational features in the ring-stretch region of the mid-Infrared (mid-IR). Four IR-active modes and one IR-inactive mode are present in the range of 1500-1800 cm^{-1}. The two lower A-like symmetry $\nu_{ArN\text{-}s}$ and B-like symmetry $\nu_{ArN\text{-}a}$ ring modes include nitrogen motion, while the upper pair of A-like symmetry $\nu_{Ar\text{-}s}$ and B-like symmetry $\nu_{Ar\text{-}a}$ ring modes include some carbonyl motion. The highest mode is the lactone carbonyl ν_{CO} stretch.

asymmetric, the lower modes in the ring mode pairs, $\nu_{ArN\text{-}s}$ and $\nu_{Ar\text{-}s}$, correspond to A-symmetry-like displacements and the higher modes, $\nu_{ArN\text{-}a}$ and $\nu_{Ar\text{-}a}$, correspond to B-Symmetry-like displacements.

The lowest four electronic singlet transitions were calculated, and the oscillator strengths and molecular orbitals involved in these transitions are displayed in Table 2.1. The lowest lying transition occurs, as is most often the case, between the highest occupied molecular orbital (H.O.M.O.) and the lowest unoccupied molecular orbital (L.U.M.O.). Higher-lying transitions occur between lower occupied molecular orbitals (O.M.O) and the H.O.M.O. to the L.U.M.O. and higher unoccupied molecular orbitals (U.M.O.).

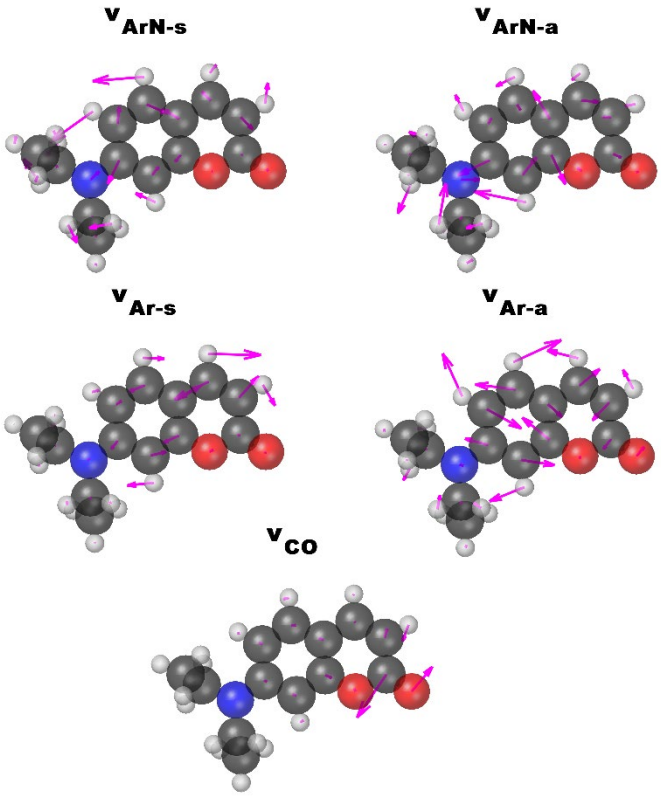

Figure 2.3) Coumarin 466 Vibrational Mode Assignments. A diagram of the 5 vibrational modes in C466 that occur in the 1500 to 1800 cm^{-1} frequency range. The $\nu_{ArN\text{-}s}$ and $\nu_{Ar\text{-}s}$ modes have A-like symmetry and the $\nu_{ArN\text{-}a}$ and $\nu_{Ar\text{-}a}$ modes have B-like symmetry. The $\nu_{ArN\text{-}s}$ and $\nu_{ArN\text{-}a}$ modes contain ring stretch and rotor stretch character, while the $\nu_{Ar\text{-}s}$ and $\nu_{Ar\text{-}a}$ modes contain mostly ring stretch character with some carbonyl motion. The ν_{CO} mode is mostly localized to the carbonyl. Displacements are exaggerated for visual effect.

Table 2.1.) Table of Coumarin 466 Electronic Excited States

State	Type	Electron Density Shift	Transition Wavelength [nm]	Oscillator Strength
S_1	Singlet-A	H.O.M.O. 58 → L.U.M.O. 59	359	0.5444
S_2	Singlet-A	O.M.O. 57 → L.U.M.O. 59 H.O.M.O. 58 → U.M.O. 60	297	0.0077
S_3	Singlet-A	O.M.O. 55 → L.U.M.O. 59 O.M.O. 56 → L.U.M.O. 59 O.M.O. 56 → U.M.O. 61	278	0.0249
S_4	Singlet-A	O.M.O. 57 → L.U.M.O. 59 H.O.M.O. 58 → U.M.O. 60	275	0.0438

The four highest occupied Kohn-Sham MOs and four lowest unoccupied MOs were calculated (Figure 2.4), and can be used to qualitatively assign character to the electronic excited states.[4] The H.O.M.O. 58 and L.U.M.O. 59 involved in the first electronic transition $S_1 \leftarrow S_0$ appear to be mostly anti-symmetric (as expected from aromatic π-like orbitals) across the plane of the aromatic core, and the molecular rotor appears to be antisymmetric in rotational symmetry. This transition $S_1 \leftarrow S_0$ can be assigned as containing some character of shifting of electron density from the aliphatic molecular rotor to the aromatic coumarin core. The O.M.O. 57 and U.M.O. 60 involved in the second and fourth electronic transitions $S_2 \leftarrow S_0$ and $S_4 \leftarrow S_0$ share similar antisymmetries, and these transitions can also be assigned as containing character of a shift of electron density from the rotor to the core. The nearly-degenerate O.M.O. 55 and 56 involved in the third electronic transition $S_3 \leftarrow S_0$ are affected by the symmetry-breaking induced by the conformational chirality of the molecule that arises from the molecular rotor orientation. Thus, this transition $S_3 \leftarrow S_0$ can be assigned as a shift of electron density that increases the electronic antisymmetry of the aromatic core.

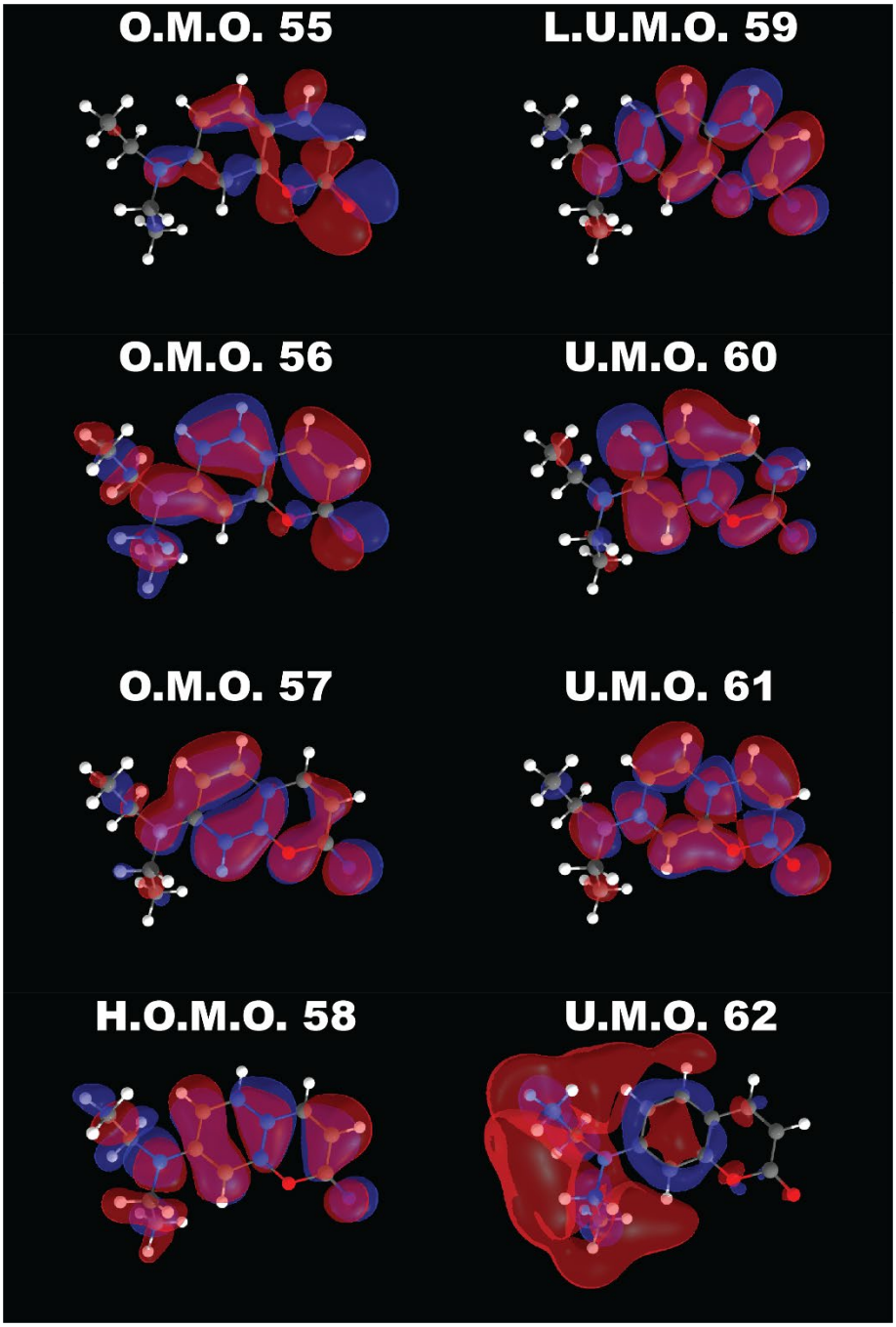

Figure 2.4) Coumarin 466 Molecular Orbitals. A diagram of the 4 highest occupied (left) and 4 lowest unoccupied (right) molecular orbitals in C466. The electron density in each is fairly distributed across the molecule (with the exception of U.M.O. 62), although the electron density appears to be higher on the ring and carbonyl and lower on the rotor moiety.

2.3.2 The Aminocoumarin Molecular Rotor

Similarly, the vibrational modes of Coumarin 466 were calculated for pseudo-stationary geometries as a function of rotor angle (Figure 2.5). The vibrational modes that contain strong rotor displacements in the optimized geometry, $\nu_{ArN\text{-}s}$ and $\nu_{ArN\text{-}a}$ are affected both in peak position and IR activity. Notably, at higher twist angles, the $\nu_{ArN\text{-}a}$ mode is predicted to be IR-active. The higher-lying ring modes that do not contain strong rotor displacements, $\nu_{Ar\text{-}s}$ and $\nu_{Ar\text{-}a}$, are both unaffected in peak position but are strongly affected in amplitude. The lactone carbonyl ν_{CO} is largely unaffected.

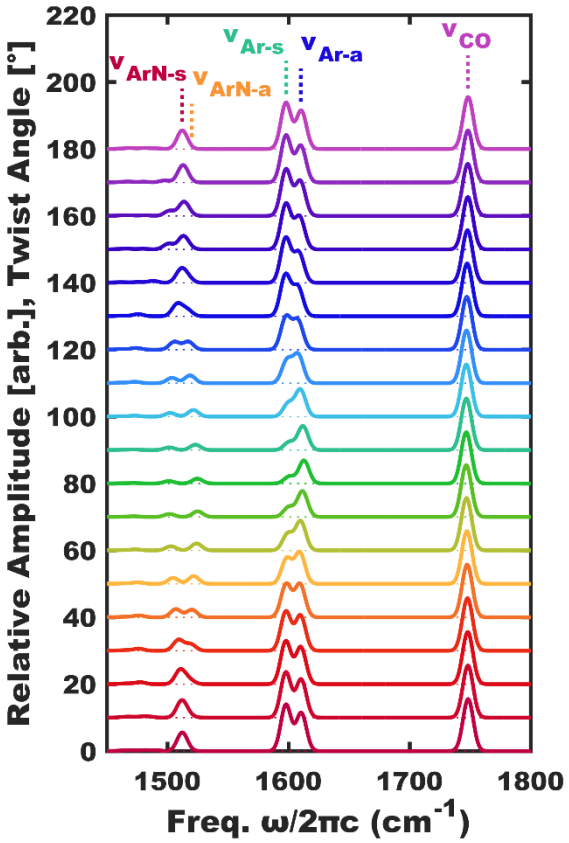

Figure 2.5) Coumarin 466 DFT Vibrational Assignments as a Function of Rotor Twist Angle. The stick spectra have been convolved with a 10 cm^{-1} FWHM gaussian. The $\nu_{ArN\text{-}s}$ and $\nu_{ArN\text{-}a}$ modes are shift in frequency with rotor twist angle, and the $\nu_{ArN\text{-}a}$ mode becomes IR-active in more twisted geometries. The $\nu_{Ar\text{-}s}$ and $\nu_{Ar\text{-}a}$ modes do not shift in frequency but their transition intensities reweight. The ν_{CO} mode is largely unaffected.

Due to the fixing of the geometry of the aromatic core in these calculations, these changes arise solely from the rotor angle and the reoptimized geometry of the rotor β-Carbon atoms (Figure 2.6A). The ethylamine N-C_α-C_β bond angle remains relatively constant around 60°, but the rotor C_β-N-$C_{\beta'}$ diethylamine angle has a strong, chiral change as the rotor "unlocks" from the core Hydrogen atoms as a function of rotor twist angle. When the rotor is twisted to negative angles (in the frame of this chiral conformer), the α-Carbon atoms are twisted past the core Hydrogen atoms and the diethylamine angle widens to reduce steric interactions between the Hydrogen atoms on the α-Carbon and the core. When the rotor is twisted to positive angles, the β-Carbon atoms are twisted past the core Hydrogen atoms and the diethylamine angle narrows to reduce steric interactions between the Hydrogen atoms on the β-Carbon and the core. In the twisted geometry, this angle is relatively constant as a function of rotor angle.

The energies of the electronic states strongly vary as a function of rotor angle (Figure 2.6B). The ground, second, and third singlet states have a global minimum at a twist angle of 6°, where the rotor is "locked" to the aromatic core and the expected angle of rotation does not extend beyond 20°. However, while the first singlet state has a local minimum at a twist angle of 6°, the global minimum of the potential with respect to rotor angle lies around 80°. Due to the chirality of the ground state conformation, the first excited state will preferentially relax to a rotated geometry by a negative twist (in this frame). This rotated geometry is often termed a "Twist-induced Charge Transfer" (TICT) state. However, as this transition $S_1 \leftarrow S_0$ can be assigned to be a transfer of electron density from the rotor to the core in the equilibrium geometry, it is more appropriate to call this a "Charge Transfer-Induced Twisting" state, as it can be assigned as a weakening of the "locked" state of the rotor as the electronic

repulsion between the Hydrogen atoms on the rotor Carbon atoms and the core is reduced as electron density shifts off of these Hydrogen atoms. The barrier to rotation is reduced from on the order of 4500 cm^{-1} (at room temperature) in the ground state to on the order of 500 cm^{-1} in the first excited state.

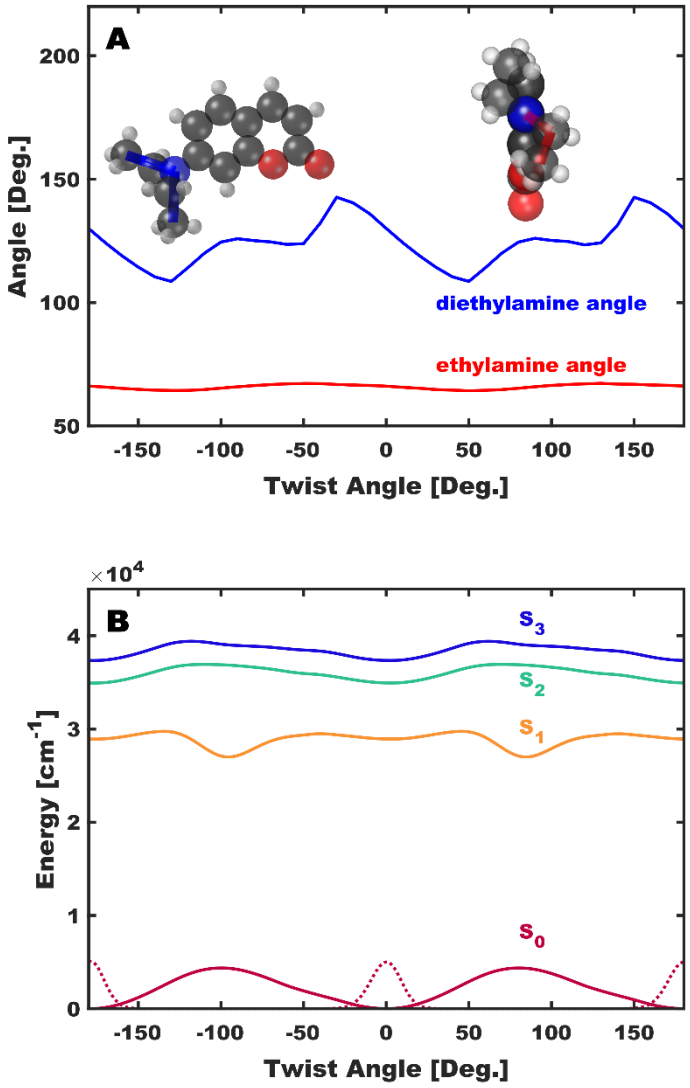

Figure 2.6) Coumarin 466 Structural and Electronic Changes as a Function of Rotor Twist Angle. A.) The ethylamine N-C_α-C_β bond angle (red) remains fairly constant around 60° as a function of rotor twisting. The C_β-N-$C_{\beta'}$ diethylamine angle (blue) has a strong change as the ethylamine groups "unlock" from the Coumarin core, based on whether the α (wider angle) or β-carbons (narrower angle) of the ethylamine groups are twisted past the core. **B.)** The energies of the electronic states are strongly affected by twisting angle. The ground state and the second and third excited singlet states have a global energy minimum at 6°, while the first excited singlet state has a local minimum at the same angle and a global minimum around 80°. The dashed line indicates the relative thermal probability of observing a rotor twist in the ground state at room temperature.

Upon relaxation to the ground state, the rotor will relax back to the "locked" position. The conformational chirality of the molecular rotor can change in the rotated geometry of the electronic excited state, and thus, under electronic excitation and relaxation, a racemic mixture of the conformational enantiomers will be observed.

2.3.3 The Structurally-Displaced Aminocoumarin

The electronic transitions were calculated as a function of displacement along the vibrational coordinate for the rotor-decoupled $\nu_{Ar\text{-}s}$, $\nu_{Ar\text{-}a}$, and ν_{CO} modes (Figure 2.7). While the ground electronic nuclear potentials of the $\nu_{Ar\text{-}s}$ and $\nu_{Ar\text{-}a}$ modes appear to be slightly anharmonic, the nuclear potential of the ν_{CO} mode is more strongly anharmonic. In the higher-lying electronic states, there is an avoided crossing between the nearly-degenerate third and fourth electronic excited singlet states near zero displacement in each coordinate. This indicates that the third and fourth adiabatic excited states in the equilibrium geometry will both contain some coupled character of different diabatic electronic states, and the electronic symmetry breaking of the molecular rotor will affect both of these states. Further, there is a crossing between the second and third excited singlet states in the ν_{CO} coordinate.

Displacements along the nuclear coordinates strongly alter the oscillator strengths of the electronic transitions (Table 2.2). The oscillator strength for the first electronic transition is altered by about 10-20% for each of the modes, while the oscillator strengths of the higher-lying modes are modulated strongly as well. While the oscillator strengths of the second-strongest higher-lying $S_4 \leftarrow S_0$ transition is low compared to the first electronic transition in the equilibrium geometry, on the order of 8% of the $S_1 \leftarrow S_0$ value for the $S_4 \leftarrow S_0$ transition, in the displaced geometry this can be as high as 21% or as low as 0%.

Likewise, the oscillator strength for the $S_3 \leftarrow S_0$ transition, on the order of 5% of that for the $S_1 \leftarrow S_0$ transition in the equilibrium geometry, can be as high as 21% or as low as 0% in the displaced geometry.

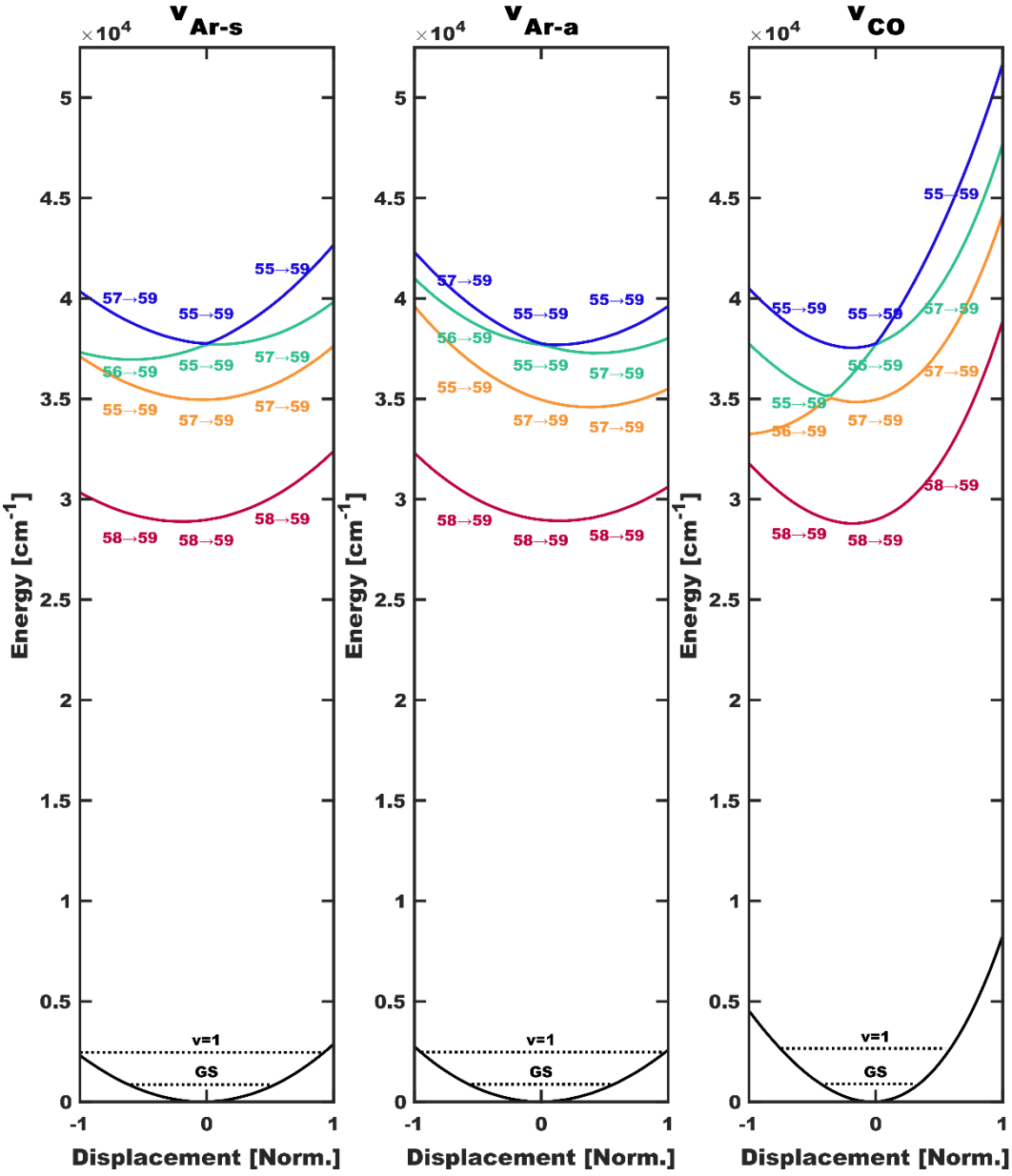

Figure 2.7) Coumarin 466 Electronic Changes as a Function of Nuclear Displacement. The nature of the $S_1 \leftarrow S_0$ transition is largely unchanged as a function of nuclear displacement for the $\nu_{Ar\text{-}s}$, $\nu_{Ar\text{-}a}$, and ν_{CO} modes, but the transition frequency will change. The higher lying states are more strongly affected by the nuclear displacements. For the $\nu_{Ar\text{-}s}$ and $\nu_{Ar\text{-}a}$ displacements, the S_3 and S_4 states show an avoided crossing. For the ν_{CO} displacement there are two avoided crossings, between the S_2 and S_3 states and the S_3 and S_4 states. The vibrational ground and first excited states in each of these modes is shown (dashed lines).

Table 2.2.) Table of Coumarin 466 Excited State Oscillator Strengths

Mode	Disp.	S_1 Oscillator Strength (%S_1)	S_2 Oscillator Strength, (%S_1)	S_3 Oscillator Strength, (%S_1)	S_4 Oscillator Strength, (%S_1)
$\nu_{Ar\text{-}s}$	+1	0.3888 (71%)	0.0154 (3%)	0.1138 (21%)	0.0001 (0%)
	0	0.5444	0.0077 (1%)	0.0249 (5%)	0.0438 (8%)
	-1	0.6706 (123%)	0.0041 (1%)	0.0001 (0%)	0.0250 (5%)
$\nu_{Ar\text{-}a}$	+1	0.4717 (87%)	0.0097 (2%)	0.0563 (10%)	0.0002 (0%)
	-1	0.5987 (110%)	0.0134 (2%)	0.0003 (0%)	0.1139 (21%)
ν_{CO}	+1	0.6137 (113%)	0.0105 (2%)	0.0624 (11%)	0.0003 (0%)
	-1	0.4955 (91%)	0.0007 (0%)	0.0272 (5%)	0.0348 (6%)

The assignments of which molecular orbitals are involved in the transition between the diabatic electronic states are largely unchanged from the equilibrium geometry; however, the energies and characters of the molecular orbitals themselves are strongly affected (Figure 2.8). The nearly-degenerate O.M.O. 55 and 56 that contribute to the third transition $S_3 \leftarrow S_0$ have an avoided crossing near zero displacement, and thus the symmetry-broken O.M.O. 55 and 56 will contain mixed character (Figure 2.9). At positive and negative displacements along the coordinate, O.M.O. 55 and 56 appear to regain some symmetry and anti-symmetry, suggesting that the two diabatic MOs are planar (σ-like) and antisymmetric (π-like) in character.

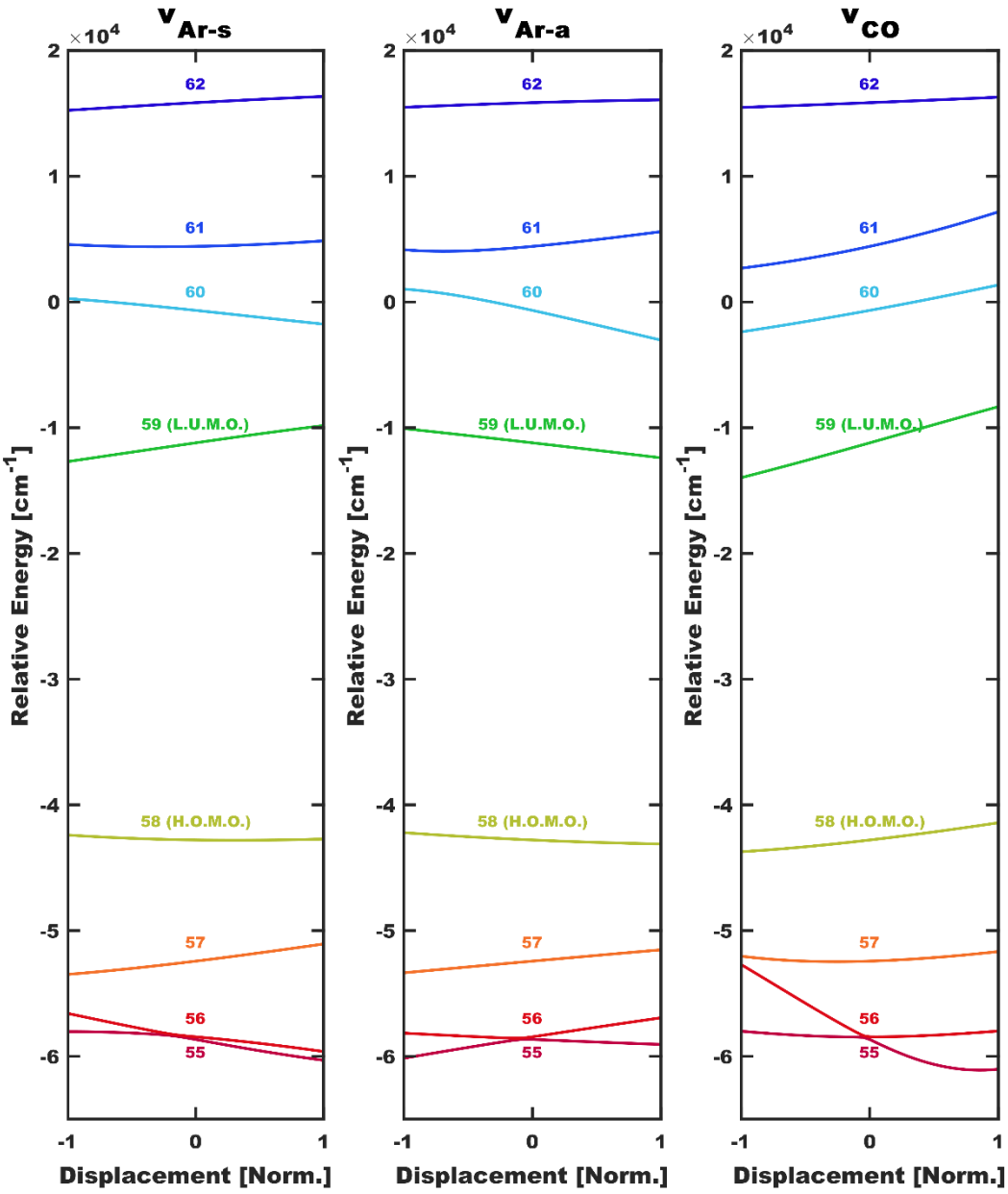

Figure 2.8) Coumarin 466 Molecular Orbital Changes as a Function of Nuclear Displacement. Similar to the electronic transitions, the KS energy eigenvalues of the molecular orbitals in C466 are affected by the nuclear displacement for the $\nu_{Ar\text{-}s}$, $\nu_{Ar\text{-}a}$, and ν_{CO} modes. However, the nearly degenerate O.M.O. 55 and 56 also show an avoided crossing. The H.O.M.O. energy eigenvalue is the only quantitatively meaningful value, as it is approximately equal to the first ionization potential.

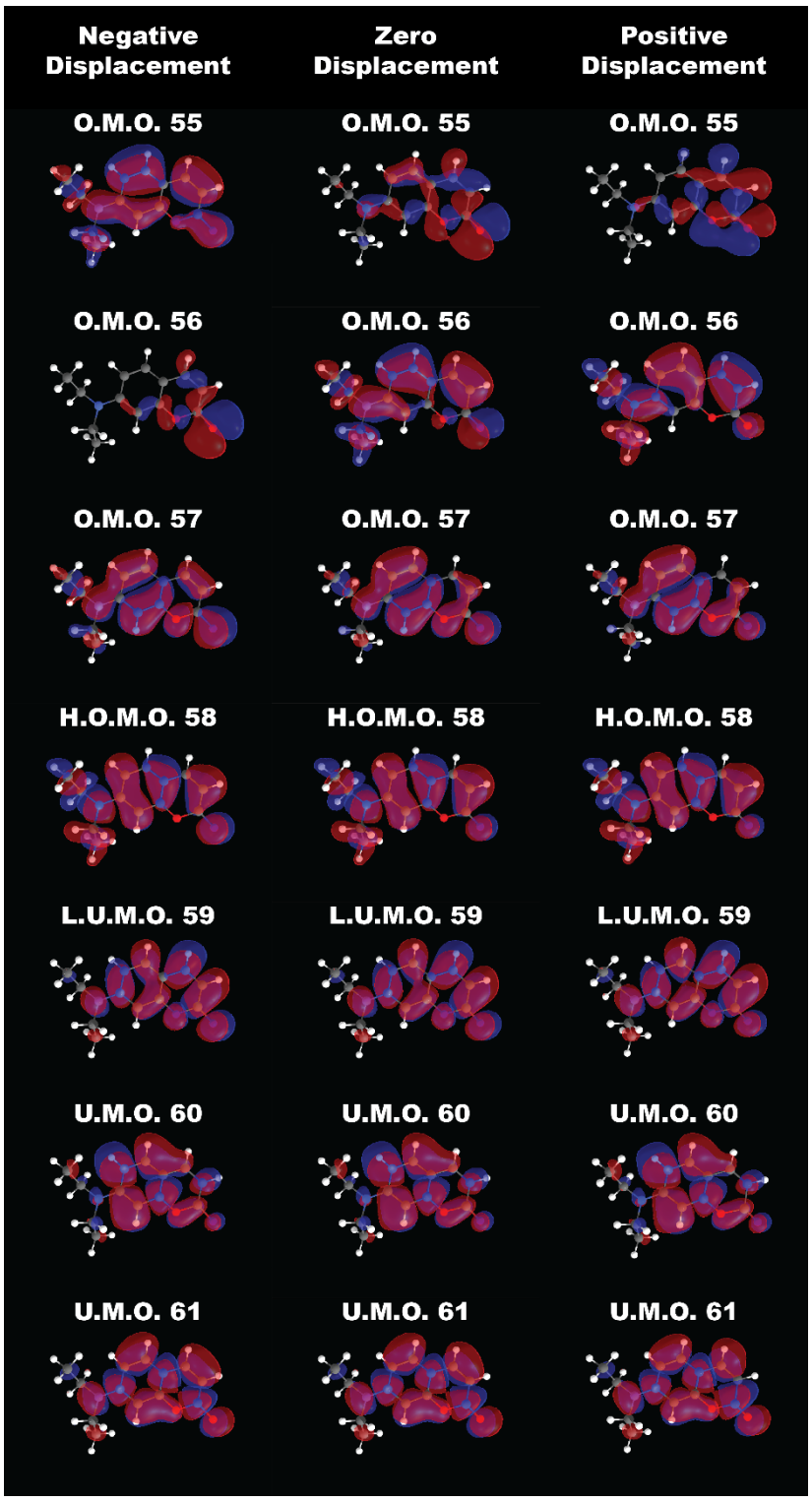

Figure 2.9) Coumarin 466 Molecular Orbital Changes as a Function of Nuclear Displacement in the ν_{CO} mode. The occupied molecular orbitals 55 and 56 in C466 are most strongly affected by the nuclear displacement of the ν_{CO} mode, and exchange some of their character when displaced past an avoided crossing.

2.4 Discussion and Conclusions

These results can be used to predict qualitative behaviors of Coumarin 466. Firstly, the ensemble of aminocoumarin molecular rotors observed in a vibrational measurement should consist mainly of molecules with little rotation of the diethylamino moiety, in a racemic mixture of conformational enantiomers due to the chiral rotor geometry. The first, second, and fourth electronic singlet transitions can be assigned as a shift of electron density from the molecular rotor to the aromatic coumarin core, while the third singlet transition can be assigned as an anti-symmetrization of the electron density from a symmetry-broken ground state. Displacements along a nuclear coordinate, such as can be observed in an excited vibrational population state, will result in a change of the electronic transition energies and oscillator strengths. Further, the nature of higher-lying electronic states will be altered due to avoided crossings of diabatic states. In sum, these results can be used to predict that a change in an electronic transition, or an observable proportional to the electronic transition, could be used to report on a change in the nuclear structure of Coumarin 466 induced by a vibrational excitation.

Chapter Bibliography

(1) Frisch, M. J.; Trucks, G. W.; Schlegel, H. B.; Scuseria, G. E.; Robb, M. A.; Cheeseman, J. R.; Scalmani, G.; Barone, V.; Mennucci, B.; Petersson, G. A.; et al. Gaussian 09, Revision D.01. *Gaussian 09, Revision D.01, Gaussian, Inc., Wallingford CT*. 2009.

(2) Tomasi, J.; Mennucci, B.; Cammi, R. Quantum Mechanical Continuum Solvation Models. *Chem. Rev.* **2005**, *105* (8), 2999–3093.

(3) Stephens, P. J.; Devlin, F. J.; Chabalowski, C. F.; Frisch, M. J. Ab Initio Calculation of Vibrational Absorption and Circular Dichroism Spectra Using Density Functional Force Fields. *J. Phys.*

Chem. **1994**, *98* (45), 11623–11627.

(4) Hamel, S.; Duffy, P.; Casida, M. E.; Salahub, D. R. Kohn-Sham Orbitals and Orbital Energies: Fictitious Constructs but Good Approximations All the Same. *J. Electron Spectros. Relat. Phenomena* **2002**, *123* (2–3), 345–363.

(5) Rauhut, G.; Pulay, P. Transferable Scaling Factors for Density Functional Derived Vibrational Force Fields. *J. Phys. Chem.* **1995**, *99* (10), 3093–3100.

(6) Irikura, K. K.; Johnson, R. D.; Kacker, R. N. Uncertainties in Scaling Factors for Ab Initio Vibrational Frequencies. *J. Phys. Chem. A* **2005**, *109* (37), 8430–8437.

(7) Stowasser, R.; Hoffmann, R. What Do the Kohn-Sham Orbitals and Eigenvalues Mean? *J. Am. Chem. Soc.* **1999**, *121* (14), 3414–3420.

(8) Ziegler, T. Approximate Density Functional Theory as a Practical Tool in Molecular Energetics and Dynamics. *Chem. Rev.* **1991**, *91* (5), 651–667.

(9) Michl, J.; Sykes, E. C. H. Molecular Rotors and Motors: Recent Advances and Future Challenges. *ACS Nano* **2009**, *3* (5), 1042–1048.

(10) Haidekker, M. a; Theodorakis, E. a. Environment-Sensitive Behavior of Fluorescent Molecular Rotors. *J. Biol. Eng.* **2010**, *4*, 11.

Chapter 3

Two-Photon-Excited Fluorescence-Encoded Infrared Spectroscopy[1]

Chapter Abstract

In this chapter, I describe a method for incoherently-detected ultrafast infrared (IR) vibrational spectroscopy in the linear case of Fluorescence-Encoded Infrared Spectroscopy (FEIR) with one Infrared (IR) pulse and one Near-Infrared (NIR) encoding pulse. Vibrational dynamics on the ground electronic state driven by femtosecond mid-infrared pulses are detected by changes in fluorescence amplitude resulting from the modulation of a two-photon visible transition. A series of aminocoumarin dyes were used as model systems to study the behavior of the FEIR signal as a function of solvent and excitation pulse parameters. The measured signal reports on the relaxation dynamics of vibrational populations and coherences, but yields different information than conventional IR transient absorption measurements. These differences result from the manner in which the ground-state dynamics are projected onto the electronic excited state during the two-photon encoding step. These results suggest that FEIR can be adapted for a variety of increased-sensitivity IR vibrational measurements.

[1] Material in this chapter was adapted from a previously published work of the same title (*J. Phys. Chem. A*, **2016**, *120* (46), pp 9178–9187; **DOI:** 10.1021/acs.jpca.6b09158)

3.1 Introduction

Ultrafast infrared (IR) vibrational spectroscopies are established techniques with the time resolution and structural sensitivity required to measure the ultrafast structural dynamics of complex molecular systems. However, these techniques can be limited by low signal levels when studying solutions and biophysical systems. IR transitions, often with an extinction coefficient on the order of 100 M^{-1} cm^{-1} or less, are commonly investigated at 0.1–5.0 molar concentrations in solution, and rarely under 10^{-4} M, for biological macromolecules whose physiological concentrations are μM–pM. Besides weak absorption cross sections and lack of radiative emission channels, the experimental sensitivity of IR spectroscopy is limited by the low band-gap IR detectors that require liquid nitrogen cooling and are less sensitive (and noisier) than those in the visible range. The lower concentration limit has driven interest in developing new types of high-sensitivity IR spectroscopy.

In gas-phase experiments, several high-sensitivity IR spectroscopies have been developed that measure the influence of IR light fields on more sensitive experimental observables, for instance in photoacoustic and ion dip detection techniques[1–5]. However, the application of these techniques to solution-phase measurements is difficult, if not fundamentally infeasible. However, the change in the resonance of a vibronic transition upon vibrational excitation suggests that an electronic transition can be used as a sensitive observable to report on vibrational dynamics in the solution phase. In this measurement, an IR-driven vibrational excitation on the ground electronic state of a system is encoded onto an excited electronic population through a nuclear-dependent electronic transition. The resulting visible fluorescence will be proportional to the encoded excited state population, and can be measured as the

experimental observable. Herein, we refer to the process of upconverting a ground-state vibrational excitation into an electronic population that fluoresces as "fluorescence encoding".

Fluorescence-encoded IR (FEIR) vibrational spectroscopy was initially investigated by Kaiser and co-workers in the 1970s as part of the then-emerging field of picosecond IR spectroscopy[6–9], but few investigations have followed up on this concept using modern ultrafast laser technology[10–14]. More recently, fluorescence encoding has also been used as a strategy for super-resolution IR vibrational imaging[15,16]. Although a growing number of coherent mixed electronic–vibrational spectroscopies are currently being used to investigate coupled electronic–nuclear dynamics[17,18], the motivation for our studies is vibrational spectroscopy on the ground electronic state[19]. By analogy to fluorescence-detected coherent electronic spectroscopies[20–25], this technique can possibly be extended to Fluorescence-Encoded Fourier transform measurements and even higher-order nonlinear FEIR measurements.

This chapter explores a fluorescence-encoding process in which the vibronic transition occurs through an electronic two-photon absorption (TPA)[26]. Two-photon-excited fluorescence induced by a femtosecond near-IR (NIR) pulse was chosen as the experimental observable to increase detection contrast, as the excitation wavelength can be easily filtered from the fluorescence emission[27]. The experimental principle of two-photon-excited fluorescence-encoded infrared (TPE-FEIR) spectroscopy is shown in Figure 3.1. The NIR encoding pulse is chosen to be at a frequency less than half of the electronic transition frequency, such that the two-photon transition between the ground and first electronic state is off-resonance at the nuclear ground state equilibrium (Figure 3.1A), and on-resonance upon nuclear excitation (Figure 3.1D). Ultrafast mid-IR pulses are used to drive resonant vibrational transitions within the pulse bandwidth (Figure 3.1C). Following an encoding-time delay, the NIR light excites a two-photon absorption ending in an excited electronic state (Figure 3.1D). The electronic

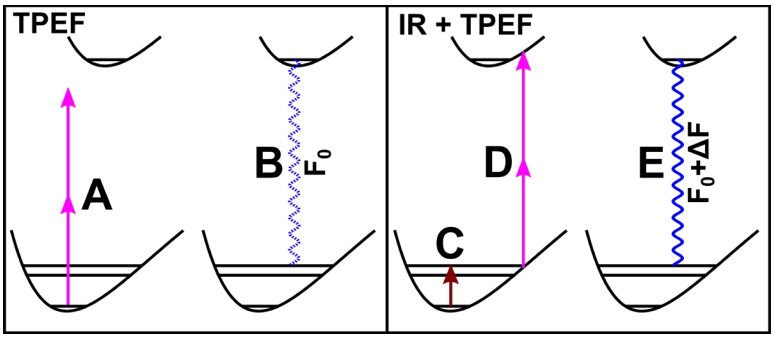

Figure 3.1) A Physical Description of the TPE-FEIR Technique. Left) In absence of nuclear excitation, the NIR two-photon absorption pulse **(A)** is off resonance with the electronic transition, resulting in the emission of little or no fluorescence **(B)**. **Right)** With the addition of a mid-IR vibrational excitation pulse **(C)**, the electronic transition is brought on-resonance with the two-photon absorption encoding pulse **(D)**, resulting in an increase of the fluorescence intensity **(E)**.

population then relaxes through the emission of incoherent fluorescence (Figure 3.1B,E). A ground-state vibrational excitation of vibronic modes will alter the TPA transition resonance, resulting in a change in electronic population and thus a change in fluorescence intensity, which is the experimental observable.

To lay the experimental groundwork for the expected incoherently-detected fluorescence signal, the steady-state vibrational and electronic spectra for the aminocoumarin samples of interest are characterized. Then, to test the experimental predictions, the simplest case of TPE-FEIR is presented: a single IR excitation pulse followed by a single TPA pulse. The resulting delay-time-dependent fluorescence signal is found to be sensitive to dynamics of the vibrational excitation, and shows contributions from both vibrational populations and coherences. The signal is characterized as a function of experimental variables such as pulse intensity and polarization, electronic transition resonance, and solvent. These observations allow the description of several physical properties governing the experimental observable and discuss future extensions to more complex pulse sequences.

3.2 Materials and Methods

3.2.1 TPE-FEIR

NIR ultrafast pulses (93 fs FWHM by autocorrelation, 800 nm, horizontally polarized, 1 kHz) from a regenerative amplifier system (Libra, Coherent Inc) were used (Figure 3.2) to pump a two-stage optical parametric amplifier (OPA) with difference frequency generation (DFG) mixer attachment (TOPAS-DFG, Light Conversion). Signal and idler from the first stage at 1430 and 1900 nm were mixed to generate the mid-IR pulses at 1735 cm^{-1} with full-width at half-maximum (FWHM) of 200 cm^{-1}. The IR was then resized and collimated with a reflective telescope (Tel1) in the Z geometry, and the residual signal and idler were removed with a coated Ge bandpass filter (F1). The IR was chopped (Ch) at 500 Hz and sent through a polarizer pair (Pol) to set and control the IR intensity at the sample. A small amount of the NIR was picked off reflectively before the TOPAS, sent through a fixed delay line to match the IR path length and attenuated with a gradated filter (Thorlabs NDL-25C-4). The NIR was then sent into a precision delay line (ANT95-L-25 stage with A3200 motion composer, Aerotech) with a retro-reflecting cube mirror to control the IR–NIR detection time delay (τ_d). After telescoping the NIR with a CaF_2 lens pair to match the IR focus (Tel2), the beams were overlapped on a 2 mm Ge Brewster plate (Ge), to transmit the p-polarized IR and reflect the NIR. IR (5 μJ) and NIR (1 μJ) were focused into the sample with a 90° silver parabolic mirror (Par1) to spot sizes of <125 μm and 50 μm, respectively. The IR pulse envelope was characterized by cross-correlating the visible and mid-IR using $(\omega_{800}+2\omega_{IR})$ $\chi^{(3)}$ up-conversion in cellulose. The resulting 160 fs FWHM response and the known NIR pulse width indicate that the mid-IR pulses have a ~90 fs FWHM pulse envelope. Without attenuation,

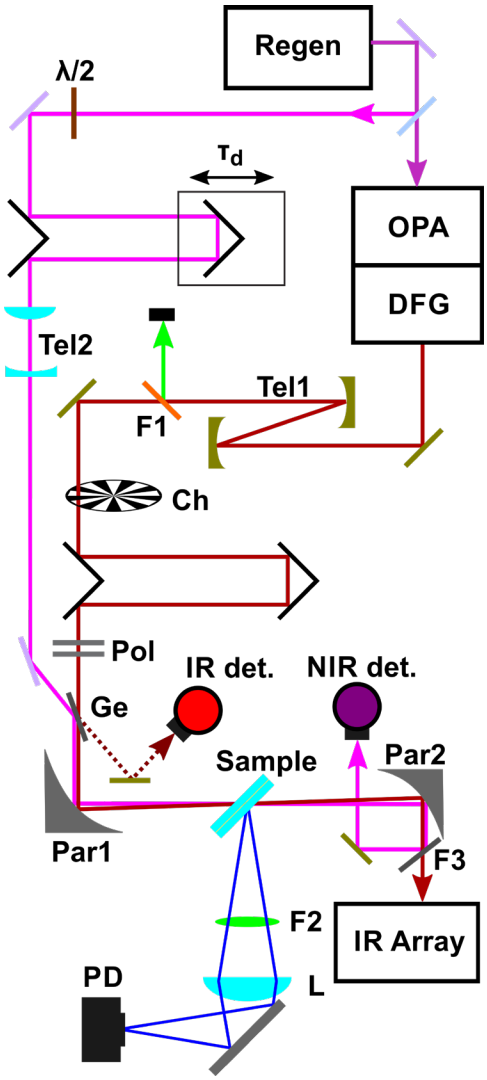

Figure 3.2) TPE-FEIR Experimental Schematic. Most abbreviations are defined in the text. Ch: phase-locked chopper; Det: detector; F1: Germanium red pass filter for mid-IR; F2: Visible fluorescence band pass filter; Ge,F3: germanium Brewster plate, L: lens at 2*f*; λ/2: 800 nm half-wave plate; Par: silver coated parabolic reflector; PD: photodiode; Pol: polarizer pair; Tel: telescope.

the average irradiation within the pulse width was 450 GW/cm^2 for the IR pulse and 570 GW/cm^2 for the NIR pulse.

The fluorescence was optically filtered (F2) with a 30 nm bandpass filter centered at λ=450 nm for C1 and C466 and a 35 nm filter centered at λ=525 nm for C153. The fluorescence polarization was not analyzed. The excitation beams were incident on the sample cell at −45° and the fluorescence was collected from the back face at 90° to the incident light. An *f*= +6 cm lens at 2*f* from the sample (L) was

used to image the fluorescent focal volume onto an avalanche photodiode visible detector (PD) at $4f$ (Thorlabs APD410A). The detector voltage output was windowed and integrated by an SR250 gated integrator, and sampled by a NI PCI 6220 data acquisition card with SCB68 block wired for BNC inputs. The measured differential signal F_1 was measured by chopping the IR beam and subtracting the background fluorescence F_0, which arises from electronic excitation in the absence of vibrational excitation, from the fluorescence, which arises from electronic excitation occurring at time delay τ_d after IR excitation, $F(\tau_d)$:

$$F_1(\tau_d) = F(\tau_d) - F_0$$

3.2.2 Sample Preparation

Samples selected to test this experiment were three coumarin dyes: 7,7-diethylamino-4-methylchromen-2-one (Coumarin 1, C1, also known as Coumarin 480), 7,7-diethylaminochromen-2-one (Coumarin 466, C466), and 2,3,6,7-tetrahydro-9-trifluoromethyl-1H,5H-quinolizino(9,1-gh)chromen-2-one (Coumarin 153, C153). Dyes and absolute ethanol solvent (EtOH) were purchased from Sigma-Aldrich. Cyclohexane-d12 (CH) and tetrahydrofuran-d8 (THF) solvents were purchased from Cambridge Isotope Laboratories. The samples consisted of 70 μL of 1–5 mM dye solution sandwiched between two 1 inch diameter CaF_2 windows (Crystran) separated by a 100 μm Teflon spacer.

3.2.3 Steady-State Spectra

UV–Vis absorption spectra were collected with a Nanodrop UV–Vis spectrometer (Thermo Scientific). FTIR absorption spectra were collected using one of two spectrometers (Tensor II and Vertex 70 with Hyperion 2000 microscope, Bruker) at 2 cm^{-1} resolution. Raman spectra were collected using a confocal

Raman microscope (LabRamHR Evolution, Horiba) with an excitation wavelength of 473 nm for C466 and C1, and 633 nm for C153. IR and Raman spectra were acquired at concentrations between 1–20 mM. Raman spectra were collected using a scattering wavelength of 473 nm for C466, C1 and 633 nm for C153. With the exception of the UV–Vis spectra, steady-state characterizations were performed with the same sample preparation and geometry as described above.

3.2.4 IR Transient Absorption

IR transient absorption (TA) traces were collected on a separate IR pump–probe spectrometer. IR TA traces were acquired using 100 fs IR pulses centered at 1650 cm^{-1} with a band width of 200 cm^{-1}, and the frequency-resolved change in absorption of the probe beam was recorded. TA measurements were acquired at concentrations between 1.8–8 mM.

3.3 Results

3.3.1 Vibrational Spectra

Aminocoumarin dyes were selected to test this experiment as they are well-studied[28–37] environmentally sensitive dyes of low symmetry, with strongly IR-active ring and carbonyl transitions and a high two-photon absorption cross section. The main aminocoumarin core consists of an aromatic group with one of the rings formed by a lactone connectivity, which includes an ester carbonyl. Each of the dyes studied also has a tertiary-amine hindered-rotor moiety linked to the main core through a nitrogen. A further characterization of one of these dyes, Coumarin 466, is presented in Chapter 2.

Vibrational spectra and structures of the coumarin dyes investigated are shown in Figure 3, overlaid with the spectrum of the femtosecond IR pulses used for vibrational excitation. Although exact peak frequencies and relative oscillator strengths differ between the samples, the IR and Raman spectra of the three coumarins studied have qualitatively similar features. All spectra reveal a peak (C153) or pair of peaks (C1, C466) between 1600–1615 cm^{-1} and similarly another between 1515–1545 cm^{-1}, which arise from delocalized in-plane ring stretching vibrations. The FTIR spectrum of C466 in CH (Figure 3.3A) shows a sharp bright transition from a carbonyl mode near 1750 cm^{-1}. This feature is present but appears to be split in both FTIR and/or Raman of C1 and C153 (Figure 3.3D,F), and is further split, weakened, and redshifted (near 1710 cm^{-1}) when C1 is dissolved in polar protic EtOH (Figure 3.3C,E). Although the carbonyl mode frequency is solvent-dependent, the ring mode frequencies do not appear to be significantly affected. The IR pulse spectrum was centered at 1735 cm^{-1} to primarily excite the higher lying ring stretch vibrations and the environmentally-sensitive carbonyl.

The peaks in FTIR and Raman spectra in the region of interest were assigned by calculating normal modes in Gaussian 09d using DFT with the B3LYP/6-31G* functional with SCRF solvent[38–40]. Calculated normal modes, IR transition intensities, and Raman activities of C466 in CH are summarized (Table 3.1), and are shown to have reasonable qualitative agreement with experimental spectra. On the basis of these calculations, the experimental modes can be assigned. The peak pair at 1521 and 1545 cm^{-1} is assigned as ring stretch modes that include C-N stretching (ν_{ArN}), the set at 1608 and 1616 cm^{-1} to ring stretch modes that are mixed with C=O stretching (ν_{Ar}), and the peak at 1748 cm^{-1} to a stretch mode centered on the carbonyl with minimal ring contribution (ν_{CO}). For both pairs of ring modes, the lower frequency mode corresponds to a more symmetric *A*-symmetry stretching motion of the coumarin core, while the higher frequency mode corresponds to a more asymmetric *B*-symmetry stretch-bend

combination motion of coumarin core. There are additional solvent effects influencing the line shape and splitting of carbonyl vibrations in particular, which are discussed in more detail below.

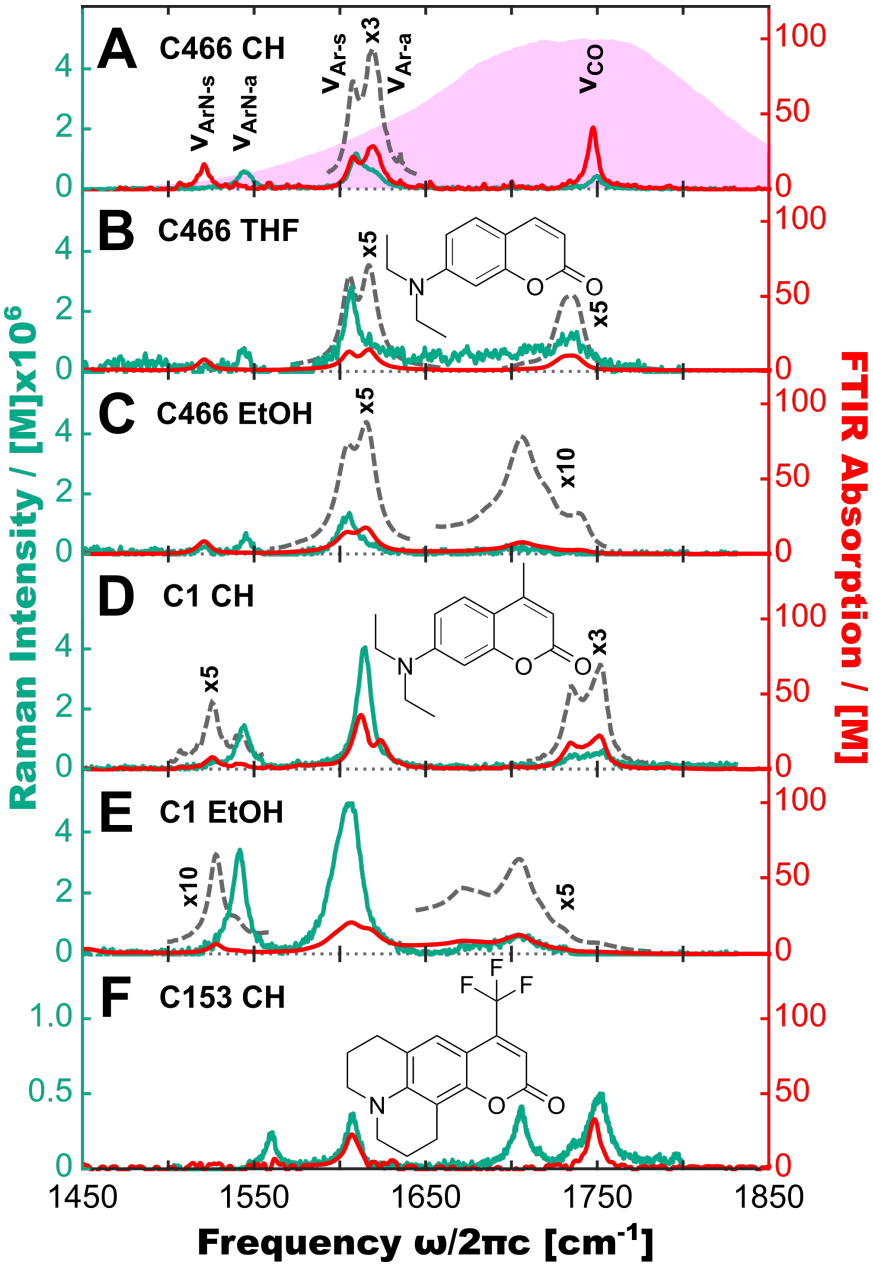

Figure 3.3) Vibrational Spectra of the Model Dyes Examined in This Chapter. The Raman (teal) and IR (red) vibrational spectra of the aminocoumarin dyes in the mid-IR range from 1500 to 1800 cm^{-1} are dominated by aromatic ring and carbonyl stretch modes. With increasing polarity of solvent **(A)** CH, **(B)** THF, **(C)** EtOH, the ν_{CO} mode of C466 is red-shifted, and splits in ethanol. The ν_{CO} mode is split in C1 in CH **(D)**, and red-shifted in EtOH **(E)**. C153 in CH has only two ring modes, and the ν_{CO} mode is strongly split **(F)**. The femtosecond IR excitation pulse spectrum is overlaid **(A, violet)**.

Table 3.1. DFT and Experimental mid-IR Vibrational Transitions in C466.

Mode		$\nu_{ArN\text{-}s}$	$\nu_{ArN\text{-}a}$	$\nu_{Ar\text{-}s}$	$\nu_{Ar\text{-}a}$	ν_{CO}
Exp.	Freq. [cm^{-1}]	1521	1545	1608	1616	1748
	IR activity	Weak	No	Strong	Strong	Strong
	Raman activity	No	Weak	Strong	No	Weak
DFT	Scaled freq. [cm^{-1}]	1513	1519	1602	1612	1766
	IR intensity [km/mol]	183	61	780	290	699
	Raman activity [$Å^4$/AMU]	2	466	1086	26	183
Character Assignment		*A*-like Ring C=C + C-N	*B*-like Ring C=C + C-N	*A*-like Ring C=C + C=O	*B*-like Ring C=C + C=O	Carbonyl stretch

3.3.2 Electronic Spectra

The 0-0 frequency and line shapes of the electronic absorption and fluorescence spectra of the aminocoumarin samples vary as a function of dye structure and solvent (Figure 3.4). In CH, the absorption and emission bands are structured, which is characteristic of a vibronic transition with high-frequency Franck–Condon active vibrational modes in a weakly or non-interacting solvent. Relative to CH, the spectra in EtOH are dominated by polar solvation, and show a strong absorption red-shift, a large increase in Stokes shift, and a loss of structuring in the absorption and emission line shapes [31,35]. The 0-0 crossing of the normalized absorption and fluorescence spectra occur at λ=376 nm, 398 nm, and 416 nm for C466 in CH, THF, and EtOH, respectively; λ=372 nm and 410 nm for C1 in CH and EtOH; and λ=422 nm in C153 in CH. These transition wavelengths can be compared with the 400 nm

resonance of the 800 nm two-photon transition used in the FEIR experiment to predict the sign of the signal. Although the peak fluorescence wavelength varies from λ=390 to 460, all of the samples have appreciable fluorescence intensity in the filtered detection window of 435–465 nm.

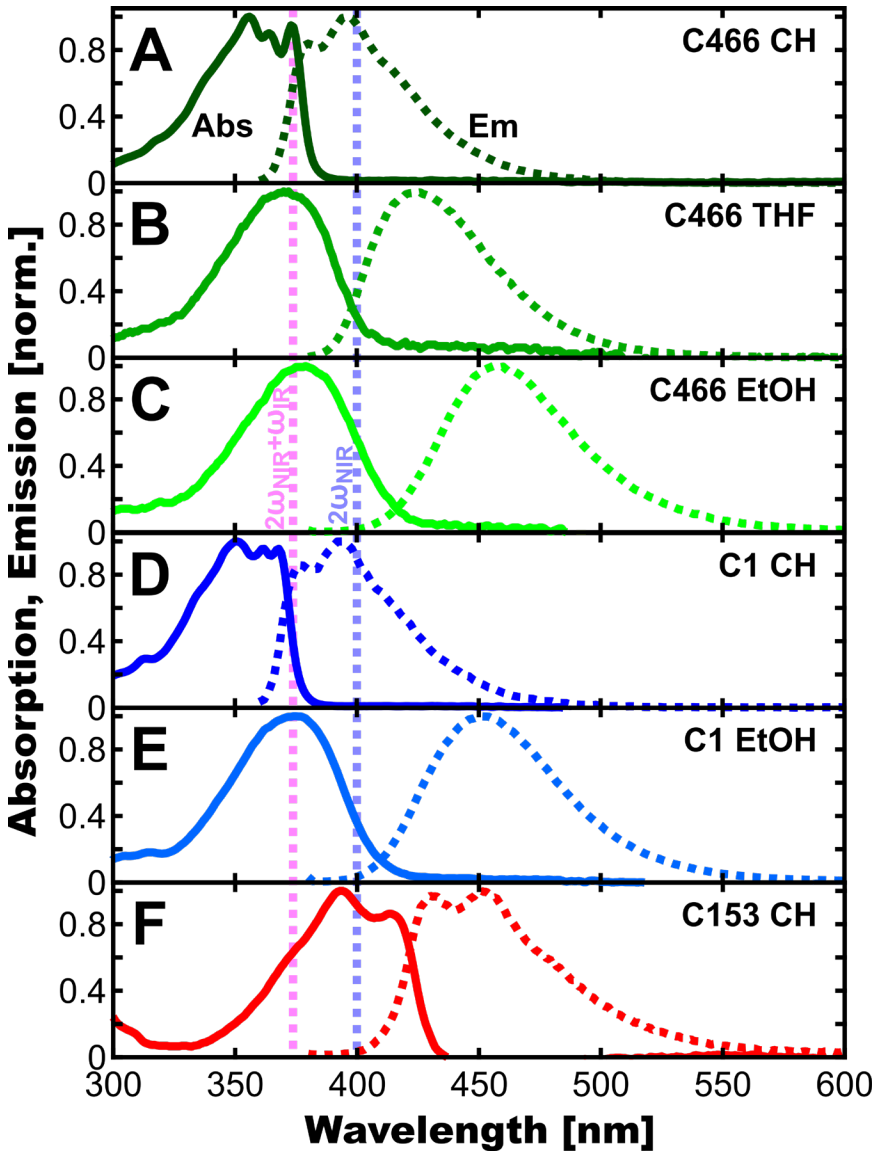

Figure 3.4) Electronic Absorption and Emission Spectra. The aminocoumarin absorption **(solid)** and emission **(dashed)** spectra of the aminocoumarins in cyclohexane are structured **(A,D,F)**, indicating a vibronic transition with Franck-Condon-active vibrational modes and non-interacting solvent. This structuring is lost in polar solvents, and the 0-0 transition frequency is red-shifted with solvent polarity **(B,C,E)**. Vertical dashed lines indicate $2\omega_{NIR}$ **(blue)** and $2\omega_{NIR}+\omega_{IR}$ **(magenta)**. Experimentally, the change upon vibrational excitation would appear as a redshift of the electronic transition.

The doubled two-photon excitation frequency (Figure 3.4, dashed baby-blue) is off-resonance at a longer wavelength than the absorption spectra of C1 and C466, but on-resonance in the case of C153. Although C1 and C466 are not two-photon resonant with 800 nm in CH, in EtOH the red-shifted absorption overlaps slightly with the excitation field. Upon IR excitation of vibrational modes that are vibronically-coupled to the electronic transition, the electronic transition is expected to redshift into resonance with the two-photon excitation frequency (Figure 3.4, dashed magenta) in C1 and C466. In the case of C153, where the two-photon excitation in absence of vibrational excitation lies near the absorption maximum, a vibrational excitation should shift the electronic transition off-resonance with the TPA pulse. From this observation, it can be predicted that the sign of the IR excitation induced change of fluorescence $F_1(\tau_d)$ will be positive in the case of C1 and C466, but negative in the case of C153.

3.3.3 Two-Photon-Excited FEIR

Femtosecond time-resolved TPE-FEIR encoding-time-delay transient traces were collected at parallel polarization (Figure 3.5). Fit timescales of the decay transients are reported in Table 3.2. Following a pulse-length limited rise at τ_d=0, the FEIR measurement of C466 in CH displays a strong 140 cm^{-1} oscillation with a 540 fs damping time, superimposed on a 1090 fs exponential decay. The picosecond exponential decay time is consistent with expected ground-state vibrational lifetime of the carbonyl vibration, which is expected to govern the relaxation of the signal. FEIR of C1 in CH displays a similar behavior, oscillating with 140 cm^{-1} beats that are damped on a timescale of 500 fs superimposed on a 960 fs exponential decay. The form of this signal is consistent with Liouville pathways where the efficiency of the two-photon electronic transition is modulated as a function of τ_d by the vibrational states prepared

by two interactions with the short IR excitation field – ground-state vibrational populations yield an exponential decay and coherences yield a damped exponential form. As predicted from UV-Vis line shapes and the two-photon resonance in §3.3.2, C1 and C466 yield positive signals, while C153 yields a negative signal with a similar oscillatory beating. However, when C466 and C1 are measured in polar solvents, the oscillations of the signal are reduced and a slower picosecond decay occurs. A negative response for $\tau_d<0$ that increases in magnitude with solvent polarity is also observed in the C466 and C1 solvent series. This dip is assigned as an electronic excitation that occurs before and is quenched by the vibrational excitation, which is affected by coupled solvent-solute interactions. As it has a different polarization-dependence from the data for $\tau_d>0$, it can be determined that this signal does not contribute significantly outside of the pulse-overlap region at delay times greater than 100 fs. In addition, the form of the decay in the encoding-time delay in polar solvents (THF and EtOH) is not well-fit by mono or biexponential functions, and can be better fit with a power-law decay (Table 3.2).

A Fourier analysis was performed on the oscillations in the fluorescence transients (Figure 3.5 insets). The highest intensity frequency component matches the ν_{CO}-$\nu_{Ar\text{-}s}$ difference frequency observed in the IR spectrum. As the solvent polarity red-shifts the carbonyl, the oscillation of the coherence between the ν_{CO}-$\nu_{Ar\text{-}s}$ modes shifts from the free carbonyl spacing at ~140 cm^{-1} to the hydrogen-bonded carbonyl spacing at ~100 cm^{-1}, and is consistent with the FTIR spectra.

To assist in the phenomenological determination of the signal origin and assess its similarity to other techniques, IR transient pump-probe traces in the waiting time delay τ_2 of the Ground State Bleach (GSB) and Excited State Absorption (ESA) features were acquired for a similar delay range (Figure 3.5, Figure 3.A1.4).[41] The ν_{CO} ESA is broad and weak and its temporal behavior could not be with much certainty. The IR pump–probe traces show some qualitative, but not quantitative, similarities to the

fluorescence-detected measurement. Similar oscillations appear at early times in CH and THF, but are much weaker in the IR TA signal than in the fluorescence-detected measurement. In addition, the

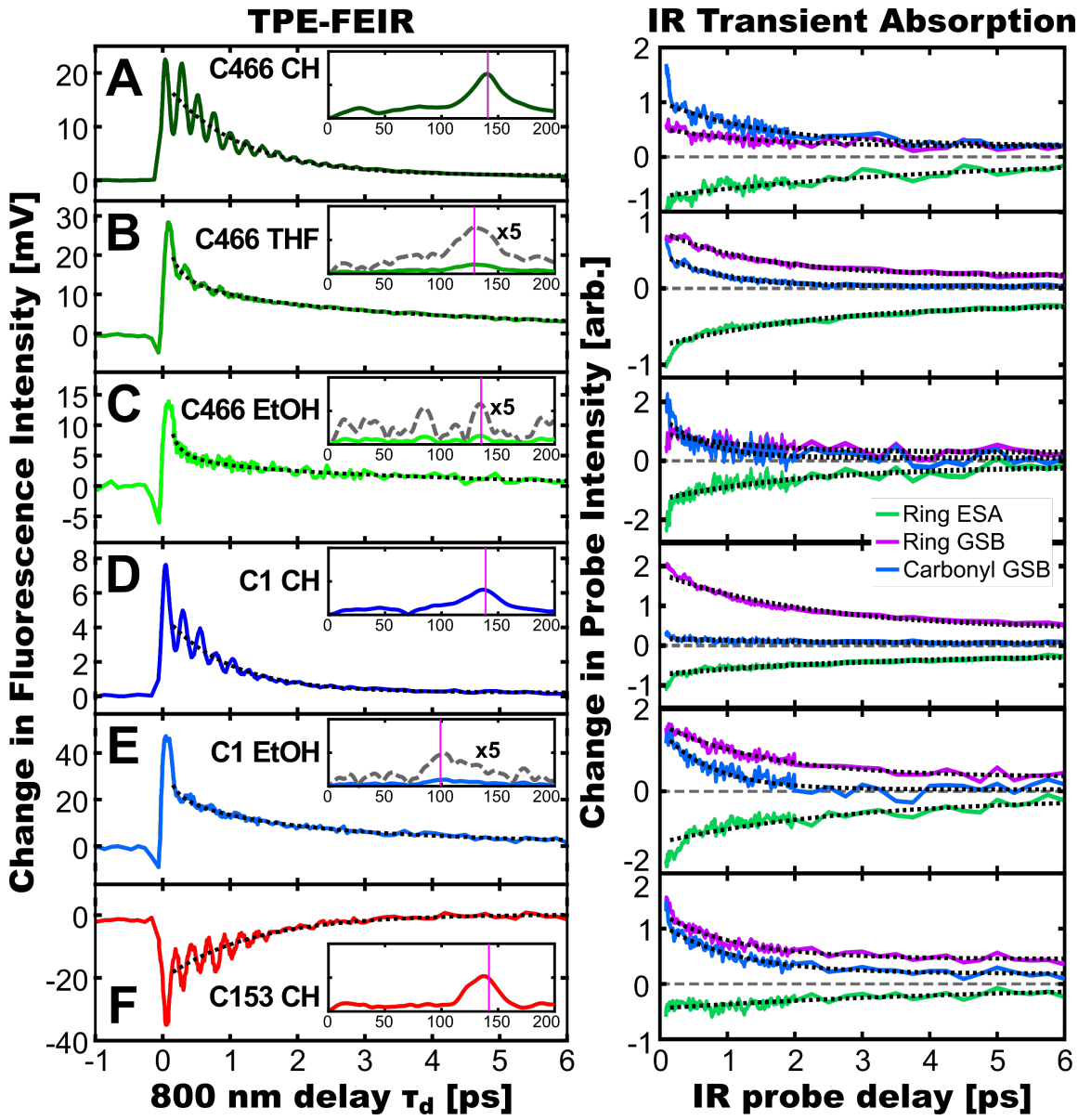

Figure 3.5) Comparison Between One-IR-Pulse FEIR and Nonlinear Pump-Probe Traces. TPE-FEIR signal **(Left)** displays significant differences from IR pump–probe measurements **(Right)**. In non-polar solvents, the FEIR of aminocoumarins contains a strong oscillatory component as a function of the encoding time τ_d **(A,D,F)**. As the solvent polarity increases, these components decrease in intensity, and the decay appears consistent with a power-law functional form **(B,C,E)**. Insets show the power spectra of the beat frequencies observed in the FEIR transients. For comparison, vertical lines corresponding to the $\nu_{Ar\text{-}s}$- ν_{CO} peak spacing calculated from the FTIR spectra are overlaid.

oscillations in the IR pump-probe transients dephase faster, and in CH appear to be π phase-shifted from the F_1 oscillations. In the case of polar solvents, the IR pump-probe oscillations are in-phase with the F_1 oscillations. This effect is consistent with what is expected by tuning the 0-0 transition frequency from a higher frequency than the doubled frequency of the TPA encoding pulse spectrum to a lower frequency. The timescales observed in the IR pump-probe decays decrease with increasing solvent polarity, similar to observed beat dephasing timescales in F_1. The F_1 decay timescales do not appear to follow the same trend as the IR TA timescales. This indicates that while similar physical processes (vibrational populations and coherences) contribute to both the F_1 and IR TA data, how they are projected onto the experimental observable (a nuclear dipole polarization that emits coherently versus an electronic population prepared through electronic dipole hyperpolarizability) will affect the signal observed.

Table 3.2. Summary of IR Pump-Probe and FEIR Relaxation Timescales.

Sample	TPE-FEIR				IR Pump–Probe		
	F_1 timescale (timescales) [fs]	Beat amp [%]	Beat Decay [fs]	F_{1Max}/F_0 [%]	Ring ESA [fs]	Ring GSB [fs]	CO GSB [fs]
C466 CH	1090 (895, 3080)	32	540	160	4590	1500	1580
C466 THF	PL exponent -0.55 (804, 6680)	9	460	9	2320	1440	820
C466 EtOH	PL -0.98 (801, 6290)	5	120	0.8	2110	1290	620
C1 CH	960 (896, 1850)	18	500	110	3110	2190	1850
C1 EtOH	PL -0.53 (800, 4220)	5	370	1.6	2820	1530	740
C153 CH	1310 (1310, 1300)	17	860	-0.9	5300	1120	1100

For comparable concentrations of C1, H-bonding solvent yields both increased signal (F_1) and reference (F_0) intensities as the electronic transition is red-shifted to be more on-resonance with the

encoding pulse in the absence of vibrational excitation. However, this trend is not observed in C466, where H-bonding solvent only increases the reference fluorescence intensity and the signal is unchanged. For comparable concentrations, C466 in CH versus C466 in EtOH yield similar signal levels, however the signal level C1 in CH is about 10% of that in EtOH. This follows the same trend observed in Raman spectra for the $\nu_{Ar\text{-}s}$ feature, which is not changed appreciably in C466 regardless of solvent but significantly increases for C1 in EtOH.

The signal intensity scales nonlinearly with IR pump intensity (Figure 3.6A) and quadratically in 800 nm intensity in both nonpolar and polar solvents (Figure 3.6B). The IR intensity dependence is best described by a sum of linear and quadratic components over the range of intensities investigated, suggesting multiphoton excitation processes can contribute to the highest intensity pump signals. However, normalized IR intensity-dependent time traces in C1 show no difference with pump intensity (Figure 3.A1.3). The FEIR signal of C1 in CH has a $\cos^4\theta$ dependence on the angle between the NIR and IR polarization axes, with a constant offset, as expected for a TPA probe (Figure 3.6C), with strongest signal at parallel polarization between IR and NIR fields (θ=0°).

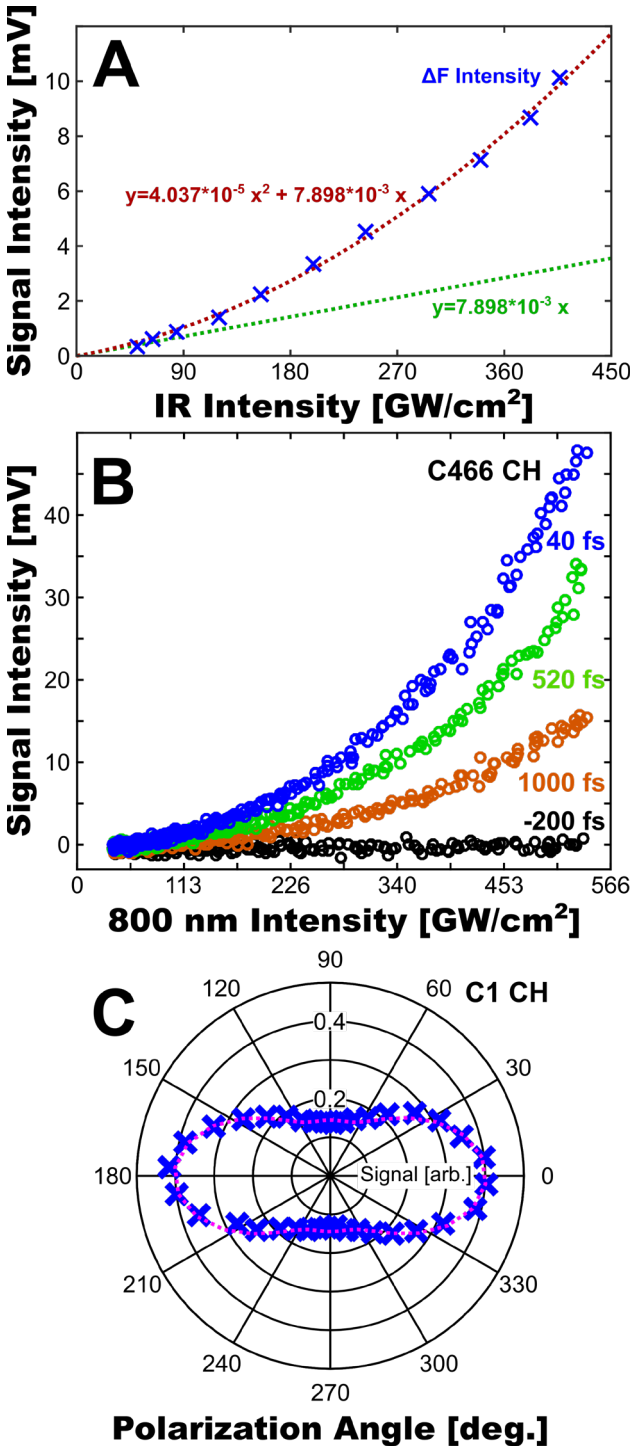

Figure 3.6) FEIR Dependence on Pulse Intensity and Polarization. A.) The FEIR signal in C466 in CH, at an encoding time τ_d=100 fs, scales quadratically with respect to IR intensity. **B.)** The FEIR signal in C466 in CH, at an encoding time τ_d=50 fs, scales quadratically with respect to NIR intensity. **C.)** The FEIR signal in C1 in CH **(blue)**, at an encoding time τ_d=100 fs, scales with the functional form $S(\theta) \approx 2\cos^4\theta+1$ **(magenta)** as a function of the angle θ between the IR and NIR polarization axes.

3.4 Discussion

3.4.1 The TPE-FEIR Signal

In this two pulse TPE-FEIR experiment, the time ordering of the pulses and causality dictate that vibrational excitations are prepared on the ground electronic state. The observed coherences indicate that it is possible to excite and detect a superposition of multiple vibrational modes, i.e. coherences and populations of vibrational modes with different nuclear coordinates. As the experimental observable is two-photon-excited fluorescence, a detected signal then reports on a change in two-photon transition probability with respect to the displacement of the nuclear coordinates. However, the nuclear motion as viewed through this process appears to contain different information than conventional fully mid-IR TA measurements, even though both experiments in principle prepare the same initial vibrational states. The dynamic timescales and functional form of the relaxation processes measured in the two experiments do not match. In a nonpolar solvent, the TPE-FEIR signal decays more quickly than in IR TA, and in polar solvent, it adopts a power-law decay not observed in the TA data. Oscillations at the same frequency are observed in the F_1 and TA decay transients, but appear to be much stronger in amplitude in the former. Of interest, then, is how the vibrational information in TPE-FEIR spectroscopy is projected onto the two-photon electronic transition.

As a detailed theory of this experiment would be too lengthy in this chapter, and is explored in detail in Chapter 7, here I will outline the elements that are needed to describe this process. As a simplification, it is practical to consider the observed TPE-FEIR signal as proportional to the electronically excited state population following the NIR encoding pulse which resulted from IR excitation at a time τ_d earlier. A

density matrix representation allows us to describe the vibrational coherences that we see in experiments. $\rho_{ee}(\tau_d) = \langle e | R^{(4)}(\tau_d) \boldsymbol{\mathcal{E}}_{IR}^2 \boldsymbol{\mathcal{E}}_{NIR}^4 | e \rangle$

Based on analogy to other incoherently detected coherent pump–probe experiments[21,24,42,43], the electronic excited state population $\rho_{ee}(\tau_d)$ can be expressed schematically in terms of a quasi-third-order response function $R^{(4)}$: $R^{(4)}(\tau_d) = \left\langle \left[\widehat{\mathrm{M}}(\tau_d), \left[\widehat{\mathrm{M}}(\tau_d), \left[\hat{\mu}, \left[\hat{\mu}, \rho_0 \right] \right] \right] \right] \right\rangle$ [II]

Here ρ_0 is the equilibrium density matrix, $\hat{\mu}$ and $\widehat{\mathrm{M}}$ are the electric dipole and two-photon transition operators in the interaction picture, and $\boldsymbol{\mathcal{E}}$ are the incident electric fields.

This response function will contain terms where ground-state vibrational coherences are encoded into excited electronic populations (Figure 3.7). These vibronic excitations ultimately relax primarily through radiative fluorescence pathways. Although there are clear similarities between the quasi-third-order response function presented here and the third-order response of third-order nonlinear spectroscopy, there are some differences between the two – primarily that not all of the terms of the full third-order response function will contribute to the FEIR signal. The four field interactions in the quasi-third-order response imply an even-order nonlinear spectroscopy, which will not emit a coherent signal in isotropic media. This necessitates that the signal observed in fluorescence-detected experiments will arise from the spontaneous emission of an ensemble of independently-radiating emitters.

Considering processes such as those in Figure 3.7 leads to

$$\rho_{ee}(\tau_d) \propto \sum_{i,m,n} P_i \; M_n(\tau_d) M_m^*(\tau_d) U_{\mathrm{nm}}(\tau_d) \mu_{ni} \mu_{mi}^* I_{IR} I_{vis}^2$$

[II] It can be shown with cyclic invariance that this nested commutator is identical to Mukamel's.

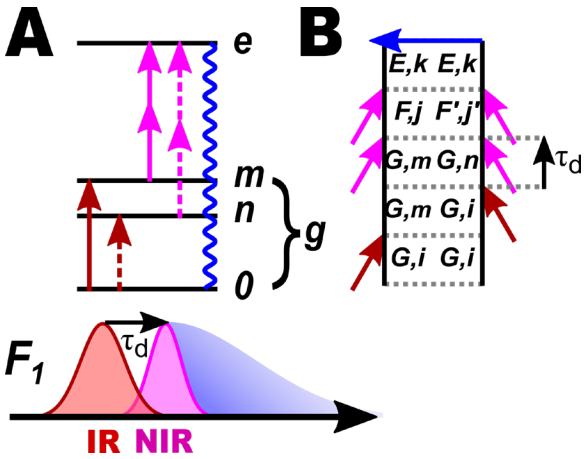

Figure 3.7) Diagrams of a Sample FEIR Liouville Pathway Containing a Vibrational Coherence. An FEIR Liouville pathway in which a vibrational coherence is prepared and then encoded into an electronic excited state population can be represented with a Lee-Albrecht Ladder Diagram **(A)** or with a Feynman diagram **(B)**. An IR excitation creates a superposition of vibrational states resonant within the bandwidth of the mid-IR pulse. Following evolution over τ_d, a two-photon excitation encodes the ground-state vibrational excitation onto an electronically excited state.

The equilibrium thermal occupation of states is $P_i = \langle i | \rho_0 | i \rangle$, U_{nm} is a propagator for the vibrational excitation on the ground electronic state, and I are the intensities of the incident electromagnetic fields. The light–matter interaction is governed by the matrix elements of the dipole operator projected onto the polarization of the incident fields, $\mu_{Gn,Em} = \langle G,n | \bar{\mu} \cdot \hat{\varepsilon} | E,m \rangle$, which can be written for vibrational transitions on the ground electronic state as $\mu_{mn} = \mu_{Gm,Gn}$. The hyperpolarizability matrix elements in the two-photon operator involve a sum over all intermediate states $|F,j\rangle$:

$$M_n = \sum_F \sum_{j,k} \mu_{Ek,Fj} \mu_{Fj,Gn}$$

In eq. (2) the result of the propagator operating on the *n* and *m* states can be written as

$$U_{\mathrm{nm}}(\tau_d) = \exp\left[-(i\omega_{\mathrm{nm}} + \gamma_{\mathrm{nm}})\tau_d\right]$$

where $\hbar\omega_{\mathrm{nm}}$ is the energy difference of the $|G,n\rangle$ and $|G,m\rangle$ states, and γ_{nm} is a phenomenological damping constant. In the time-domain representation, resonance line shape functions for the IR and

TPA excitation are not explicitly defined, but result from the frequency-domain representation for monochromatic electric fields and the propagator U_{nm}.

The quasi-third-order polarization predicts that the TPE-FEIR signal will scale linearly with IR intensity, quadratically with visible intensity, and have a $\cos^4\theta$ dependence on the angle between the IR and visible field polarizations. The NIR intensity-dependence shows that the observed F_1 signal intensity scales quadratically with the NIR intensity, with a $\cos^4\theta$ dependence on the angle between the IR and NIR polarization axes, as expected. The mid-IR power dependent measurements, however, also show a nonlinear scaling of signal intensity with respect to I_{IR}, rather than a fully linear dependence (Figure 3.6A). From this observation it can be inferred that the IR intensities used might drive FEIR signals that are non-linear in the IR. If so, the form of the FEIR decay should be intensity dependent; however, the time-resolved FEIR decay transients appear identical when the IR pump intensity is varied (Figure 3.A1.3). Thus, a further investigation of nonlinear FEIR is necessary, and I present efforts toward this end in Chapter 6.

Although orientational relaxation during τ_d has not been fully characterized in these experiments, the polarization dependence of orientational relaxation should follow the six point correlation functions derived for resonant fifth order nonlinear experiments[44]. These expressions predict that the orientational response function for parallel and perpendicular polarizations should scale as $S_{\parallel} = 1 + \left(\frac{8}{7}\right) c_2(\tau_d)$ and $S_{\perp} = 1 - \left(\frac{4}{7}\right) c_2(\tau_d)$, where the orientational correlation function for the alignment of the IR dipole transition dipole moment and two photon transition is

$c_2(\tau_d) = \langle P_2(\mu(0)M(\tau_d)) \rangle$. This implies that a magic angle of 54.7° exists for suppressing signal contributions from orientational relaxation in the detection time τ_d.

3.4.2 The Two-Photon Encoding Interaction

The enhancement of the coherence amplitudes in TPE-FEIR over IR TA are an indication of how the two-photon encoding process projects the IR-initiated ground-state dynamics onto an electronic population. In the case of one-photon encoding, the FEIR signal requires a vibronic coupling of the vibrational coordinate to a resonant electronic transition. However, in the two-photon-encoded case, the observable depends on double-overlap matrix elements for transitions involving numerous intermediate electronic states. Some of these transitions can be more strongly varied as a function of nuclear coordinate than that for the single-photon-encoding probe case. Additionally, as the symmetry of the initial, intermediate, and final electronic and vibrational states contribute, different selection rules apply than for those excited by a linear encoding process. As a product of two transition dipole elements, the two-photon transition will be larger for initial and final states with similar symmetries.

3.4.3 Coumarin Solvation and Spectroscopy

Although the primary objective was to test the proposed TPE-FEIR experiment, the investigation in this chapter also provided new insights into the spectroscopy and dynamics of coumarins. Returning to the vibrational spectra (Figure 3.3), I note that split pairs of carbonyl peaks are observed in some cases while only a single peak is predicted by DFT calculations of isolated aminocoumarins. Although an extra resonance could result from Fermi resonance or another anharmonic effect, the solvent dependence suggests another origin. In cyclohexane, the ν_{CO} mode is not split in C466 but is split in C1 and C153. In ethanol, the ν_{CO} mode of C466 is split, and the carbonyl stretch mode is reduced and broadened and red-

shifted for both C1 and C466 in hydrogen-bonding ethanol. These differences arise despite the fact that the only structural difference between C1 and C466 is the addition of a methyl at the 4 position of the lactone ring, *meta* to the carbonyl. As a weakly electron-donating group, the addition of the methyl could stabilize C-O^- character in the carbonyl, and upon weakening and lengthening of the carbonyl bond, the stretch mode should redshift. As a peak pair is observed, this suggests a bimodal distribution of carbonyl bond strengths in the experimental ensemble of C1 molecules. The behavior in EtOH is very likely due to varying hydrogen bond configurations between the solvent and the carbonyl oxygen that result in a lengthening of the CO bond and stabilization of the negative partial charge on the carbonyl oxygen. DFT calculations predict a ~50 cm^{-1} peak shift in ν_{CO} for C466 and C1 when an explicit ethanol molecule is hydrogen bonded to the carbonyl (Figure 3.A1.2A,B). However, variation in carbonyl-solvent interactions is an unlikely explanation for C1 carbonyl splitting in a weakly interacting solvent such as cyclohexane. Therefore, this might arise from indirect effects that are not local to the carbonyl, such as conformational changes of the conjugated C-N rotor and resonance structures involving the two oxygens of the pyranone group.

The effects of electronic state on the molecular rotor have been well studied, both in literature and in Chapter 2. In the ground electronic state, there is a single potential energy minimum as a function of rotor angle for a rotor in-plane with the coumarin core, while the excited electronic state has a local minimum at the same twist geometry as well as a global minimum in a more twisted state. In order to elucidate the effect of rotation on the ground-state vibrational spectra, DFT calculations were perfomed at these geometries, fixing the rotation angle (Figure 3.A1.2C, Figure 2.5). These calculations reveal that the ring modes change in frequency and intensity with rotor angle, but the carbonyl frequency is not strongly affected. As the diethylamino group rotates away from the ground-state optimized geometry,

splitting of the $\nu_{ArN\text{-}s}$–$\nu_{ArN\text{-}a}$ peak pair at 1520–1545 cm^{-1} increases from ~5 cm^{-1} to ~23 cm^{-1}, and the intensity of the $\nu_{Ar\text{-}a}$ mode increases relative to the $\nu_{Ar\text{-}s}$ peak. From this, it can be predicted that C466 exhibits the most ground-state twisting character in the experimentally observed FTIR ring modes, while C153 exhibits the least, as expected due to structure. While the potential energy scan in chapter 2 predicts that the rotor should be "locked" in the ground state configuration, that calculation does not include entropic effects that might contribute experimentally. While molecular rotation is dependent on the solvent viscosity[29], CH and EtOH have similar viscosities and show differences in vibrational twisting signatures. Experimentally, the spectra reflect an inverse relationship between the signatures of ground-state twisting and the observed carbonyl splitting, which implies that resonance structures involving the carbonyl and rotor nitrogen might be responsible for the carbonyl splitting effect. Thus, the FTIR and Raman spectra of the coumarin dyes simultaneously provide information about both the electronic character and the state of the molecular rotor in the observed ensemble.

In the linear electronic absorption and emission spectra, typical polar solvation trends[31,35] are observed. A change of solvent from nonpolar CH to polar-protic EtOH causes a loss of structuring in the spectra and a redshift of the absorption, as well as a Stokes' shifting of the emission. The observed ensemble of coumarins then experiences a wider distribution of polar environments due to solvent orientation dependence as well as changes in the rotamer distribution as discussed above. Additionally, samples in polar solvents do not display a mono-or bi-exponential TPE-FEIR decay as in IR TA, but are best described by a power-law decay. The appearance of a power-law decay in interacting solvents implies that the TPE-FEIR decay may be sensitive to environmental interactions and coupling to solvent molecules, and may reflect a solvent-coordinated vibrational or orientational relaxation. As several processes might yield power-law behavior, a molecular origin of this behavior has not been assigned.

3.5 Conclusions

This chapter builds on the DFT predictions presented in Chapter 2, and provides a groundwork for later chapters, and future work. The one-IR-pulse TPE-FEIR response of aminocoumarin dyes in solution has been characterized in this chapter. This experiment was designed to study ground-electronic-state vibrational dynamics using IR excitation followed by two-photon excitation to the first electronic singlet state. This experiment reports on the relaxation of vibrational populations and coherences prepared by the IR pump field, however the information content differs from the corresponding IR pump–probe experiments. This difference can possibly be explained though the selection rules for the two-photon probing interaction, which appear to make FEIR more sensitive to vibrational coherences than the nuclear dipole polarization as probed with IR. The results lay the groundwork for future chapters. The obvious next step for this experiment is the expansion of FEIR as presented here with one IR pulse to a linear Fourier-Transform experiment using two IR pulses from an interferometer followed by the encoding pulse as a function of both the interferometric and encoding time delays. The resulting signal should result in a free induction decay that can be Fourier transformed to reveal a ground-state IR spectrum of vibrational modes that participate in the FEIR process (as projected onto the electronic excited state). This experiment is closely related to fluorescence wave-packet interferometry experiments[20,42], but explores the effect of interference of vibrational wave-packets on the ground state rather than the excited state. This experiment should provide control over the populations and coherences prepared before the encoding process and more clearly indicate which vibrational states

participate in the final signal. I will discuss the development of Fourier transform FEIR methods in Chapter 4.

As nonlinear IR excitations appear to contribute to the FEIR signal, further extensions to fluorescence-encoded 2D IR experiments are apparent, which are closely related to fluorescence-detected electronic 2D experiments. Such experiments would make use of sequences of multiple IR pulses, and efforts toward a nonlinear FEIR expansion are discussed in Chapter 6.

Finally, as fluorescence measurements are possible on the single-molecule concentration scale, a study of the sensitivity limits of this technique will prove to be important. Although this was not explored in detail in this chapter, I note that the samples used in the TPE-FEIR experiment were on the order of 2-3 times more dilute than the minimum concentration necessary for IR TA measurements, and are well above the low concentration limit of this technique. It is expected that changing the resonance conditions by tuning the visible pulses for optimal contrast will provide the sensitivity necessary to push to low sample concentrations. With the use of a one-photon encoding process and high-repetition rate photon counting, it is expected that this technique will be applicable to concentrations that are orders of magnitude lower than explored here. Based on the work in this and other chapters, this experiment is currently being pursued by other members of this research group.

Chapter Bibliography

(1) Kanstad, S. O.; Nordal, P. E. Infrared Photoacoustic Spectroscopy of Solids and Liquids *Infrared Phys.* **1979**, *19* (3–4), 413–422.

(2) Burke, N. L.; Redwine, J. G.; Dean, J. C.; Mcluckey, S. A.; Zwier, T. S. UV and IR Spectroscopy of Cold Protonated Leucine Enkephalin *Int. J. Mass Spectrom.* **2015**, *378*, 196–205.

(3) Hutchison, J. M.; Holiday, R. J.; Bach, A.; Hsieh, S.; Crim, F. F. Action Spectroscopy and Photodissociation of Vibrationally Excited Methanol *J. Phys. Chem. A* **2004**, *108* (39), 8115–8118.

(4) Likar, M. D.; Baggott, J. E.; Sinha, A.; Ticich, T. M.; Vander Wal, R. L.; Crim, F. F. Vibrationally Mediated Photodissociation *J. Chem. Soc. Farad. Trans. II* **1988**, *84* (9), 1483–1497.

(5) Fournier, J. A.; Wolk, A. B.; Johnson, M. A. Integration of Cryogenic Ion Vibrational Predissociation Spectroscopy with a Mass Spectrometric Interface to an Electrochemical Cell *Anal. Chem.* **2013**, *85* (15), 7339–7344.

(6) Seilmeier, A.; Kaiser, W.; Laubereau, A.; Fischer, S. F. A Novel Spectroscopy Using Ultrafast Two-Pulse Excitation of Large Polyatomic Molecules *Chem. Phys. Lett.* **1978**, *58* (2), 225–229.

(7) Laubereau, A.; Seilmeier, A.; Kaiser, W. A New Technique to Measure Ultrashort Vibrational Relaxation Times in Liquid Systems *Chem. Phys. Let.* **1975**, *36* (2), 232–237.

(8) Seilmeier, A.; Kaiser, W.; Laubereau, A. Vibrational Combination States of Polyatomic Molecules Investigated by Ultrashort Two-Pulse Spectroscopy *Opt. Comm.* **1978**, *26* (3), 441–445.

(9) Ding, K.; Kranitzky, W.; Fischer, S. F.; Kaiser, W. Structured UV-Spectrum of Naphthalene Obtained by Ultrafast Two-Pulse Excitation *Chem. Phys. Lett.* **1980**, *72* (1), 39–42.

(10) Lettenberger, M.; Emmerling, F.; Gottfried, N. H.; Laubereau, A. Orientational Motion of Anthracene in Liquid Solution Studied by IR/UV Double-Resonance Spectroscopy *Chem. Phys. Lett.* **1995**, *240* (4), 324–329.

(11) Emmerling, F.; Lettenberger, M.; Laubereau, A. Vibrational Dynamics of Anthracene in Liquid Solution Studied by Picosecond IR/UV Spectroscopy with Polarization Resolution *J. Phys. Chem.* **1996**, *100* (50), 19251–19256.

(12) Gottfried, N. H.; Emmerling, F. High-Resolution Two-Pulse Spectroscopy of Anthracene in Solution *J. Lumin.* **1999**, *81* (2), 143–147.

(13) Sakai, M.; Fujii, M. Vibrational Energy Relaxation of the 7-Azaindole Dimer in CCl 4 Solution Studied by Picosecond Time-Resolved Transient Fluorescence Detected IR Spectroscopy *Chem. Phys. Lett.* **2004**, *396* (4–6), 298–302.

(14) Sakai, M. Vibrational Energy Relaxation Process of the 7-Azaindole Dimer in Gas Phase and Solution *J. Spectrosc. Soc. Japan* **2005**, *54* (3), 163–169.

(15) Bokor, N.; Inoue, K.; Kogure, S.; Fujii, M.; Sakai, M. Visible-Super-Resolution Infrared Microscopy Using Saturated Transient Fluorescence Detected Infrared Spectroscopy *Opt. Commun.* **2010**, *283* (3), 509–514.

(16) Sakai, M.; Kawashima, Y.; Takeda, A.; Ohmori, T.; Fujii, M. Far-Field Infrared Super-Resolution Microscopy Using Picosecond Time-Resolved Transient Fluorescence Detected IR Spectroscopy *Chem. Phys. Lett.* **2007**, *439* (1–3), 171–176.

(17) Courtney, T. L.; Fox, Z. W.; Slenkamp, K. M.; Khalil, M. Two-Dimensional Vibrational-Electronic Spectroscopy *J. Chem. Phys.* **2015**, *143* (15), 0–15.

(18) Oliver, T. A. A.; Lewis, N. H. C.; Graham, R. Correlating the Motion of Electrons and Nuclei with Two-Dimensional Electronic–vibrational Spectroscopy *Proc. Natl. Acad. Sci.* **2014**, *111* (46), 16628–16628.

(19) Wilderen, L. J. G. W. Van; Messmer, A. T.; Bredenbeck, J. Mixed IR / Vis Two-Dimensional Spectroscopy : Chemical Exchange beyond the Vibrational Lifetime and Sub-Ensemble Selective Photochemistry** *Angew. Chem. Int. Ed.* **2014**, *53*, 2667–2672.

(20) Scherer, N. F.; Carlson, R. J.; Matro, A.; Du, M.; Ruggiero, A. J.; Romero-Rochin, V.; Cina, J. a.; Fleming, G. R.; Rice, S. a. Fluorescence-Detected Wave Packet Interferometry: Time Resolved Molecular Spectroscopy with Sequences of Femtosecond Phase-Locked Pulses *J. Chem. Phys.* **1991**, *95* (August), 1487.

(21) Li, C.; Wagner, W.; Ciocca, M.; Warren, W. S. Multiphoton Femtosecond Phase-Coherent Two-Dimensional Electronic Spectroscopy *J. Chem. Phys.* **2007**, *126* (16).

(22) Wagner, W.; Li, C.; Semmlow, J.; Warren, W. Rapid Phase-Cycled Two-Dimensional Optical Spectroscopy in Fluorescence and Transmission Mode. *Opt. Express* **2005**, *13* (10), 3697–3706.

(23) Karki, K. J.; Kringle, L.; Marcus, A. H.; Pullerits, T. Phase-Synchronous Detection of Coherent and Incoherent Nonlinear Signals *J. Opt.* **2016**, *18* (1), 15504.

(24) Tekavec, P. F.; Lott, G. A.; Marcus, A. H. Fluorescence-Detected Two-Dimensional Electronic Coherence Spectroscopy by Acousto-Optic Phase Modulation *J. Chem. Phys.* **2007**, *127* (21).

(25) Widom, J. R.; Johnson, N. P.; Von Hippel, P. H.; Marcus, A. H. Solution Conformation of 2-Aminopurine Dinucleotide Determined by Ultraviolet Two-Dimensional Fluorescence Spectroscopy *New J. Phys.* **2013**, *15*.

(26) Göppert-Mayer, M. Uber Elementarakte Mit Zwei Quantensprüngen *Ann. Phys.* **1931**, *401* (3), 273–294.

(27) So, P. T.; Dong, C. Y.; Masters, B. R.; Berland, K. M. Two-Photon Excitation Fluorescence Microscopy. *Annu. Rev. Biomed. Eng.* **2000**, *2*, 399–429.

(28) Goh, W. L.; Lee, M. Y.; Joseph, T. L.; Quah, S. T.; Brown, C. J.; Verma, C.; Brenner, S.; Ghadessy, F. J.; Teo, Y. N. Molecular Rotors as Conditionally Fluorescent Labels for Rapid Detection of Biomolecular Interactions *J. Am. Chem. Soc.* **2014**, *136* (17), 6159–6162.

(29) Haidekker, M. a; Theodorakis, E. a. Environment-Sensitive Behavior of Fluorescent Molecular Rotors. *J. Biol. Eng.* **2010**, *4*, 11.

(30) Hessz, D.; Hégely, B.; Kállay, M.; Vidóczy, T.; Kubinyi, M. Solvation and Protonation of Coumarin 102 in Aqueous Media: A Fluorescence Spectroscopic and Theoretical Study *J. Phys. Chem. A* **2014**, *118* (28), 5238–5247.

(31) Jin, H.; Baker, G. A.; Arzhantsev, S.; Dong, J.; Maroncelli, M. Solvation and Rotational Dynamics of Coumarin 153 in Ionic Liquids: Comparisons to Conventional Solvents *J. Phys. Chem. B* **2007**, *111* (25), 7291–7302.

(32) Michl, J.; Sykes, E. C. H. Molecular Rotors and Motors: Recent Advances and Future Challenges *ACS Nano* **2009**, *3* (5), 1042–1048.

(33) Palit, D. K.; Zhang, T.; Kumazaki, S.; Yoshihara, K. Hydrogen-Bond Dynamics in the Excited State of Coumarin 102 - Aniline Hydrogen-Bonded Complex *J. Phys. Chem. A* **2003**, *107* (409), 10798–10804.

(34) Park, M. O.; Moon, M. G.; Kang, T. J. Fluorescence Enhancement of 7-Diethylamino-4-Methylcoumarin by Noncovalent Dipolar Interactions with Cucurbiturils *Bull. Korean Chem. Soc.* **2013**, *34* (5), 1378–1382.

(35) Ramegowda, M.; Sreepad, H. R. Effect of Polar Solvents on Absorption Spectra of Coumarin 1: PCM-TDDFT Study *Acta Chim. Indica* **2013**, *3* (2), 119–126.

(36) Su, J.; Tian, D. Strengthening of Hydrogen Bonded Coumarin 102 in Ethanol Solvent upon Photoexcitation *New J. Chem.* **2014**, *38* (2), 568.

(37) Wagner, B. D. The Use of Coumarins as Environmentally-Sensitive Fluorescent Probes of Heterogeneous Inclusion Systems *Molecules* **2009**, *14* (1), 210–237.

(38) Frisch, M. J.; Trucks, G. W.; Schlegel, H. B.; Scuseria, G. E.; Robb, M. A.; Cheeseman, J. R.; Scalmani, G.; Barone, V.; Mennucci, B.; Petersson, G. A.; Nakatsuji, H.; Caricato, M.; Li, X.; Hratchian, H. P.; Izmaylov, A. F.; Bloino, J.; Zheng, G.; Sonnenberg, J. L.; Hada, M.; Ehara, M.; Toyota, K.; Fukuda, R.; Hasegawa, J.; Ishida, M.; Nakajima, T.; Honda, Y.; Kitao, O.; Nakai, H.; Vreven, T.; Montgomery, J. A.; Peralta, J. E.; Ogliaro, F.; Bearpark, M.; Heyd, J. J.; Brothers, E.; Kudin, K. N.; Staroverov, V. N.; Kobayashi, R.; Normand, J.; Raghavachari, K.; Rendell, A.; Burant, J. C.; Iyengar, S. S.; Tomasi, J.; Cossi, M.; Rega, N.; Millam, J. M.; Klene, M.; Knox, J. E.; Cross, J. B.; Bakken, V.; Adamo, C.; Jaramillo, J.; Gomperts, R.; Stratmann, R. E.; Yazyev, O.; Austin, A. J.; Cammi, R.; Pomelli, C.; Ochterski, J. W.; Martin, R. L.; Morokuma, K.; Zakrzewski, V. G.; Voth, G. A.; Salvador, P.; Dannenberg, J. J.; Dapprich, S.; Daniels, A. D.; Farkas; Foresman, J. B.; Ortiz, J. V; Cioslowski, J.; Fox, D. J. *Gaussian 09, Revision D.01, Gaussian, Inc., Wallingford CT*. 2009.

(39) Tomasi, J.; Mennucci, B.; Cammi, R. Quantum Mechanical Continuum Solvation Models *Chem. Rev.* **2005**, *105* (8), 2999–3093.

(40) Stephens, P. J.; Devlin, F. J.; Chabalowski, C. F.; Frisch, M. J. Ab Initio Calculation of Vibrational Absorption and Circular Dichroism Spectra Using Density Functional Force Fields *J. Phys. Chem.* **1994**, *98* (45), 11623–11627.

(41) DeFlores, L. P.; Nicodemus, R. a; Tokmakoff, A. Two-Dimensional Fourier Transform Spectroscopy in the Pump-Probe Geometry *Opt. Lett.* **2007**, *32* (20), 2966.

(42) Cina, J. A. Wave-Packet Interferometry and Molecular State Reconstruction: Spectroscopic Adventures on the Left-Hand Side of the Schrödinger Equation. *Annu. Rev. Phys. Chem.* **2008**, *59* (February), 319–342.

(43) Mukamel, S. *Principles of nonlinear optical spectroscopy*; 1995; Vol. 6.

(44) Tokmakoff, A. Orientational Correlation Functions and Polarization Selectivity for Nonlinear Spectroscopy of Isotropic Media . II . Fifth Order Orientational Correlation Functions and Polarization Selectivity for Nonlinear Spectroscopy of Isotropic Media . II . Fifth O *J. Chem. Phys.* **1996**, *105*, 13–21.

Appendix 1
Supplementary Figures to Chapter 3

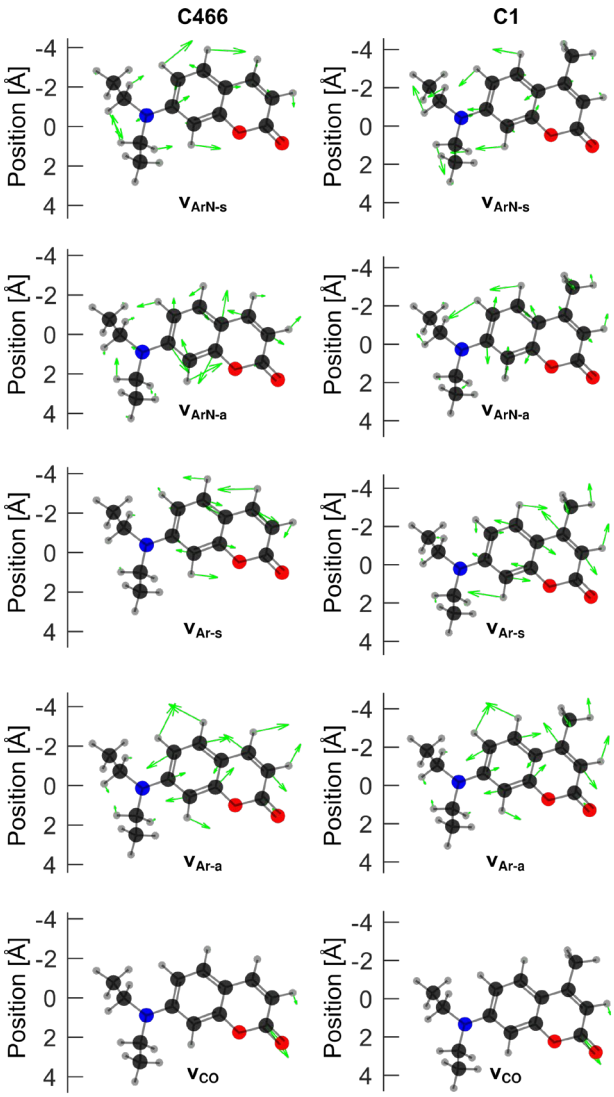

Figure 3.A1.1) DFT Vibrational Displacements of C466 and C1. DFT vibrational normal modes and character assignments were calculated using Gaussian 09d with the B3LYP/6-31G* functional. As these were calculated for a geometry without fixing any atoms, the displacement vectors vary somewhat from those presented in Chapter 2; however, the mode character assignments remain the same. Displacements are normalized. Left: C466, Right: C1.

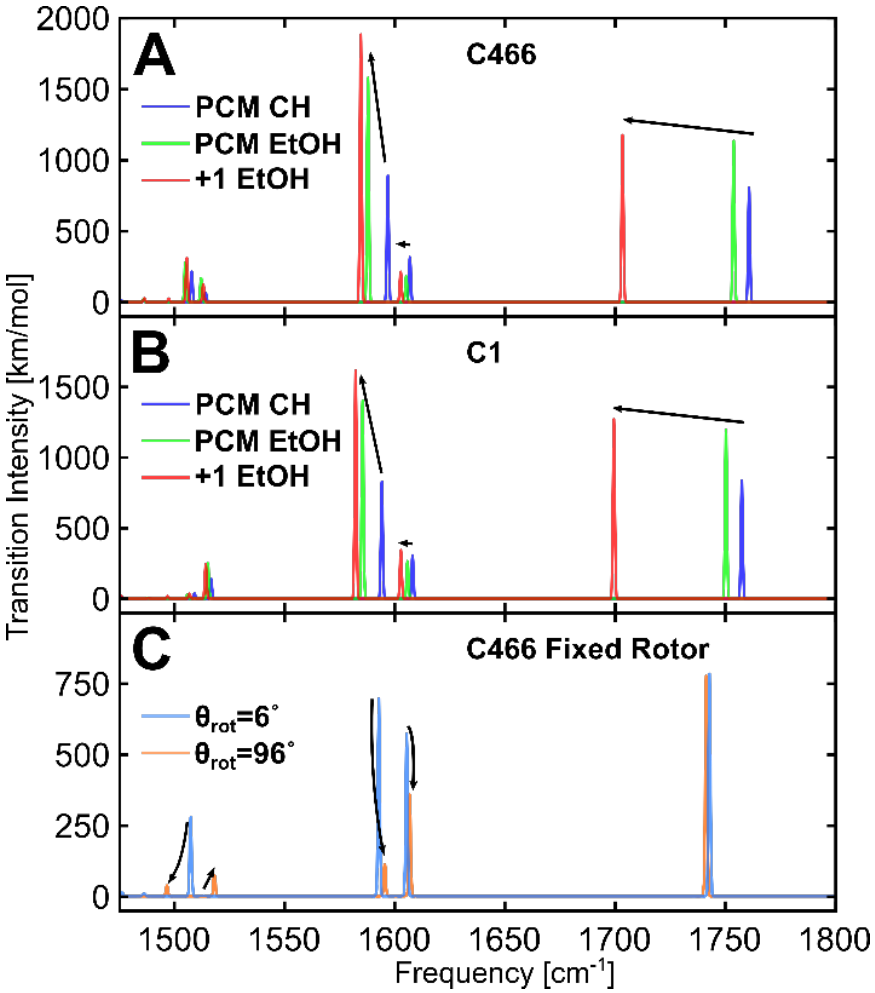

Figure 3.A1.2) The Effects of Solvent and Rotor Angle on DFT normal modes. Frequencies are scaled by a frequency scaling factor of 0.96 from NIST CCCBDB. **A.)** C466 in Polarizable Continuum Model (PCM) cyclohexane (CH) **(blue)**, C466 in PCM EtOH **(green)**, and C466 in PCM EtOH with one explicit ethanol molecule hydrogen bonded to the CO **(red)** predict the effect of polarity and Hydrogen bonding on the ν_{CO} mode. **B.)** A similar series can be calculated for C1 in PCM CH **(blue)**, C1 in PCM EtOH **(green)**, C1 in PCM EtOH with explicit EtOH at the CO **(red)**. In polar solvents, C466 **(A)** and C1 **(B)** modes redshift. With the addition of an explicit EtOH molecule near the coumarin CO, the ν_{CO} mode redshifts significantly. **C.)** DFT spectra of C466 in PCM CH at the ground-state minimum, which has a rotor angle of 6° with respect to the chromen-2-one core **(cyan)**, and at the excited-state potential energy minimum, with the rotor at 96° with respect to the core **(orange)**. Upon rotation, there is negligible redshift of the ν_{CO} mode. The $\nu_{Ar\text{-}s}$ and $\nu_{Ar\text{-}a}$ modes invert in intensity, and the $\nu_{ArN\text{-}s}$ and $\nu_{ArN\text{-}a}$ modes become more separated in frequency.

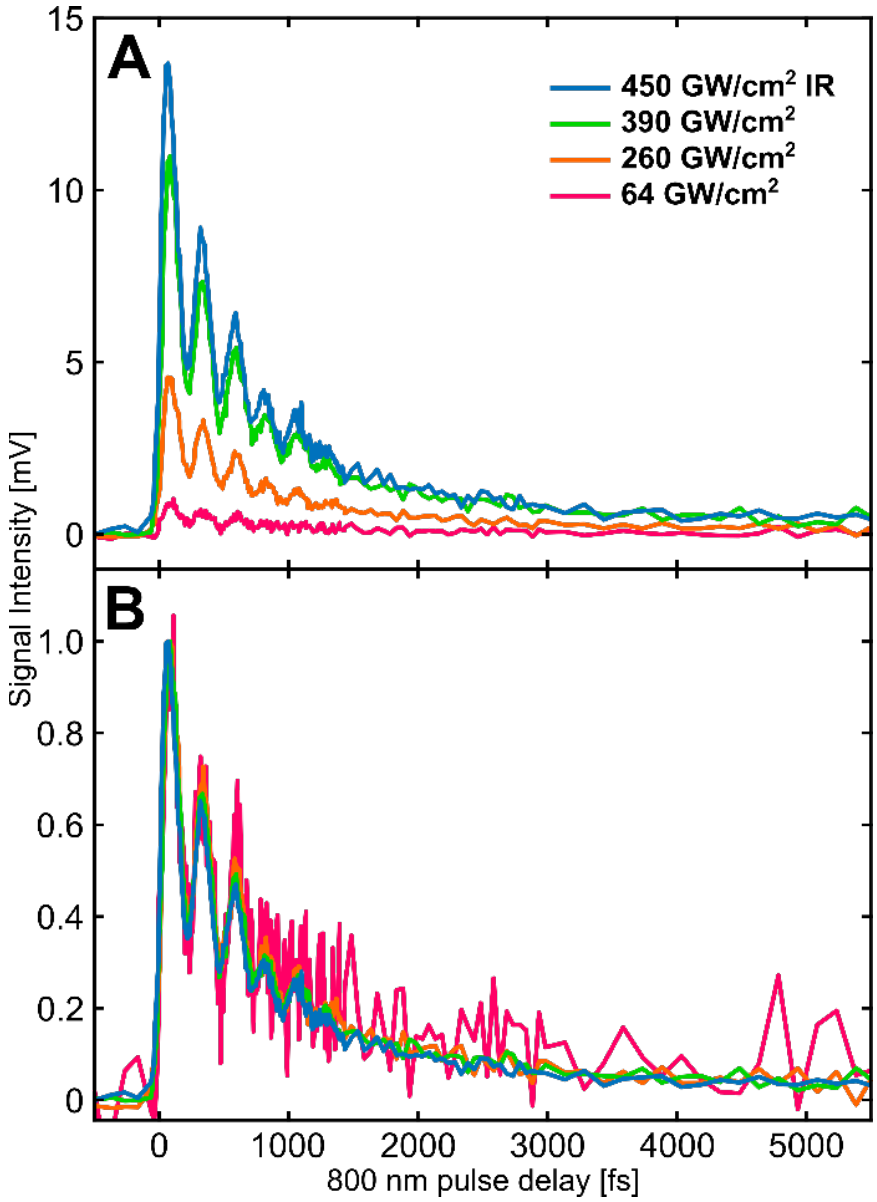

Figure 3.A1.3) IR Intensity-Dependent Traces. IR Intensity-dependent TPE-FEIR traces for C1 in cyclohexane **(A)** scale nonlinearly with the IR intensity, but when normalized to their value at τ_d=0 **(B)**, the same time-traces all overlay, and the oscillations do not appear to change.

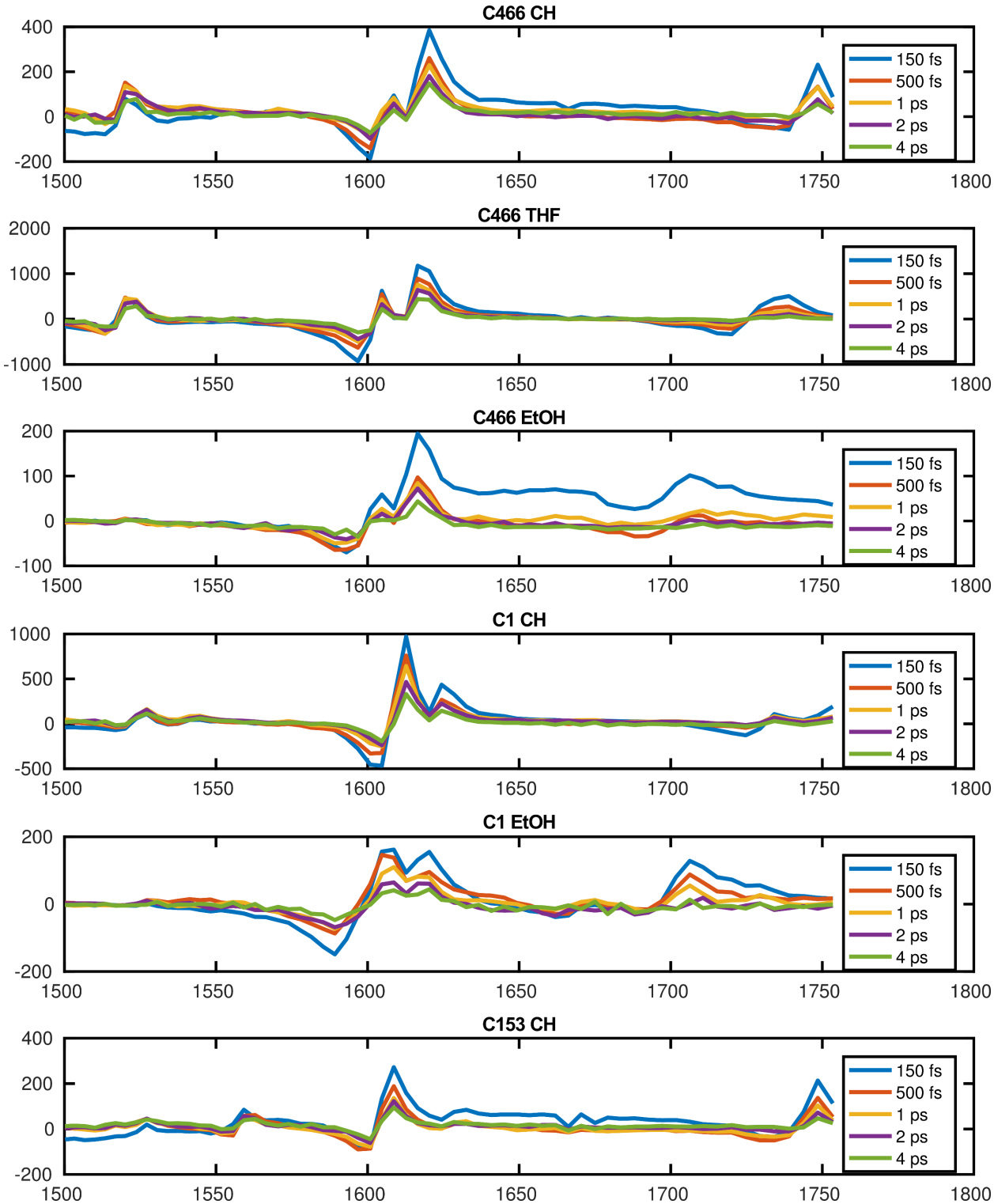

Figure 3.A1.4) IR Pump-Probe Slices for the Dye-Solvent Systems. The 150 fs traces, particularly C466 in EtOH, may contain non-resonant response from IR pulse overlap.

Chapter 4
Fourier Transform Fluorescence-Encoded Infrared Spectroscopy[1]

Chapter Abstract

While time-resolved infrared (IR) vibrational spectroscopy provides insight on structural dynamics of solution-phase systems, current techniques are limited to high concentrations. Fluorescence-encoded infrared spectroscopy (FEIR) can be used to encode IR-driven vibrational excitations into excited electronic states that fluoresce, which can be detected at lower concentrations than a coherently-detected IR signal. In this chapter, I report on the development of Fourier transform FEIR as an alternative approach for high sensitivity linear IR spectroscopy. Upon driving a vibrational excitation with a pair of IR pulses separated in time by a variable delay, I observed an interferometric component in the encoded fluorescence. This signal can be Fourier transformed to obtain a vibrational spectrum. By additionally varying the time delay of the encoding pulse following the second IR pulse, I observed frequency-difference coherence oscillations as previously. The resolution of these allows the construction of a 2D-mapped correlation representation of coupled vibrations. Response functions for this experiment have been modelled, and relate the observed spectral features to Liouville excitation pathways. The pathways observed in FT FEIR spectrum are confirmed to arise from vibrationally-excited populations and coherences between coupled modes.

[1] Material in this chapter was adapted from a previously published work of the same title (*J. Phys. Chem. A*, **2018**, *122* (2), pp 554–562; **DOI:** 10.1021/acs.jpca.7b10305)

4.1 Introduction

The structural dynamics of solution-phase systems at low concentrations of μM to pM are of interest in many open research questions. Multidimensional vibrational spectroscopies have been demonstrated to be widely applicable tools for studying dynamical properties of molecules in condensed matter through the ability to reveal structural correlations with ultrafast time-resolution. However, nonlinear vibrational spectroscopies that are detected through the coherent emission of an IR signal field from an odd-order nonlinear polarization suffer the drawback of limited sensitivity, typically requiring experimental concentrations on the order of 0.01-5 M. This motivates the development of ultrafast vibrational spectroscopies with the time resolution and structural sensitivity of existing IR techniques while additionally extending experimental sensitivity to lower concentrations.

To achieve a higher level of sensitivity it is advantageous to detect the influence of resonant IR pulses on solution-phase systems through a more sensitive experimental observable. Several high-sensitivity methods indirectly detect IR-driven vibrational dynamics;[1–5] however, their applicability to solution phase systems is limited. One approach is to up-convert a vibrational excitation into a visible observable, where sensitive visible detectors can be used.[6] In particular, the detection of incoherent fluorescence allows the measurement of optical phenomena at concentrations down to the single molecule level. Fluorescence-detected 2D electronic spectroscopies have been successful in optical systems.[7–14] They utilize even-order, nonlinear excitation pathways that contain comparable information in the incoherently-detected signal to the odd-order emissive pathways in their coherently-detected counterparts.[10,14,15] Unfortunately, fast non-radiative relaxation processes to coupled bath modes in the

vibrational manifold and less-sensitive detector technology render the measurement of incoherently-emitted IR signals nearly impossible.

To perform IR vibrational spectroscopy in solution-phase systems, while utilizing the heightened sensitivity of fluorescence detection, I continue an investigation of fluorescence-encoded infrared spectroscopy (FEIR). Originating in the 1970s with Kaiser and coworkers,[16–19] in FEIR vibrational information is encoded into an electronic state that fluoresces. Upon coherent IR excitation of vibrational modes on the electronic ground state, a vibronically-coupled electronic transition is brought on resonance with an otherwise off resonant optical field, leading to an electronic excited state population that is detected through the fluorescence emitted during relaxation. This process can be described as *encoding*, as information regarding a nuclear displacement is encoded into an excited electronic population. Although modern exploration of this technique has been limited,[20–24] it retains ongoing relevance as a strategy for super-resolution IR vibrational measurements.[25,26] In the previous chapter, I discuss my development of a modernized Two-Photon-Excited Fluorescence-Encoded IR (TPE-FEIR) experiment using an ultrafast IR pulse followed by a near-IR (NIR) two-photon-transition encoding pulse.[27] Using this technique, I observed difference frequency oscillations in the time delay between the short IR pulse and the NIR encoding pulse, which arise from vibrational coherences on the ground electronic state.

FEIR is one of several nonlinear spectroscopies investigated in recent years that utilize relationships between an IR vibrational excitation and optical electronic resonances. Several techniques to study coupled nuclear-electronic dynamics have been developed using mixed visible and IR pulses.[28–31] As vibronic coupling is necessary in the encoding process to change the resonance of an electronic transition, the FEIR experiment is an incoherently-detected analogue to the mixed vibrational-electronic

V pathway observed in 2D Vibrational-Electronic Spectroscopy.[30,31] Utilizing a similar principle, Vibrationally-Promoted Electronic Resonance Spectroscopy (VIPERS) measurements prepare coherences between an electronic excited state and a vibrationally excited electronic ground state, which decay on timescales much longer than the unperturbed vibrational lifetime, allowing the examination of vibrational exchange on atypically long timescales.[32–34] However, techniques such as VIPERS and Two Dimensional Electronic-Vibrational Spectroscopy present similar challenges to 2D IR experiments in detecting a coherent IR signal, and are further complicated by the inclusion of vibrational features arising from both ground and electronic states. My work seeks to perform IR vibrational measurements purely on the ground electronic state.

Expanding on the previous chapter, I will discuss here a further development of FEIR in which a Fourier transform method was used to obtain FEIR spectra that are vibrationally resolved. In Fourier Transform FEIR (FT FEIR), an IR pulse pair with a variable time delay interferometrically resolves the vibrational excitation used to drive FEIR. The resulting fluorescence-encoded signal is then Fourier transformed to obtain a vibrational frequency axis. As in the one-IR-pulse FEIR experiment, I also observe difference frequency beats in FT FEIR in the encoding time delay between the second IR pulse and the NIR encoding pulse, which are further resolved in the vibrational frequency axis. Thus, although this technique is linear with respect to IR intensity, as the data obtained using FT FEIR contain information as a function of two independent time delays, FT FEIR is intrinsically a higher-order measurement that encodes more information that linear FTIR. With experimental examples and a theoretical description of the FEIR response function, I demonstrate how this technique can be used to map FT FEIR surfaces in the frequency domain to 2D correlation maps between coupled vibrational modes.

4.2 Methods and Experimental

4.2.1 FEIR pulse sequence and signal acquisition

As the FT FEIR signal measured depends on three ultrafast pulses, two time delays are relevant to FT FEIR data collection. The interferometric delay between the vibrationally resonant IR pulses 1 and 2 is defined as τ_1, and the encoding time delay between IR pulse 2 and the NIR encoding pulse 3 is defined as τ_d. I also define the pulse delay between pulse 1 and the encoding pulse as $\tau_d' = \tau_d + \tau_1$ (Figure 4.1). There are four contributions to the fluorescence detected in this experiment, of which one is the desired signal. I define F_0 as previously as the background fluorescence due to off-resonant excitation by the encoding pulse 3 in the absence of IR pulses 1 and 2, $F_1(\tau_d')$ or F_1' as the one-pulse FEIR signal which arises from a vibrational excitation driven by pulse 1 and encoded into an electronic population by pulse 3, $F_1(\tau_d)$ or F_1 as the FEIR signal arising from pulses 2 and 3, and $F_2(\tau_1,\tau_d)$ as the two-dimensional FEIR signal driven by both pulses 1 and 2 and encoded into the electronic observable with pulse 3. F_1 and F_1' represent the two-pulse FEIR experiments described in the previous chapter.[27]

My strategy to isolate F_2 begins by modulating the IR pulse 2 using an optical chopper at half of the pulsed-laser repetition rate while sweeping τ_1 in a differential detection scheme, allowing the removal of the F_0+F_1' signal contributions from the full signal to obtain F_1+F_2, an interferometric signal with an offset. The resulting differential signal can be separated into F_1 and F_2 components by Fourier transformation in τ_1, as the $F_2(\tau_1,\tau_d)$ signal oscillates at high frequency in τ_1, while $F_1(\tau_d)$ is constant in τ_1. This yields a frequency-domain FT FEIR spectrum in ω_1, $F_2(\omega_1,\tau_d)$. A two-dimensional frequency-

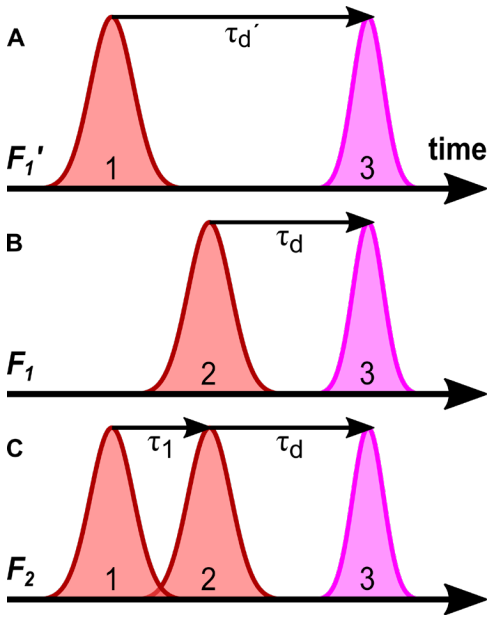

Figure 4.1) Pulse Diagram of FEIR Signals in a Two-IR-Pulse Experiment. There are three contributions to the fluorescence measured in FT-FEIR that depend on a vibrational excitation: **(A)** the F_1' FEIR signal from IR pulse 1 and NIR pulse 3, separated by a single time delay τ_d', **(B)** the F_1 FEIR signal from IR pulse 2 and NIR pulse 3, separated by τ_d, and **(C)** the F_2 FEIR signal originating from interactions with both IR pulses 1 and 2, separated by τ_1 and NIR pulse 3, arriving at τ_d after IR pulse 2.

domain data set can be obtained upon with a further Fourier transformation of the data as a function of the encoding time delay τ_d.

4.2.2 Experimental

The experimental setup is a modification on the setup described in the previous chapter for one-IR pulse TPE-FEIR experiments (Figure 4.2).[27] Ultrafast NIR pulses at 800 nm (93 fs FWHM) from a 1 kHz regenerative amplifier system (Libra, Coherent) were used to pump a two-stage OPA with DFG mixer attachment (TOPAS-C, Light Conversion), resulting in mid-IR pulses with a tunable center frequency and a bandwidth of ~200 cm^{-1} (FWHM). After a λ/2 wave plate and polarizer, the IR was sent through a Mach-Zehnder interferometer using CaF_2 beam splitters (ISP Optics 50/50 2-8 μm coated) to generate a collinear IR pulse-pair. The interferometer τ_1 delay was controlled by scanning Pulse 1 with a variable

time delay using a precision stage (ANT-95-50L, Aerotech). Pulse 2, which originated from the fixed arm of the interferometer, was chopped at 500 Hz. The primary output of the interferometer was used to pump the sample, while the other was detected on a single-channel MCT detector as a reference for timing and phase correction in the τ_1 delay.[35] The IR field temporal FWHM was measured by interferometric autocorrelation in $AgGaS_2$ to be 126 fs at the sample. For fluorescence-encoding experiments, a small amount (~5 μJ) of the NIR was split off before the OPA input, controllably delayed with a second stage to set τ_d, and used to drive the two-photon encoding process. The NIR polarization was set with a λ/2 wave plate to be parallel to the IR polarization.

The IR and NIR excitation beams were incident on the sample cell at 20° and -20° respectively from normal incidence. The IR was focused to a spot size of ~125 μm in the sample with a silver parabolic mirror while the NIR was size-matched to the IR focus using a fused silica lens. The fluorescence was collected at 90° from the incident NIR beam (50° from NIR reflected off the sample). An achromatic lens doublet pair (MAP103075-A, Thorlabs) was used to image the fluorescent focal volume onto an avalanche photodiode visible detector (APD410A, Thorlabs), and the fluorescence was optically filtered with a 335-610 nm visible bandpass filter (Thorlabs FGB37M) to remove any residual pump scatter. The resulting voltage was gated and integrated (SRS, SR250), and sampled with a NI PCI 6220 data acquisition card. The fluorescence polarization was not analyzed. The typical IR peak intensity used was 140 GW/cm^2, in a range where the IR intensity dependence of the FT FEIR signal was measured to be linear (Figure 4.A2.1).

During data collection, the τ_1 stage was scanned at a constant velocity of 250 μm/s from a delay of -500 fs to 9000 fs while collecting single-shot data at 1 kHz. For the 2D measurements presented here, 6 averages were taken in the τ_1 axis per τ_d point, and the τ_d stage was stepped between 150 fs and 4000 fs in

25 fs steps. For each laser shot in τ_1, the integrated fluorescence intensity, IR reference intensity, and chopper state were collected. For each sweep, the τ_1 stage delay for each laser shot was assigned using a

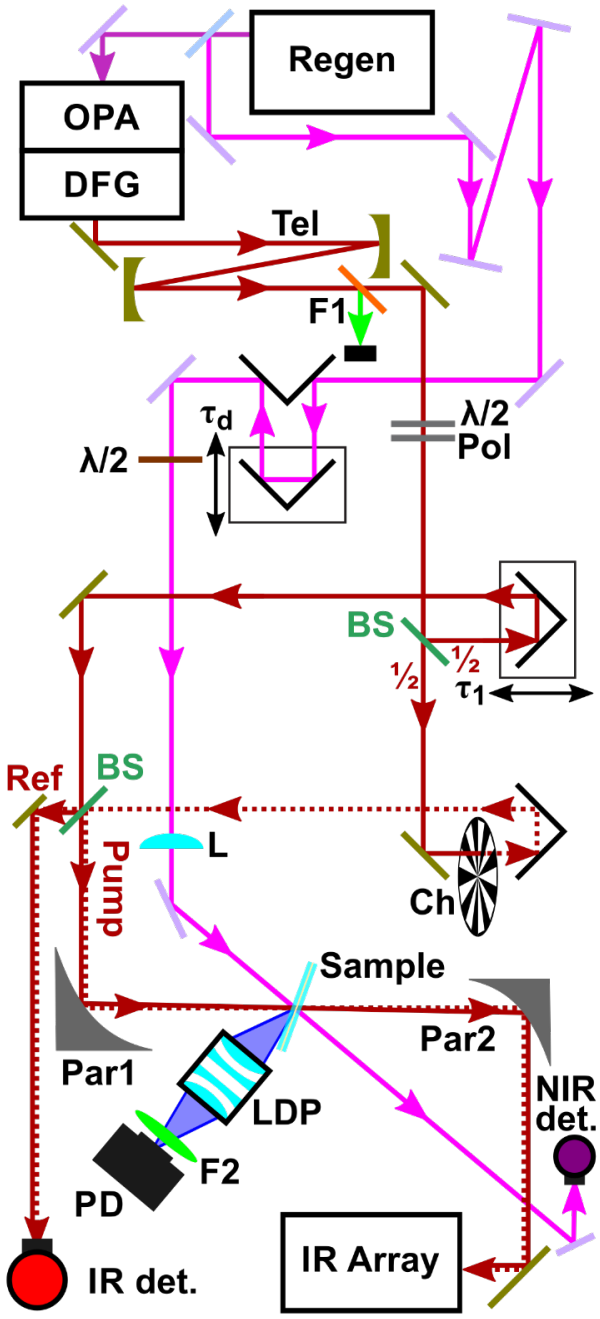

Figure 4.2) FT FEIR experimental schematic. IR beam paths are shown in red and NIR beam path in magenta. Key: BS, CaF2 beamsplitter; Ch, phase-locked chopper; Det, detector; F1, germanium red pass filter for mid-IR; F2, visible fluorescence band-pass filter; L, 200 mm UV fused silica lens; LDP, Achromatic Lens Doublet Pair; λ/2, half-wave plate; Par, 100 mm silver coated parabolic reflector; PD, avalanche photodiode; Pol, polarizer; Tel, telescope.

fit of the τ_1 times obtained from sampling the stage encoder every 60 ms. Using the measured chopper state, the interleaved chopped and unchopped data points of each scan in τ_1 were separated to give a final τ_1 point spacing of 3.3 fs.

Before Fourier transformation in each dimension, the data were filtered with a Hann windowing function, and zero padded to 2 times the original length in both τ_1 and τ_d. The data in τ_1 were cut at τ_1=0 as measured with the IR reference, and Fourier transformed in τ_1 to yield a spectrum with an axis of ω_1 with frequency resolution of 1.8 cm^{-1}. The chopped signal was subtracted from the unchopped signal in the frequency domain as they share the same discrete frequency axis after the Fourier transformation. The IR reference phase was subtracted from the FEIR phase, and the FEIR signal was divided by the IR reference amplitude to correct for finite IR bandwidth. The data were cut in τ_d at the $F_1(\tau_d)$ maximum where I set τ_d=0 to remove the pulse overlap region, and a second Fourier analysis was performed in the τ_d delay, yielding a two-dimensional FEIR surface with a second frequency axis of ω_d with frequency resolution of 2.8 cm^{-1}. 2D IR spectra were collected with a separate pump-probe geometry 2D IR spectrometer using ~100 fs IR pulses. To stitch 2D IR surfaces acquired in different IR windows, 2D spectra were first normalized by their respective pump spectra, and averaged in their overlapping regions in the frequency domain. The signal-to-noise ratios for the measured FT FEIR and 2D IR spectra are respectively 60 and 145, and are roughly similar after normalizing by the experimental concentrations.

The samples selected to demonstrate the FEIR measurement were solutions of 7-(diethylamino)coumarin (Coumarin 466, C466) in Cyclohexane (CH, from Sigma-Aldrich), as this system was previously demonstrated to have high contrast between the F_0 background and the F_1 signal, a relatively long vibrational coherence lifetime, and previously assigned and well-characterized ring and lactone ester carbonyl stretch modes.[27] Samples were prepared at concentrations of 4.8 mM for most

FEIR measurements and at 10 mM for 2D IR measurements. The samples consisted of 70 μL of solution sandwiched between two 1-inch diameter, 1 mm thick CaF_2 windows (Crystran) separated by a ~100 μm Teflon spacer for FEIR measurements and 30 μL of solution with a ~50 μm spacer for 2D IR measurements.

4.3 Results

The signal components of the raw FEIR data were characterized in the time-domain as a function of τ_1 delay. The full fluorescence signal with all four signal contributions, $F_0+F_1'+F_1+F_2$, appears to contain an interferometric component in τ_1 which is not observed in the chopped signal F_0+F_1'. These are subtracted to yield the differential signal, F_1+F_2, with a vertical offset which depends on τ_d. Outside the pulse overlap region, the F_1+F_2 signal further contains oscillations in the encoding time τ_d, the phase of which depends on the τ_1 delay (Figure 4.3).

After F_1 is separated in Fourier analysis, the imaginary[II] parts of the F_2 spectra of C466 in ω_1 display three primary peaks at 1521 cm^{-1}, 1608 cm^{-1} and 1748 cm^{-1}. These peaks correspond to the C466 FTIR modes previously assigned as A-symmetry-like rotor-N-coupled ring stretch $\nu_{ArN\text{-}s}$, the A-symmetry-like ring stretch $\nu_{Ar\text{-}s}$, and the lactone ester carbonyl stretch ν_{CO} vibrations, respectively. A shoulder at 1616 cm^{-1}

[II] When data are cut at time-zero value, the signal will begin at the half-way point of the pulse-length-limited rise time, and the imaginary part of the frequency-domain data (the sine transform) will be absorptive. For a slowly-varying functional form, the rise time can introduce artifacts in the Fourier transform, and for quickly-varying interferometric functional forms, cutting the data at exactly the halfway point can prove difficult. Thus, it is easier in practice to cut the data at a maximum point, and take the real part of the frequency-domain (the cosine transform). This sacrifices one quarter of a wave cycle to remove rising signal artifacts, and will introduce phase error at high frequency bandwidths.

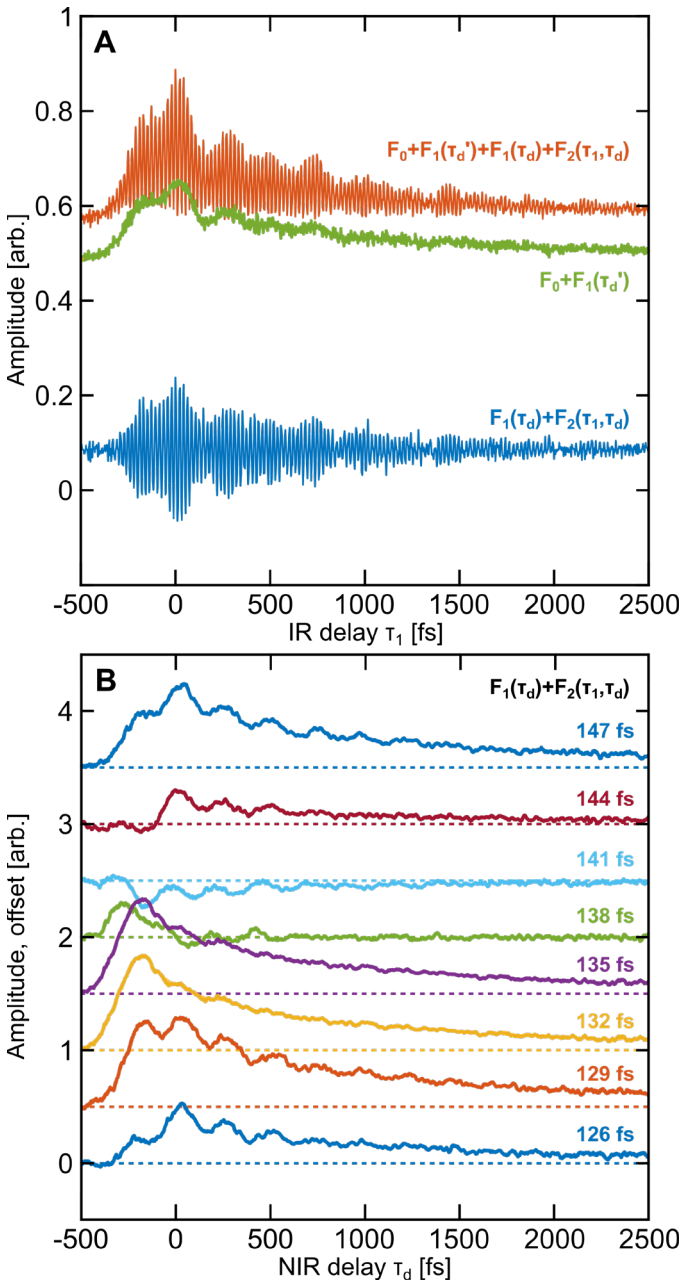

Figure 4.3) FT FEIR Signal Components as a Function of Two Time Delays. A.) The raw FEIR signal of C466 at 4.8 mM in CH, excited at 1680 cm^{-1}, as a function of τ_1 for τ_d = 250 fs, demonstrates an interferometric component with pulse 2 unchopped **(orange)** that was not present when pulse 2 was chopped **(green)**. The differential signal between unchopped and chopped is offset vertically **(blue)**. **B.)** The F_1+F_2 FEIR signal as a function of τ_d for several τ_1 points demonstrates a τ_1-dependent phase shift of coherence oscillations and a functional form that appears to vary. Data before τ_d=0 contain pulse overlap effects due to scanning across the IR pulses delayed in τ_1. Note that some τ_1 values yield similar traces to the F_0+F_1'signal in τ_d, and the τ_d = 0 point here is set by matching the maximum of the τ_1=147 fs signal to the F_0+F_1'maximum in part **(A)** for best comparison.

on the blue side of the $\nu_{Ar\text{-}s}$ mode, observed at longer τ_d delays, may be a weak contribution from the asymmetric $\nu_{Ar\text{-}a}$ mode. The phase of the Lorentzian line shape varies with τ_d (Figure 4.4). The dispersive line shapes observed in F_2 reflect the complex phase relationship of the signals in both τ_1 and τ_d, and correspond to damped oscillations in the τ_d axis which lie on top of a biexponential decay. This decay was found to agree with 900 and 3100 fs timescales as reported previously, but with a frequency dependence to the relative decay amplitudes.

The phase twisting that depends on both time delays observed in the F_2 data obscures a more detailed interpretation without further analysis, although the $F_2(\omega_1,\tau_d)$ data display some of the vibrational modes observed in the FTIR. This dependence of the phase twisting on both time delays reflects the fac that this technique is not a purely linear measurement that is fully analogous to FTIR. As the phase twist in the $F_2(\omega_1,\tau_d)$ data appears as an oscillation in the τ_d delay, I apply a second Fourier transform in τ_d to result in a two-dimensional frequency-domain FT FEIR surfaces of $F_2(\omega_1,\omega_d)$.

The FT FEIR spectrum plotted as a function of the Fourier conjugate frequency axes (ω_1,ω_d) displays a series of peaks along ω_1 that correspond to the $\nu_{ArN\text{-}s}$, $\nu_{Ar\text{-}s}$, and ν_{CO} resonances and are centered on $\omega_d = 0$. Additionally, peaks with positive or negative values of ω_d that lie within the bandwidth of our IR pulses are present. These correspond to oscillations in τ_d at difference frequencies between vibrational resonances (Figure 4.5A). Upon Fourier transformation, a time-domain signal component that oscillates in τ_1 but does not oscillate in τ_d results in peaks at $\omega_d = 0$, and arises from the excitation of a vibrationally excited population. Similarly, a time-domain signal that further oscillates in τ_d results in low frequency peaks in ω_d, and arises from the excitation of a vibrational coherence between coupled modes that share a common ground state.[27] The linewidths of these features in ω_1 and ω_d are inversely proportional to decay timescales in their Fourier conjugate time axes.

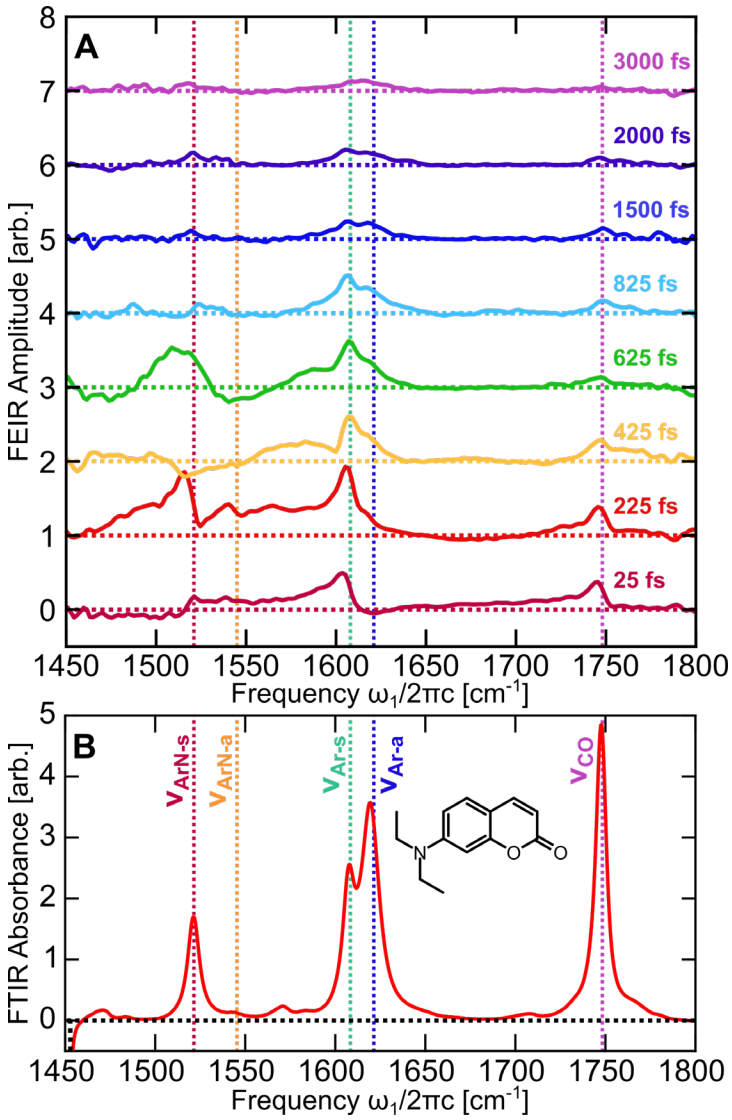

Figure 4.4) Frequency-Domain FEIR Slices as a Function of Encoding Time Delay. The imaginary component of the frequency-domain FEIR signal $F_2(\omega_1, \tau_d)$ of C466 in CH at several encoding time delays **(A)**, pumped with an IR center frequency of 1680 cm^{-1}, displays features which correspond to modes observed in the solvent-subtracted FTIR absorbance spectrum **(B)**. Peaks observed at 1521 cm^{-1}, 1608 cm^{-1}, and 1748 cm^{-1} correspond to the $\nu_{ArN\text{-}s}$, $\nu_{Ar\text{-}s}$, and ν_{CO} modes of C466. Some phase twisting is apparent at earlier times in the FEIR signal, and a shoulder to the right of the $\nu_{Ar\text{-}s}$ mode remains at later times.

Vibrational coherence peaks, which lie off the ω_d=0 axis, are a signature of vibrational couplings that also result in cross-peaks in 2D IR spectra. As 2D IR and FEIR both report on coupling information in different ways,[III] to facilitate a comparison, the $F_2(\omega_1,\omega_d)$ data can be transformed to a more intuitive cross-peak representation. A reflection of the $F_2(\omega_1,\omega_d)$ spectrum across the ω_d axis, followed by a

vertical skew at an angle of $\pi/2$, equivalent to a change of coordinate system to an abscissa of ω_1 and a skewed ordinate of $\omega_2=\omega_1-\omega_d$, transforms the difference-frequency components in ω_d to cross peaks between vibrational frequencies in ω_2. Further, the zero-frequency components in ω_d transform to diagonal features in ω_2.

The intuitively-mapped FT FEIR spectrum of C466 in CH resolves the $\nu_{ArN\text{-}s}$, $\nu_{Ar\text{-}s}$, and ν_{CO} populations and coherences. Cross peaks are observed between the $\nu_{ArN\text{-}s}$ and $\nu_{Ar\text{-}s}$ peaks, as well as between the $\nu_{Ar\text{-}s}$ and ν_{CO} peaks (Figure 4.5B). In the (ω_1, ω_2) representation, FT FEIR peaks appear elongated vertically and along the diagonal, due to the skew operation. The width along the diagonal projected onto ω_1 appears to be wider than the vertical width in the FEIR peaks, indicating a faster decay timescale in τ_1 than τ_d. The horizontal line width along the diagonal is determined by the free-induction decay timescale in τ_1 and corresponds to that observed in FTIR spectra. The vertical line width of diagonal peaks in ω_2 is determined by the population relaxation rate of vibrational excited states, and likewise the widths of the cross peaks are determined by coherence damping rates.

In this representation, one can directly compare the positions of diagonal and cross peaks in the FT FEIR spectrum with a 2D IR spectrum. The similarities indicate that the two experiments report on the presence of vibrational couplings in different ways, although the number of independent time-delays (dimensionality) and the types of ground state vibrational coherences measured vary between the two measurements. One immediately apparent difference is that the FT FEIR spectrum does not display the common Ground State Bleach (GSB) and Excited State Absorption peak pair line shapes observed in

[III] Cross peaks in FT FEIR correspond to coherences excited between coupled modes but do not report on the strength of this coupling, rather on the number of molecules in the ensemble where these modes are coupled. The GSB-ESA anharmonicity observed in cross peaks in 2D IR can be used to report on the strength of the coupling between modes.[38]

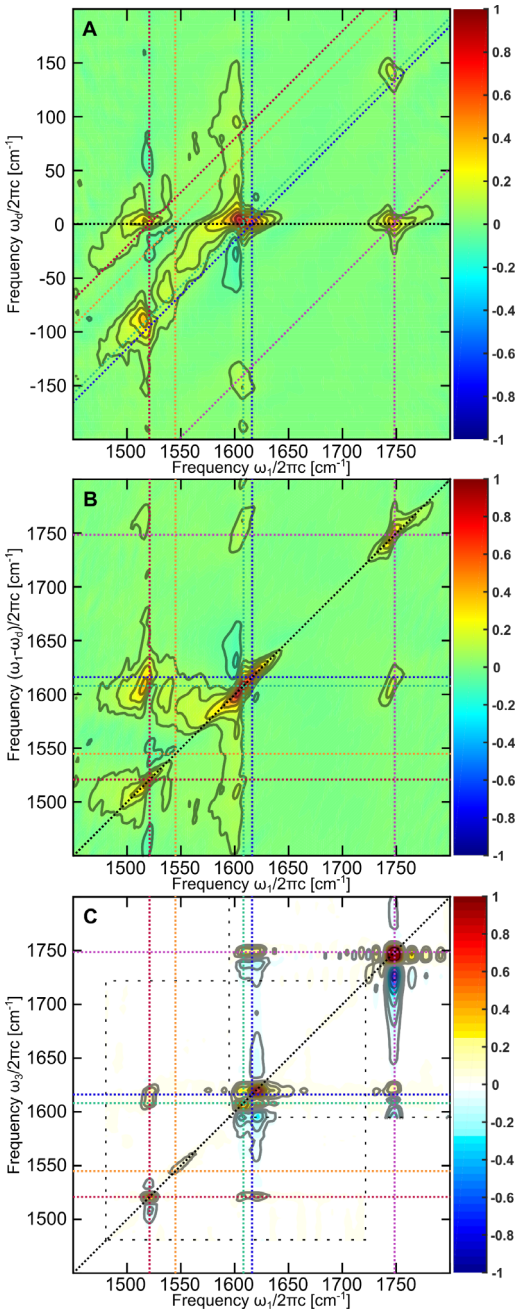

Figure 4.5) FT FEIR and 2D IR Surfaces. A.) The imaginary component of the phased C466 $F_2(\omega_1, \omega_d)$ 2D FEIR spectrum with the IR frequency centered at 1680 cm^{-1} displays zero-frequency components in ω_d, corresponding to vibrational populations in τ_d, as well as low-frequency features, corresponding to coherences. **B.)** The $F_2(\omega_1,\omega_2)$-mapped representation of the 2D FEIR spectrum displays more intuitive cross peaks between coupled modes. **C.)** The absorptive 2D IR spectrum of C466 at a 500 fs waiting time, stitched together by averaging the overlap region of pulse-spectrum-corrected 2D spectra taken in two different IR windows (dashed boxes). Normalized 2D spectra are plotted with 20 contours, spaced cubically for the FEIR spectra in **(A)** and **(B)** to highlight low amplitude features, and linearly in **(C)**. C466 vibrational modes are marked with dashed lines: $\nu_{ArN\text{-}s}$, red; $\nu_{ArN\text{-}a}$, orange; $\nu_{Ar\text{-}s}$, green; $\nu_{Ar\text{-}a}$, blue; and ν_{CO}, purple.

2D IR. Instead, the peaks observed in the FT FEIR spectrum correspond only to the positions of the GSB features in the 2D IR. While the cross peaks are more intense in the FEIR data than in the 2D IR data, they occur between the same vibrational modes. However, the B-symmetry $\nu_{Ar\text{-}a}$ mode, which contributes strongly to a complex diagonal structure in 2D IR, only appears as a weak shoulder on the $\nu_{Ar\text{-}s}$ mode in FT FEIR (Figure 4.5C). Off-diagonal negative features appear to be present between these modes. Further, the FT FEIR line widths do not correspond to those observed in 2D IR, as the latter originate from high frequency vibrational coherence lifetimes in a third time delay not present in FT FEIR.

4.4 Discussion

4.4.1 Description of FT FEIR Signal

To better understand the origin of resonances and line shapes in Fourier transform FEIR spectra, it is helpful to model these features. I expand on the previously proposed phenomenological framework for the single-IR pulse F_1 signal[27] to include a delay between the two IR interactions to describe the F_2 signal. This formalism is similar to that used for describing fluorescence-detected 2D electronic spectroscopies.[8,10,14,15,36] The electronic excited state population ρ_{EE} prepared by the FEIR pulse sequence can be expressed in terms of a nonlinear response function[37] as a nested commutator.[IV]

$$\rho_{EE}^{(4)}(\tau_1,\tau_d) \propto Tr_E\Big[\mathrm{M}(\tau_1+\tau_d),\Big[\mathrm{M}(\tau_1+\tau_d),\Big[\mu(\tau_1),\big[\mu(0),\rho_0\big]\Big]\Big]\Big]$$

[IV] It can be shown with cyclic invariance that this form of the nested commutator is identical to that presented by Mukamel.[40]

Here ρ_0 is the equilibrium density matrix and the trace is taken over the electronic excited states, neglecting excited state dynamics and fluorescence quantum yields for simplicity. The light–matter interaction in this expression is governed by the dipole operator matrix elements projected onto the incident field polarization, $\mu_{Gn,Em} = \langle G,n \,|\, \overline{\mu} \cdot \hat{\varepsilon} \,|\, E,m \rangle$, which will be simplified for vibrational transitions on the ground electronic state as $\mu_{mi} = \mu_{Gm,Gi}$. The matrix elements of the time-ordered two-photon operator M can be represented as a sum over all electronic states F of products of vibronic transition dipole operators between the ground and excited electronic states, mediated by higher-lying off-resonance states in the vibronic manifold, $|F,j\rangle$:

$$M_n = \sum_F \sum_{j,k} \mu_{Ek,Fj} \mu_{Fj,Gn}$$

For the present work, I consider the FEIR signal to be proportional to the excited electronic population resulting from the interaction with two IR pulses and one NIR encoding pulse. Furthermore, I assume the electronic interaction can be described as a two-photon absorption for simplicity; and that the encoding pulse is on resonance with an electronic two-photon transition from the excited vibrational manifold, and off resonance with the two-photon transition from the vibrational ground state population, in a similar manner to other mixed IR-Vis Pulse sequences.[31–33] Under those assumptions, this expression can be reduced to one that depends on a three-point time-correlation function

$$\rho^{(4)}_{EE}(\tau_1, \tau_d) \propto \mathrm{Re}\left[C^{(4)}_{FEIR}(\tau_1, \tau_d) \right]$$

where the correlation function takes a form of

$$C^{(4)}_{FEIR}(\tau_1, \tau_d) = Tr_e \left[\mathrm{M}(\tau_1 + \tau_d) \mu(0) \rho_0 \mu(\tau_1) \mathrm{M}(\tau_1 + \tau_d) \right]$$

Typical interaction sequences for this expression can be described using diagrammatic perturbation theory for $C^{(4)}_{FEIR}(\tau_1,\tau_d)$ in the simplest model of two vibrations coupled to an electronic transition (Figure 4.6). The time dependence corresponding to each term can be written in an eigenstate representation using phenomenological propagators of the form:

$$U_{nm}(\tau_j) = \exp\left[-(i\omega_{nm}+\gamma_{nm})\tau_j\right]$$

The application of these propagators results in the Liouville pathways:

$$P_1 = |\mu_{ni}|^2 |M_n|^2 \exp\left[-i\omega_{ni}\tau_1 - \Gamma_{ni}\tau_1 - \Gamma_{nn}\tau_d\right]$$
$$P_2 = |\mu_{mi}|^2 |M_m|^2 \exp\left[-i\omega_{mi}\tau_1 - \Gamma_{mi}\tau_1 - \Gamma_{mm}\tau_d\right]$$
$$P_3 = \mu_{ni}\mu^*_{mi} M_n M^*_m \exp\left[-i\omega_{ni}\tau_1 - \Gamma_{ni}\tau_1 - i\omega_{nm}\tau_d - \Gamma_{nm}\tau_d\right]$$
$$P_4 = \mu_{mi}\mu^*_{ni} M_m M^*_n \exp\left[-i\omega_{mi}\tau_1 - \Gamma_{mi}\tau_1 - i\omega_{mn}\tau_d - \Gamma_{mn}\tau_d\right]$$

In these expressions, *i* refers to the equilibrated ground state $|G,i\rangle$; and *n,m* are shorthand for single quantum excitations of the ground electronic state vibrational modes $|G,n\rangle$ and $|G,m\rangle$.

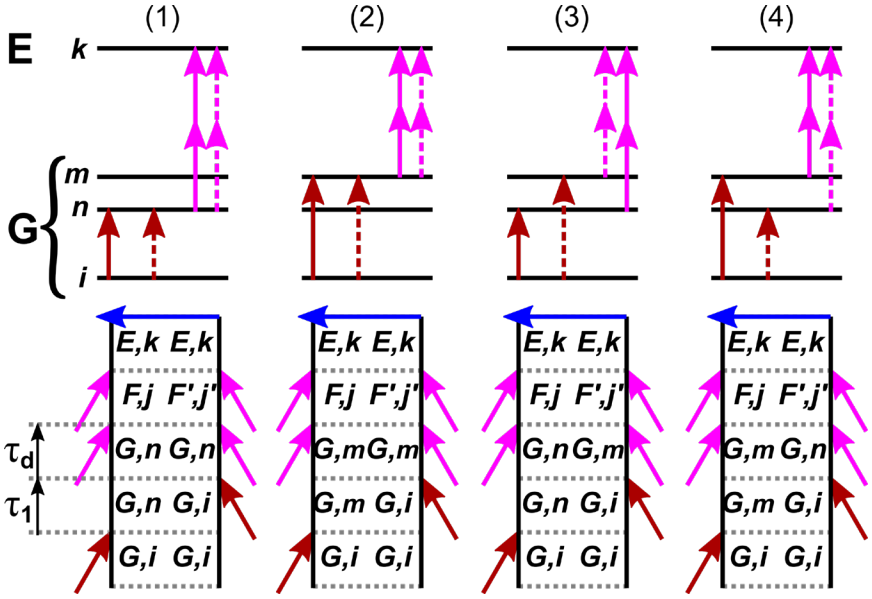

Figure 4.6) Diagrams of Terms in the Response Function for Linear FEIR. Representative Lee-Albrecht Ladder **(top)** and Feynman diagrams **(bottom)** for $C^{(4)}$ can be drawn for a system of two vibrations coupled to an electronic transition, arising in P_1-P_4 Liouville pathways, from left to right. Horizontal arrows, blue, represent the trace over electronic excited states resulting in incoherent fluorescence.[15]

Pathways P_1 and P_2 describe the excitation of vibrational populations on the ground electronic surface, and pathways P_3 and P_4 describe the excitation of vibrational coherences. As such, P_3 and P_4 only contribute in the presence of coupling between modes n and m that share a common ground state. These expressions also illustrate how coherent evolution in τ_d appears as a phase shift in the τ_1 interferogram, and vice versa (Figure 4.4A). Since $-\omega_{nm} = \omega_{mn}$, this phase shift ϕ is of equal magnitude but opposite sign for the two coupled modes (Figure 4.7):

$$\phi = \omega_{nm}\tau_d = -\omega_{mn}\tau_d$$

Applying a 2D Fourier transformation with respect to both τ_1 and τ_d, and shifting to the skewed ordinate $\omega_2 = \omega_1 - \omega_d$, the 2D spectral representation of these Liouville pathways is obtained:

$$P_1 = \frac{-|\mu_{ni}|^2 |M_n|^2}{(\omega_1 - \omega_{ni} + i\Gamma_{ni})(\omega_2 - \omega_1 - i\Gamma_{nn})}$$

$$P_2 = \frac{-|\mu_{mi}|^2 |M_m|^2}{(\omega_1 - \omega_{mi} + i\Gamma_{mi})(\omega_2 - \omega_1 - i\Gamma_{mm})}$$

$$P_3 = \frac{-\mu_{ni}\mu_{mi}^* M_n M_m^*}{(\omega_1 - \omega_{ni} + i\Gamma_{ni})(\omega_2 - (\omega_1 - \omega_{nm}) - i\Gamma_{nm})}$$

$$P_4 = \frac{-\mu_{mi}\mu_{ni}^* M_m M_n^*}{(\omega_1 - \omega_{mi} + i\Gamma_{mi})(\omega_2 - (\omega_1 - \omega_{mn}) - i\Gamma_{mn})}$$

These expressions illustrate that population pathways P_1 and P_2 lead to diagonal peaks, whereas coherence pathways P_3 and P_4 lead to cross peaks. In P_3, a resonance exists when $\omega_1 = \omega_{ni}$ and when $\omega_2 = \omega_1 - \omega_{nm} = \omega_{mi}$, while in P_1, a resonance exists when $\omega_1 = \omega_2 = \omega_{ni}$. Thus, a skewed ordinate of $\omega_2 = \omega_1 - \omega_d$ results in an intuitive mapping to similar axes as 2D IR.

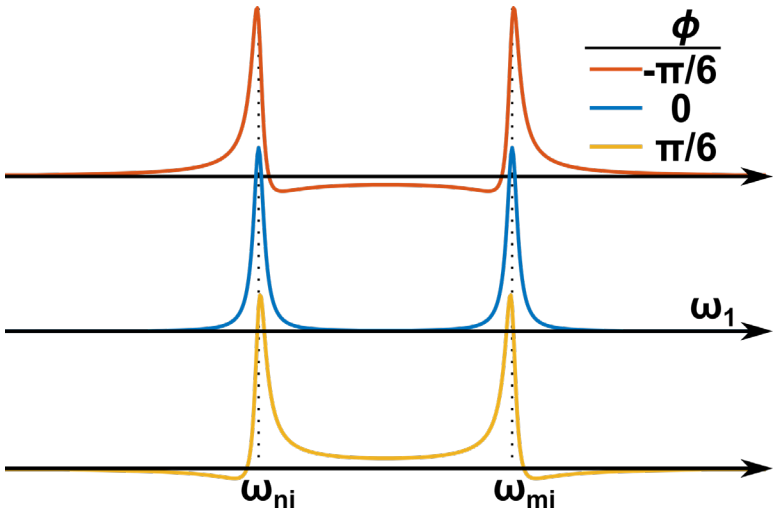

Figure 4.7) Coherence-Induced Phase Twisting in FT FEIR Slices in τ_d. Modelled imaginary part of two Lorentzian line shapes with a variable phase shift of equal magnitude but opposite sign displays similar phase twisting to 2D FEIR slices in τ_d.

Under this framework, I can model the spectral components which contribute to this measurement. I note that the predicted 2D line shapes appear to resemble those obtained in other experiments which take a one-sided Fourier transform in two dimensions,[10,13–15,38,39] resulting in a 2D product of complex Lorentzian line shapes when contoured in axes of ω_1 and ω_d (Figure 4.8). In 2D IR measurements, the phase of the coherence prepared in τ_3 is variable relative to that prepared in τ_1 and can be independently controlled, resulting in rephasing and non-rephasing line shapes with oppositely-signed dispersive components that can be added to produce an absorptive line shape. However, in the reduced dimensionality of the 2D FEIR measurement, the phase of the signal in τ_d depends on the phase of the signal in τ_1, which prevents the measurement of a purely absorptive line shape. Thus, the imaginary part of the predicted complex Lorentzian line shape is not purely absorptive but contains negative features that contribute to the off-diagonal negative features observed in the 2D FEIR spectrum (Figure 4.5). Further, phase error introduced in τ_d by cutting the data outside of the pulse-overlap region can contribute to a slight phase twist in the line shape that introduces a small contribution from the dispersive part of the spectrum.

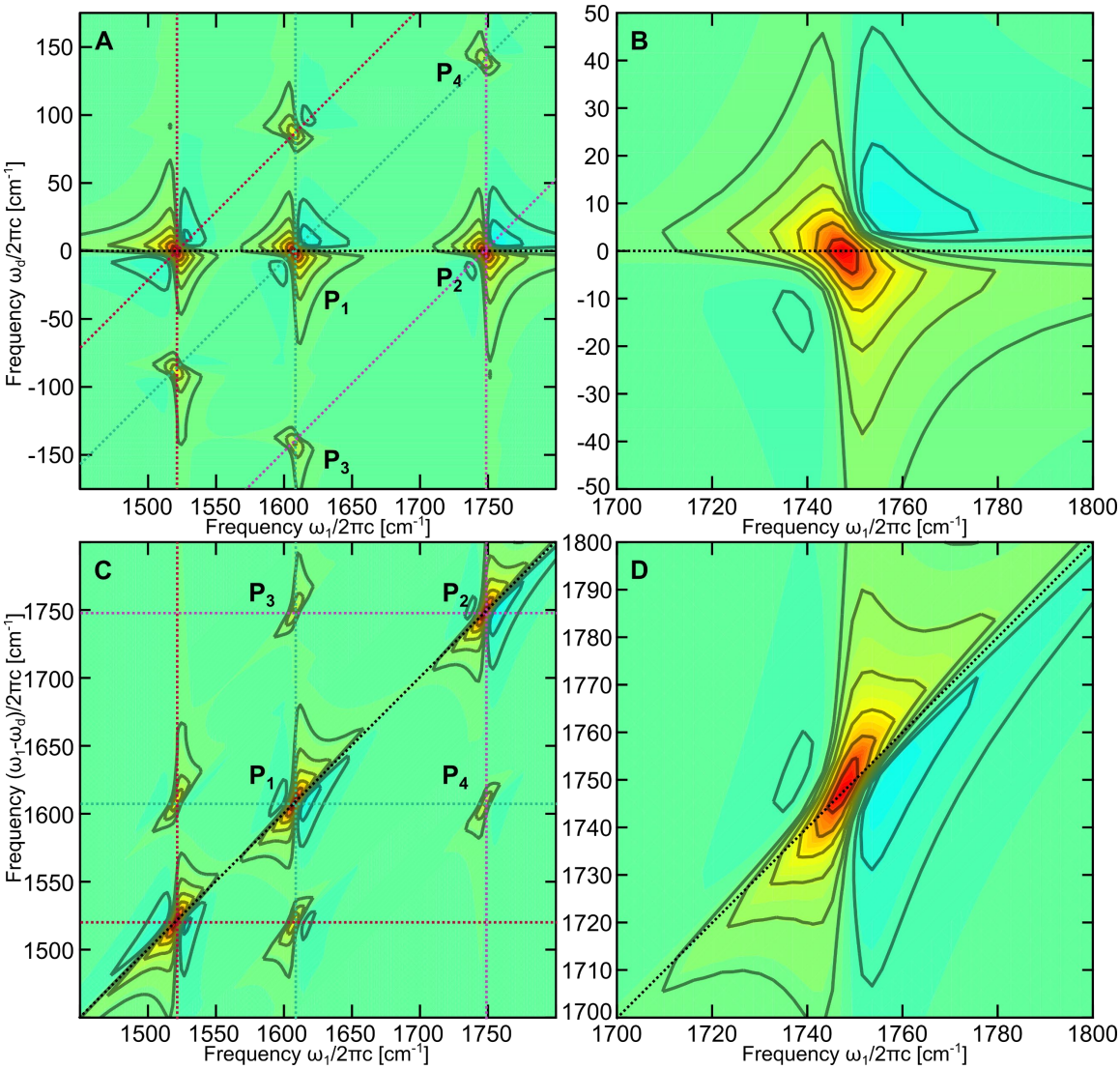

Figure 4.8) FT FEIR Line Shape Model Surface in Two Frequency Axes. 2D FEIR spectra obtained from phenomenological modelling are shown in (ω_1,ω_d) representation **(top)** and (ω_1,ω_2) representation **(bottom) A.)** The imaginary part of spectrally modelled features at frequencies of the C466 $\nu_{ArN\text{-}s}$, $\nu_{Ar\text{-}s}$ and ν_{CO} modes, with linewidths corresponding to decay in τ_1 and τ_d of 1000 fs, diagonal peak intensities of 1, and cross peak intensities of 0.2 $(\nu_{ArN\text{-}s}\text{-}\nu_{Ar\text{-}s})$ and 0.1 $(\nu_{Ar\text{-}s}\text{-}\nu_{CO})$. Here we label the coupled peak quartet of $\nu_{Ar\text{-}s}$ and ν_{CO} as P_1-P_4. **B.)** The simulated ν_{CO} peak in detail. **C.)** The same spectrum as *A*, reflected across the abscissa and skewed vertically by $\pi/2$. This transformation is identical to plotting against a skewed ordinate of $\omega_2=\omega_1-\omega_d$. **D.)** The same spectrum as **(B)**, applying the same transformation as in **(C)**.

In TPE-FEIR measurements, under the assumptions made above, a full calculation of the observed intensities requires the projection of the vibrationally excited electronic ground state onto the electronic excited state by the two-photon operators, *M*. To quantify the matrix elements of *M* in the simplest case

under the Condon approximation and assuming one off-resonance electronic intermediate, *F*, requires a calculation of the product of two Franck-Condon overlap integrals involving this higher-lying intermediate state. Further, by expanding the nested commutators to consider each of the dipole operators in the two-photon operator separately, it is possible to describe additional oppositely-signed off resonant impulsive Raman-like excitation pathways that can occur in the encoding process. These terms involving higher-lying electronic states, which affect the experimental amplitudes of the vibrational modes observed in the 2D FEIR signal, are difficult to calculate accurately for a two-photon encoding process. However, as the vibrational coherences and populations are excited on the ground electronic state prior to the encoding process, the peak center frequencies of coupled homogeneous modes that contribute should be identical to those measured with FTIR. The effect of vibrational spectral diffusion on the electronic transition is not considered in this chapter – while environmental inhomogeneity can contribute to broadening in ω_1 as will be explored in Chapter 5, a model of spectral diffusion will be presented in Chapter 7 for the higher-order FEIR terms of the response function.

4.4.2 FT FEIR signal measured in C466

As previously predicted from F_1 traces,[27] the IR and Raman-active C466 $\nu_{\text{Ar-s}}$ (1608 cm^{-1}) and ν_{CO} (1748 cm^{-1}) modes indeed contribute to the FEIR signal, as well as cross peaks between these modes. Additionally, the IR-active, Raman-inactive $\nu_{\text{ArN-s}}$ (1521 cm^{-1}) mode is observed, with strong cross peaks to the $\nu_{\text{Ar-s}}$ mode. However, cross peaks are not observed between the $\nu_{\text{ArN-s}}$ and ν_{CO} modes. This may be a result of the spatial separation of the rotor amine group and the carbonyl moiety; however, we note that the frequency separation between the $\nu_{\text{ArN-s}}$ and ν_{CO} modes is close to the bandwidth of our NIR pulse, which might also limit the cross peaks that can be observed. The modes which contribute to both 2D IR

and 2D FEIR measurements appear to show similar cross peaks in both; however, these measurements correspond to different physical processes. 2D IR corresponds to a coherently-detected vibrational response in 3 time delays, while FT FEIR corresponds to an incoherently-detected mixed vibrational-electronic response that is experimentally resolved in 2 time delays. The peak intensities measured do not directly correspond to either the IR or Raman excitation selection rules, indicating a difference in how the two-photon encoding in the TPE-FEIR process projects the vibrational excitation onto the electronic excited state. The A-like symmetry ring modes contribute more strongly than the B-like symmetry ring modes. The IR-inactive, Raman-active 1545 cm^{-1} $\nu_{ArN\text{-}a}$ mode is not observed, and the IR-active, Raman-inactive 1616 cm^{-1} $\nu_{Ar\text{-}a}$ mode contributes only weakly in FT FEIR, while it is more intense than the $\nu_{Ar\text{-}s}$ mode in the FTIR and 2D IR. Above the diagonal, a negative feature between the $\nu_{Ar\text{-}s}$ and $\nu_{Ar\text{-}a}$ modes might arise from the 2D complex Lorentzian line shape modelled above. Further, a peak in both the FTIR and FEIR data at 1570 cm^{-1} does not appear to correspond to an assigned C466 vibrational mode despite potential cross peaks to the $\nu_{Ar\text{-}s}$ mode in C466. While the solvent is of sufficient purity that it does not fluoresce in absence of the dye, the vibrational resonances detected in C466 solutions might be of an inter- or intra-molecular character as part of the solution-phase molecular ensemble.

4.5 Conclusions

In this work, Fourier Transform FEIR has been demonstrated to contain qualitatively similar, but not identical, information on coupled vibrational modes to conventional 2D IR measurements. Upon interferometrically resolving an IR pump frequency axis in the F_2 FEIR signal, further information was

elucidated about which vibrational modes contribute to the FEIR signal observed with one IR pulse. Using a response function formalism, I have modelled the vibrational spectral features in 2D FEIR, noting that vibrational coherence terms in the density matrix between coupled vibrational modes will result in cross peaks in this representation. The presence of coupling observed between vibrational modes in 2D FEIR agrees with the greater degree of information on coupling that is reported on by traditional coherent 2D IR. This suggests that FEIR can be used to spectrally resolve coupled vibrational modes in lower concentration systems using the heightened sensitivity of fluorescence detection methods. As existing fluorescence techniques have proven sensitive down to the single molecule level by utilizing higher repetition rate systems and high numerical aperture microscope objectives, an FEIR instrument with these features is under development to extend the technique to the dilute concentration limit, orders of magnitude lower than presented here. By analogy to other fluorescence-detected 2D electronic methods, it may be possible to expand FT FEIR to a higher order experiment with the addition of two more IR interactions to measure absorptive line shapes similar to 2D IR.

Many questions regarding the properties and applications of FEIR remain, which need to be explored in further detail. From this work, it is unclear how inhomogeneous broadening and spectral diffusion will influence the FT FEIR line shapes. Inhomogeneous broadening will be considered in Chapter 5. Spectral diffusion in higher orders of FEIR will be modelled in Chapter 7. Finally, if FEIR is to be a generally applicable technique, it will prove important to demonstrate how the FEIR spectrum reports on interactions with the local environment of the model system. I plan to initially investigate this through polar solvation dynamics studies in Chapter 5.

Chapter Bibliography

(1) Kanstad, S. O.; Nordal, P. E. Infrared Photoacoustic Spectroscopy of Solids and Liquids. *Infrared Phys.* **1979**, *19* (3–4), 413–422.

(2) Burke, N. L.; Redwine, J. G.; Dean, J. C.; Mcluckey, S. A.; Zwier, T. S. UV and IR Spectroscopy of Cold Protonated Leucine Enkephalin. *Int. J. Mass Spectrom.* **2015**, *378*, 196–205.

(3) Hutchison, J. M.; Holiday, R. J.; Bach, A.; Hsieh, S.; Crim, F. F. Action Spectroscopy and Photodissociation of Vibrationally Excited Methanol. *J. Phys. Chem. A* **2004**, *108* (39), 8115–8118.

(4) Bonn, M.; Hess, C.; Funk, S.; Miners, J.; Persson, B.; Wolf, M.; Ertl, G. Femtosecond Surface Vibrational Spectroscopy of CO Adsorbed on Ru(001) during Desorption. *Phys. Rev. Lett.* **2000**, *84* (20), 4653–4656.

(5) Yamaguchi, S.; Tahara, T. Precise Electronic $\chi(2)$ Spectra of Molecules Adsorbed at an Interface Measured by Multiplex Sum Frequency Generation. *J. Phys. Chem. B* **2004**, *108* (50), 19079–19082.

(6) Boyle, E. S.; Neff-Mallon, N. A.; Handali, J. D.; Wright, J. C. Resonance IR: A Coherent Multidimensional Analogue of Resonance Raman. *J. Phys. Chem. A* **2014**, *118* (17), 3112–3119.

(7) Scherer, N. F.; Carlson, R. J.; Matro, A.; Du, M.; Ruggiero, A. J.; Romero-Rochin, V.; Cina, J. a.; Fleming, G. R.; Rice, S. a. Fluorescence-Detected Wave Packet Interferometry: Time Resolved Molecular Spectroscopy with Sequences of Femtosecond Phase-Locked Pulses. *J. Chem. Phys.* **1991**, *95* (August), 1487.

(8) Wagner, W.; Li, C.; Semmlow, J.; Warren, W. Rapid Phase-Cycled Two-Dimensional Optical Spectroscopy in Fluorescence and Transmission Mode. *Opt. Express* **2005**, *13* (10), 3697–3706.

(9) Li, C.; Wagner, W.; Ciocca, M.; Warren, W. S. Multiphoton Femtosecond Phase-Coherent Two-Dimensional Electronic Spectroscopy. *J. Chem. Phys.* **2007**, *126* (16).

(10) Tekavec, P. F.; Lott, G. A.; Marcus, A. H. Fluorescence-Detected Two-Dimensional Electronic Coherence Spectroscopy by Acousto-Optic Phase Modulation. *J. Chem. Phys.* **2007**, *127* (21).

(11) Widom, J. R.; Johnson, N. P.; Von Hippel, P. H.; Marcus, A. H. Solution Conformation of 2-Aminopurine Dinucleotide Determined by Ultraviolet Two-Dimensional Fluorescence Spectroscopy. *New J. Phys.* **2013**, *15*.

(12) Karki, K. J.; Kringle, L.; Marcus, A. H.; Pullerits, T. Phase-Synchronous Detection of Coherent and Incoherent Nonlinear Signals. *J. Opt.* **2016**, *18* (1), 15504.

(13) De, A. K.; Monahan, D.; Dawlaty, J. M.; Fleming, G. R. Two-Dimensional Fluorescence-Detected Coherent Spectroscopy with Absolute Phasing by Confocal Imaging of a Dynamic Grating and 27-Step Phase-Cycling. *J. Chem. Phys.* **2014**, *140* (19), 0–8.

(14) Grégoire, P.; Kandada, A. R. S.; Vella, E.; Leonelli, R.; Silva, C. Incoherent Population Mixing Contributions to Phase-Modulation Two-Dimensional Coherent Excitation Spectra. *J. Chem. Phys.* **2017**, *147* (114201).

(15) Perdomo-Ortiz, A.; Widom, J. R.; Lott, G. A.; Aspuru-Guzik, A.; Marcus, A. H. Conformation and Electronic Population Transfer in Membrane-Supported Self-Assembled Porphyrin Dimers by 2D Fluorescence Spectroscopy. *J. Phys. Chem. B* **2012**, *116* (35), 10757–10770.

(16) Laubereau, A.; Seilmeier, A.; Kaiser, W. A New Technique to Measure Ultrashort Vibrational

Relaxation Times in Liquid Systems. *Chem. Phys. Let.* **1975**, *36* (2), 232–237.
(17) Seilmeier, A.; Kaiser, W.; Laubereau, A. Vibrational Combination States of Polyatomic Molecules Investigated by Ultrashort Two-Pulse Spectroscopy. *Opt. Commun.* **1978**, *26* (3), 441–445.
(18) Seilmeier, A.; Kaiser, W.; Laubereau, A.; Fischer, S. F. A Novel Spectroscopy Using Ultrafast Two-Pulse Excitation of Large Polyatomic Molecules. *Chem. Phys. Lett.* **1978**, *58* (2), 225–229.
(19) Ding, K.; Kranitzky, W.; Fischer, S. F.; Kaiser, W. Structured UV-Spectrum of Naphthalene Obtained by Ultrafast Two-Pulse Excitation. *Chem. Phys. Lett.* **1980**, *72* (1), 39–42.
(20) Lettenberger, M.; Emmerling, F.; Gottfried, N. H.; Laubereau, A. Orientational Motion of Anthracene in Liquid Solution Studied by IR/UV Double-Resonance Spectroscopy. *Chem. Phys. Lett.* **1995**, *240* (4), 324–329.
(21) Emmerling, F.; Lettenberger, M.; Laubereau, A. Vibrational Dynamics of Anthracene in Liquid Solution Studied by Picosecond IR/UV Spectroscopy with Polarization Resolution. *J. Phys. Chem.* **1996**, *100* (50), 19251–19256.
(22) Gottfried, N. H.; Emmerling, F. High-Resolution Two-Pulse Spectroscopy of Anthracene in Solution. *J. Lumin.* **1999**, *81* (2), 143–147.
(23) Sakai, M.; Fujii, M. Vibrational Energy Relaxation of the 7-Azaindole Dimer in CCl 4 Solution Studied by Picosecond Time-Resolved Transient Fluorescence Detected IR Spectroscopy. *Chem. Phys. Lett.* **2004**, *396* (4–6), 298–302.
(24) Sakai, M. Vibrational Energy Relaxation Process of the 7-Azaindole Dimer in Gas Phase and Solution. *J. Spectrosc. Soc. Japan* **2005**, *54* (3), 163–169.
(25) Sakai, M.; Kawashima, Y.; Takeda, A.; Ohmori, T.; Fujii, M. Far-Field Infrared Super-Resolution Microscopy Using Picosecond Time-Resolved Transient Fluorescence Detected IR Spectroscopy. *Chem. Phys. Lett.* **2007**, *439* (1–3), 171–176.
(26) Bokor, N.; Inoue, K.; Kogure, S.; Fujii, M.; Sakai, M. Visible-Super-Resolution Infrared Microscopy Using Saturated Transient Fluorescence Detected Infrared Spectroscopy. *Opt. Commun.* **2010**, *283* (3), 509–514.
(27) Mastron, J. N.; Tokmakoff, A. Two-Photon-Excited Fluorescence-Encoded Infrared Spectroscopy. *J. Phys. Chem. A* **2016**, *120* (46), 9178–9187.
(28) DeFlores, L. P.; Nicodemus, R. a; Tokmakoff, A. Two-Dimensional Fourier Transform Spectroscopy in the Pump-Probe Geometry. *Opt. Lett.* **2007**, *32* (20), 2966.
(29) Oliver, T. A. A.; Lewis, N. H. C.; Graham, R. Correlating the Motion of Electrons and Nuclei with Two-Dimensional Electronic–vibrational Spectroscopy. *Proc. Natl. Acad. Sci.* **2014**, *111* (46), 16628–16628.
(30) Courtney, T. L.; Fox, Z. W.; Slenkamp, K. M.; Khalil, M. Two-Dimensional Vibrational-Electronic Spectroscopy. *J. Chem. Phys.* **2015**, *143* (15), 0–15.
(31) Gaynor, J. D.; Khalil, M. Signatures of Vibronic Coupling in Two-Dimensional Electronic-Vibrational and Vibrational-Electronic Spectroscopies. *J. Chem. Phys.* **2017**, *147* (9).
(32) Wilderen, L. J. G. W. Van; Messmer, A. T.; Bredenbeck, J. Mixed IR / Vis Two-Dimensional Spectroscopy : Chemical Exchange beyond the Vibrational Lifetime and Sub-Ensemble Selective Photochemistry**. *Angew. Chem. Int. Ed.* **2014**, *53*, 2667–2672.
(33) Wilderen, L. J. G. W. van; Messmer, A. T.; Bredenbeck, J. VIPER 2D-IR: Novel Pulse Sequence to Track Exchange Beyond the Vibrational Lifetime. *Springer Proc. Phys.* **2015**, *162*, 572–575.
(34) Cosel, J. Von; Cerezo, J.; Kern-michler, D.; Neumann, C.; Wilderen, L. J. G. W. Van;

Bredenbeck, J.; Santoro, F.; Burghardt, I. Vibrationally Resolved Electronic Spectra Including Vibrational Pre-Excitation : Theory and Application to VIPER Spectroscopy. *arXiv* **2017**, *1707* (03476v1).

(35) Mertz, L. AUXILIARY COMPUTATION FOR FOURIER SPECTROMETRY. *Infrared Phys.* **1967**, *7*, 17–23.

(36) De, A. K.; Monahan, D.; Dawlaty, J. M.; Fleming, G. R. Two-Dimensional Fluorescence-Detected Coherent Spectroscopy with Absolute Phasing by Confocal Imaging of a Dynamic Grating and 27-Step Phase-Cycling. *J. Chem. Phys.* **2014**, *140* (19), 1–9.

(37) Sung, J.; Silbey, R. J. Four Wave Mixing Spectroscopy for a Multilevel System. *J. Chem. Phys.* **2001**, *115* (20), 9266–9287.

(38) Khalil, M.; Demirdöven, N.; Tokmakoff, A. Coherent 2D IR Spectroscopy : Molecular Structure and Dynamics in Solution. *J. Phys. Chem. A* **2003**, No. 107, 5258–5279.

(39) Khalil, M.; Demirdöven, N.; Tokmakoff, A. Obtaining Absorptive Lineshapes in Two-Dimensional Infrared Vibrational Correlation Spectra. *Phys. Rev. Lett.* **2003**, *90* (January), 47401–47404.

(40) Mukamel, S. *Principles of Nonlinear Optical Spectroscopy*; 1995; Vol. 6.

Appendix 2

Supplementary Figures to Chapter 4

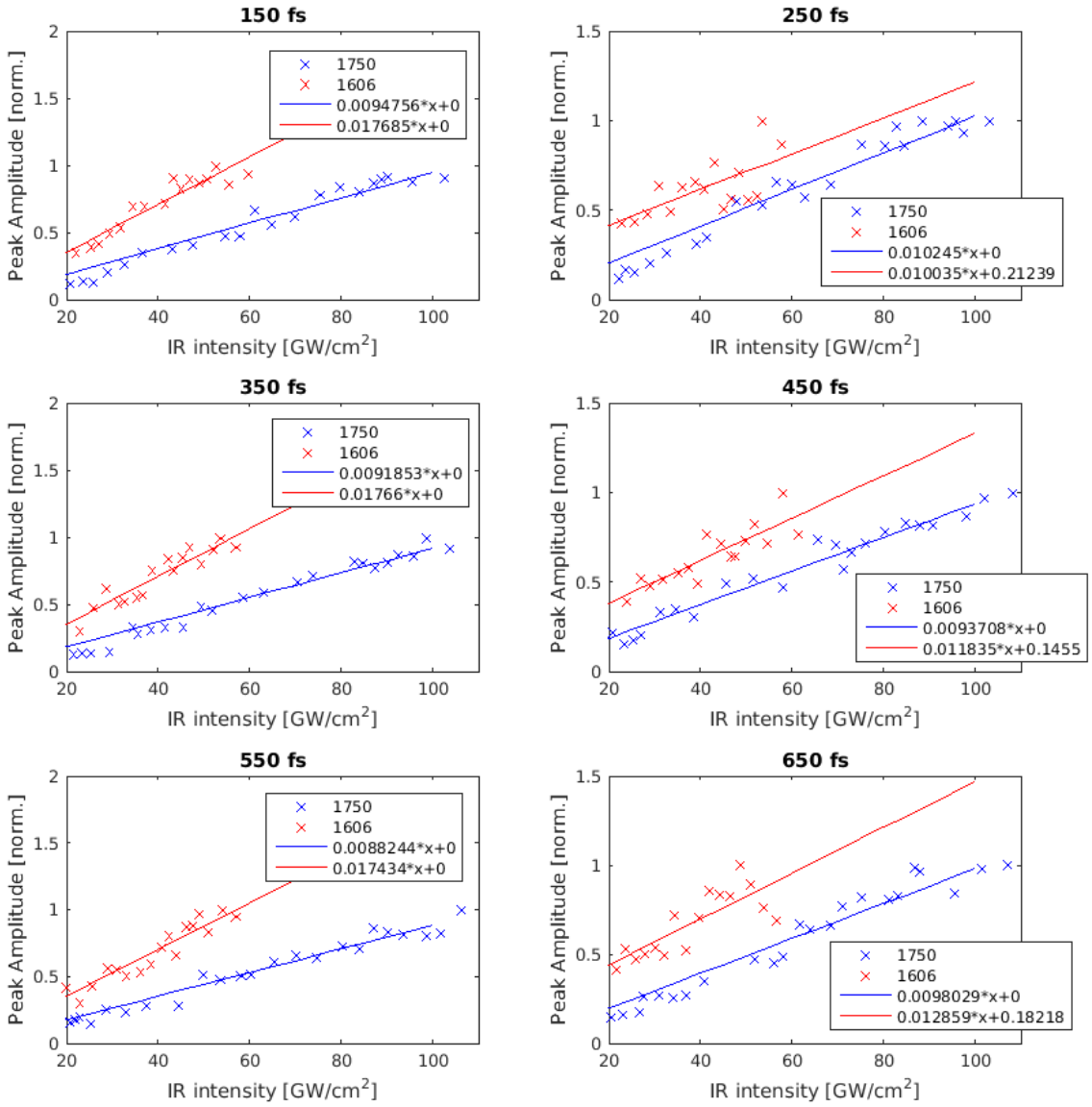

Figure 4.A2.1) Frequency-Resolved FEIR dependence on IR Pump Intensity. IR intensity dependence of $\nu_{Ar\text{-}s}$ and ν_{CO} modes of C466 in CH-d_{12} with IR centered at 1775 cm^{-1} showing linearity in the measured intensity range. Intensity dependence was measured by varying the IR intensity with the IR waveplate ($\lambda/2$) and polarizer (Pol, Figure 4.2). The waveplate was randomly rotated using a DC motor, allowed to settle, and 6 waiting times were measured. This was repeated for 25 intensity points. The intensity of the reference IR spectrum was used with a measured conversion factor to calculate the IR intensity at each of the peaks in the absolute value FT FEIR spectra.

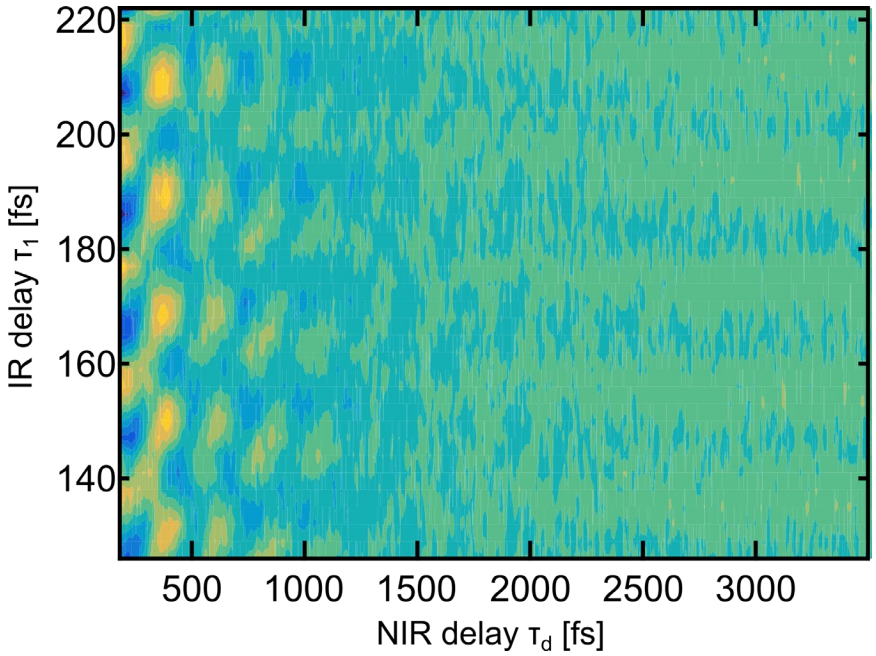

Figure 4.A2.2) FT FEIR Surface in Two Time Delays. Interferometric beating can be observed to depend on both the τ_1 and τ_d delays in a surface of $F_1(\tau_d)+F_2(\tau_1,\tau_d)$ after subtracting an exponential background. This is the same phase shift observed as a dispersive line shape in $F_2(\tau_1,\omega_d)$ slices.

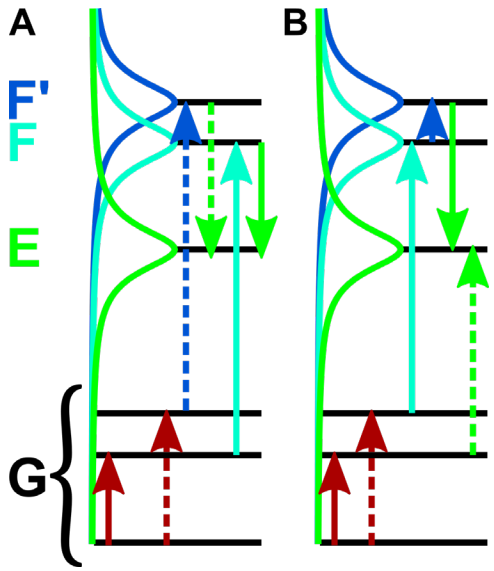

Figure 4.A2.3) Ladder Diagrams of the Two-Photon-Encoding Process. As this Lee-Albrecht Ladder Diagram shows **(A)**, different higher-lying states may participate in the two-photon encoding process. The two-photon excitation occurs through an off-resonance transition to a higher lying excited state, F or F', after which an on-resonance transition ends in the first electronic state. The nature of this higher-lying state may vary with the vibrational coordinate of each term in the coherence. Additionally, taking a full expansion of the nested commutators described in the main text leads to Transient-Raman-Like electronic transitions **(B)**. These Raman-like terms will be oppositely signed with their complex conjugates and cancel.

Chapter 5
Solvation and Environmental Effects in FT FEIR

Chapter Abstract

In previous chapters, I have demonstrated FT FEIR as a technique that provides vibrational frequency resolution with the benefits of visible detection. Until this point, applications to more diverse local environments have not been explored in detail. For FEIR to be useful as a more general technique, studies of the environmental influences on the dye as can be measured with FEIR, and the differences with FTIR in information content, is necessary to plan for future applications of the technique to more complex systems. To this end, I have measured a number of solvation systems, tuning the local environment of the model dye. This chapter explores the effects of tuning solvent proticity (that is, the ability of the solvent to donate a hydrogen bond) and polarity on the coumarin molecule and models the FEIR measurements of these systems. Hydrogen-bonding fractions of coumarin molecules are extracted spectrally as a function of the hydrogen bond donor concentration. The observed frequencies of the coumarin carbonyl undergo a vibrational Stark shift with relative solvent polarity, which also increases inhomogeneity in the local environment. Vibrational energy transfer between dark and bright FEIR modes can be observed as a growth of a dark mode in the encoding time delay. These findings indicate that FEIR can be useful to measure hydrogen bonding and local solvent polarity, and suggest the feasibility of such measurements at fluorescence-accessible concentrations.

5.1 Introduction

As previously demonstrated, Fourier-Transform Fluorescence-Encoded Infrared Spectroscopy (FT FEIR) is an incoherently-detected analogue to linear FTIR measurements. FT FEIR is linear in IR pump intensity like FTIR (quadratic in IR pump field), but it differs in information content. FT FEIR encodes information from two vibrationally-dependent time axes, τ_1 and τ_2, into a higher order incoherently-detected response. The data in these axes are transformed to the frequency domain to reveal a two-dimensional surface.[1] The frequency-domain 2D surface maps onto similar frequencies to conventional 2D IR measurements following reflection and skew operations, and vibrational populations and coherences between coupled modes in the excited superposition appear as distinct population peaks and coherence cross peaks in this frequency-domain representation. Further, modes that display high Franck-Condon overlap with one or more electronic excited states will appear more prominently in FEIR than modes with low Franck-Condon factors.

Spectroscopic species can be identified and separated by observing population and coherence peak quartets in FT FEIR. Different spectroscopic species display distinct population-coherence quartets. However, these peak line shapes do not correspond to the same information content as 2D IR peak quartets and arise from different means. Cross peaks in FT FEIR correspond to the excitation and oscillatory decay of a vibrational coherence whereas cross peaks in 2D IR correspond to the excitation of one vibrational species followed by the observation of another through stimulated emission (the ground state bleach feature) or absorption (the induced absorption feature). Cross peaks in 2D IR can arise through chemical exchange or vibrational relaxation, while these processes do not contribute to cross

peaks in FT FEIR but appear as growth of certain features with encoding time delay. Through this difference in behavior, FEIR can be useful as a complementary technique to conventional IR spectroscopies, sitting somewhere between FTIR and 2D IR. Although I will not discuss it in further detail here, an FEIR process could be used to resolve Franck-Condon factors directly in the limit of a single-photon encoding process where each electronic interaction is interferometrically resolved, in which case it could be described as an incoherently-detected analogue to the 2D-VE measurement.

It is not only necessary to demonstrate the potential to separate distinct spectral species. For FEIR to prove useful as a general technique, it must be applicable to questions of how differing solvation environments and local environmental dynamics affect the vibrational signatures, and thus the structure, of the fluorescent probe. Aminocoumarin molecular rotors are a good choice of model system to probe environmental effects on vibrational features, as they have previously demonstrated a sensitivity in FEIR to solvation environment in the encoding time delay.[2] Coumarins of this type are very soluble in solvents of middling to high relative polarity, such as THF, acetone, ethers, or longer-chain alcohols. While coumarins dissolve in lower concentrations in cyclohexane and other nonpolar solvents due to their polar nature (on the order of 10 mM) they are also limited in their ability to dissolve in water (on the order of 10 mM), methanol (on the order of 40 mM), and other highly-polar solvents that cannot solvate the nonpolar parts of the molecule. As seen in methanol, this effect is mitigated somewhat by the coumarin lactone carbonyl's hydrogen-bond-accepting character. Both solvent polarity and hydrogen-bonding donating strength have the potential to affect the aminocoumarin structural dynamics upon solvation, which can then be probed by FEIR measurements as a test of the technique's sensitivity to these factors.

I have selected several model systems to test the applicability of FT FEIR to studies of Coumarin solvation. First, solvent proticity, that is, the availability of hydrogen bond donors in the pure solvent or solvent mixture, can be controlled through the concentration of a hydrogen bond donor species to provide an experimental handle on hydrogen bonding. I measured an aminocoumarin dissolved in a series of binary solvent mixtures of cyclohexane and n-propanol, with alcohol concentrations ranging from micromolar to molar, to demonstrate how solvent hydrogen bond donation to the highly FEIR-active coumarin lactone carbonyl alters its FEIR response.[3,4] Two-dimensional SVD of these data can be used to separate the free coumarin features from the titrated hydrogen-bonded coumarin features. Next, tuning the solvent polarity provides an experimental handle on the local electric field through the vibrational Stark effect, as the vibrational frequency will shift in a local electric field induced by the polar solvent.[5–7] We measured aminocoumarins in several solvation environments and ternary mixtures to demonstrate this effect. A simple line-shape model elucidates the effects of spectral inhomogeneity that might be induced by varying the solvation environment of the aminocoumarin probe, through modeling of how spectral features are affected by correlations of the spectral frequencies of vibrational modes. Spectral line shape models will be discussed in more detail in Chapter 8. 2D IR measurements were used to complement the FEIR data where necessary.

5.2 Materials and Methods

For the solvent proticity series, I prepared the aminocoumarin samples as follows. Coumarin 466 was weighed and a calculated volume of cyclohexane (CH) was added via micropipette to prepare a concentration of 9.6 mM for the Coumarin 466 (C466) stock solution. The sample was sonicated and

centrifuged iteratively until no precipitate was visible after centrifugation to confirm dissolution. Separately, n-propanol (n-prOH) in cyclohexane mixtures were prepared at 2 M and 632 mM, and sequentially diluted by factors of 10 in cyclohexane twice for a total of 6 initial samples. These binary solvent mixtures were then mixed 1:1 with the Coumarin 466 stock solution for ternary mixtures of 4.8 mM C466, 1M n-prOH in CH; 4.8 mM C466, 316 mM n-prOH in CH; &c as listed below. Further mixtures listed below were obtained by combining these samples in fixed ratios. I note that the change in volume due to mixing the two liquids is potentially non-zero and could introduce a slight error in the calculated concentrations of the binary solvent mixtures; however, the concentration of coumarin remains constant.

Table 5.1.) Table of mixtures

C466 at 4.8 mM in CH:n-prOH with n-prOH conc.	Other solvation mixtures
1 mM	p-Xylene
3.2 mM	p-X:NDMA (90 mM)
10 mM	CH:t-BuOH
32 mM	THF
100 mM	CDCl3
210 mM	Mineral Oil
320 mM	
660 mM	
830 mM	

In addition to the CH:n-prOH ternary mixtures, I prepared samples of C466 at 4.8 mM in the following solvents/mixtures: para-Xylene (p-X), p-X:n,n-Dimethylacetamide (NDMA), CH:t-Butanol (t-BuOH), Tetrahydrofuran (THF), Deuterated chloroform, and medium viscosity mineral oil (as a test of viscosity in a nonpolar medium).

The sample geometry and preparation varied by spectroscopic technique. The steady-state UV-Vis spectrometer (Thermo Fisher Nanodrop) required only a droplet of dilute sample. The sample cell used

for transmission FTIR measurements consisted of 30 μL of sample sandwiched between two Calcium Fluoride windows (Crystran 1" Ø, 1 mm thickness) separated by a 50 μm PTFE spacer. A custom-machined brass jacket held the sandwich cell to maintain a good seal from the environment. The same sample cell was used for 2D IR ultrafast measurements in pump-probe geometry[8] with C466 samples at ~10 mM concentrations. The sample cell used for FEIR measurements followed a similar design but was scaled down in size to accommodate a smaller sample volume of ~18 μL sandwiched between two 15 mm Ø, 1 mm thickness CaF2 windows separated by a 75 μm spacer. The custom-machined brass jacket that held this sandwich cell measures 1" diameter and was held in the FEIR setup in a commercially available magnetic-release 1" optic mount with 1 μm repeatability (Thorlabs KB1P). This sample geometry allowed for high reproducibility when changing samples and made it easy to change alignment optics such as pinholes or nonlinear crystals at the beam focus.

The analysis on the resulting data remained consistent with previous analyses. A Fourier transform of the FT FEIR data in the interferometric time delay τ_1 reveals frequency-domain vibrational pump information. A second Fourier transform in the encoding waiting time results in 2D FEIR surfaces as discussed previously in Chapter 4. When applied to these surfaces, SVD analysis extracted two-dimensional component surfaces.[9] The methodology for this two-dimensional SVD analysis is trivial and consists of reshaping 2D surfaces into vector arrays before analysis and reshaping the resulting components back into 2D surfaces. DFT calculations provided assignments of vibrational features as discussed previously in Chapter 2. Briefly, we assigned the spectral effects on the coumarin carbonyl in protic solvents using Gaussian 09 by explicitly placing one or two ethanol molecules as hydrogen bond donors at various locations and orientations around a C466 molecule.[10,11] The bulk solvation was modeled using polarizable continuum model (PCM) solvation in ethanol. After geometry optimization,

vibrational frequencies were calculated, and the corresponding atomic displacements were used to assign the character of the modes.

A qualitative model of line shapes in frequency[1,12] allows for a more detailed interpretation of the experimental results in terms of local homogeneity or inhomogeneity of the solvation environment. While a more detailed discussion of these models is reserved for Chapter 8, a brief discussion of applicable models is appropriate here. The simplest possible model of the 2D FEIR data arises from a Liouville pathway that ends in a vibrational population after two IR interactions. In absence of environmental inhomogeneity, this pathway should contribute to a peak at a vibrational frequency in ω_1 and at 0 in ω_d. The line shape of this peak will appear as the product of complex Lorentzian line shapes in ω_1 and ω_d, with Lorentzian widths corresponding to the lifetime of the vibrational coherence lifetime in τ_1 and the vibrational population lifetime in τ_d in the Bloch model, assuming exponential dephasing and population decay. The excitation of a vibrational superposition will result in a peak quartet that can be mapped to a 2D surface, as will be discussed in chapter 8. A simple model of static inhomogeneity can be derived by allowing a Gaussian distribution of the energies of one or both vibrational modes involved. The resulting average peak quartet spectra depend on if the peak frequencies are correlated, anticorrelated, or uncorrelated.

5.3 Experimental Results

5.3.1 Solvent Proticity Series of FT FEIR of C466

Solvent proticity affects the FT FEIR spectra of C466 through the appearance of spectral features that correspond to C466 species wherein the carbonyl oxygen acts as a hydrogen bond acceptor from the protic solvent. The non-Hydrogen-bonded carbonyl mode at 1748 cm^{-1} is lost with increasing concentration of n-prOH in the ternary mixture and two redshifted features grow in at 1726 cm^{-1} and 1708 cm^{-1}, consistent with FTIR measurements. DFT calculations with one and two hydrogen bond donors at the coumarin carbonyl suggest that these redshifted features correspond to singly and doubly hydrogen bonded species respectively. The carbonyl red shifts upon initial formation of a hydrogen bond, $\nu_{CO\text{-}1H}$, and further red shifts on the addition of a second, $\nu_{CO\text{-}2H}$.

5.3.2 2D IR of Coumarin 466 in CH:n-PrOH

This redshift and splitting of the carbonyl feature also appear in 2D IR measurements (Figure 5.2). Cross peaks appear between the lower two carbonyl features, as well as between the singly hydrogen bonded carbonyl and the free carbonyl. At perpendicular polarization, the cross peak between the vars and $\nu_{CO\text{-}H}$ modes is less intense than the cross peak between the $\nu_{Ar\text{-}a}$ and $\nu_{CO\text{-}H}$ modes.

In addition to the expected effects on the hydrogen bond accepting carbonyl mode, the 2D IR data in conjunction with the FEIR proticity series reveal the delocalized character of the vibrational excitation on the coumarin core as other vibrational modes are affected by increased hydrogen bonding character. In FEIR, the vars carbonyl coupled ring stretch mode broadens in ω_1 as the apparent vibrational lifetime shortens in τ_1. The FEIR-active $\nu_{ArN\text{-}s}$ and FEIR-inactive $\nu_{Ar\text{-}a}$ modes also appear to increase in relative

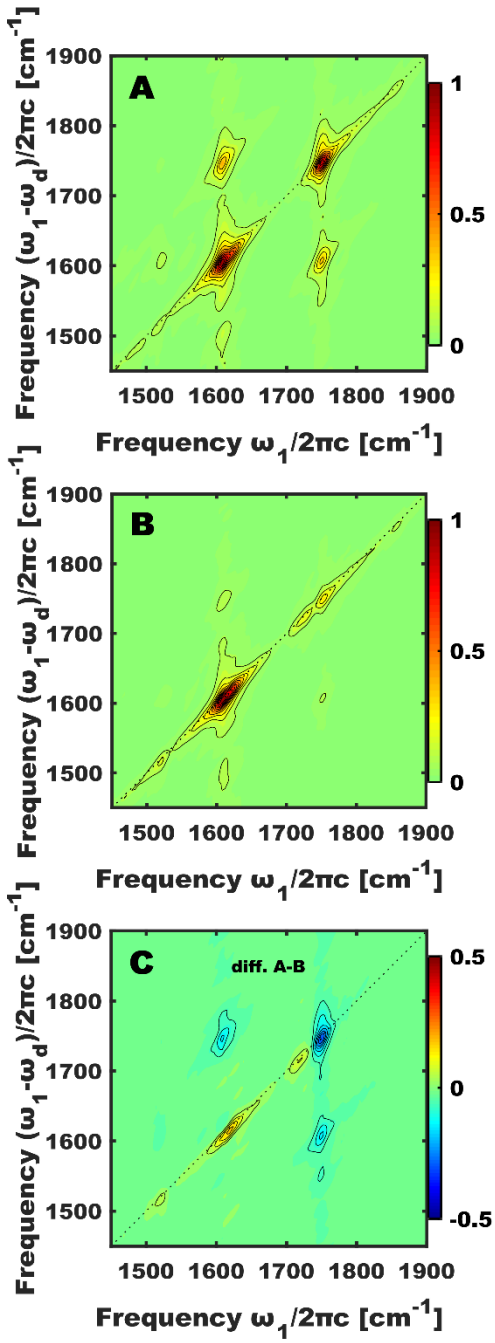

Figure 5.1) Solvent Proticity Series FEIR Results. A.) Absolute value 2D FEIR surface of C466 in CH serves as a benchmark for the solvent proticity series. Vibrational coherences between the $\nu_{ArN\text{-}s}$-$\nu_{Ar\text{-}s}$ and $\nu_{Ar\text{-}s}$-ν_{CO} modes appear strongly and peak linewidths are relatively similar in ω_1 and ω_d. **B.)** 2D FEIR of C466 in CH:n-prOH at 320 mM n-prOH demonstrates broadening in ω_1 and narrowing in ω_d. The carbonyl feature is split with a redshifted feature, and $\nu_{Ar\text{-}s}$-ν_{CO} cross peaks appear less intense. **C.)** The difference spectrum between normalized surfaces demonstrates an increased contribution from the $\nu_{Ar\text{-}a}$ mode to the blue of the $\nu_{Ar\text{-}s}$ peak as well as the redshifted ν_{CO} modes. The $\nu_{ArN\text{-}s}$ mode also appears to grow slightly in relative intensity.

intensity, and the $\nu_{ArN\text{-}s}$ mode appears to be split slightly. Additionally, the cross peaks between excited modes appear to decrease in intensity. In 2D IR, the $\nu_{Ar\text{-}a}$ mode, and to a lesser extent the vars mode, are coupled to the hydrogen bonded carbonyl. Increasing the n-prOH concentration in the solvation mixture has more structural effects on the coumarin than just an increase in hydrogen bonding to the carbonyl, although this change is likely mediated by hydrogen bonding.

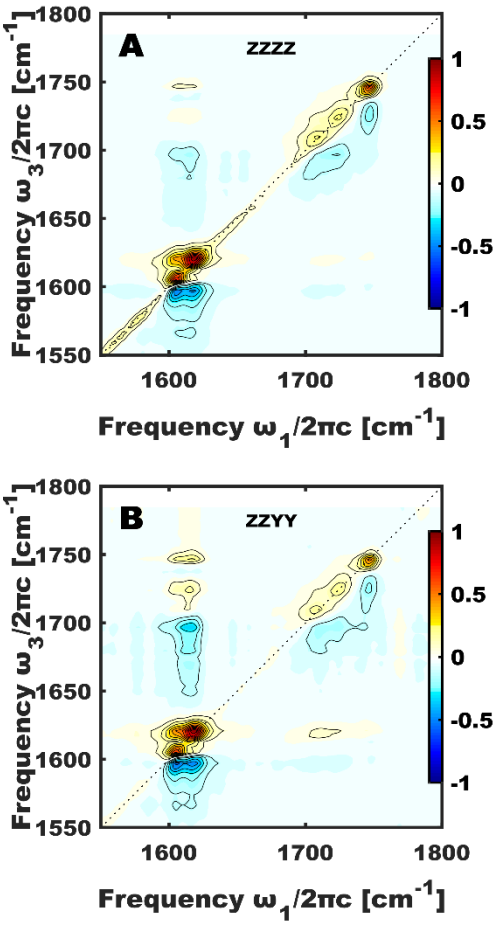

Figure 5.2) Solvent Proticity 2D IR Results. A.) The 500 fs waiting time 2D IR surface of C466 in CH:n-prOH at parallel polarization shows clearly two carbonyl features. **B.)** 2D IR at perpendicular polarization more clearly resolves cross peaks between features. The $\nu_{Ar\text{-}a}$ mode appears to be more strongly coupled to the hydrogen bonded species than the vars mode. The congested spectra make calculation of anharmonicity and anharmonic couplings difficult.

5.3.3 Solvent Polarity Series of FT FEIR of C466

A change in the polarity of the solvation environment affects vibrational features in similar ways to an increase of the solvent proticity. The coumarin carbonyl redshifts with increasing solvent polarity, indicating a lengthening of the C=O bond. This trend appears to be consistent with the red shift of the carbonyl observed upon hydrogen bonding. The vibrational stark effect can be applied to explain this red shift in frequency due to the local electric field of the polar solvent acting on the static vibrational dipole resulting in a frequency shift.[5,7,13] Ternary systems with an added polar aprotic component appear to redshift the frequency further than systems in absence of this component, as evidenced by a further redshift of the coumarin carbonyl from p-Xylene to p-X:NDMA ternary mixtures. Interestingly, in hydrogen bonding environments, the free carbonyl appears to blue shift with increasing solvent polarity, indicating a shortening of the C=O bond length. In many of these systems, a reduction in cross peak intensity and a broadening of features in ω_1 is observed but this effect appears uncorrelated to the solvent polarity, indicating a more nuanced physical origin.

The FEIR dark $\nu_{Ar\text{-}a}$ mode appears to grow in relative intensity at later encoding times in various solvation environments. The time scale of this growth of the FEIR dark $\nu_{Ar\text{-}a}$ mode is inversely correlated to the solvent viscosity. Coumarin in less viscous solvents such as THF appears to have a longer timescale of this growth, and the ratio between the $\nu_{Ar\text{-}s}$ and $\nu_{Ar\text{-}a}$ peaks appears to be exponential in encoding delay. Coumarin in more viscous solvents, such as CH or medium chain mineral oil, shows a reduction in the overall final intensity of this feature, and the ratio observed does not behave exponentially in the encoding time delay. This effect does not, however, appear to depend on the solvent polarity. The dependence of the behavior of molecular rotors on solvent viscosity has been well-

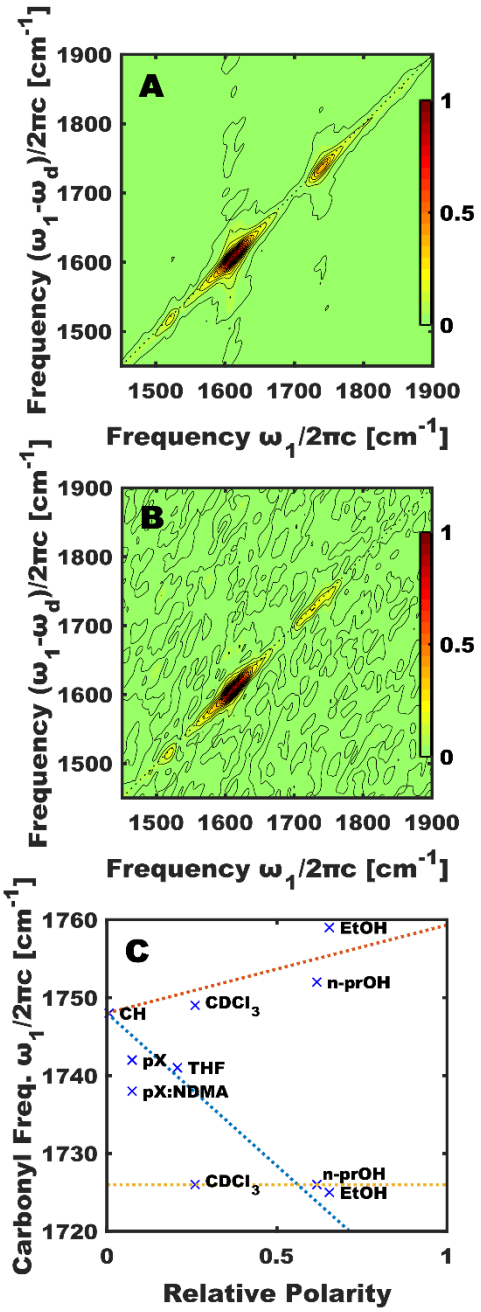

Figure 5.3) Solvent Polarity FEIR Results. A.) The absolute value 2D FEIR surface of C466 in THF shows a reduction of coherence cross peak features, a redshift of ν_{CO} mode, and increased broadening in ω_1. **B.)** 2D FEIR of C466 in $CDCl_3$ further follows this trend. Additionally, the ν_{CO} peak is split similarly as in proticity series, indicating hydrogen bonding between the chloroform and coumarin. **C.)** A plot of carbonyl frequencies versus relative solvent polarity[18] indicates two trends. In non-H-bonding solvents, the ν_{CO} frequency (blue dashed line) redshifts with increasing solvent polarity. In H-bonding solvents, the peak of the free carbonyl (red dashed line) is blue shifted with increasing polarity, although this can be attributed to fit error due to a sloping baseline from the hydrogen bonded $\nu_{CO\text{-}H}$ peak. The hydrogen bonded $\nu_{CO\text{-}H}$ frequency (yellow dashed line) appears relatively constant at 1726 cm^{-1}.

studied,[14–16] and a more viscous solvent will hinder the molecular rotor. In a more-viscous solvent, a vibrational relaxation through coupling to the rotor state is more hindered, and so this equilibration will

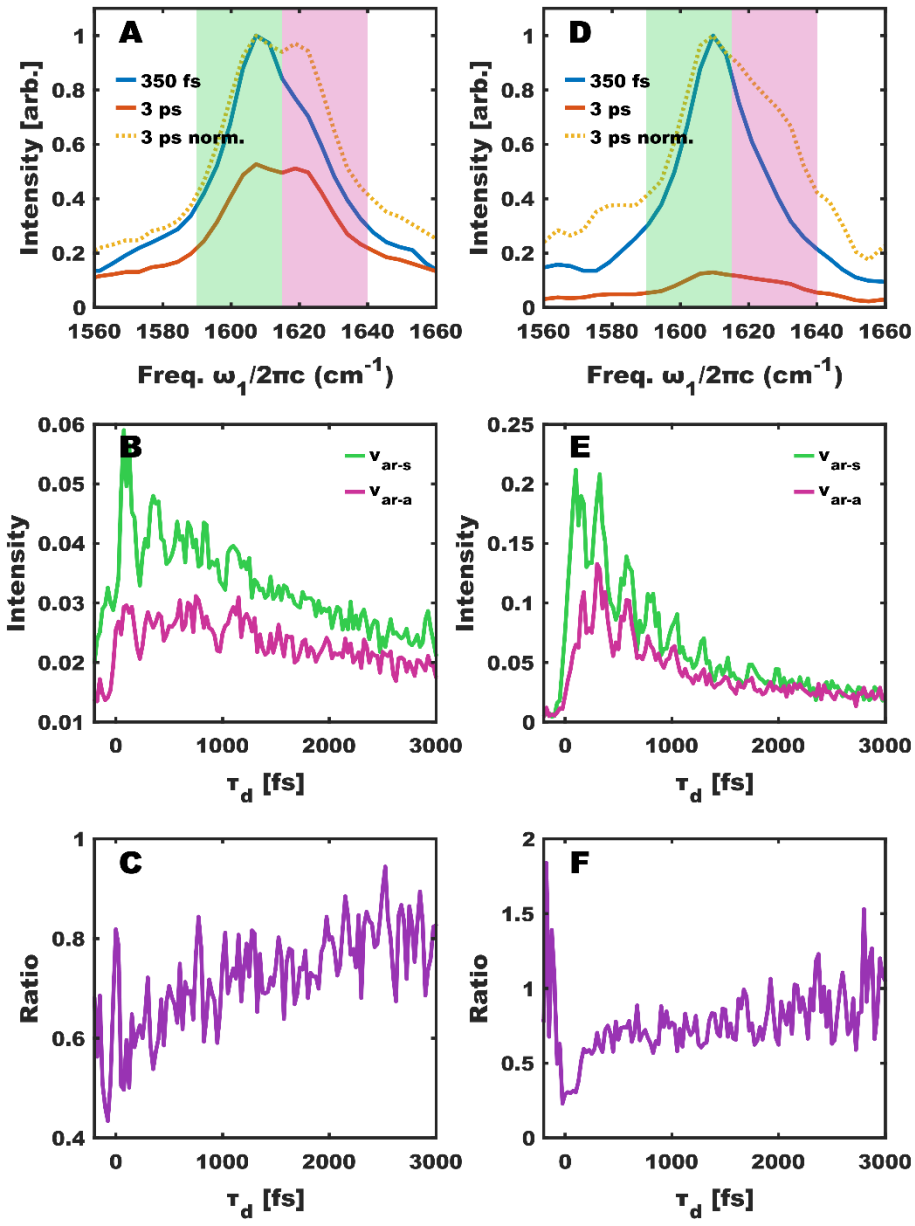

Figure 5.4) Growth in $\nu_{Ar\text{-}a}$ mode at later encoding time delays. A.) FT FEIR slices of C466 in THF show an apparent growth or equilibration of the dark or weakly FEIR active $\nu_{Ar\text{-}a}$ mode at later times. **B.)** Time traces corresponding to integration over frequency ranges indicated in **(A)** show this effect more strongly. The $\nu_{Ar\text{-}a}$ mode appears to grow in at early times followed by a slower decay. **C.)** The ratio between the modes appears to decay exponentially in encoding time delay. **D.)** The $\nu_{Ar\text{-}a}$ mode grows in more weakly in FT FEIR slices of C466 in CH. **E.)** Time traces in CH suggest the $\nu_{Ar\text{-}a}$ mode grows in for less time before decaying more quickly. **F.)** The ratio between modes in the more viscous cyclohexane decays more quickly with a nonexponential functional form.

be reduced in intensity.

5.4 Discussion

5.4.1 Hydrogen-Bonding in FT FEIR

While the n-prOH concentration affects the percentage of hydrogen bonded coumarin and tunes the average solvent polarity, the local solvent polarity appears to not be gradated. As measured by the coumarin carbonyl frequency through the vibrational Stark effect, the local solvent electric field is quantized by hydrogen bonding state and not continuous with concentration of n-prOH.

Increased hydrogen bonding to the solvent changes the character of the coumarin ring modes beside the carbonyl stretch, indicating a delocalization of vibrational excitation among coupled ring modes.[3,16] While it is relatively unsurprising that ring stretch modes $\nu_{Ar\text{-}s}$ and $\nu_{Ar\text{-}a}$ that contain significant carbonyl character are affected by the addition of a hydrogen bond, the increase in $\nu_{Ar\text{-}a}$ FEIR activity with hydrogen bonding, unaffected by solvent polarity, suggests that solvation effects on the ground vibrational state are possibly not the only contributing factor to this experiment. As the first electronic transition red shifts in hydrogen bonding solvents, the creation of a hydrogen bond to the coumarin carbonyl likely affects Franck-Condon factors between electronic excited states. This is a possible explanation for the increase in intensity in the $\nu_{ArN\text{-}s}$ mode that is predicted by DFT to be decoupled from the carbonyl displacement. It is also possible that hydrogen bonding alters the vibrational coupling, affecting which modes contribute to the delocalized vibrational excitation. However, it is difficult to determine the vibrational anharmonicities and anharmonic couplings from the 2D IR surfaces, as spectra are congested with too many overlapping GSB and ESA features. Whether through vibrational

frequency shifts or increased FEIR character, it appears that FEIR in coumarins can be used a probe of hydrogen bonding in solution, given the presence of a significant concentration of hydrogen bond donors.

The concentration of hydrogen bonded coumarin should be well-described using an equilibrium formalism. The ratio of hydrogen bonded coumarin to free coumarin, [HB]/[B] in the presence of a limited number of hydrogen bond donors [H] should be independent of the initial concentration of coumarin in a reaction rate limited regime. This ratio instead depends linearly on the concentration of the hydrogen bond donor species, and can be expressed as the product of donor concentration [H] and the equilibrium constant K. We note that diffusive terms in the forward and reverse reaction rates divide out in the limit of fast orientational diffusion. In the limit of slow orientational diffusion, the forward rate constant will contain an additional orientational diffusion term as the molecular orientation will affect association. We do not consider diffusion separately in this simple model.

$$H + B \rightleftharpoons H \cdots B$$

$$K_{hb\ form.} = \frac{[HB]}{[H][B]}$$

$$\frac{[HB]}{[B]} = [H]\, K_{hb\ form.} = [H] \frac{k_a P_{eq}(\sigma)}{k_d}$$

The relative concentrations of free and hydrogen bonded coumarin can be determined spectrally by subtracting the spectrum of a free coumarin from a ternary mixture spectrum, minimizing the free carbonyl feature at 1748 cm^{-1}, to arrive at a predicted spectrum of the fully hydrogen bonded coumarin species (Figure 5.5A). From this spectrum the relative FEIR activity of the hydrogen bonded ν_{CO} mode can be observed to be about half of the free hydrogen bonded carbonyl, and the hydrogen bonded feature is split, corresponding to singly and doubly hydrogen bonded species as predicted by DFT

calculations and observed in 2D IR measurements (Figure 5.2). In comparison, even in bulk ethanol, there appear to be coumarin molecules that are not hydrogen bonded at equilibrium. As distinct species, the cross peaks between the free and singly hydrogen bonded carbonyl and the cross peaks between the

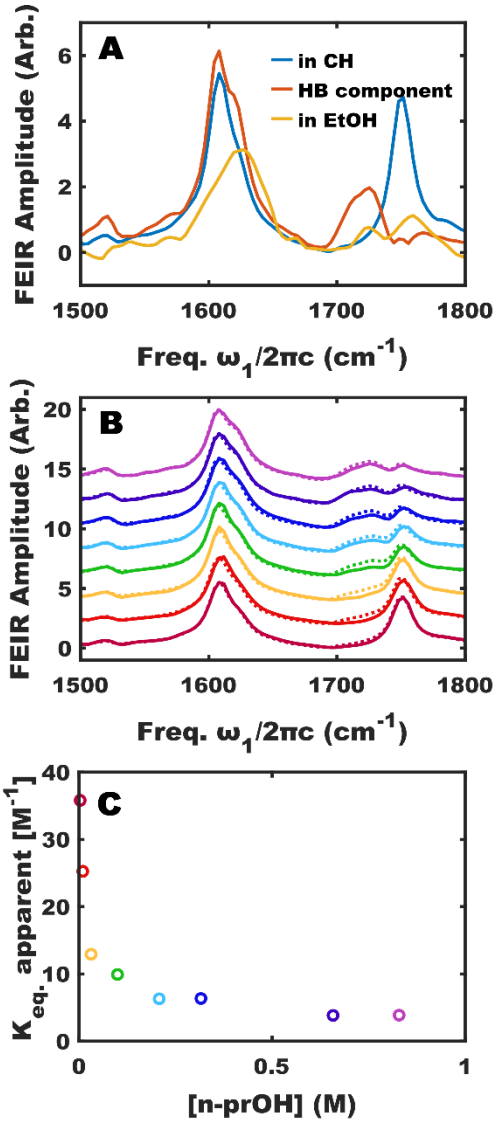

Figure 5.5) Extraction of Hydrogen Bonding percentages. A.) An absolute value hydrogen bonded coumarin spectrum can be reconstructed from an SVD analysis on the diagonal features of the 2D FEIR proticity series. The hydrogen bonded species demonstrates a red shifted and split carbonyl peak feature. A comparison to C466 in EtOH shows that even in bulk EtOH, many coumarin molecules remain unbonded. **B.)** The proticity series, solid lines, can be fit to a linear combination, dashed lines, of the hydrogen bonded and free C466 spectra to extract relative populations of each species. **C.)** The equilibrium constant calculated from the extracted relative concentrations deviates at lower concentrations.

singly and doubly hydrogen bonded carbonyl observed in 2D IR can indicate chemical exchange between these features at equilibrium under the following scheme:

$$2H + B \rightleftharpoons H + H \cdots B \rightleftharpoons H \cdots B \cdots H$$

A fit of intermediate spectra to a linear combination of the free and hydrogen bonded coumarin component spectra yields local concentrations of these species (Figure 5.5B). The calculated equilibrium constant appears to deviate at lower concentrations, more than can be accounted to fitting error (Figure 5.5C). This might indicate a co-solvation environment in the binary solvent mixture with local solvation domains[17], wherein the concentration of n-propanol local to the solvated coumarin could be higher than the average bulk concentration, causing more hydrogen bonding than expected.

The vibrational frequency shift observed in coumarins is not only useful as a probe of hydrogen bonding state but also lends utility as a probe of solvent polarity through measurement of the local electric field using the vibrational Stark effect in systems with inhomogeneity of local electric fields, such as solvents with nonpolar components and polar head groups or ternary mixtures of solvents.

5.4.2 FT FEIR in Inhomogeneous Environments

Simple spectral modeling explains the origin of the reduction in cross peak intensity and broadening in frequency in inhomogeneous environments as the result of intrinsic environmental inhomogeneity. While these features are not as direct of a reporter of environmental inhomogeneity as other methods, and provide no information on spectral diffusion, this model indicates that FT FEIR can encode more information on inhomogeneity through the effects of frequency correlations than purely linear techniques such as FTIR. Allowing for a Gaussian distribution of peak frequencies within a distribution

will cause an apparent broadening in frequency, and due to the complex Lorentzian line shape,[12] the

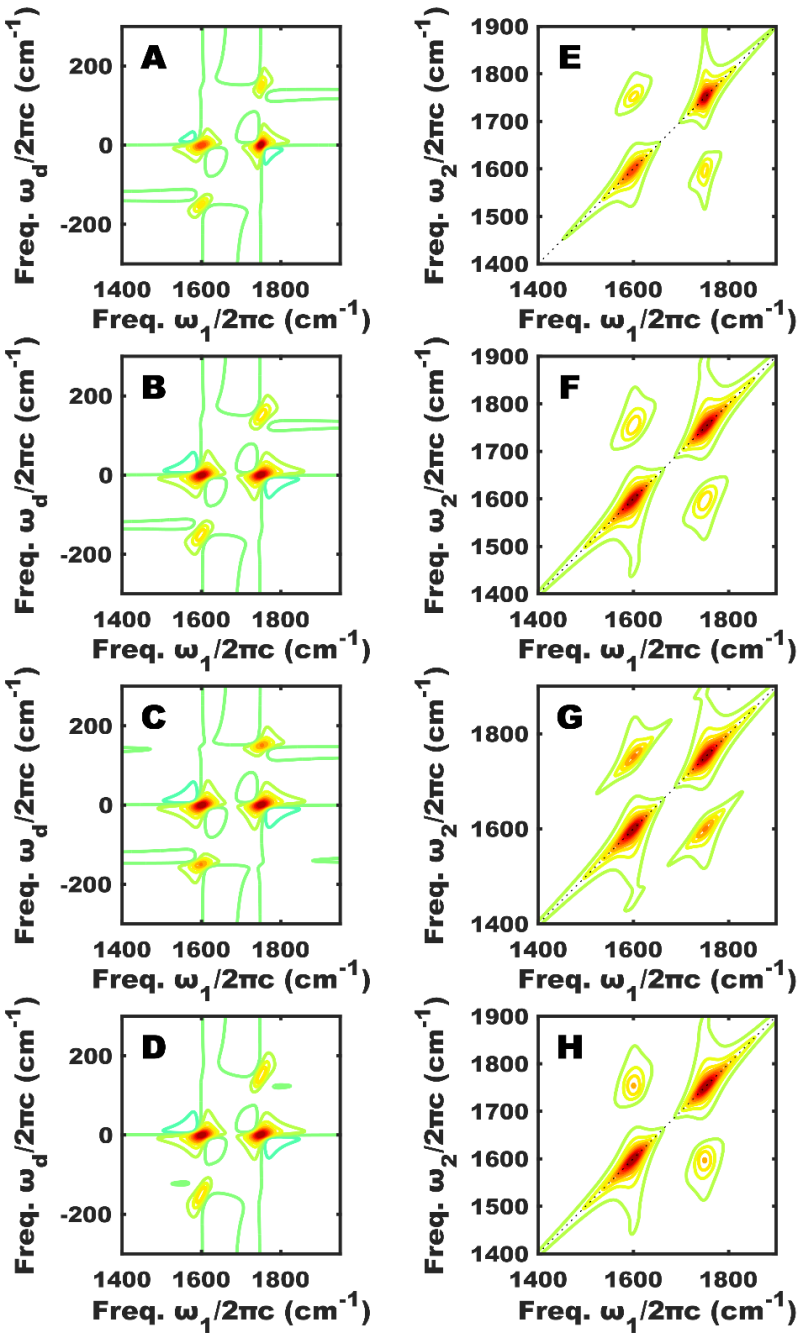

Figure 5.6) Modelling Environmental Inhomogeneity through Frequency Correlations. A.) Frequency broadening in the lower mode in ω_1 flattens the CLS of the population feature. The CLS of the upper coherence cross peak is steepened. **B.)** Uncorrelated broadening in both peaks flattens the population peaks' CLS. **C.)** Correlated broadening flattens the cross peaks' CLS. **D.)** Anticorrelated broadening steepens the cross peaks' CLS. **E-H.)** The corresponding absolute value surfaces to the left column demonstrate this behavior mapped to the ω_2 axis. A flattening of the CLS corresponds to a broadening along the diagonal in the mapped representation, while a steepening of the CLS corresponds to a broadening along ω_2.

cross peaks within a peak quartet partially cancel to a lower intensity. Further, the cross peaks within the quartet will take on a different shape and center line slope (CLS) depending on whether the vibrational modes involved are correlated, anticorrelated, or uncorrelated in their broadened frequency distribution. In the simplest case, where environmental inhomogeneity affects the frequency of a single of two modes, A, while the other is unaffected, B, the population peak at frequency A will be broadened with a shallower CLS, while the population peak at frequency B will not be affected (Figure 5.6A). The AB coherence cross peak will retain the CLS of the B peak, while the BA coherence cross peaks will have a steepened CLS relative to the A mode. In the case where the frequencies of A and B both vary within a Gaussian distribution but are uncorrelated to each other, the CLS of the coherence cross peaks are unaltered while the A and B population peaks are broadened with a shallower CLS (Figure 5.6B). If the frequencies are correlated within the distribution, with a red shift in A corresponding to a red shift in B and vice versa, the CLS of the coherence cross peaks will become shallower like the population peaks (Figure 5.6C). The opposite trend holds for anticorrelated frequencies of the two modes, which result in increased steepness in the CLS of the cross peaks (Figure 5.6D). This model allows us to interpret the FEIR spectra in terms of intrinsic environmental inhomogeneity with cross peak line shapes and slopes that are affected differently by different types of frequency correlations. The peak quartet model will be considered in more detail in Chapter 8.

5.4.3 Kinetic Model of Vibrational Equilibration in FEIR

As FT FEIR encodes vibrational information differently from 2D IR techniques, a qualitative model of time-dependent processes such as chemical exchange, energy transfer, and vibrational relaxation is necessary to interpret how these processes contribute. While a three-state kinetic model is sufficient to

describe the results in a conventional measurement of chemical equilibration, I build here a higher-state kinetic model to qualitatively describe the evolution of the FT FEIR signals in the encoding time delay. In this model, initially prepared states are distinguished from observed states to explain the spectral behavior observed in FT FEIR evolution. Two initial states correspond to a FEIR bright (S) and a FEIR dark mode (A). The initial FEIR dark mode can relax through a solvent-mediated exchange process to an intermediate FEIR bright mode (S') and the FEIR bright mode can relax similarly to an intermediate FEIR dark mode (A'). All these modes can relax to a FEIR dark ground state, and the rates of population transfer between the modes are scaled by a detailed balance of relative mode energies. This detailed balance holds as the energy difference between the equilibrating system vibrational modes is below KT, thus coupling between the vibrational system and a thermally-populated bath of solvent modes allows for exchange between the two modes. The population in state S corresponds to molecules initially excited in the FEIR bright mode and are observed, while the population in state S' corresponds to molecules initially excited in the FEIR dark mode that relax with some lifetime to the FEIR bright mode and are observed. To a simple approximation, the FEIR experimental signal corresponds to the sum of S and S'. This model predicts that a FEIR frequency component that appears to grow in at later encoding time delays corresponds to the frequency of a FEIR dark mode that relaxes to a FEIR bright mode. Thus, while vibrational energy relaxation appears as growth of the resulting vibrational feature in 2D IR measurements, e.g. the FEIR bright mode, energy transfer from a dark to bright FEIR mode appears as the growth of the initial vibrational feature, the FEIR dark mode. Thus, 2D IR resolves the destination mode that increases in population due to energy relaxation, while in this case, FEIR resolves the origin mode that decreases in population as it equilibrates.

As solvent viscosity is increased from THF to CH to mineral oil, this behavior is reduced and the ratio between modes decays more quickly in a nonexponential fashion. These ratios can potentially be fit to

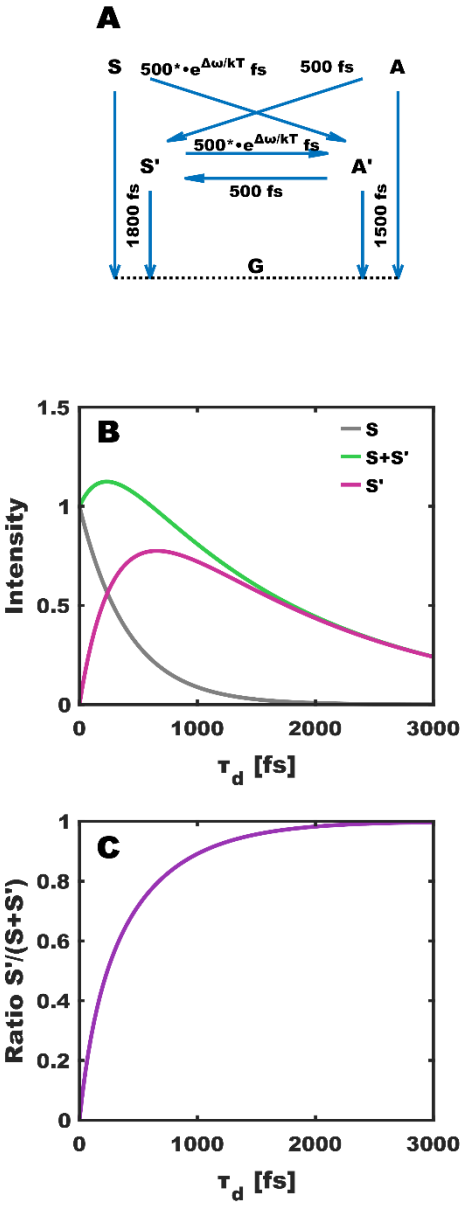

Figure 5.7) Modelling of Vibrational Energy Relaxation. A.) A modified kinetic model, illustrated in this schematic, separates initially excited states, S and A, from identical final states, S' and A'. The observed signal corresponds to the sum of the bright S and S' states. **B.)** Model time traces of the solvent bath-mediated relaxation using the parameters defined in **(A)** qualitatively match those observed in the experimental data. **C.)** The ratio of the magenta and green time traces in **(B)** also qualitatively matches the experimental data and appears as the inverse of a sum of exponentials with a constant offset. Due to the detailed balance of a solvent-bath-mediated process, this functional form is independent of the mode lifetimes, and holds even if the lifetimes are identical.

biexponential or power law functional forms, suggesting a more complicated decay kinetics than modelled here. As this effect depends on solvent viscosity, it is possible that the equilibration between vibrational modes is hindered by the viscosity of solvent bath.

5.5 Conclusions

In this chapter, I have demonstrated that FEIR is indeed applicable to a number of studies of how the local environment affects the structure of the coumarin probe. Solvent proticity, polarity, and viscosity all affect the coumarin vibrational features observed in FEIR in different ways. The hydrogen bonded coumarin spectrum can be extracted by SVD analysis on a data set tuning the hydrogen bond donor concentration, and experimental ratios between hydrogen bonded and free coumarin concentrations can be calculated. This ratio should depend linearly on the hydrogen bond donor in reaction limited kinetics. However, it is observed to depend sub-linearly on donor concentration, possibly indicating local domains in the binary solvent mixture.[17]

Several effects of solvent polarity were also observed in FEIR measurements, including the Stark shifting of the frequency of the coumarin carbonyl mode. Increased local inhomogeneity can be modeled with a simple line shape model accounting for a distribution of frequencies. Lastly, vibrational relaxation between modes can be observed as FEIR dark modes grow in at later encoding times. This effect can be described with a solvent-bath-coupled kinetic state model that qualitatively matches the experimental results. Deviations from this behavior in more viscous solvents suggest that a higher solvent viscosity that hinders the molecular rotor might interfere with vibrational equilibration if this involves a mutual coupling of vibrational modes to the molecular rotor twisting state.

These findings suggest that FEIR is applicable to similar studies at the lower concentrations that fluorescence excitation makes accessible. Particularly, the solvent proticity series provides insight into experimental parameters that will lend value to further applications of the FEIR technique to molecular binding problems at low dye concentrations. However, some information on the vibrational superpositions prepared on the dye molecules is lost as inhomogeneity washes out the coherence cross peaks. This indicates that higher order expansions of the FEIR technique, given the right experimental conditions, might provide value as an incoherently-detected analogue to full 2D IR measurements. I will discuss the challenges of, and efforts toward, such development in the following chapter.

Chapter Bibliography

(1) Mastron, J. N.; Tokmakoff, A. Fourier Transform Fluorescence-Encoded Infrared Spectroscopy *J. Phys. Chem. A* **2018**, *122* (2), 554–562.

(2) Mastron, J. N.; Tokmakoff, A. Two-Photon-Excited Fluorescence-Encoded Infrared Spectroscopy *J. Phys. Chem. A* **2016**, *120* (46), 9178–9187.

(3) Su, J.; Tian, D. Strengthening of Hydrogen Bonded Coumarin 102 in Ethanol Solvent upon Photoexcitation *New J. Chem.* **2014**, *38* (2), 568.

(4) Ramegowda, M.; Sreepad, H. R. Effect of Polar Solvents on Absorption Spectra of Coumarin 1: PCM-TDDFT Study *Acta Chim. Indica* **2013**, *3* (2), 119–126.

(5) Baiz, C. R.; Kubarych, K. J. Ultrafast Vibrational Stark-Effect Spectroscopy: Supporting Information *J. Am. Chem. Soc.* **2010**, *132* (37), 12784–12785.

(6) Chattopadhyay, A.; Boxer, S. G. Vibrational Stark Effect Spectroscopy *J. Am. Chem. Soc.* **1995**, *117* (4), 1449–1450.

(7) Bishop, D. M. The Vibrational Stark Effect *J. Chem. Phys.* **1993**, *98* (4), 3179–3184.

(8) DeFlores, L. P.; Nicodemus, R. a; Tokmakoff, A. Two-Dimensional Fourier Transform Spectroscopy in the Pump-Probe Geometry *Opt. Lett.* **2007**, *32* (20), 2966.

(9) Ding, C.; Ye, J. In *Proceedings of the 2005 SIAM International Conference on Data Mining*; 2005; pp 32–43.

(10) Frisch, M. J.; Trucks, G. W.; Schlegel, H. B.; Scuseria, G. E.; Robb, M. A.; Cheeseman, J. R.; Scalmani, G.; Barone, V.; Mennucci, B.; Petersson, G. A.; Nakatsuji, H.; Caricato, M.; Li, X.; Hratchian, H. P.; Izmaylov, A. F.; Bloino, J.; Zheng, G.; Sonnenberg, J. L.; Hada, M.; Ehara, M.; Toyota, K.; Fukuda, R.; Hasegawa, J.; Ishida, M.; Nakajima, T.; Honda, Y.; Kitao, O.; Nakai, H.; Vreven, T.; Montgomery, J. A.; Peralta, J. E.; Ogliaro, F.; Bearpark, M.; Heyd, J. J.; Brothers, E.; Kudin, K. N.; Staroverov, V. N.; Kobayashi, R.; Normand, J.; Raghavachari, K.; Rendell, A.; Burant, J. C.; Iyengar, S. S.; Tomasi, J.; Cossi, M.; Rega, N.; Millam, J. M.; Klene, M.; Knox, J. E.; Cross, J. B.; Bakken, V.; Adamo, C.; Jaramillo, J.; Gomperts, R.; Stratmann, R. E.; Yazyev, O.; Austin, A. J.; Cammi, R.; Pomelli, C.; Ochterski, J. W.; Martin, R. L.; Morokuma, K.; Zakrzewski, V. G.; Voth, G. A.; Salvador, P.; Dannenberg, J. J.; Dapprich, S.; Daniels, A. D.; Farkas; Foresman, J. B.; Ortiz, J. V; Cioslowski, J.; Fox, D. J. *Gaussian 09, Revision D.01, Gaussian, Inc., Wallingford CT*. 2009.

(11) Stephens, P. J.; Devlin, F. J.; Chabalowski, C. F.; Frisch, M. J. Ab Initio Calculation of Vibrational Absorption and Circular Dichroism Spectra Using Density Functional Force Fields *J. Phys. Chem.* **1994**, *98* (45), 11623–11627.

(12) Mukamel, S. *Principles of nonlinear optical spectroscopy*; 1995; Vol. 6.

(13) Jin, H.; Baker, G. A.; Arzhantsev, S.; Dong, J.; Maroncelli, M. Solvation and Rotational Dynamics of Coumarin 153 in Ionic Liquids: Comparisons to Conventional Solvents *J. Phys. Chem. B* **2007**, *111* (25), 7291–7302.

(14) Goh, W. L.; Lee, M. Y.; Joseph, T. L.; Quah, S. T.; Brown, C. J.; Verma, C.; Brenner, S.; Ghadessy, F. J.; Teo, Y. N. Molecular Rotors as Conditionally Fluorescent Labels for Rapid Detection of Biomolecular Interactions *J. Am. Chem. Soc.* **2014**, *136* (17), 6159–6162.

(15) Haidekker, M. a; Theodorakis, E. a. Environment-Sensitive Behavior of Fluorescent Molecular Rotors. *J. Biol. Eng.* **2010**, *4*, 11.

(16) Donovalová, J.; Cigán, M.; Stankovičová, H.; Gašpar, J.; Danko, M.; Gáplovský, A.; Hrdlovič, P. Spectral Properties of Substituted Coumarins in Solution and Polymer Matrices *Molecules* **2012**, *17* (3), 3259–3276.

(17) Dunbar, J. A.; Arthur, E. J.; White, A. M.; Kubarych, K. J. Ultrafast 2D-IR and Simulation Investigations of Preferential Solvation and Cosolvent Exchange Dynamics *J. Phys. Chem. B* **2015**, *119* (20), 6271–6279.

(18) Reichardt, C. *Solvents and Solvent Effects in Organic Chemistry*; Wiley-VCH Publishers, 2003.

Chapter 6
Signal Isolation: Strategies Toward Higher-Order Measurements

Chapter Abstract

In previous chapters, I have demonstrated the linear (in intensity) FEIR techniques and their applications. However, as of yet, an incoherently-detected FEIR analogue of higher order measurements such as 2D IR has not yet been demonstrated. I have built an experiment to measure such signal, and have developed a number of strategies to isolate this type of signal and collect data on a reasonable experimental time-frame. In this chapter, I will discuss the development of dual to quadruple chopped signal isolation strategies, stage scanning, and Inverse Radon transform data collection methods, as well as the combined integration of these methods. Although the F_2 FEIR signal as measured previously can be reproduced with this experiment, my search for a higher-order FEIR signal was not fruitful. The available IR intensity and low signal level provide an experimental limitation to this end that can be potentially overcome in future work, and I conclude with a discussion of other possible applications of these signal acquisition and separation methods.

6.1 Introduction

Although our previous developments of the FEIR technique have been successful in expanding this technique in two time delays to a frequency-resolved measurement comparable to a pump-probe spectroscopy, it remains to be demonstrated that this type of technique can resolve higher orders of vibrational excitation in a manner not unlike fluorescence-detected 2D Electronic Spectroscopy (2D FS).[1–8] To this end, I have developed an experimental design to explore these types of higher order signals, and methodology to separate different signal contributions and pathways. I will consider practical concerns of experimental geometry and motion control that will be vital to experimental expansions that utilize a greater number of pulses. I will then detail a method of signal separation for these multi-pulse measurements, and present alternative methods of data collection with consideration of signal fidelity and speed of acquisition. This work is motivated by the goal of developing an incoherently-detected analogue to full two-dimensional Infrared (2D IR) measurements. I will discuss the results of these measurements in this chapter, as well as the challenges and limitations of this experiment.

By analogue to 2D FS, a higher order FEIR signal can be described that contains similar vibrational Liouville pathway terms as 2D IR, and reports on the same physical information, e.g. anharmonicities and the degree of coupling between modes, as well as the environmental inhomogeneity and exchange between local environments through spectral diffusion. This process will be pseudo-third-order in the IR interactions, and can be described with a $S^{(3+1)}$ response function (with respect to the IR interactions) that ends in a vibrational population state.[1,5,7] Feynman diagrams for the Liouville pathway terms that

arise from the nested commutator formalism[9] are plotted in Appendix 3 at the end of this chapter (Figure 6.A3.1). As this signal will depend on four IR interactions, an appropriate experimental design and signal separation process will be discussed here.

6.2 Methods

6.2.1 Experimental Setup

In the quasi-third-order FEIR experiment, to detect a signal analogous to 2D IR one must independently resolve at least time delays τ_1 and τ_3 between IR interactions to result in frequency axes ω_1 and ω_3 at a fixed waiting time τ_2. To do so, more than two IR pulses will be needed (Figure 6.1). A three-IR-pulse experiment will result in a surface at zero waiting time in τ_2, with two interactions with the center IR pulse Y, while a four-IR-pulse experiment can be used for a non-zero waiting time series in τ_2. In this experiment, the encoding time delay τ_d will be set with a fixed delay to the last IR pulse using a separate delay stage before reflecting both on the same retroreflecting cube mirror delay arm.

To generate these pulses, a modified interferometric setup was used, which nests a pair of Mach-Zehnder interferometers inside a larger interferometer.[4] First, a vertically displaced pulse pair is generated using a 50:50 beam splitting periscope, and then these two pulses split again using another

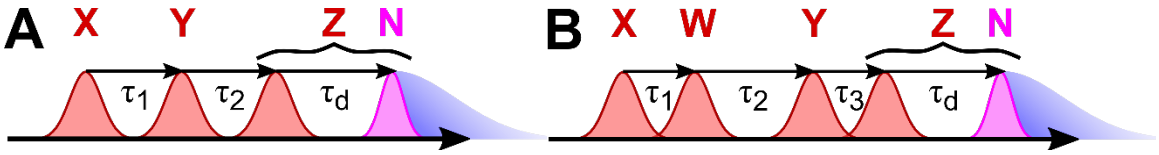

Figure 6.1) Pulse Sequence Schematic A.) For a three-pulse experiment, the second pulse is fixed with the Y delay, and the τ_d detection time relative to the third IR pulse is fixed with the N delay. The X stage can be stepped or scanned to vary the τ_1 delay and the Z stage can be stepped or scanned to vary the τ_2 delay while keeping the τ_d delay fixed. **B.)** For a four-pulse experiment, the τ_2 delay is set with the Y stage relative to the fixed stage W. The X stage can be stepped or scanned to vary the τ_1 delay and the Z stage can be moved to vary the τ_3 delay while keeping the τ_d delay fixed.

50:50 beam splitter, resulting in four pulses with independently variable time delays. Due to the vertical displacement of the pulses, each arm can be diverted into a different retroreflecting cube mirror before being recombined into pairs on two separate 50:50 beam splitters. Due to the properties of the cube mirrors, vertical displacement can be compensated for using the retroreflector, and the two collinear pairs can be recombined on a final 50:50 beam splitter, resulting in four overlapped collinear arms. Although this geometry loses ~75% of the input light to dark arms of the various interferometers, with a final IR energy of ~1 μJ per pulse, the loss is comparable to that of commercial pulse shapers[1].

Similar to the experimental setup discussed in Chapter 4, the IR is sent into the sample in a collinear geometry to avoid generating a transient grating that would potentially wash out the signal spatially (although it is possible that a non-collinear geometry could be used if the center fringe of the grating generated were imaged onto the detector).[10] In this experiment, the five beam splitters used, as well as the dispersion compensating plates, were composed of coated Zinc Selenide (ZnSe) partial reflectors with an antireflective back coating to prevent back reflections. The encoding time τ_d was fixed relative to one of the IR pulse arms Z using a variable stage and reflected off the same retroreflector, allowing coordinated motion of the last IR pulse with the NIR pulse at a fixed τ_d delay (Figure 6.2).

As before, the timing between IR pulses was found using interferometry and pulse length and compression characterized at ~100 fs using interferometric autocorrelation measurements. Second order dispersion in the IR from ZnSe transmissive optics was corrected using an appropriate thickness of

[1] While pulse-shapers have an advantage for signal separation, due to phase-cycling methods, they are often costlier than precision delay stages. Further, commercial mid-IR pulse shapers are limited to time delays of 4-6 ps (A maximum interferometric delay of 1.4-2.1 ps for a two-time-delay measurement). Further, the time resolution is determined by the memory capacity of the radio-frequency generator, and even an extension to three pulses is not always possible.

Ge, ~12 mm, as described previously. Higher orders of dispersion were not accounted for here. Timing between IR and visible or NIR pulses was found by measuring the IR transient absorption response of Silicon charge carriers upon pumping the bandgap with the NIR.[11] One arm was fixed to reduce number of delay stages needed, and the timing of every pulse was found with respect to the fixed pulse arm W.

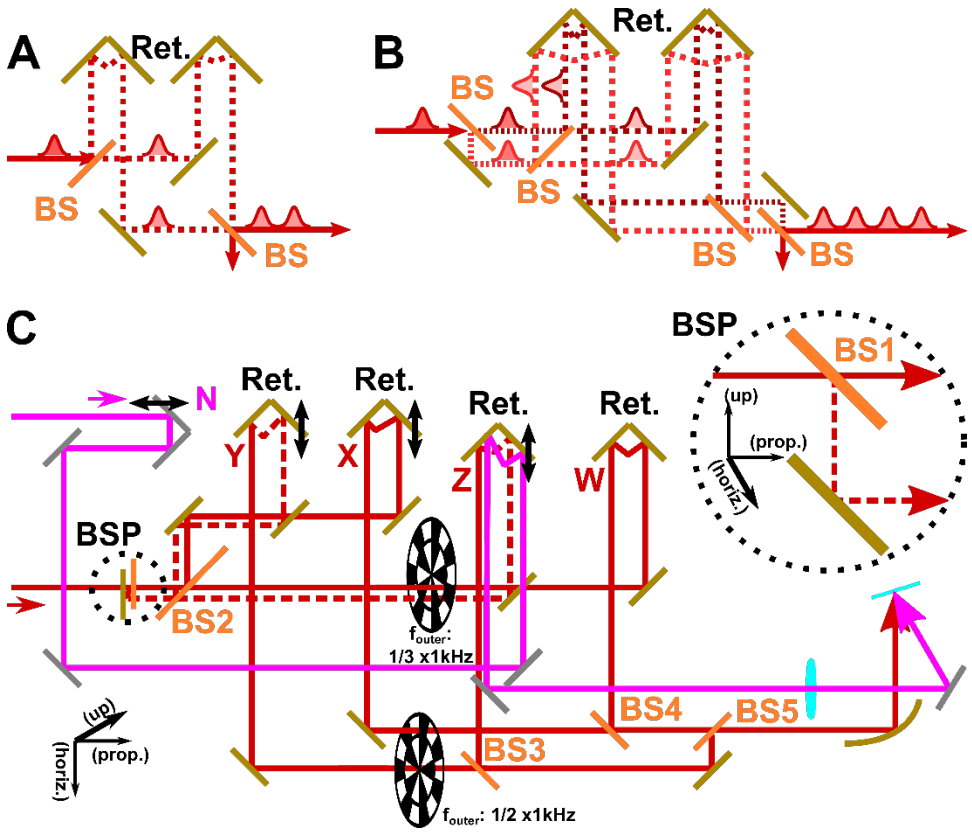

Figure 6.2) The Multi-Pulse Experimental Setup. A.) A Mach-Zehnder interferometer as presented in Chapter 4 can be used to generate a pulse pair. **B.)** A similar interferometer can nested within another interferometer to generate a pair of pulse pairs.[4] **C.)** The four-pulse experimental setup integrates independent delays for each pulse arm. Dashed lines represent vertically displaced beams. The four IR pulses are labelled **(X, Y, Z, W)**. The NIR delay **(N)** is fixed by an independent delay stage and is then reflected on the same retroreflector such that it moves in time with the last IR pulse **(Z)**. Each beam is chopped at a different frequency using a pair of 5:7 optical choppers. **Key:** BS, ZnSe Beam splitter; BSP, Beam splitting periscope; Ret., Hollow Corner Cube Retroreflector. Inset: Side-view of the beam splitting periscope that generates co-propagating pulses with a vertical displacement.

6.2.2 Chopping Methods

When measuring an interferometric signal between two pulses, or when finding a non-interferometric two-pulse pump-probe signal with a large enough signal and slowly-varying background, it is simple to separate the signal contribution that depends on both pulses using an optical chopper to periodically block and unblock (i.e. chop) one of the pulse arms at some fraction of the pulse repetition rate, typically half, so as to interleave chopped and un-chopped measurements. As described in Chapter 4 for the FEIR experiment, the signal with one pulse chopped will consist of the signal generated from the pulse that is not chopped, while the signal with both pulses un-chopped will contain this signal, a similar signal generated from the chopped pulse, and a time delay-dependent component generated from both pulses. The contribution from the chopped pulse arm can be removed by subtracting the chopped data from the un-chopped data. It is not even strictly necessary to chop the signal for some interferometric measurements, as the time-dependent signal can be identifiable when the background signal is a constant offset or slowly-varying.

Alternatively, when one desires to remove the constant offset signal contributions arising from each of the pulses and isolate only the signal that arises from both pulses, it has been well-established that this can be achieved by chopping both pulse arms using a chopper wheel with both inner and outer sets of chopping blades at different chopping frequencies. When one pulse is sent through the outer wheel f_{outer} and another is sent through the inner wheel f_{inner}, the signal contribution from each pulse will be modulated at the two respective frequencies, and the signal contribution from both pulses will be

modulated at the difference frequency of the two[II] $f_{outer} - f_{inner}$. To reduce the duty cycle, the frequencies are often set using ratios of prime numbers; most frequently, a ratio of 7:5 outer to inner frequency is set using an outer wheel with 7 openings (14 chopped and un-chopped states per full revolution) and an inner wheel with 5 openings. The chopping frequency of the pulse sent through the outer wheel will typically be set to half of the pulse repetition rate $f_{rep} = 1000hz$ as in the singly-chopped case $f_{outer} = 500hz \therefore f_{inner} = {}^{2500}\!/_{7}\, hz$; thus the signal arising from both pulses will be modulated at the difference: 2/7 of the outer frequency $f_{outer} - f_{inner} = {}^{1000}\!/_{7}\, hz$. This scheme has been used traditionally in lock-in amplification systems {references}.

However, a lock-in amplifier is not strictly necessary for this type of difference-frequency data collection, as a software-analogue to the lock-in method can be implemented using a Fourier analysis, allowing one to simultaneously isolate multiple signal components. In contrast to lock-in detection, where the product of the signal and a waveform of variable phase is integrated to produce the amplitude and phase of the signal, digital lock-in through a Fourier-transform methodology decomposes the signal into all possible sinusoidal components, and as discussed later in this chapter, is convenient to resolve multiply-chopped interferometric signals. In the Fourier analysis, the beam width relative to the chopper wheel aperture will affect the occurrence of harmonic artifacts due to the Fourier-transform of a square-wave-like signal.[12] This temporal profile can be modeled as an infinite sum of error functions:

[II] As the pulse repetition rate limits the sampling frequency; for CW light, the sum frequency can also be observed.

$f(\tau) = \sum_{n=-\infty}^{\infty} \left\{ erf\left(\frac{x - 2\pi n}{w} \right) - erf\left(\frac{x - 2\pi n + \pi}{w} \right) \right\}$, where w is proportional to the spatial beam width (Figure 6.3A,B). The limit of this temporal profile as the beam width approaches infinity will approach a constant offset in the form of a sinusoidal function with zero amplitude. Thus, there is a practical tradeoff to optimize between the reduction of harmonic artifacts and loss of amplitude (Figure 6.3C). A beam width wherein the chopper wheel aperture is between the FWHM and $1/e^2$ width will demonstrate significantly reduced square wave artifacts without much amplitude loss. The experimental beam width, $1/e^2$ ~10 mm is somewhat smaller than the chopper aperture ~15 mm, and thus the signal observed will preserve the signal amplitude but contain a small contribution from the first harmonic artifact. While these square-wave harmonic artifacts do not contribute to the outer chopper wheel frequency component when chopped at one half of the pulse repetition rate (Figure 6.3D), they will contribute to the oversampled inner wheel frequency components (Figure 6.3E). I note that this methodology will contain contributions from diffraction on the chopper edge,[13] but these components should be under-sampled temporally by the pulsed laser and thus contribute only as a low intensity periodic noise in the frequency domain.

The sign of the signal was extracted in digital Fourier-processing methods by phasing the data using a simultaneous optical measurement of the inner and outer chopper wheel phases optically, with a CW diode laser beam on a photodiode (the outer wheel phase is measured using a similar device integrated into the chopper head). Data were collected in a number of points at a multiple of full chopper revolutions i.e. a multiple of the duty cycle of 14 shots (Figure 6.A3.2) and were phased by applying the reverse of the experimentally-measured phase to the data. In these measurements, collection of between

350 and 1400 shots per data point yielded good results with a trade-off between noise reduction from increasing the number of points with slightly increased longer-term drift components. The real part of

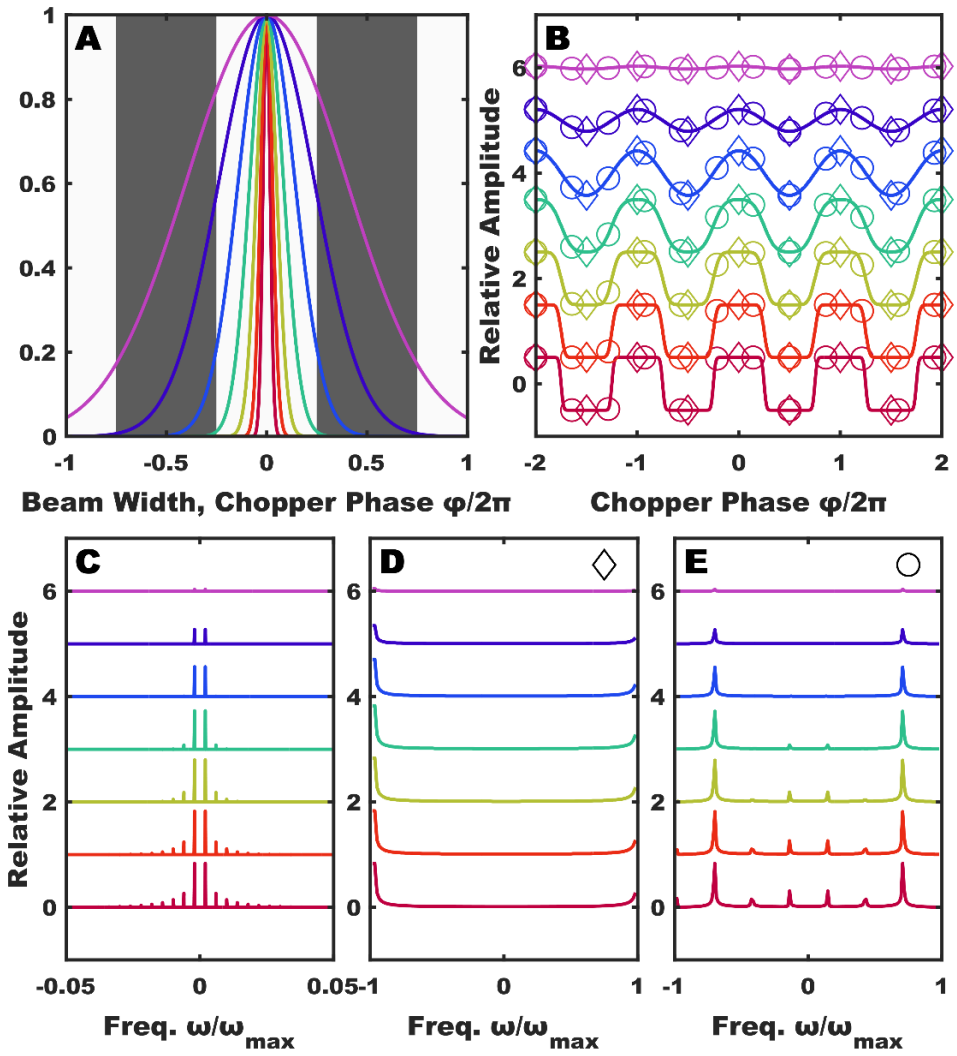

Figure 6.3) Dual-Chopping Schematic. A.) The spatial width of a gaussian beam **(Colored lines)** sent through the chopper will affect the temporal profile of the signal measured. **B.)** In the limit of a small beam width **(red)** relative to the chopper wheel aperture, the resulting temporal component of a CW laser appears as a square wave with a rise time determined by the beam width. For a large beam **(Indigo, Purple)**, the temporal profile appears sinusoidal with reduced amplitude. **C.)** In the frequency-domain representation, smaller beam widths will demonstrate increased contributions from harmonic artifacts. **D.)** For pulsed lasers, the chopper will appear to be a stationary mask. The pulse intensity transmitted through the outer chopper wheel at a frequency of twice the repetition rate will correspond to a sampling of the temporal profile in **(B)** at twice the chopper frequency **(diamonds)**. When Fourier transformed, this component will appear at the highest and lowest frequencies without artifacts. **E.)** For an inner chopper wheel of a 7:5 chopper, the intensity transmitted will appear as a sampling at more than twice the chopper frequency **(circles)**. This component will appear at ±5/7 of the highest frequency.

the Fourier-analyzed data starting at the shot of maximum transmission of both references corresponds to the cosine transform of the data, and produces the correctly-signed amplitude of each frequency component.

This dual-chopping scheme was extended to a higher order quadruple-chopping scheme by considering the signal from two pulses to be similar to a single pulse modulated at the difference frequency between the chopper wheels. The addition of another chopper at one-third of the pulse repetition rate, or similarly a second dual 7:5 inner-outer chopping scheme for a third $f_{outer2} = {}^{1000}\!/_{3}\, hz$ and fourth pulse $f_{inner2} = {}^{5000}\!/_{21}\, hz$, will result in signal components that oscillate in the collection time at further sum and differences of the various frequencies, listed in table 6.1. It should be noted that in this case, as the higher order signal will be modulated at the chopping frequency of every pulse involved, the signal contribution measured at each individual chopping frequency will depends on at least, but not generally only limited to, the pulses that are chopped at that frequency. For example, the signal originating from a pulse X that oscillates at the unique chopping frequency ω_X will contain contributions from every signal component that depends on pulse X. Signals that depend on both pulse Y, at ω_X, and pulse X, at ω_X, will be modulated at both frequencies and thus appear at the sum and difference of both frequencies, $\omega_X + \omega_Y, \omega_X - \omega_Y$. Signals that depend on three pulses will thus be modulated at three frequencies, and oscillate at all permutations of sums and differences, and similarly for four pulses. I note here the similarity between signal contributions that occur at sum and difference chopping frequencies and the analogous frequency of the emitted signal that occurs at sum and difference frequencies of the pulses

involved in a spectroscopic measurement[III]. In the case of higher-order chopping, the phase of each chopper wheel should not be applied to the entire data array as different signal components may not depend on every chopped pulse arm. To phase each difference frequency component correctly, the data array can be circularly shifted (if the length is a multiple of the duty cycle of 42 shots) or truncated such

Table 6.1: List of Difference Frequencies of Four Pulses in Quadruple chopping

f_{outer1}: 1/2 [ω_X/1kHz]	f_{inner2}: 5/21 [ω_W/1kHz] ($5/7\omega_Z$)	f_{inner1}: 5/14 [ω_Y/1kHz] ($5/7\omega_X$)	f_{outer2}: 1/3 [ω_Z/1kHz]	Relative Difference Frequency [$\omega_{\Delta f}$/1 kHz]
☑			☑	$\lvert\omega_X - \omega_Z\rvert$: 1/6
☑		☑		$\lvert\omega_X - \omega_Y\rvert$: 1/7
☑	☑			$\lvert\omega_X - \omega_W\rvert$: 11/42
		☑	☑	$\lvert\omega_Z - \omega_Y\rvert$: 1/42
	☑		☑	$\lvert\omega_Z - \omega_W\rvert$: 2/21
	☑	☑		$\lvert\omega_Y - \omega_W\rvert$: 5/42
☑		☑	☑	$\lvert\omega_Y - \omega_{XZ}\rvert$: 4/21 $\lvert\omega_X - \omega_{ZY}\rvert$: 10/21
☑	☑		☑	$\lvert\omega_W - \omega_{XZ}\rvert$: 1/14 $\lvert\omega_X - \omega_{ZW}\rvert$: 17/42
☑	☑	☑		$\lvert\omega_W - \omega_{XY}\rvert$: 2/21 $\lvert\omega_X - \omega_{YW}\rvert$: 8/21
	☑	☑	☑	$\lvert\omega_Z - \omega_{YW}\rvert$: 3/14 $\lvert\omega_Y - \omega_{ZW}\rvert$: 11/42
☑	☑	☑	☑	$\lvert\omega_Z - \omega_{XYW}\rvert$: 1/21 $\lvert\omega_Z - \omega_{WXY}\rvert$: 5/21

[III] There is a direct correspondence in the CW case between the dual-chopping signal and the terms of the second-order $S^{(2)}$ response that are absorptive pathways; likewise, the same holds for higher-order chopping schemes (Figure 6.A3.3). However, in the case of pulsed lasers, terms that oscillate at higher frequencies than the pulse repetition rate will be under-sampled.

that the first data point contains the maximum transmission of both reference beams through the chopper before Fourier analysis.

6.2.3 Data Collection on a Grid in Multiple Time Delays

After a suitable signal separation scheme is developed, practical concerns toward data collection can be considered. The standard method of data collection is the step scan method on a grid, wherein a time delay is stepped to a fixed time delay, data are averaged for a set amount of time, and the delay stage is then stepped to a new position (Figure 6.4A). This process is repeated iteratively for every combination of experimental delay times. The practical benefit of this method is that it provides a superior noise reduction in the absence of long-term drift or low frequency variations in laser intensity.

However, this method is slow for several reasons. First, there is a time delay due to the stage motion – in stepped measurements the stage must equilibrate at the appropriate delay before data collection, and this stage settling time can be on the order of tens to hundreds of milliseconds. Further, one must average longer over long-term variations in laser intensity. Additionally, there is a delay for each time point due to the time required to buffer each data point from the instrument to the lab PC. In collection of multiple time delays, this method can be prohibitively slow, and a Fourier transform measurement in two time delays that is an adequately sampled for quadruple-chopping can take multiple days to collect.

Stage scanning is a faster method of data collection at the expense of a reduced number of shots averaged per time delay.[14,15] In this method, the time delay is scanned at a precise fixed velocity while data are collected simultaneously. The stage velocity and pulse repetition rate will determine the final time resolution of the measurement, where a single pulse will correspond to a single time point. Multiple scans can be collected and averaged in the frequency domain to utilize Felgett's advantage,[16] where in

the detector-noise-limited regime, the signal to noise of Fourier-transformed time-domain data yields an additional noise reduction by $\sqrt{n_{shots}}$. This reduces the collection time in a single time delay axis from the order of an hour to the order of tens of seconds, as stage settling and data buffering occurs once per scan instead of hundreds of times. Using this method, a two-dimensional surface in two time delays can be collected on the order of a few hours; and a well-averaged pump-probe geometry 2D IR surface at a single waiting-time can be collected on the order of minutes. This method was utilized with success in Chapter 4.

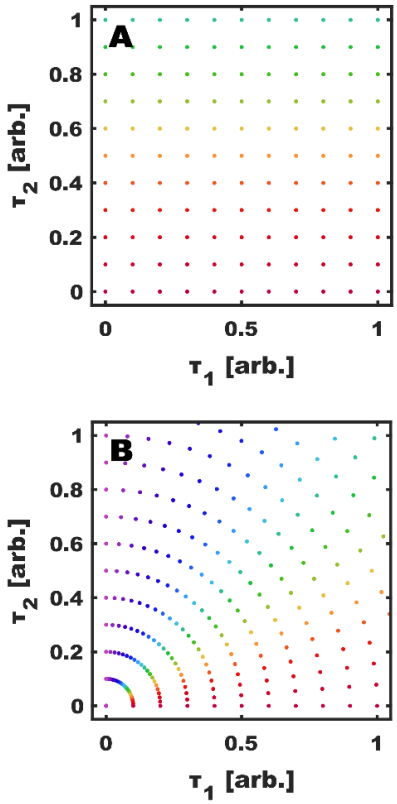

Figure 6.4) Diagram of Data Collection Schema. A.) 2D measurements are traditionally collected in a grid stepping format. This data collection methodology evenly samples the entire time-time surface. **B.)** In IRT measurements, data points are instead collected on angular slices through time zero. This method more finely samples time points near time zero. The data are then Fourier transformed along these angular slices.

6.2.4 Inverse Radon Transform Data Collection

Inverse-Radon transform (IRT) methods are growing increasingly popular in optical spectroscopies[17] as alternatives to two-dimensional data collection on a grid, having been long implemented in NMR spectroscopies.[18–21] In this type of measurement, instead of collecting a two-dimensional surface in two time delays by stepping each delay in a grid (Figure 6.4A), the data is collected on angular slices[IV] through this time-time surface (Figure 6.4B). These slices can be Fourier transformed, and through the projection-slice theorem,[22] will correspond in the frequency domain to projections of the two-dimensional frequency-domain surface (Figure 6.5A,B,C) onto lines at the same angles as the slices in the time domain (Figure 6.5D,E,F). Then, through an inverse-Radon back-projection operation as used in computer-aided tomography,[21,23,24] a two-dimensional frequency surface can be reconstructed (Figure 6.5G,H,J) from the frequency-domain projections as a function of angle[V]. One benefit of the IRT methods is that this reconstruction can simplify phasing of the signal, as the projection of a simple antisymmetric dispersive line shape in two dimensions will be zero, while the projection of an absorptive line shape will be nonzero. Thus, one can take the absolute value of the frequency domain slices (Figure 6.5D) before back projection and still reconstruct a phased 2D surface (Figure 6.5G), although I note this property does not hold for line shapes where the absorptive component is asymmetric.

[IV] Although the Radon transform has been generalized to higher-dimensional spaces; I did not attempt to implement this method in more than two time delays.

[V] The 2D Radon transform is a transformation of a 2D surface in two axes to a 2D surface in one axis and angle. The Inverse Radon transform will exactly reconstruct the original 2D surface from a continuous surface of projections as a function of angle. In the case of a discrete sampling of the angular projections, the Inverse Radon transform surface will contain noise in the form of ridges originating at signal components.

The components of the IRT surface can be predicted visually from observing the frequency-domain projections. A doubly-arced ( ) shape (Figure 6.5D) will correspond to a diagonal feature at the same

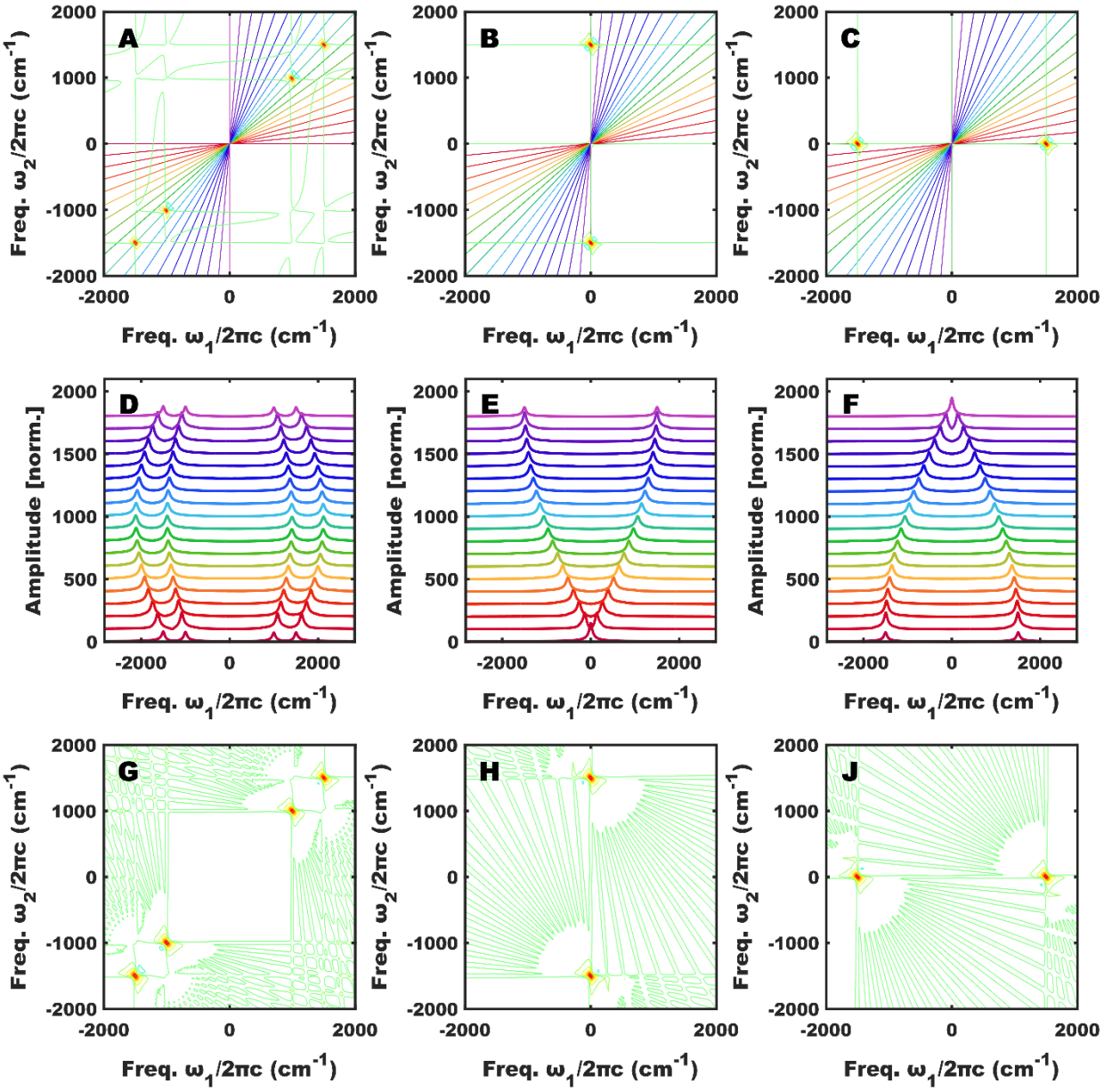

Figure 6.5) Inverse Radon Transform Model Spectra. A,B,C.) Sample 2D frequency-domain surfaces can be generated. The lower peak in **(A)** was generated with a phase error of $\pi/4$. **D,E,F.)** The absolute value of the Radon transform of these surfaces shows a characteristic behavior of each type of feature as a function of angle, and corresponds to the Fourier transform of slices through a time-domain surface. **G,H,J.)** The Inverse Radon-transform back-projection reconstructs the frequency-domain surfaces. The phase-twisted peak in **(A)** is reconstructed without a phase error in **(G)**.

value in abscissa and ordinate (Figure 6.5A), where the maximum frequency of the arc is scaled by the square root of two. A capital V shape (Figure 6.5E) will correspond to a similar feature lying on the ordinate axis (Figure 6.5B), while a capital lambda Λ shape (Figure 6.5F) will correspond to a feature lying on the abscissa axis of the two-dimensional frequency-domain surface (Figure 6.5C).

6.2.5 IRT Data Collection with Stage Scanning

Similar to the step scan method of data collection on a grid, the IRT methods can be collected by measuring each point on the time-time surface discretely. However, with coordinated precision stages, a stage scan method can be used to obtain these time-time slices by moving two coordinated stages simultaneously at fixed velocities. In this case, a waiting time surface should be obtained by fixing W and Y stages (for the four-IR-pulse experiment, Y for the three-IR-pulse experiment) and scanning the X stage forward in time and the Z stage backward in time. For this application, I used Aerotech delay stages that are engineered for precision coordinated motion on multiple axes for CNC machining. Experimental characterization of this coordinated scanning method indicates precision of slices passing through time zero with a standard deviation of less than two tenths of a femtosecond, similar precision as in a stepped measurement. It is necessary to re-home the stages in between scans to prevent stage drift over many scans. However, this adds only a trivial amount of time to the measurement and a two-dimensional frequency-frequency surface can be reconstructed on the order of an hour, in less than two percent of the time necessary for a step scan measurement to obtain similar frequency axes. The timing between the pulses is further characterized by detecting their interference on an MCT detector.

6.2.6 Differential Chopping with Stage Scanning

Differential frequency chopping can be combined with fast stage scanning to extract different signal components while retaining the speed of the latter method. This is possible when the data scans are digitally processed with a discrete Fourier transform (d-FT[VI]). The frequency of the outer chopper wheel, at half the pulse repetition rate, will appear at the highest positive (and symmetrically, the lowest negative) frequency of the d-FT data, as the highest frequency that can be resolved. An optical frequency component that is also modulated at this chopper frequency will appear to the d-FT to be shifted to a higher frequency than can be sampled, and like other under-sampled frequencies, will be aliased, i.e. mirrored across the highest frequency. Using this method, assuming the chopper frequency in lab time oscillates much faster than the interferometric oscillations in the signal data (that is, the interferogram is very over-sampled due to a slower stage scanning velocity), the signals that oscillate at lower chopper frequencies will show up with a similar frequency shift, and signals at difference frequencies will be shifted likewise. If the interferogram is sufficiently oversampled, these signal components can be resolved in the frequency domain. The degree of oversampling necessary to avoid overlapping features can be calculated for the dual chopping case. The DC signal that is not shifted in frequency will have a maximum in the IRT frequency of the square root of 2 times the regular signal maximum. This component will be resolved from the difference-frequency chopped component, which occurs at 2/7 of the maximum frequency when the following inequality is satisfied:

$$\sqrt{2}\, f_{sig} < \frac{2}{7}\, f_{max}\,,\ \therefore \frac{samp}{cycle} > nyquist\ rate \times \frac{7\sqrt{2}}{2} \approx 10\ samples\ per\ cycle$$

[VI] To distinguish DFT – the discrete Fourier-transform, from DFT – Density Functional Theory

10 samples per cycle of the interferometric component are necessary to resolve the difference frequency component from DC contributions, roughly a 1.9 fs sampling for a signal at 1750 cm^{-1}. Twice this sampling rate is necessary to resolve the higher frequency components from the inner or outer chopper wheels, roughly a 1 fs sampling for a signal at 1750 cm^{-1}.

$$\frac{5}{7} f_{max} + \sqrt{2}\, f_{sig} < f_{max} - \sqrt{2}\, f_{sig}, \therefore \frac{samp}{cycle} > nyquist\ rate \times \frac{7\sqrt{2}}{2} \approx 10\ samples\ per\ cycle$$

The square root term in the calculation originates from the radon transform, where the apparent signal frequency for a diagonal feature in a diagonal projection will appear to be scaled by the square root of two.

6.2.7 IRT with Stage Scanning and Dual-Chopping

When the signal is sufficiently oversampled, signals can be isolated in stage scanning IRT methods by Fourier transform to projection space. Several signal components will appear in the raw d-FT of the data. Any interferometric signal that is not modulated by the chopper (i.e. from scanning one of two pulses that are not chopped) will appear at the fundamental frequencies. Interferometric signal originating from the pulse chopped by the outer wheel, at half the repetition rate, will appear as the fundamental signal shifted by the outer chopper wheel frequency, i.e. the maximum and minimum frequency. This is the equivalent of an oppositely signed reflection of each half of the data (Figure 6.6A,B). Signal originating from the pulse chopped by the inner chopper wheel at 5/14 of the repetition rate, will be shifted by the inner chopper wheel frequency, 5/7 of the maximum and minimum frequency (Figure 6.6A,C). The signal that originates from both of these pulses will be shifted by the difference frequency, at 2/7 of the maximum and minimum frequency (Figure 6.6A,D). The appropriate inverse frequency shifting can be applied for each desired signal (Figure 6.6B,C,D), followed by IRT back-projection to

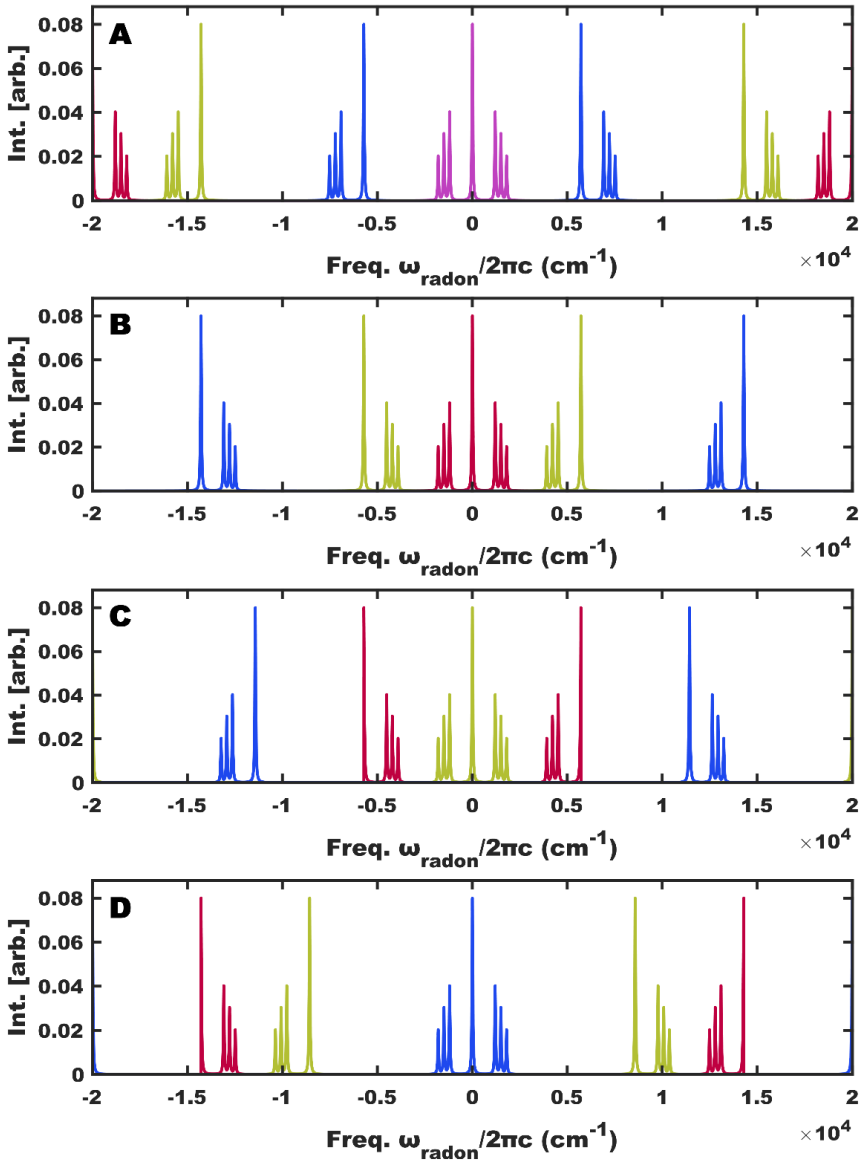

Figure 6.6) Model FT Frequency Components From two 7:5 Chopped Beams. A.) DC components that are not modulated by the chopper will appear at the fundamental frequencies (purple). Interferometric signal modulated by the outer chopper wheel will be shifted by the maximum frequency (red). Signal modulated at 5/14 of the repetition rate will be shifted by 5/7 of the maximum frequency (yellow). Signal modulated at both frequencies will be shifted by 2/7 of the maximum frequency (blue). **B.)** The signal from pulse X can be isolated by circularly shifting the data by ½ of the array length. **C.)** The signal from pulse Y can be isolated by inwardly circularly shifting each half of the data in opposite directions by 5/14 of the array length. **D.)** The signal that originates from both pulses can be isolated by inwardly circularly shifting each half of the data in opposite directions by 2/14 of the array length.

reconstruct surfaces for each signal. While I used dual-chopping for stage-scanning IRT measurements, the expansion to quadruple-chopping at a very low scanning velocity can allow the measurement of the

18 separate signals that can likewise be isolated in IRT stage-stepped measurements. With a higher repetition rate, faster chopping, and faster coordinated stage motion, this collection time could be shortened further.

6.3 Experimental Results and Discussion

6.3.2 Angular IRT Slices

The experimental apparatus was characterized and was determined to have high-enough precision coordinated stage motion for scanned IRT measurements, with a stage position error within the sampling time required, comparable to that of stage stepping methods (Figure 6.7A). A three-pulse measurement was performed on C466 at 4.8 mM in CH as prepared previously, using stage scanning and a 7:5 differential chopping scheme on two of the arms, as described in §6.2.7. Four averages per angular slice were taken to reduce the noise of the frequency-domain projections, and angular slices were collected in 2° increments between 0° (a trace in τ_1 at a fixed τ_3 of 0 fs) and 90° (a trace in τ_3 at a fixed τ_1 of 0 fs). The waiting time τ_1 was fixed at 0 fs and the encoding time delay τ_d was fixed relative to the last IR pulse Z at 100 fs. The two different chopping frequency components, as well as the difference frequency component (Figure 6.7B-D), are isolated with array shifting methods (Figure 6.6).

When angular projection data are plotted with a vertical offset in order of increasing Radon angle, signal components can be identified visually (Figure 6.5D,E,F). By eye, these signals appear to show components on each of the two-dimensional frequency axes, one that appears on the diagonal in the X-pulse-dependent signal, as well as a DC component (as a vertical line at zero frequency) at zero frequencies (Figure 6.7B-C). However, aside from the DC component, only the signal that lies on the ω_1

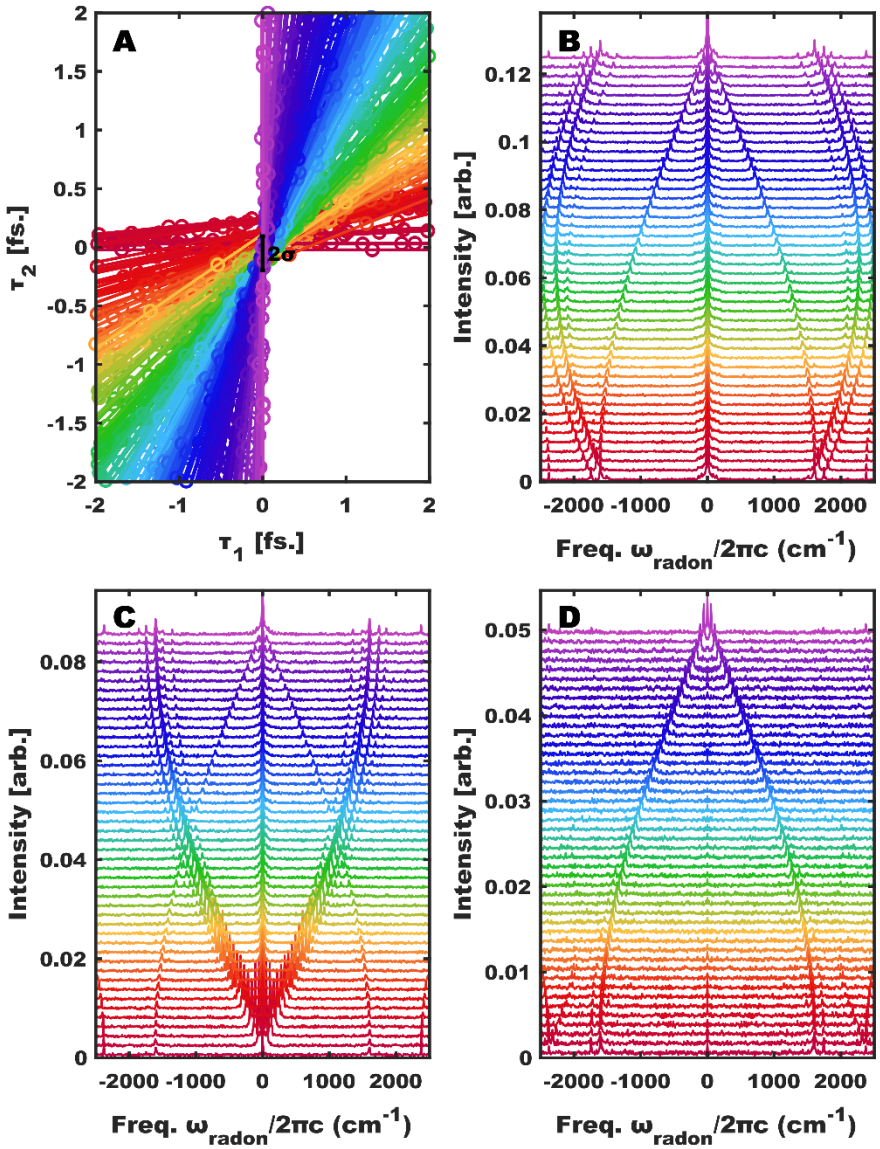

Figure 6.7) Three-Pulse Angular Data Slices. A.) The recorded τ_1 and τ_2 positions for stage-scanned IRT measurements shows a slight variability in the y-intercept. The standard deviation of this variability is reproducible on the order of 0.15 fs, and is within the error of stepped-stage measurements. **B.)** The signal that depends on at least the X pulse oscillates at the outer chopper wheel frequency, and is thus shifted as in Fig. 6.5B. When vertically offset in order of increasing Radon angle, there is a Λ shape of the peaks in the data, corresponding to a component at nonzero frequency in the ω_1 axis and at zero frequency in the ω_2 axis. Further, there is a doubly-arced ( ) shape corresponding to a component at nonzero frequencies in both ω_1 and ω_2 axes. The DC component at zero frequency in both ω_1 and ω_2 appears as a vertical line. **C.)** The signal that depends on at least the Y pulse oscillates at the inner chopper wheel frequency, and is shifted as in Fig. 6.5C. In addition to a Λ shape and vertical line DC component as described above, there is a V shape that corresponds to a component at zero frequency in the ω_1 axis and a nonzero frequency in the ω_2 axis. **D.)** The signal that depends on both pulses oscillates at the difference frequency, and is shifted as in Fig. 6.5D. There is a Λ shape and slight vertical line DC component as described above.

axis is present in the differential chopper frequency signal (Figure 6.7D). This implies that a higher-order signal dependent on all three pulses cannot be resolved.

6.3.2 Reconstructed IRT Surfaces

While the form of the two-dimensional surface can be predicted visually from the Radon-frequency projections, the two-dimensional surfaces were reconstructed to verify these results using both IRT dual-chopping stage scanning as described above (Figure 6.8A-C) and IRT quadruple-chopping stepping methods[VII] (Figure 6.8D-F). From which signal components depend on each of the pulses, and which components depend on both, every signal component can be assigned to different F_2 FEIR signals that originate from interactions with different pulses, as shown in Figures 6.8 and 6.9. The F_2 FEIR signal that originates from IR pulses X and Y occurs in all three surfaces, although the differential chopping frequency surface demonstrates significantly reduced noise on top of this signal in comparison to the others (Figure 6.9). The reconstructed surface of the signal that depends on at least the X pulse contains features centered around (ω_1, ω_2) values of (0, 0), (1608, 0), and (1608, 1608). The (0, 0) feature corresponds to the DC offset that appears as a vertical line in Figure 6.7B, and is assigned to the F_0 fluorescence background value plus an offset. The features centered around (1608, 0) are assigned to the F_2 FEIR signal that originates from pulses X and Y, while the features centered around (1608, 1608) are assigned to the F_2 FEIR signal that originates from scanning both pulses X and Z. The surface that

[VII] 2100 shots were collected per data point (although the duty cycle is reduced for low difference frequencies), and angular slices were collected in 3° increments between 0° (a trace in τ_1) and 90° (a trace in τ_3). The waiting time τ_1 was fixed at 100 fs and the encoding time delay τ_d was fixed relative to the last IR pulse Z at 100 fs. This method took roughly 18 times the stage-scanning IRT method to produce data of similar quality.

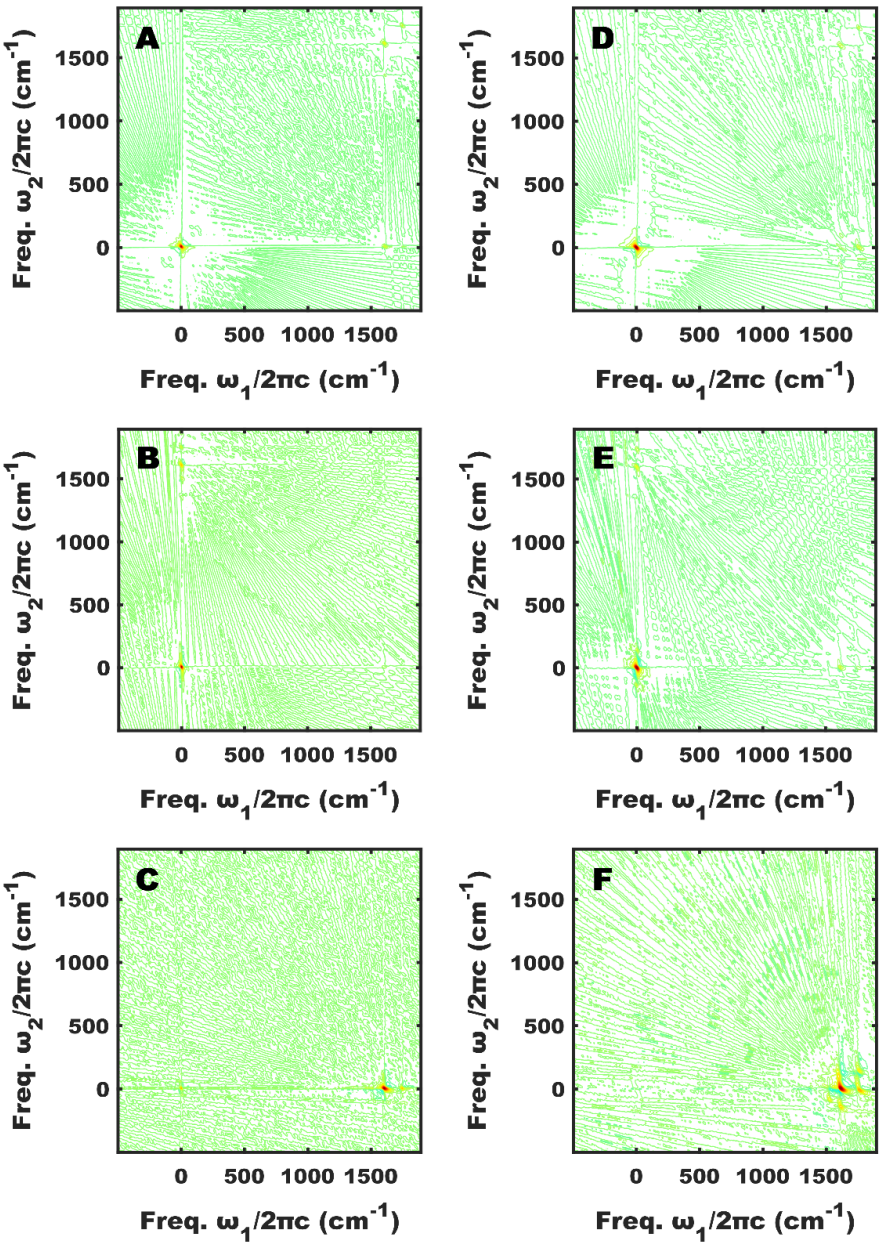

Figure 6.8) Three-Pulse Inverse Radon Transformed Data Surfaces. A,D.) The reconstructed X surface contains components at (ω_1, ω_2) values of $(0, 0)$, corresponding to the F_0 background; $(1608, 0)$, corresponding to the F_2 Signal between Pulses X and Y; and $(1608, 1608)$, corresponding to the F_2 Signal between Pulses X and Z. **B,E.)** The Y surface contains features centered around (ω_1, ω_2) values of $(0, 0)$, corresponding to the F_0 background; $(1608, 0)$, corresponding to the F_2 Signal between Pulses X and Y; and $(0, 1608)$, corresponding to the F_2 Signal between Pulses Y and Z. **C,F.)** The XY surface shows $(0, 0)$ and $(1608, 0)$ features that are assigned similarly as in **(A)** and **(B)**. No signal component was observed around $(1608, 1608)$. **(A-C)** were collected using stage scanning IRT methods over 1.5 hours. **(D-F)** were collected using stage stepping IRT methods over 27.5 hours.

depends on at least the Y pulse contains features centered around (ω_1, ω_2) values of $(0, 0)$, $(1608, 0)$, and

(0, 1608). The (0, 0) and (1608, 0) features are assigned similarly to the F_0 fluorescence background value and the F_2 FEIR signal that originates from X and Y, and the features centered around (0, 1608) are assigned to the F_2 FEIR signal that originates from pulses Y and Z. The surface that depends on at both pulses X and Y shows (0, 0) and (1608, 0) features that are assigned similarly to the F_0 fluorescence background and the F_2 FEIR signal that originates from X and Y. Notably, no significant signal component appears around (1608, 1608), indicating that either none of the observed signal depends on all of the pulses X, Y, and Z, or that any such signal is not resolved above the noise of this experiment (Figure 6.A3.4). As a result of the symmetric line shapes, the F_2 FEIR signal is properly phased without prior consideration toward phasing, as the absolute value was taken after the initial Fourier Transform to Radon-frequency space projections. I do not observe significant signal contributions occurring in any of the three surfaces in the diagonal region that cannot be assigned to F_2 FEIR signals, and thus cannot rule out the null hypothesis in this case. However, a small component that occurs at difference frequencies in both axes cannot be assigned to the F_2 FEIR signal, of the intensity expected for the higher-order signal ($\sim F_2^2$). If these features arise from the higher-order signal, they can potentially be assigned to Stimulated Emission and Excited State Absorption pathways of a higher order signal (Figure 6.A3.5), but the signal to noise ratio is too low to definitively assign these features as such.

Although I attempted to measure possible 3 and 4-pulse signals using both grid stepping and IRT methods, using both referenced stage-stepped and stage-scanned FT processing methods for each, the lack of significantly-resolved higher order signal was reproducible. It may be that such signal is not measurable in this model system, however, I note that the loss of >75% of the IR light due to the nested interferometer geometry places the IR intensity within the more linear regime of the intensity dependence of the FEIR signal observed in Chapters 3 and 4 (Figures 3.6, 4.A2.1). Further, the dual-

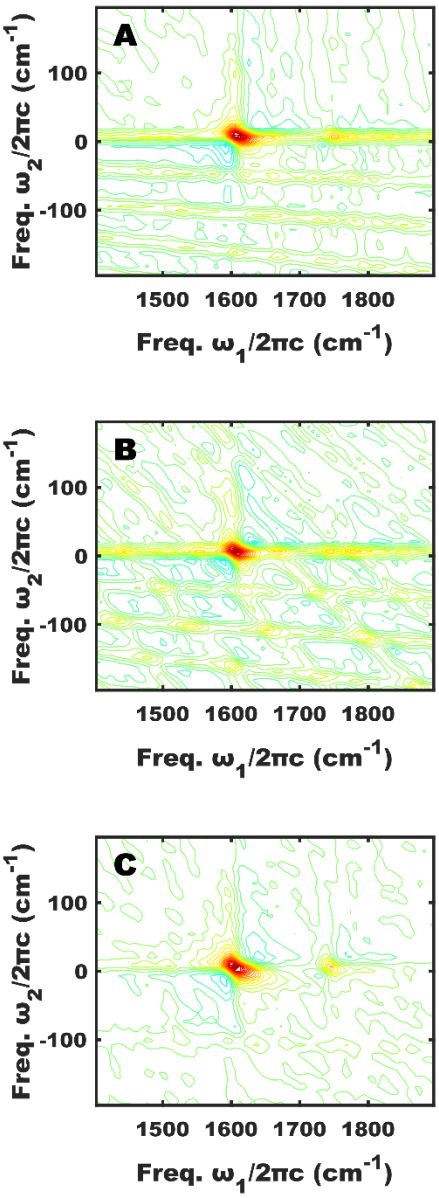

Figure 6.9) Three-Pulse Surface F2 FEIR Signal Components. A.) The reconstructed X surface contains the F_2 FEIR signal that originates from pulses X and Y. **B.)** The Y surface contains the same F_2 FEIR signal component. **C.)** The XY surface isolates this signal from the background noise. Due to the symmetry of the absorptive line shape that projects to positive values and the antisymmetry of the dispersive line shape that projects to zero value, the IRT processing produces phased line shapes with no external phasing procedure. This property holds if the dispersive line shape is antisymmetric, and will not hold for highly asymmetric peak line shapes.

chopped signal may be reduced in intensity as more of the signal is lost due to chopping at different frequencies than in the singly-chopped case. Thus, it is possible that the signal is present but not significantly resolved above the noise, as the measured noise is on the order of half of the expected signal

(Figure 6.A3.4,5). While stage scanning measurements reduce the speed needed to resolve the F_2 FEIR signal, it may be that more averaging is needed to resolve the higher-order signal from the noise. Despite this null result, it may be that with more IR power still, a less lossy geometry (such as one utilizing knife edge beam splitting), or a high numerical aperture objective, enough IR fluence could be achieved at the sample to increase the intensity of the signal above the noise– a twofold increase in total IR intensity should yield a four-fold increase of the signal, which might be enough to resolve above the noise. Otherwise, extended averaging might be necessary to resolve the signal – pulse-shaping with phase cycling could be a potential solution toward data collection in a reasonable time-frame. Independent phase cycling of each interferometer arm as in Marcus' work could be implemented with this current scheme to improve the detection.

6.3.3 Proposed IRT 2D IR methods

Naturally, one could consider extending the IRT methods demonstrated here to 2D IR spectroscopies in the pump-probe or box car geometries using the 3 and 4 pulse isolation strategies as demonstrated here to collect every waiting time in one measurement. This will necessitate that the maximum extent of the Radon time axis collected is greater than double of that necessary for the 2D signal to decay to zero (or rather, to within the experimental noise) to fully isolate the decay. In this type of experiment, one would step or scan both the interferometric delay and the waiting time delay in a coordinated fashion similar to that implemented above. This data could be used to reconstruct an IRT surface for each pixel of the array detector, and then an inverse d-FT applied to these surfaces along the waiting frequency axis to result in a set of 2D surfaces, one per detector pixel in ω_3, in the interferometric axis ω_1 and the waiting time τ_2. When causality is imposed on the data by cutting negative waiting times, one is left with a three-

dimensional data set that can be reshaped into a finely-sampled 2D IR waiting time series, where the time resolution of the waiting time matches that of the interferometric delay. Where such precision is not needed, the same procedure can be applied with a scaling factor on the waiting time axis in the IRT collection. This type of experiment would be expected to take on the order of an hour.

6.4 Conclusions

In this chapter, I have discussed the experimental setup, data collection methods, and signal separation strategies I have developed in an attempt to measure a higher-order FEIR signal. Starting with a more theoretical description of optical chopping, I have expanded the commonly-used dual-chopping scheme to higher orders, and related the observed signal modulation to terms of a response function. The resulting quadruple-chopped data can be processed by Fourier transform to separate individual "pathways" or signal contributions. A 2D frequency-domain surface can be collected by measuring angular slices in the time-domain and Fourier transforming them into frequency-domain projections that can be used with an Inverse-Radon-Transform back projection to reconstruct a 2D surface. This strategy has been implemented to collect data in both stage-stepped, quadruple-chopped and stage-scanned, dual-chopped methods. While I have been able to measure various properly-phased F_2 FEIR signal components, higher order signal remains elusive and unresolved from the noise. This can be attributed to a combination of low IR fluence and reduced averaging time. However, with further experimental developments to increase the IR intensity, more averaging, and different model systems of a stronger nonlinear response, this type of signal might be possible to measure. To that end, the methods I have developed here will be valuable to isolate it and collect it in reasonable experimental data

collection times. These methods can be conceivably be applied to 2D IR measurements as well. In the next chapter, I will discuss the mathematical modelling of FT FEIR, higher order FEIR, and other incoherently-detected measurements.

Chapter Bibliography

(1) De, A. K.; Monahan, D.; Dawlaty, J. M.; Fleming, G. R. Two-Dimensional Fluorescence-Detected Coherent Spectroscopy with Absolute Phasing by Confocal Imaging of a Dynamic Grating and 27-Step Phase-Cycling *J. Chem. Phys.* **2014**, *140* (19), 0–8.

(2) Li, C.; Wagner, W.; Ciocca, M.; Warren, W. S. Multiphoton Femtosecond Phase-Coherent Two-Dimensional Electronic Spectroscopy *J. Chem. Phys.* **2007**, *126* (16).

(3) Wagner, W.; Li, C.; Semmlow, J.; Warren, W. Rapid Phase-Cycled Two-Dimensional Optical Spectroscopy in Fluorescence and Transmission Mode. *Opt. Express* **2005**, *13* (10), 3697–3706.

(4) Tekavec, P. F.; Lott, G. A.; Marcus, A. H. Fluorescence-Detected Two-Dimensional Electronic Coherence Spectroscopy by Acousto-Optic Phase Modulation *J. Chem. Phys.* **2007**, *127* (21).

(5) Perdomo-Ortiz, A.; Widom, J. R.; Lott, G. A.; Aspuru-Guzik, A.; Marcus, A. H. Conformation and Electronic Population Transfer in Membrane-Supported Self-Assembled Porphyrin Dimers by 2D Fluorescence Spectroscopy *J. Phys. Chem. B* **2012**, *116* (35), 10757–10770.

(6) Karki, K. J.; Kringle, L.; Marcus, A. H.; Pullerits, T. Phase-Synchronous Detection of Coherent and Incoherent Nonlinear Signals *J. Opt.* **2016**, *18* (1), 15504.

(7) Grégoire, P.; Kandada, A. R. S.; Vella, E.; Leonelli, R.; Silva, C. Incoherent Population Mixing Contributions to Phase-Modulation Two-Dimensional Coherent Excitation Spectra *J. Chem. Phys.* **2017**, *147* (114201).

(8) Tiwari, V.; Matutes, Y. A.; Gardiner, A. T.; Jansen, T. L. C.; Cogdell, R. J.; Ogilvie, J. P. Spatially-Resolved Fluorescence-Detected Two-Dimensional Electronic Spectroscopy Probes Varying Excitonic Structure in Photosynthetic Bacteria *Nat Comm* **2018**, *9* (4219).

(9) Mukamel, S. *Principles of nonlinear optical spectroscopy*; 1995; Vol. 6.

(10) De, A. K.; Monahan, D.; Dawlaty, J. M.; Fleming, G. R.; De, A. K.; Monahan, D.; Dawlaty, J. M.; Fleming, G. R. Two-Dimensional Fluorescence-Detected Coherent Spectroscopy with Absolute Phasing by Confocal Imaging of a Dynamic Grating and 27-Step Phase-Cycling Two-Dimensional Fluorescence-Detected Coherent Spectroscopy with Absolute Phasing by Confocal Imaging of a *J. Chem. Phys.* **2014**, *140*.

(11) Gauster, W. B.; Bushnell, J. C. Laser-Induced Infrared Absorption in Silicon *J. Appl. Phys.* **1970**, *41* (9), 3850–3853.

(12) Benjamin, K. D.; Armitage, A. F.; South, R. B. Harmonic Errors Associated with the Use of Choppers in Optical Experiments *Meas. J. Int. Meas. Confed.* **2006**, *39* (8), 764–770.

(13) Gambhir, S.; Singh, M. Diffraction Effects in Mechanically Chopped Laser Pulses *Am. J. Phys.* **2018**, *86* (6), 406–411.

(14) Mastron, J. N.; Tokmakoff, A. Fourier Transform Fluorescence-Encoded Infrared Spectroscopy *J. Phys. Chem. A* **2018**, *122* (2), 554–562.

(15) Anna, J. M.; Nee, M. J.; Baiz, C. R.; McCanne, R.; Kubarych, K. J. Measuring Absorptive Two-Dimensional Infrared Spectra Using Chirped-Pulse Upconversion Detection *J. Opt. Soc. Am. B* **2010**, *27* (3), 382.

(16) Bates, J. B.; Kelman, R. B. Fourier Transform Spectroscopy *Comp. Maths with Appls.* **1978**, *4*, 73–84.

(17) Hutson, W. O.; Spencer, A. P.; Harel, E. Ultrafast Four-Dimensional Coherent Spectroscopy by Projection Reconstruction *J. Phys. Chem. Lett.* **2018**, *9* (5), 1034–1040.

(18) Zalevsky, Z.; Mendlovic, D. Fractional Radon Transform: Definition *Appl. Opt.* **1996**, *35* (23), 4628–4631.

(19) Press, W. H. Discrete Radon Transform Has an Exact, Fast Inverse and Generalizes to Operations Other than Sums along Lines *Proc. Natl. Acad. Sci.* **2006**, *103* (51), 19249–19254.

(20) Kupče, E.; Freeman, R. The Radon Transform: A New Scheme for Fast Multidimensional NMR *Concepts Magn. Reson. Part A Bridg. Educ. Res.* **2004**, *22* (1), 4–11.

(21) Kupče, E.; Freeman, R. Mapping Molecular Perturbations by a New Form of Two-Dimensional Spectroscopy *J. Am. Chem. Soc.* **2013**, *135* (8), 2871–2874.

(22) Bracewell, R. In *Fourier Analysis and Imaging*; 2003; pp 493–504.

(23) Zhao, S.; Yang, K.; Yang, K. Fan Beam Image Reconstruction with Generalized Fourier Slice Theorem *J. Xray. Sci. Technol.* **2014**, *22* (4), 415–436.

(24) Levoy, M. In *Proceedings of Graphics Interface*; 1992; pp 61–69.

Appendix 3
Supplementary Figures to Chapter 6

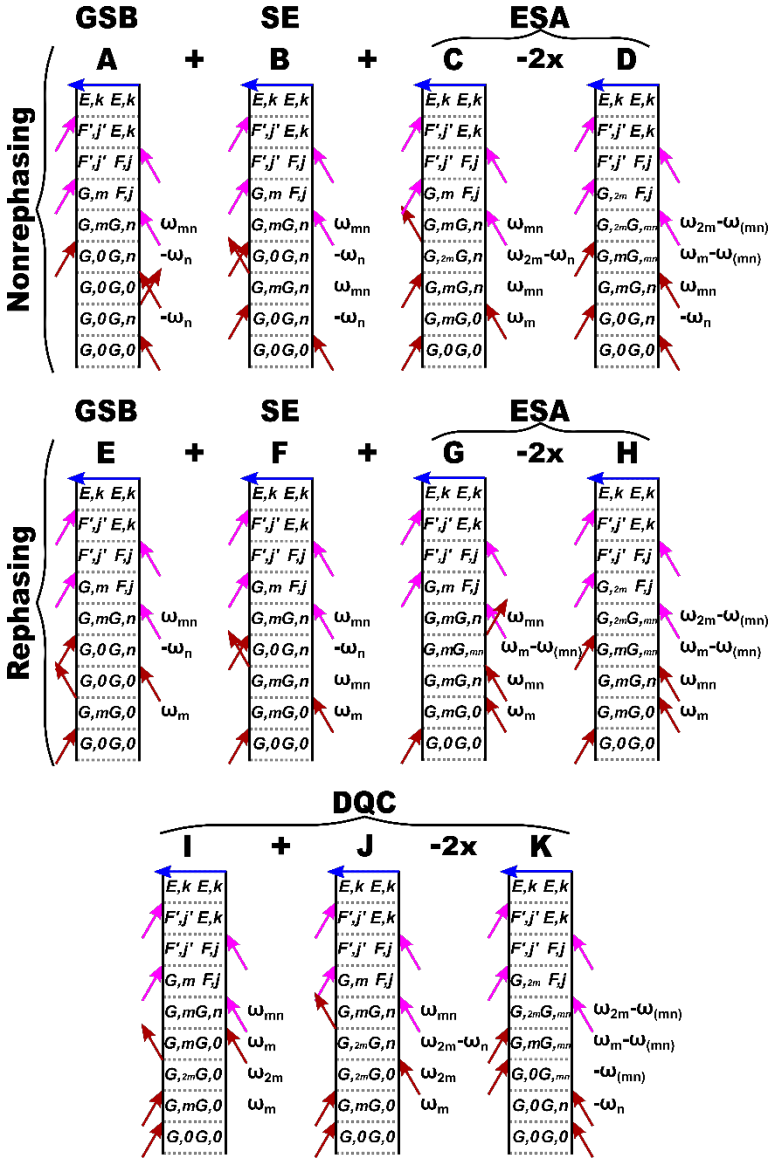

Figure 6.A3.1) Liouville Pathways for higher order FEIR of a three level system. The quasi-third-order pathways here correspond to analogue pathways of those described for 2D FS, with Ground State Bleach-Analogue terms (GSB), Stimulated Emission-Analogue terms (SE), Excited State Absorption terms (ESA), and Double Quantum Coherence terms (DQC). 14 of 16 total $S^{(3+1)}$ pathways will end in an excited vibrational population.

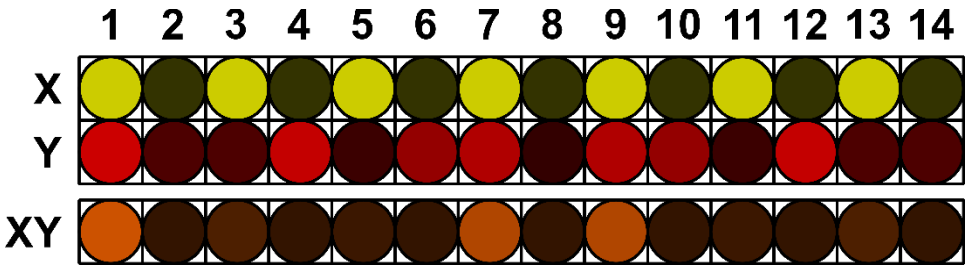

Figure 6.A3.2) Chopping Schematic. When chopped at half of the pulse repetition rate, the outer chopped arm X will be modulated as on-off-on, and appear as a sampling of a cosine waveform at twice its frequency (yellow). The inner arm Y will be modulated at 5/7 of this rate, and will appear as a sampling of a cosine waveform at greater than twice its frequency (red). The signal XY that occurs due to both pulse arms will be modulated at sum and difference frequencies of these two frequencies (orange).

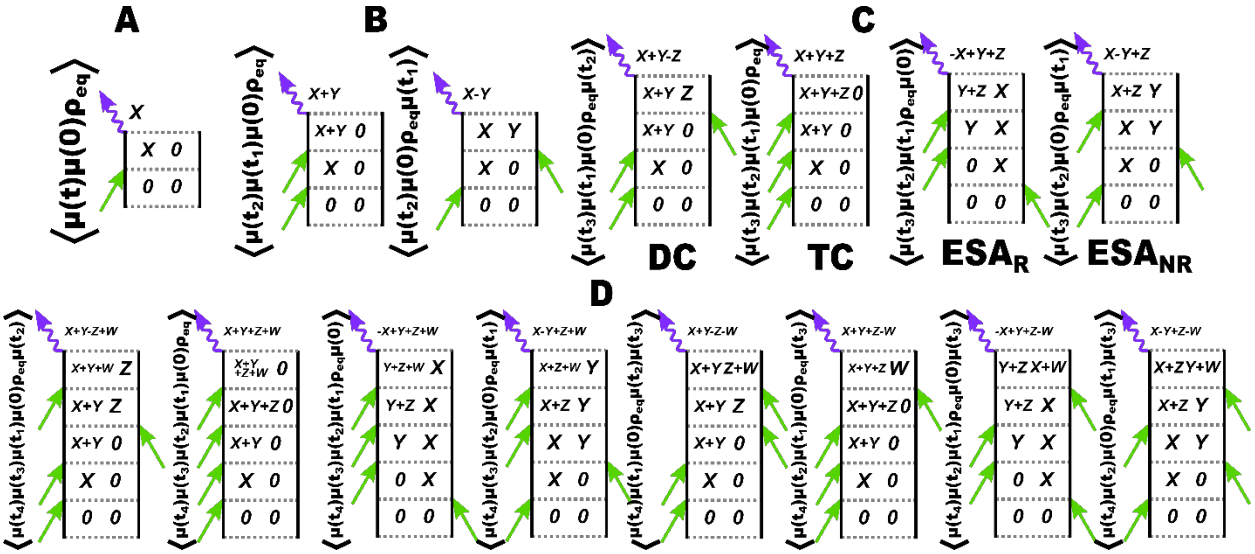

Figure 6.A3.3) Chopping Response Functions. A.) In single chopping, the signal will be modulated at the chopper frequency. **B.)** In dual-chopping, the signal will be modulated at sum and difference frequencies of the two chopper frequencies. **C.)** In triple-chopping, the signal will be modulated at further sum and difference frequencies. These correspond to third order double-coherence, triple-coherence, and rephasing and non-rephasing excited state absorption pathways. **D.)** Similar pathways can be drawn for the quadruple-chopping scheme.

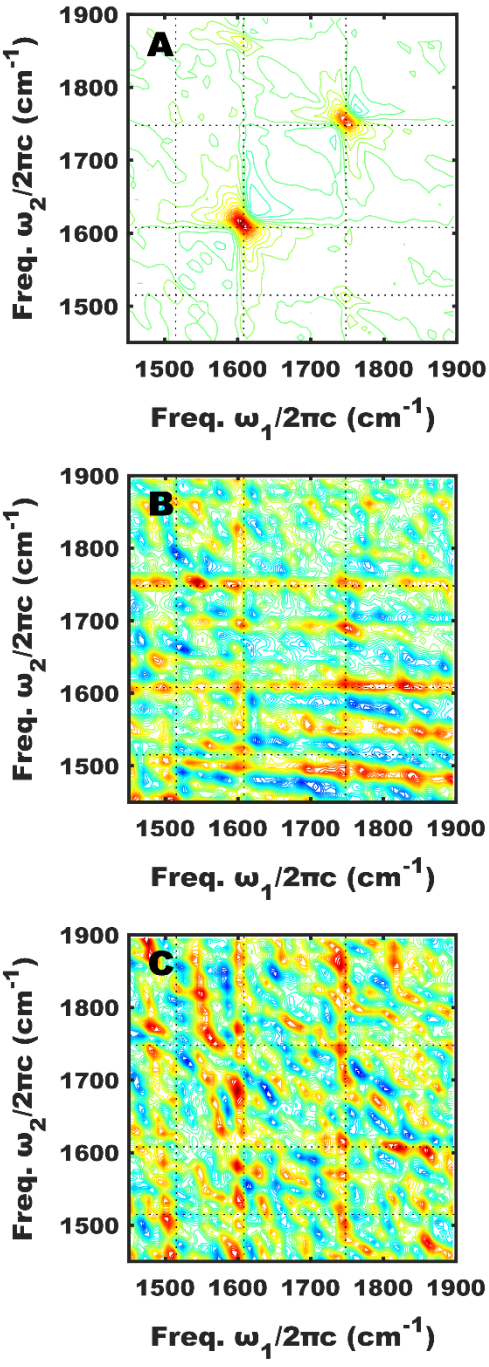

Figure 6.A3.4) Higher-Order FEIR Diagonal Region. A.) The signal that depends on pulse X shows a diagonal feature that can be assigned to the F_2 signal between X and Z. **B,C.)** The signal that depends on Y **(B)** and the signal that depends on both X and Y **(C)** might show diagonal features but the SNR is too low to be certain. The predicted line shape (Figure 8.7) is not present.

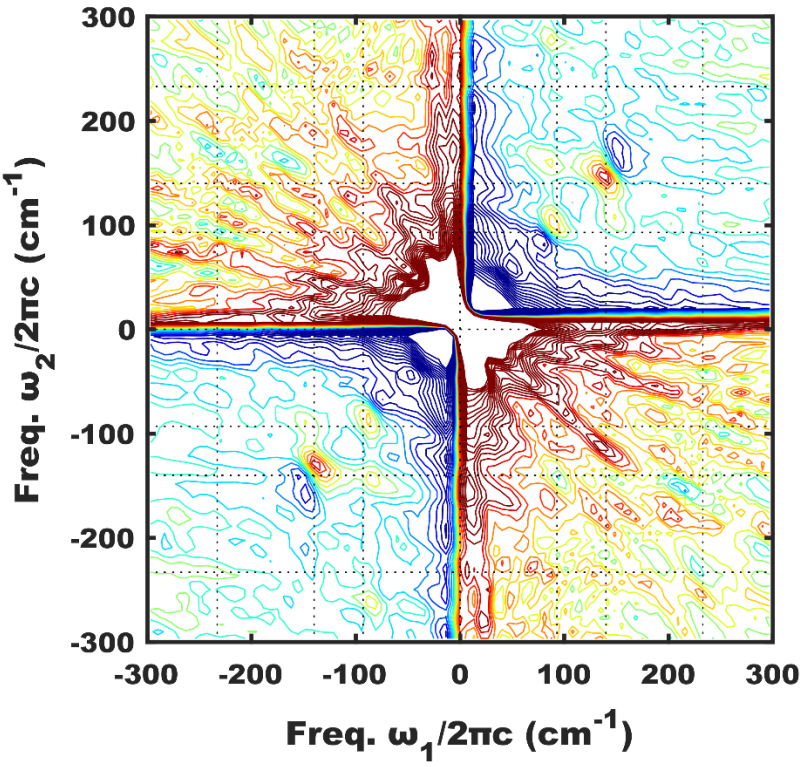

Figure 6.A3.5) Possible Difference-Frequency Features in the Higher-Order FEIR DC Region. The signal that depends on pulse X show diagonal features at difference frequencies. These cannot be assigned to the F_2 signal between X and Z, and possibly correspond to higher order SE and positive ESA pathways, with two interactions with pulse X, two interactions with pulse Y, and none with pulse Z. Dashed lines correspond to difference frequencies between FEIR-active modes. The feature near (100,100) could correspond to a pathway with a coherence between $\nu_{ArN\text{-}s}$ and $\nu_{Ar\text{-}s}$ in both τ_2 and τ_d. The feature near (140,140) could correspond to a pathway with a coherence between $\nu_{Ar\text{-}s}$ and ν_{CO} in both τ_2 and τ_d. Both of these features could correspond to SE and positive ESA features. The features at (100,140) and (140,100) could correspond to SE pathways with a coherence between $\nu_{ArN\text{-}s}$ and $\nu_{Ar\text{-}s}$ in τ_2 and a coherence between ν_{CO} and $\nu_{Ar\text{-}s}$ in τ_d, and a coherence between ν_{CO} and $\nu_{Ar\text{-}s}$ in τ_2 and a coherence between $\nu_{ArN\text{-}s}$ and $\nu_{Ar\text{-}s}$ in τ_d, respectively. The negative feature near (150,150) could correspond to a negative ESA feature. These features are around the intensity expected for the higher-order signal.

Chapter 7

Mathematical Modelling & Theory of Incoherently-Detected Spectroscopies

Chapter Abstract

The purpose of this chapter is to describe FEIR mathematically from physical, spectroscopic principles. Beginning with a response function formalism, I will discuss the population relaxation processes that result in an incoherently-emitted signal. Expanding on the simplest case of electronic fluorescence spectroscopy, linear FEIR, nonlinear FEIR, and incoherently-detected 2D Electronic Spectroscopies can be described. Once the form of the Liouville pathways is established, the corresponding line shapes can be explored in some detail. The higher-order FEIR signal can be modelled from the terms of the response function, and the effects of spectral diffusion expected in higher-order FEIR experiments can be predicted.

7.1 Introduction

Until now, I have treated the optical response functions for the FEIR process in a truncated manner, wherein the infrared interactions that prepare vibrational populations and coherences of interest are prioritized. The resonance of an optical pulse with a vibronic transition can be modulated by the excitation of a vibrational state, resulting in a change in the resulting electronic population prepared by the encoding process. In this chapter, I will use Mukamel's formalism[1] for incoherent fluorescence spectroscopy, analogous to a coherent spectroscopy, to describe the class of incoherently-detected experiments explicitly. I will begin with the excitation and fluorescence relaxation of an electronic population, and expand upon this simple case with various different methods that end in an electronic population. Although my presentation and description may at times appear to challenge literature descriptions of incoherently-detected experiments, this formalism should be consistent with the body of literature on ultrafast spectroscopies.[2–9]

As standardized by Mukamel, time domain spectroscopies with n orders of optical interactions can be described with an nth-order polarization $P^{(n)}$. The nth-order polarization can be described as the multidimensional integral of an nth-order response function $S^{(n)}$, which itself can be recast as a nth-order nested commutator of optical dipole operators $\hat{\mu}(\tau)$, enforcing causality with Heaviside step functions $\theta(\tau)$.

$$P^{(n)} = \int_0^\infty dt_n \int_0^\infty dt_{n-1} \cdots \int_0^\infty dt_1 S^{(n)}(t_n, t_{n-1}, \cdots, t_1) \prod_{\alpha=1}^{n} E\left(\vec{r}, t - \left(\sum_{\beta=1}^{n} t_\beta - \sum_{\beta=1}^{\alpha-1} t_\beta\right)\right)$$

$$S^{(n)}(t_n,t_{n-1},\cdots,t_1)\equiv\left(\frac{i}{\hbar}\right)^n\left(\prod_{\alpha=1}^{n}\theta(t_\alpha)\right)\left\langle\left[\left[\left[\cdots\left[\hat{\mu}\left(\sum_{\beta=1}^{n}t_\beta\right),\hat{\mu}\left(\sum_{\beta=1}^{n-1}t_\beta\right)\right],\cdots\right],\hat{\mu}(t_1)\right],\hat{\mu}(0)\right]\rho_0\right\rangle$$

How the response function $S^{(n)}$ and its terms relate to the macroscopic susceptibility $\chi^{(n)}$ is complicated and relates to the spatial distribution of the number of point particles p in the system. In the dilute, isotropic (on average) limit, $\chi^{(n)}$ will simply be proportional to $S^{(n)}$ and even-order terms vanish. However, at higher concentrations, interactions between the radiative point particles cast the system as a multi-body problem, and $\chi^{(n)}$ will be a more complex function of $S^{(n)}$. For the FEIR experiment, as the dilute limit is the regime of interest, the latter case can be neglected in favor of the former. In this dilute limit, the macroscopic susceptibility for the FEIR experiment can be represented as $\chi^{(n)}=\left(\frac{(-1)^n}{n!}\right)p\sum_{\beta}S^{(n)}$ where the sum over β corresponds to a sum over the $n!$ permutations of time delays (or frequencies in the frequency-domain representation). I will describe incoherently-detected experiments in terms of response functions and not macroscopic susceptibilities, as the following formalism can be generalized to calculate susceptibilities for other cases beyond dilute, isotropic systems.

The nested commutator for the response function will result in a sum of terms. These terms will correspond to individual Liouville pathways that describe the evolution of a system's density matrix under various permutations of the optical interactions, retaining cyclic invariance within individual traces. This is demonstrated for the first and second order response functions using a diagrammatic representation (Figure 7.1).

$$S^{(1)} \propto \left\langle \left[\mu(t), \mu(0) \right] \rho_{eq.} \right\rangle = \left\langle \left(\mu(t)\mu(0) - \mu(0)\mu(t) \right) \rho_{eq.} \right\rangle = \left\langle \mu(t)\mu(0)\rho_{eq.} \right\rangle - \left\langle \mu(t)\rho_{eq.}\mu(0) \right\rangle$$

$$S^{(2)} \propto \left\langle \left[\left[\mu(t_2), \mu(t_1) \right], \mu(0) \right] \rho_{eq.} \right\rangle = \left\langle \left(\mu(t_2)\mu(t_1) - \mu(t_1)\mu(t_2) \right) \mu(0)\rho_{eq.} \right\rangle + c.c.$$
$$= \left\langle \mu(t_2)\mu(t_1)\mu(0)\rho_{eq.} \right\rangle - \left\langle \mu(t_2)\mu(0)\rho_{eq.}\mu(t_1) \right\rangle + c.c.$$

Due to inversion symmetry, the polarization vanishes for even-order pathways in isotropic media. Spontaneous signal emission from a prepared polarization occurs from pathways that end in an off-diagonal coherence element of the density matrix, i.e. with ket and bra sides of the wavefunction in different states, that oscillates at the emission frequency – the difference between the ket and bra states' energies.

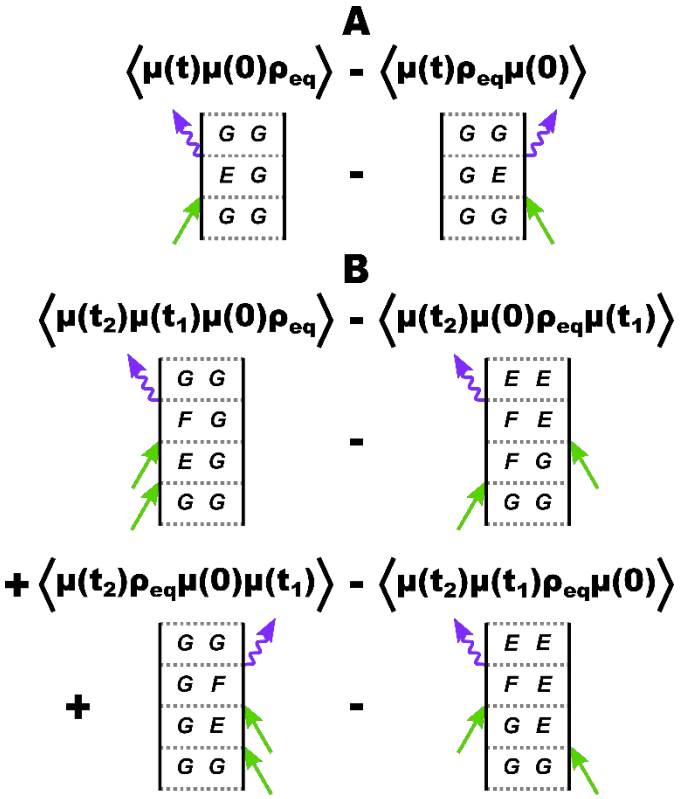

Figure 7.1) Diagrammatic Representation of the First and Second-Order Response Functions. A.) The two trace terms that emerge from the first-order response function correspond to two Liouville pathways of the density matrix. The vertical axis indicates time, the central column represents density matrix elements, and the arrows represent interactions resulting in the absorption and emission of light. The final coherence state results in an emitted signal, represented as a wavy arrow. **B.)** Four terms arise from the second-order response function in a three-level system with a higher-lying excited state F.

7.2 Coherence and Population Lifetimes

Experimentally it can be observed that the lifetime of excited state populations, on the order of nanoseconds for an electronic excitation and multiple picoseconds for a vibrational excitation, is longer than the lifetime and dephasing of coherence matrix elements, on the order of tens of femtoseconds for electronic coherences and hundreds of femtoseconds to picoseconds for vibrational coherences. This can be explained in a reductive manner with the Mandlestam-Tamm inequality,

$\tau_E \Delta E \geq \frac{\hbar}{2}; \tau_E = \frac{\Delta E}{\left| d/dt \langle E \rangle \right|}$, which recasts the Heisenberg uncertainty principle in terms of an inverse rate and uncertainty in energy.[10,11] As a consequence of this relationship[1], greater uncertainty in the energy of a quantum state will lead to a shorter lifetime of that state, leading to

the difference between the lifetimes of the highly uncertain coherence states and the more certain population states.

However, the discrepancy between electronic and vibrational lifetimes in the solution phase cannot be attributed to this inequality – and appears to deviate from that predicted by Fermi's Golden Rule, which results in a relaxation rate that will increases with increasing energy of transition $\frac{1}{\tau} \propto \upsilon^3$, or under the Förster rate for electronic relaxation, $\frac{1}{\tau} \propto -\frac{\upsilon^3}{3} + 3\upsilon^2\upsilon_{0-0} - 12\upsilon\upsilon_{0-0}{}^2 + 8\upsilon_{0-0}{}^3 \ln(\upsilon)$.[12] To resolve this apparent discrepancy, one must recall that the Feynman diagrams that are often used in nonlinear

[1] A similar uncertainty relationship can be derived for non-commuting operators. Similarly, there is a relationship between the behavior in the Fourier conjugates time and frequency.

spectroscopies to describe the propagation of density matrix elements with a series of interactions are incomplete. Under the semiclassical approximation, the diagrams are drawn as a light-matter interaction between the quantum system and a classical electric field. However, a full description would require the electric field to be quantized, with photons as the bosonic mediators of an electromagnetic force. Although a full Quantum Electrodynamical description is beyond the scope of this work, the interaction of two dipoles (one of which is the polarization of a molecule) can be thought of as nonlocally mediated by transfer of a photon. Under the semiclassical approximation, this can be reframed as the generation from a source polarization of an electric field that then interacts with a sink polarization (Figure 7.2B).

This approximation, complemented by the fluctuation-dissipation theorem, can be used to explain the shorter vibrational population lifetimes in the condensed phase compared to electronic population lifetimes under similar conditions. The lower-energy vibrational states are more likely than the higher-energy electronic states to encounter and couple to bath modes of a similar energy. Assuming that the system and the solvent bath are coupled through a dipole interaction (Figure 7.2A), and thus the

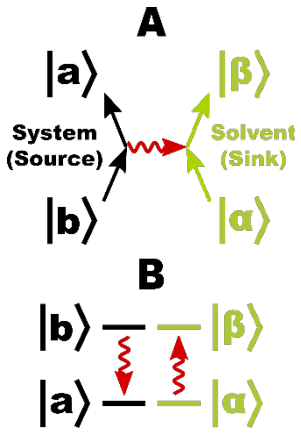

Figure 7.2) Feynman diagrams including other interacting species. A.) The relaxation of a system mode coupled to fluctuating solvent bath modes in Hilbert space can be represented as a dipole-operator-mediated energy transfer event. **B.)** Local to system and solvent wavefunctions, this process appears as two light-matter interactions: one emission from the system and one absorption to the bath.

coupling operator is the dipole operator $\hat{\mu}(\tau)$, the system-to-bath population relaxation can be described using a third order response, treating the wavefunction of the coupled system and bath as a product wavefunction of the system and bath wavefunctions. I first consider the case with no time delay between interactions, modelling the emission and absorption events to be simultaneous without propagation. The energy of the coupled bath mode must be identical to the system mode in this zero-time model (although it need not be if quantum fluctuations are considered in the time domain). Similarly to the rate derived from Fermi's Golden Rule, the relaxation rate can be described in terms of a correlation function between system modes when nonzero time delays are included, which will be explored further below.

A trace over the state or states where the system population energy has dissipated to the bath will yield the desired response of this relaxation process. While the four time-ordered terms R_1 through R_4 and their complex conjugates emerge as in an emissive spectroscopy, not every pathway will contribute.

$$S_{SB}^{(3)}(0)=\left(\frac{i}{2\hbar}\right)^3\begin{pmatrix}\left\langle\hat{\mu}_s\hat{\mu}_0\rho_{b\alpha b\alpha}\hat{\mu}_1\hat{\mu}_2\right\rangle_{a\beta a\beta}+\left\langle\hat{\mu}_s\hat{\mu}_1\rho_{b\alpha b\alpha}\hat{\mu}_0\hat{\mu}_2\right\rangle_{a\beta a\beta}+\left\langle\hat{\mu}_s\hat{\mu}_2\rho_{b\alpha b\alpha}\hat{\mu}_0\hat{\mu}_1\right\rangle_{a\beta a\beta}\cdots\\+\left\langle\hat{\mu}_s\hat{\mu}_2\hat{\mu}_1\hat{\mu}_0\rho_{b\alpha b\alpha}\right\rangle_{a\beta a\beta}-\left\langle\hat{\mu}_s\hat{\mu}_2\hat{\mu}_1\rho_{b\alpha b\alpha}\hat{\mu}_0\right\rangle_{a\beta a\beta}-\left\langle\hat{\mu}_s\hat{\mu}_2\hat{\mu}_0\rho_{b\alpha b\alpha}\hat{\mu}_1\right\rangle_{a\beta a\beta}\cdots\\-\left\langle\hat{\mu}_s\hat{\mu}_1\hat{\mu}_0\rho_{b\alpha b\alpha}\hat{\mu}_2\right\rangle_{a\beta a\beta}-\left\langle\hat{\mu}_s\rho_{b\alpha b\alpha}\hat{\mu}_0\hat{\mu}_1\hat{\mu}_2\right\rangle_{a\beta a\beta}\end{pmatrix}$$

As it does not contain all of the terms of a third-order process, this response is properly described as quasi-third-order. All terms that cannot be represented with an equal number of interactions on each side of the density matrix were eliminated to enforce the condition that each side of the density matrix must emit from the system part of the wavefunction and absorb into the bath part of the wavefunction,

i.e. that the process results in an excited bath population. Three terms (and complex conjugates) satisfy this condition (Figure 7.3).

$$S_{SB}^{(3)} = \left(\frac{i}{2\hbar}\right)^3 \begin{pmatrix} \langle a\beta | \hat{\mu}_s \hat{\mu}_0 \rho_{b\alpha b\alpha} \hat{\mu}_1 \hat{\mu}_2 P_{a\beta} | a\beta \rangle + \langle a\beta | \hat{\mu}_s \hat{\mu}_1 \rho_{b\alpha b\alpha} \hat{\mu}_0 \hat{\mu}_2 P_{a\beta} | a\beta \rangle \cdots \\ + \langle a\beta | \hat{\mu}_s \hat{\mu}_2 \rho_{b\alpha b\alpha} \hat{\mu}_0 \hat{\mu}_1 P_{a\beta} | a\beta \rangle + c.c. \end{pmatrix}$$

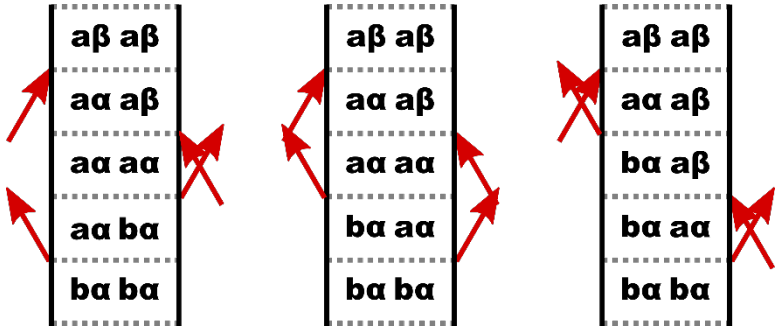

Figure 7.3) Feynman diagrams for quasi third-order relaxation of system modes to coupled bath modes. While these diagrams indicate a total of four interactions, due to the product wavefunctions of system and bath modes, these pathways can occur with the exchange of, at minimum, two photons due to interactions between the system and the bath modes. The quasi third-order diagrams end in population states. Other terms that do not end in population transfer to bath modes were not diagrammed or included in the full calculation.

When the trace over the desired bath population state is expanded, the probability of coupling to the final bath state $P_{a\beta}$ is included, which contributes to the discrepancy between electronic and vibrational lifetimes in the condensed phase. The probability of coupling to a high-energy bath state is much lower than that of for a low-energy bath state in the thermal regime, as described with the Boltzmann distribution.

$$S_{SB}^{(3)} = \left(\frac{i}{2\hbar}\right)^3 \left(6P_{a\beta}\left(\left|\mu_{ab}\mu_{\beta\alpha}\right|\right)^2\right) \propto \left(e^{-\varepsilon_{\beta\alpha}/kT}\left(\left|\mu_{ab}\mu_{\beta\alpha}\right|\right)^2\right)$$

When time evolution is allowed using the auxiliary Green's function $I_{mn} = e^{-i(\omega_m - \omega_n)t}$ (in absence of a decay parameter), the terms can be expressed in terms of correlation functions, as can be done in a

similar manner in the linear case of Fermi's Golden Rule.[13] These correlation functions differ, however, in that they include fluctuations of the bath modes, and describe the time-dependent correlations of both the system and bath modes. Further, even when every time delay is set to zero, the same Boltzmann probability term contributes as above.

$$S^{(3)}{}_{SB}(t_3,t_2,t_1)=\left(\frac{i}{2\hbar}\right)^3 P_{a\beta}\begin{pmatrix}\langle a\beta|\hat{\mu}_{ab}\hat{\mu}_{\beta\alpha}I_{\alpha\beta}(t_3)I_{ab}(t_1)|b\alpha\rangle\langle b\alpha|\hat{\mu}_{\alpha\beta}\hat{\mu}_{ba}|a\beta\rangle+\cdots\\ \langle a\beta|\hat{\mu}_{ab}\hat{\mu}_{\beta\alpha}I_{\alpha\beta}(t_3)|b\alpha\rangle\langle b\alpha|\hat{\mu}_{\alpha\beta}\hat{\mu}_{ba}I_{ba}(t_1)|a\beta\rangle+\cdots\\ \langle a\beta|\hat{\mu}_{ab}\hat{\mu}_{\beta\alpha}I_{\alpha\beta}(t_2+t_3)|b\alpha\rangle\langle b\alpha|\hat{\mu}_{\alpha\beta}\hat{\mu}_{ba}I_{ba}(t_1+t_2)|a\beta\rangle+c.c.\end{pmatrix}$$

$$S^{(3)}{}_{SB}(t_3,t_2,t_1)=\left(\frac{i}{2\hbar}\right)^3 P_{a\beta}\begin{pmatrix}\langle\mu_{ab}(t_1)\mu_{\beta\alpha}(t_3),\mu_{ba}(0)\mu_{\alpha\beta}(0)\rangle_\beta+\cdots\\ \langle\mu_{ab}(0)\mu_{\beta\alpha}(t_3),\mu_{ba}(t_1)\mu_{\alpha\beta}(0)\rangle_\beta+\cdots\\ \langle\mu_{ab}(0)\mu_{\beta\alpha}(t_2+t_3),\mu_{ba}(t_1+t_2)\mu_{\alpha\beta}(0)\rangle_\beta+c.c.\end{pmatrix}$$

Here I note the similarity between this formalism and that used for FEIR previously – a nonradiative process where the final spontaneous interaction ends in an excited state population can be described using a subset of the terms arising from an odd-order response function.[4–6] Beyond this simple example, how such populations evolve and emit will be of importance when describing the experimental observable of incoherently-detected techniques.

7.3 Third-Order Formalism of Electronic Fluorescence

While fluorescence-detected techniques have been applied successfully to 2D ES, and with my research, to IR spectroscopies, the formalism presented within literature often considers the response ending with an electronic excited state population.[4–6,8] While this is a general case for actinic spectroscopies where an observable is proportional to an excited state population, I will here describe the incoherent detection

process in more detail using Mukamel's formalism to arrive at a description of incoherently-detected spectroscopies that is applicable to purely isotropic media as well as anisotropic media. This formalism begins with a simple electronic fluorescence measurement and then can be expanded to higher orders of technique that use fluorescence as an observable.

Incoherently-detected spectroscopies are commonly described as even-order $\chi^{(n+1)}$ analogues to odd-order $\chi^{(n)}$ experiments, for the same reasoning as presented above: the same order of response function formalism results in terms that can be used to describe an odd-order spectroscopy, or a subset of which to describe a process that ends in an excited state population. For an experiment where the observable depends on the electronic excited state population, e.g. photocurrent-detected techniques, this description is adequate. However, it is incomplete for techniques where the observable is the electric field emitted by a macroscopic polarization. While the population state is prepared with an even order of interactions, in an isotropic distribution, inversion symmetry of the polarization necessitates that even-order signals emitted from a macroscopic polarization cancel. Thus, an alternative description is necessary. The literature for incoherently-detected technique simplifies the fluorescence relaxation process from an electronic excited state using a trace over electronic excited states, projecting the final electronic state onto an electronic population.[5,8] To present a formalism for incoherently-detected techniques such as FEIR, I will begin from the simplest possible case of population excitation and relaxation, electronic fluorescence spectroscopy, to explicitly describe the nature of this projection-trace operator.

Electronic fluorescence spectroscopy is a quasi-third-order process, albeit one wherein only two of the interactions are controlled in the lab frame (Figure 7.4A), and is nearly identical to conventional Raman

spectroscopy, differing only in the ordering of interactions. In electronic fluorescence spectroscopy, the two lab frame interactions prepare a long-lived electronic population that then emits in absence of a third controlled interaction. As the lifetime of an electronic population, on the order of nanoseconds, is usually much longer than the reorientation time of a molecule, on the order of hundreds of femtoseconds to tens of picoseconds depending on the size and shape of the molecule as well as the solvent viscosity, in solution phase this emission will occur from an isotropic ensemble of independent emitters and not from a macroscopic polarization. For this reason, it is often referred to as a spontaneous emission process, and is often confused with a first or second-order process. However, emission from an independent emitter prepared in an electronic population state is not a spontaneous process in the sense that it strictly and stochastically arises from the system alone[II].

In spontaneous emission, the system can be stimulated to emit by interaction with the electric field generated by a spontaneous dipole interaction with a coupled bath mode[III]. The physical nature of this bath widely varies with the environmental conditions. In the condensed phase, this interaction can arise from either resonant or off-resonance interactions with a fluctuating coupled solvent bath of modes (or phonon modes in the case of solids), blackbody absorbers, and other sinks of scattered light. However, in the absence of any other environmental interactions, i.e. in the gas phase or in a vacuum, spontaneous emission is disallowed in the semiclassical approximation, and a quantum electromagnetic field must be

[II] Even in odd-order spectroscopies, spontaneous signal emission cannot arise from an isolated system in the semiclassical approximation, and requires an interaction with a coupled bath mode.
[III] In odd-order spectroscopies the final signal emission can be stimulated by one such system-bath interaction; in an ensemble such as that which composes a macroscopic polarization, the spontaneous emission of one radiator in this way can stimulate other radiators to emit. In incoherently-detected spectroscopies the final signal emission is stimulated by two interactions.

invoked to describe this occurrence. In this case, the preparation of a system in an exited state population can be described in the semiclassical approximation, but its relaxation must be described as an interaction between the system and the coupled zero-point quantum state of the electromagnetic field in the Quantum Electrodynamic Vacuum, which can act as an energy sink.[14]

The difference between population and coherence lifetimes can be related to the rate of spontaneous interaction of a quantum state with a coupled bath mode. The coherence state is uncertain in energy, and oscillates in time between the energies of the modes involved; thus, it will have a relatively broader energy range of bath modes it can interact with to emit. A population state however has a relatively narrow energy range of modes it can interact with, and a limited quantum probability of sink modes with which to interact. Thus, when the system is prepared in an electronic population state in the lab frame (Figure 7.4A) in the absence of a bath abundant in sink modes, a long-lived electronic population lifetime is observed due to the dearth of high energy bath transitions. In the condensed phase, the abundance of solvent sink modes close in energy to system vibrational modes allows for much faster relaxation.

I adopt the graphical shorthand established by Marcus of representing an emission from a prepared population as a leftward facing arrow.[5] Although it is better described as a number of further interactions with a coupled bath rather than a trace over population states, it is a good shorthand for the population relaxation process when it is more complex as in the case of structural relaxation in the electronic excited state, i.e. Stokes shifting. For actinic spectroscopies wherein the prepared electronic population is detected through another observable, the trace notation remains more convenient.

7.4 Electronic Fluorescence in a Vibronic Regime

Due to the differing Franck-Condon overlap between ground-electronic vibrational levels and excited-electronic vibrational levels, a vibronic transition can occur to a higher vibrational level of the excited electronic state $|E,k\rangle$, which then can equilibrate to the ground vibrational level[IV] of the excited electronic state (Figure 7.4B). Restated, upon electronic excitation under the Born-Oppenheimer approximation[V], upon electronic excitation, the nuclei will relax from the most stable structural configuration for the electronic ground state to the most stable configuration for the electronic excited state. As is the case of other vibrational excitations in the condensed phase, this relaxation is mediated by interactions with coupled bath modes that act as an energy sink. If these modes are coupled through a dipole interaction in the semiclassical approximation, the relaxation can occur as the stimulated emission of an electric field from the system that interacts with the bath, as previously described.

The electronic excited state population can then relax in another vibronic transition through fluorescence as described above, resulting in a population in a higher vibrational level[VI] of the ground electronic state, which then thermally equilibrates with the bath. Thus, the fluorescence occurs at a lower energy than is used to pump the initial electronic transition, i.e. a Stokes shifting[VII] occurs due to

[IV] A state of the nuclear wavefunction; while a coherence between nuclear wavefunctions can indeed lead to a "vibration" or structural oscillation in time, a population should appear as a change in the probability of observing nuclei at a certain position.
[V] The nuclear wavefunction can be projected onto the basis set of the electronic excited state nuclear wavefunctions, with Franck-Condon factors as the coefficients of this projection. Unless the nuclear potentials are identical, generally a vibronic transition will result in a superposition of nuclear configurations in the electronic excited state.
[VI] Rather, a superposition of vibrational levels due to the back projection.
[VII] The system consists of the molecule of interest as well as the surrounding solvent molecules and the structural relaxation of the system includes local solvent reorganization.

the vibronic nature of the states involved. The initial excitation of an electronic excited state population does not need to occur directly, and pathways with higher order electronic interactions can be invoked. In an example most relevant to this work, the electronic excited state population can be prepared by a process similar to a "two-photon absorption" (Figure 7.4D), wherein 4 off-resonance interactions occur with light at half of the transition frequency to result in an electronic population excited through an

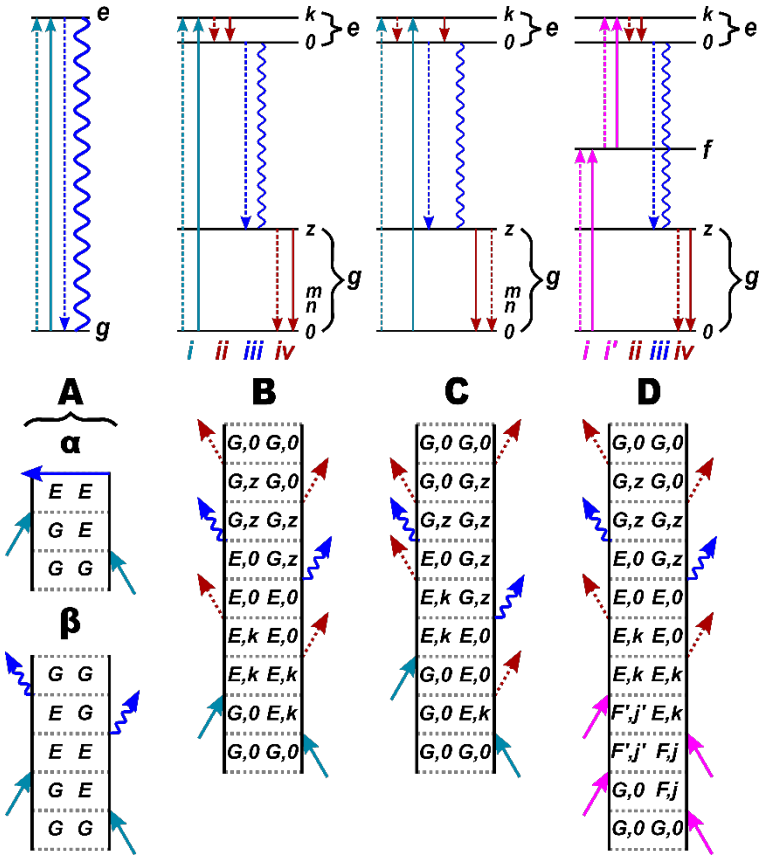

Figure 7.4) Diagrams of Liouville Pathways for Electronic Population Excitation and Relaxation Processes. The top row consists of Lee-Albrecht Ladder Diagrams, while the bottom row presents the corresponding Feynman diagrams. **A.)** Electronic fluorescence spectroscopy can be represented under Marcus' formalism **(α)**, with a full expansion of the diagram **(β)**. **B.)** When vibronic states are considered, the electronic population will structurally relax by interacting with bath modes **(ii)** before fluorescence emission to a vibrationally excited ground electronic state **(iii)** that then thermally equilibrates by through further bath interactions **(iv)**. **C.)** Different permutations of these interactions can be considered so long as the time ordering on each individual side of the density matrix is preserved. **D.)** A similar formalism can be applied when the excited electronic population is prepared by a "two-photon" absorption process with off-resonance light in a two-photon-excited fluorescence measurement. In this case, the transition occurs through an intermediate state (or superposition of intermediate states).

intermediate state.[15–17] An off-resonance higher-lying electronic state or a highly-vibrationally-excited ground vibronic state can act as this intermediate state; the overall "two-photon absorption" process sums over pathways through all intermediate states.

In these diagrams, I have adopted the convention that the final interaction that prepares an electronic population occurs on the left-hand side of the density matrix. For linear measurements, while the diagrams for complex conjugate terms can be drawn, both result in an excited state population, and thus both will contribute to an increase in observed fluorescence. Without referencing, all such pathways will yield positive signals as a result of the quasi-third-order response function[VIII]. However, this does not hold for higher orders, where the sign of the terms in the response function will differ.[5] This formalism for the excitation and incoherent relaxation of an electronic excited state can then be extended to explain both FEIR techniques and incoherently-detected 2D ES techniques.

7.5 Extending Vibronic Fluorescence Formalism to FEIR

The "single-photon" vibronic excitation pathway (Figure 7.4B) can be expanded with an initial vibrational excitation to result in the simplest possible case of FEIR (Figure 7.5A). This vibrational excitation alters the resonance between the electronic state and the encoding light pulse(s). When the resulting fluorescence signal is referenced against the signal in absence of vibrational excitation, this type of pathway will result in a positive signal for increased resonance or negative signal for decreased

[VIII] As previously, by definition the quasi-odd-order response function ends in an excited population and does not necessarily contain all terms of the odd-order response function. For orders higher than linear, nearly every term can result in a population with the exception of only terms where every interaction occurs on one side of the density matrix.

resonance. Likewise, in TPE FEIR, the resonance of a "two-photon absorption" process (Figure 7.4D) can be altered by a vibrational excitation (Figure 7.5B).[16] It is possible to extend this formalism to higher orders, wherein a doubly-excited vibrational state (or combination band) alters an electronic resonance (Figure 7.5C). Ignoring the thermal equilibration steps, the "single-photon-encoded" FEIR experiment

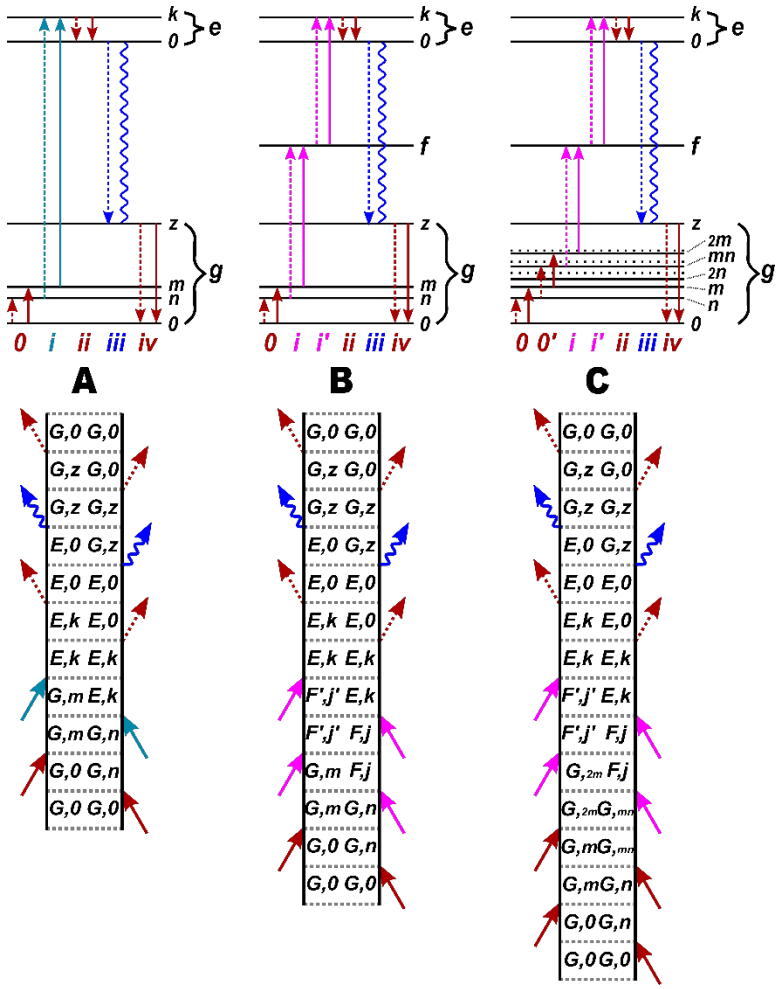

Figure 7.5) Diagrams of Liouville Pathways for FEIR Processes. The top row consists of Lee-Albrecht Ladder Diagrams, while the bottom row presents the corresponding Feynman diagrams. **A.)** An example pathway of FEIR in the "one-photon" encoding case. A vibrational transition **(0)** alters the resonance of a vibronic transition **(i)** with the encoding pulse. The resulting electronic population relaxes structurally **(ii)** before relaxing by fluorescence **(iii)**, which is the experimental observable. The molecule then thermally equilibrates **(iv)**. **B.)** In TPE-FEIR, the electronic transition occurs through an intermediate state **(i,i')** in a TPA process. **C.)** Higher orders of FEIR measurements analogous to 2D IR can be predicted, in which a doubly-excited vibrational level is excited **(0')** preceding the encoding process.

can be described as a quasi-third-order process that is fourth-order with respect to lab-frame interactions, and likewise the TPE FEIR experiment can be described as a quasi-fifth-order process, sixth-order in the lab frame, for the linear process and quasi-seventh-order, eighth-order in the lab frame, for the nonlinear FEIR analogue to 2D IR. A full expansion of the terms in the linear response function (with respect to the infrared excitations) that will contribute to linear FEIR measurements for a 3-level system can be found in Appendix 4 (Figure 7.A4.1), while a similar expansion for the higher-order FEIR technique can be found in Appendix 3 (Figure 6.A3.1).

7.6 Extending the Fluorescence Formalism to 2D ES[5]

For linear techniques such as FT FEIR, negatively-signed terms will not contribute as they will not prepare a population in the quasi-third-order response function; however, for higher-order techniques such as nonlinear FEIR or incoherently-detected 2D ES (or 2D FS), both positively and negatively-signed terms can contribute to the final signal.[5] How these terms contribute differs from coherently-detected 2D ES. In 2D FS, pathways analogous to the Ground State Bleach (GSB) in 2D ES will be positively instead of negatively-signed (Fig 7.6A), at the same position in the frequency-domain as the GSB in 2D ES. A positive Stimulated Emission (SE) pathway will also occur in the same location. Two oppositely-signed ESA pathways will occur – one positively signed that ends in a population in the first excited state and one negatively signed that ends in a population in a higher-lying excited state. Both of these signal contributions will appear at the same position in the frequency-domain as the coherently-detected ESA. In the negative ESA pathway, the higher-lying excited state population must relax to the first excited state before fluorescing (Kasha's rule) through internal conversion. As some population can be lost through internal conversion to the ground state, the contribution from such negative pathways is

often of much lower amplitude than that of the positive ESA pathway, and thus the ESA will not cancel completely but remain the same sign as the GSB. This contrasts with coherent 2D ES, where the ESA is the opposite sign of the GSB.

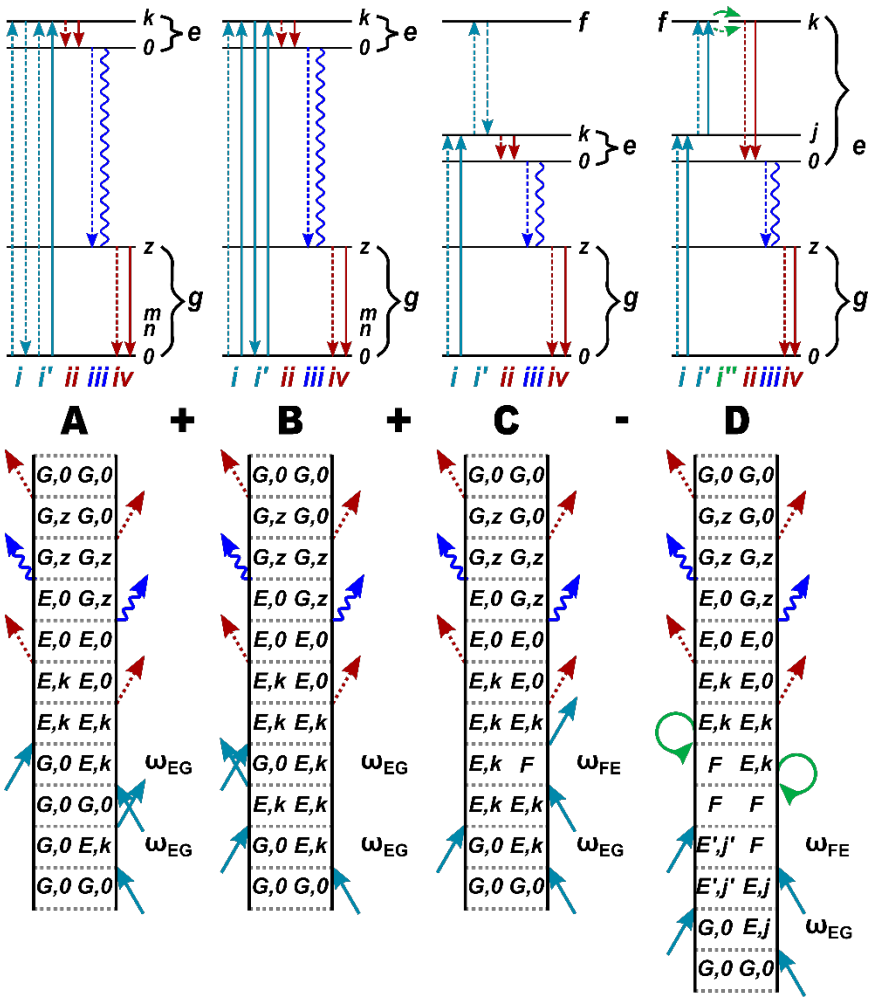

Figure 7.6) Nonrephasing Diagrams of Liouville Pathways for Incoherently-Detected 2D Electronic Spectroscopies. The top row consists of Lee-Albrecht Ladder Diagrams, while the bottom row presents the corresponding Feynman diagrams. **A.)** An example GSB-analogue pathway in 2D FS. The signal will oscillate at a fundamental frequency in the first time delay **(i)** and at the same fundamental frequency in the third time delay **(i')** and appear at the same position in a 2D frequency-domain surface as the GSB in 2D ES. **B.)** In a SE pathway, the signal will appear at the same position as the GSB. **C.)** In the positively-signed ESA pathway, the system oscillates at the frequency difference between the first and higher-lying excited states but ends in a population in the first excited state. This signal appears at the same location as the ESA in 2D ES. **D.)** In the negatively-signed ESA, a higher-lying excited state population is prepared that internally converts to the first excited state (green loops). This pathway will be negatively signed but occur at the same position as **(C)**.

A similar consideration can be applied to the higher-order FEIR pathways, where different signal contributions will be differently-signed, as found in Appendix 3 (Figure 6.A3.1).

7.7 Line Shape Modelling in FEIR

The line shape of the FEIR pathways with respect to the IR interactions can be modelled under the optical Bloch model with reduced equations of motion for the density matrix, resulting in the complex Lorentzian two-dimensional frequency-domain line shape described in Chapter 4.[1,17]

$$P(n,m) = \frac{-\mu_{ni}\mu_{mi}^{*}M_{n}M_{m}^{*}}{(\omega_{1} - \omega_{ni} + i\Gamma_{ni})(\omega_{d} - \omega_{nm} - i\Gamma_{nm})}$$

This can be alternatively expressed in terms of the absorptive Lorentzian line shape, $P_A(\omega, \omega_A, \gamma_A)$, and the dispersive line shape, $P_D(\omega, \omega_D, \gamma_D)$, with center frequencies ω_A, ω_D, and decay parameters γ.[18]

$$P_A(\omega, \omega_A, \gamma_A) = \frac{1}{\pi\gamma\left(1 + \left(\frac{\omega - \omega_A}{\gamma_A}\right)^2\right)}$$

$$P_D(\omega, \omega_D, \gamma) = \frac{\left(\frac{\omega - \omega_D}{\gamma_A}\right)}{\pi\gamma\left(1 + \left(\frac{\omega - \omega_D}{\gamma_A}\right)^2\right)}$$

The full line shape in two frequency axes $P(\omega_1, \omega_a, \gamma_a, \omega_2, \omega_b, \gamma_b)$ is then

$$P(n,m) = P(\omega_1,\omega_a,\gamma_a,\omega_2,\omega_b,\gamma_b) = \mu_n\mu_m^* M_n M_m^* \begin{Bmatrix} \begin{pmatrix} P_D(\omega_1,\omega_a,\gamma_a)\times P_A(\omega_2,\omega_b,\gamma_b)-\cdots \\ P_A(\omega_1,\omega_a,\gamma_a)\times P_D(\omega_2,\omega_b,\gamma_b) \end{pmatrix}+\cdots \\ i\begin{pmatrix} P_A(\omega_1,\omega_a,\gamma_a)\times P_A(\omega_2,\omega_b,\gamma_b)+\cdots \\ P_D(\omega_1,\omega_a,\gamma_a)\times P_D(\omega_2,\omega_b,\gamma_b) \end{pmatrix} \end{Bmatrix}$$

and the observed signal will be the imaginary part of this response.

$$P_3(\omega_1,\omega_n,\gamma_{ni},\omega_d,\omega_n-\omega_m,\gamma_{nm})_{obs.} = imag\left(P(\omega_1,\omega_n,\gamma_{ni},\omega_d,\omega_n-\omega_m,\gamma_{nm})\right)$$
$$= \mu_n\mu_m^* M_n M_m^* \left(P_A(\omega_1,\omega_n,\gamma_{ni})\times P_A(\omega_d,\omega_n-\omega_m,\gamma_{nm}) + P_D(\omega_1,\omega_n,\gamma_{ni})\times P_D(\omega_d,\omega_n-\omega_m,\gamma_{nm})\right)$$

For a single time-ordered pathway, such as a nonrephasing pathway, the 2D line shape will contain a symmetric, absorptive term $P_A \times P_A$, and an asymmetric, dispersive term $P_D \times P_D$.

For a three-level system in a linear measurement, a peak quartet will arise due to the four pathways that end in a population, as described in Chapter 4.

$$P_{quart}\left(\omega_1,\omega_n,\omega_d,\omega_m\right) = P_1(\omega_1,\omega_n,\gamma_n,\omega_d,0,\gamma_{nn})_{obs.} + P_2(\omega_1,\omega_m,\gamma_m,\omega_d,0,\gamma_{mm})_{obs.}+\cdots$$
$$P_3(\omega_1,\omega_n,\gamma_n,\omega_d,\omega_n-\omega_m,\gamma_{nm})_{obs.} + P_4(\omega_1,\omega_m,\gamma_m,\omega_d,\omega_m-\omega_n,\gamma_{mn})_{obs.}$$

We can extend this formalism to any number of time delays as follows.

$$let: D_1 \equiv P_D(\omega_1,\omega_a,\gamma_a), A_2 \equiv P_A(\omega_2,\omega_b,\gamma_b),\ldots$$
$$P(\omega_1,\omega_a,\gamma_a,\omega_2,\omega_b,\gamma_b,\cdots,\omega_n,\omega_\upsilon,\gamma_\upsilon)_{obs.} = \left(\prod_{j=a}^{\upsilon}\mu_j\right) MM^* \left\{ imag.\left(i\times\prod_{k=1}^{n}\left(D_k + (-1)^{k+1} iA_k\right)\right)\right\}$$

Rephasing pathways in τ_3 will reverse the sign of the D_3 line shape, and for four time delays (between four IR pulses and a NIR pulse), one obtains the following for the nonrephasing signal:

$$P_{NR}(\omega_1,\omega_a,\gamma_a,\omega_2,\omega_b,\gamma_b,\omega_3,\omega_c,\gamma_c,\omega_4,\omega_d,\gamma_d)_{obs.} = \cdots$$
$$\mu_a\mu_b\mu_c\mu_d MM^* \begin{Bmatrix} -D_1A_2D_3A_4 - A_1D_2A_3D_4 + A_1D_2D_3A_4 + D_1A_2A_3D_4\cdots \\ +A_1A_2A_3A_4 + A_1A_2D_3D_4 + D_1D_2A_3A_4 + D_1D_2D_3D_4 \end{Bmatrix}$$

and the rephasing signal.

$$P_R(\omega_1,\omega_a,\gamma_a,\omega_2,\omega_b,\gamma_b,\omega_3,\omega_c,\gamma_c,\omega_4,\omega_d,\gamma_d)_{obs.}=\cdots$$
$$\mu_a\mu_b\mu_c\mu_d MM^*\begin{Bmatrix} D_1A_2D_3A_4-A_1D_2A_3D_4-A_1D_2D_3A_4+D_1A_2A_3D_4\cdots \\ +A_1A_2A_3A_4-A_1A_2D_3D_4+D_1D_2A_3A_4-D_1D_2D_3D_4 \end{Bmatrix}$$

Their sum will thus cancel out the dispersive line shapes in ω_3.

$$P_R+P_{NR}=2\mu_a\mu_b\mu_c\mu_d MM^*\left\{-A_1D_2A_3D_4+D_1A_2A_3D_4+A_1A_2A_3A_4+D_1D_2A_3A_4\right\}$$

Experimentally, it is time consuming and difficult to collect a multidimensional surface in each of these time delays. If one or more of the experimental time delays are set to zero, that is, if the frequency-domain response is integrated over the corresponding frequency axis or axes, terms that are dispersive in that frequency axis will vanish, and terms that are absorptive in that frequency axis will become constant at 1. If delays 2 and 4 in this example are set to zero, then the following results for the nonrephasing pathway

$$P_{NR}(\omega_1,\omega_a,\gamma_a,\cancel{\phi_2},\omega_b,\gamma_b,\omega_3,\omega_c,\gamma_c,\cancel{\phi_4},\omega_d,\gamma_d)_{obs.}=\mu_a\mu_b\mu_c\mu_d MM^*\left\{-D_1A_2D_3A_4+A_1A_2A_3A_4\right\}$$
$$=\mu_a\mu_b\mu_c\mu_d MM^*\left\{-D_1D_3+A_1A_3\right\}$$

and the sum of the phasing and nonrephasing pathways.

$$P_R+P_{NR}=2\mu_a\mu_b\mu_c\mu_d MM^*\left\{A_1A_3\right\}$$

However, non-zero time delays of t_2 in τ_2 and t_4 in τ_4 will appear in the frequency domain as a phase shift.

$$P_{NR}(\omega_1,\omega_a,\gamma_a,\cancel{\phi_2},\omega_b,\gamma_b,\omega_3,\omega_c,\gamma_c,\cancel{\phi_4},\omega_d,\gamma_d)_{obs.}=\mu_a\mu_b\mu_c\mu_d MM^*\cdots$$
$$\times\left\{imag.\left(i\times\left(D_1+iA_1\right)\times\left(D_2-iA_2\right)\times e^{-i\left(2\pi t_2/\tau_2\right)}\times e^{-(\gamma_b t_2)}\times\left(D_3+iA_3\right)\times\left(D_4-iA_4\right)\times e^{-i\left(2\pi t_4/\tau_4\right)}\times e^{-(\gamma_a t_4)}\right)\right\}$$

For a nonrephasing pathway, this will appear as

$$P_{NR}(\omega_1,\omega_a,\gamma_a,\cancel{\phi_2},\omega_b,\gamma_b,\omega_3,\omega_c,\gamma_c,\cancel{\phi_4},\omega_d,\gamma_d)_{obs.}$$
$$=\mu_a\mu_b\mu_c\mu_d MM^* e^{-(\gamma_b t_2+\gamma_d t_4)}\left[\begin{array}{l}\mathrm{Re}\left(e^{-2\pi i(t_4\tau_2+t_2\tau_4)/(\tau_2\tau_4)}\right)(A_1A_3-D_1D_3)\cdots\\+\mathrm{Im}\left(e^{-2\pi i(t_4\tau_2+t_2\tau_4)/(\tau_2\tau_4)}\right)(D_1A_3+A_1D_3)\end{array}\right]$$

and for the sum of rephasing and nonrephasing pathways,

$$P_R+P_{NR}=2\mu_a\mu_b\mu_c\mu_d MM^* e^{-(\gamma_b t_2+\gamma_d t_4)}\left[\begin{array}{l}\mathrm{Re}\left(e^{-2\pi i(t_4\tau_2+t_2\tau_4)/(\tau_2\tau_4)}\right)(A_1A_3)\cdots\\+\mathrm{Im}\left(e^{-2\pi i(t_4\tau_2+t_2\tau_4)/(\tau_2\tau_4)}\right)(D_1A_3)\end{array}\right].$$

These line shapes can be used to model the 14 terms of the response function for the higher order FEIR experiment (Figure 6.A3.1). These terms will occur at the fundamental frequency of a singly-excited vibrational level ω_f and/or at the difference between the singly and doubly-excited vibrational levels $\omega_F=\omega_{2f}-\omega_f$. The FEIR response for a system with a single vibrational mode can then be modelled as:

$$\begin{aligned}S(\omega_1,\omega_3)&=P_{R\underset{GSB}{}}(\omega_1,\omega_f,\omega_3,\omega_f)+P_{NR\underset{GSB}{}}(\omega_1,\omega_f,\omega_3,\omega_f)\cdots\\&+P_{R\underset{SE}{}}(\omega_1,\omega_f,\omega_3,\omega_f)+P_{NR\underset{SE}{}}(\omega_1,\omega_f,\omega_3,\omega_f)+P_{R\underset{ESA}{}}(\omega_1,\omega_f,\omega_3,\omega_F)+P_{NR\underset{ESA}{}}(\omega_1,\omega_f,\omega_3,\omega_F)\cdots\\&-P_{R\underset{ESA}{}}(\omega_1,\omega_f,\omega_3,\omega_F)-P_{NR\underset{ESA}{}}(\omega_1,\omega_f,\omega_3,\omega_F)-P_{R\underset{ESA}{}}(\omega_1,\omega_f,\omega_3,\omega_F)-P_{NR\underset{ESA}{}}(\omega_1,\omega_f,\omega_3,\omega_F)\cdots\\&+P_{NR\underset{DQC}{}}(\omega_1,\omega_f,\omega_3,\omega_f)+P_{NR\underset{DQC}{}}(\omega_1,\omega_f,\omega_3,\omega_F)-P_{NR\underset{DQC}{}}(\omega_1,\omega_f,\omega_3,\omega_F)-P_{NR\underset{DQC}{}}(\omega_1,\omega_f,\omega_3,\omega_F)\end{aligned}$$

which simplifies to:

$$S(\omega_1,\omega_3)=\Big[2P_R(\omega_1,\omega_f,\omega_3,\omega_f)+3P_{NR}(\omega_1,\omega_f,\omega_3,\omega_f)\Big]\cdots$$
$$-\Big[\underset{ESA-like}{P_R(\omega_1,\omega_f,\omega_3,\omega_F)}+2P_{NR}(\omega_1,\omega_f,\omega_3,\omega_F)\Big]$$

In the case where the encoding pulse is equally on resonance with the transition to the electronic excited state from the singly-excited vibrational and the doubly-excited vibrational state, this model then predicts that the amplitude of the GSB feature in higher-order FEIR should be roughly twice that of the ESA feature.

7.8 Spectral Diffusion Model for FEIR

This simple model does not specifically account for inhomogeneous line widths, which can be included explicitly in linear FEIR line shapes as a gaussian broadening as described in Chapter 5. In 2D IR, inhomogeneous broadening along the diagonal in ω_1 corresponds to an initial environmental inhomogeneity of the system and the time-dependence in τ_2 of the relaxation of this broadening corresponds to the timescale for interconversion between local environmental conditions, i.e. spectral diffusion. While linewidths in FT FEIR can be broadened similarly in ω_1 (Figure 5.6), it cannot resolve spectral diffusion in the encoding time delay, as the frequency observed will correspond to the frequency initially excited. However, a higher-order of FEIR experiment should be able to resolve spectral diffusion in the second time delay as in 2D IR.

While spectral diffusion can appear as a gaussian broadening, the process physically originates in a stochastic diffusion process – a random walk between environments. The gaussian broadening in Chapter 5 was modelled with a pseudo-ensemble of particles that was generated using an array of peak frequencies selected randomly with gaussian weighting from a distribution of peak center frequencies.

The spectrum for each particle was calculated and the resulting surfaces were summed across the ensemble, resulting in a gaussian frequency broadening that arises from a distribution of local environments. Such inhomogeneous broadening will lead to a correlation between excited and observed frequencies that is lost as the molecule (or environment) diffuses. In a simple model of spectral diffusion, each particle in the pseudo-ensemble is propagated in time with some probability of frequency switching per time step, i.e. a reassignment of frequency from the gaussian distribution (Figure 7.7).

For this model, I have included FEIR-active $\nu_{Ar\text{-}s}$ and ν_{CO} modes, and calculated the full expected signal for the higher-order FEIR measurement resolved in the τ_1 and τ_3 time delays from the terms in of the nonlinear response function (Appendix 3, Figure 6.A3.1). Aphysical anharmonicities were included of 20 cm^{-1} for diagonal modes and 25 cm^{-1} for cross peaks. As internal conversion is not necessary for the negative ESA features to be encoded, and thus a loss of amplitude comparable to 2D ES is not expected[IX], a GSB/ESA doublet feature is expected as in 2D IR. However, due to differing signs of the pathways, the modulus of the ESA will be roughly half relative to that of the GSB – they are nearly equal in 2D IR.

This model predicts how spectral diffusion should be expected to contribute to the higher-order FEIR measurement. The frequency broadening introduced in the simple model in Chapter 5 contributes to an inhomogeneous broadening of features that decays as the detection frequency decorrelates from the excitation frequency. In linear FEIR and FTIR, inhomogeneous broadening can be observed in the excitation frequency, but, like 2D IR, higher orders of FEIR are needed to resolve the spectral diffusion

[IX] In the off-resonance case, doubly-excited vibrational modes should further increase the electronic resonance with the encoding pulse.

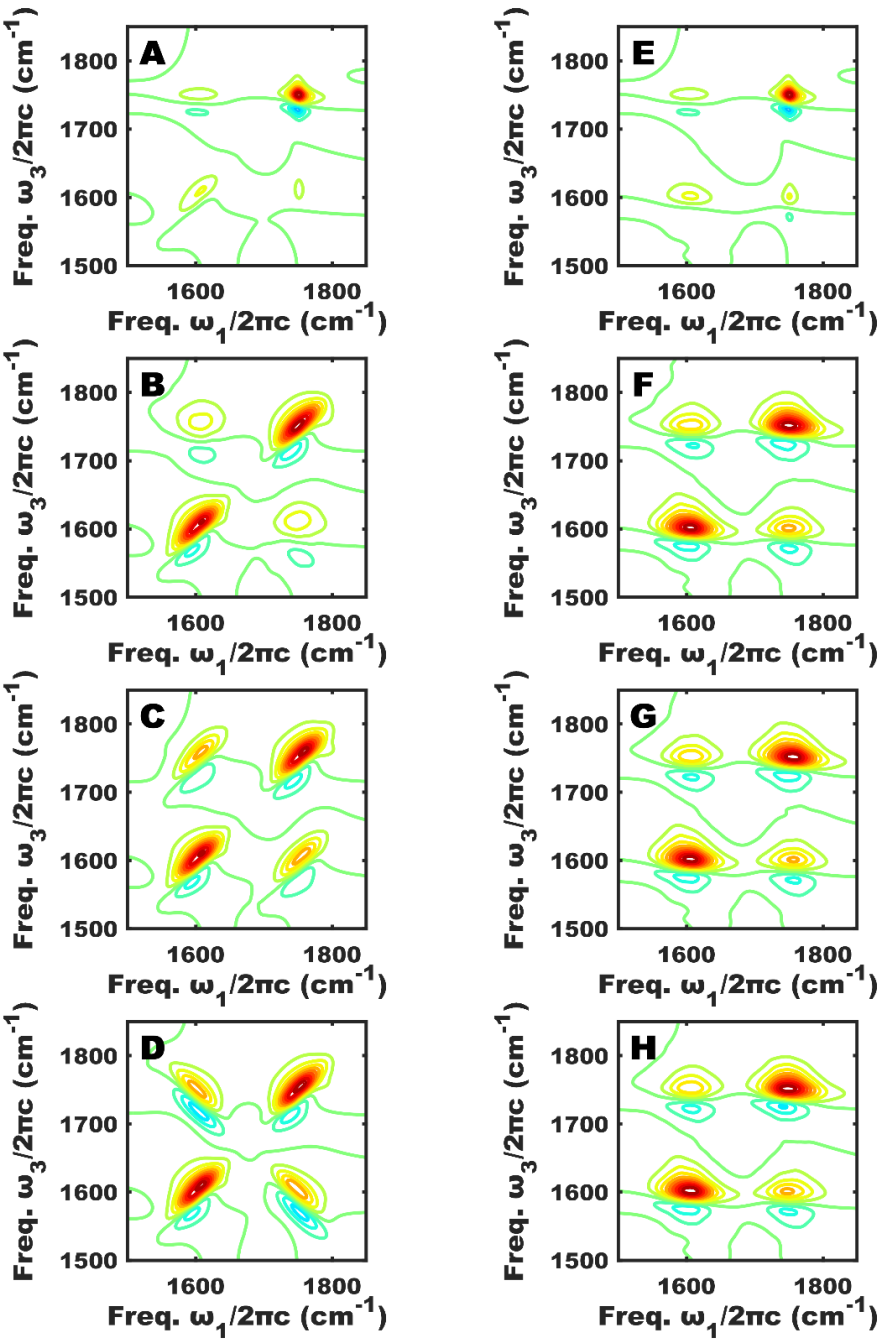

Figure 7.7) Spectral Diffusion Model for Various Types of Frequency Correlations in Higher-Order FEIR. A.) Frequency broadening in the lower mode results in an inhomogeneous broadening along the diagonal of the GSB/ESA doublet. **B.)** Uncorrelated broadening in both peaks results in inhomogeneous broadening of diagonal features but not cross peaks. **C.)** Correlated broadening results in inhomogeneous broadening of all features. **D.)** Anticorrelated broadening results in inhomogeneous broadening of diagonal features but not cross peaks. **E-H.)** At larger time delays, the observed frequency is decorrelated from the excitation frequency due to stochastic changes in the local environment.

of frequency correlations. The line shape asymmetry observed in the nonlinear FEIR model arises from an interesting effect of the quasi-third-order pathways used to calculate individual spectra. While rephasing and nonrephasing pathways sum together in pairs to generate purely absorptive line shapes, the phase of the double quantum coherence pathways in τ_3 depends on the phase in τ_1, similarly to signals in FT FEIR, with no rephasing counterpart. Thus, a slight asymmetry is introduced into the line shapes due to the dispersive $D_1 D_3$ component of these pathways.

7.9 Conclusions

Beginning with the response function formalism, in this chapter I explore incoherent detection of Liouville pathways for processes that are prepared in a population state by some interaction. In the case of a dipole-coupling-mediated relaxation from a system to a bath, the solvent-solute interaction can be expressed in terms of optical interactions, and the relaxation process can be described with a quasi-third-order response function. From this, I explore Mukamel's formalism as described for spontaneously-emitting electronic fluorescence measurements and apply this formalism to FEIR and 2D FS. I have described response functions for incoherently-detected linear FEIR measurements as in Chapters 3, 4, and 5; and predicted the form of nonlinear response functions that will contribute to a 4-IR-pulse higher-order FEIR measurement (Figure 6.4.1). A frequency-domain line shape model is discussed in more detail, and can be used with the terms of the response functions to calculate the linear FEIR spectra and predict the nonlinear FEIR spectra. Using the higher-order FEIR terms, the effect of spectral diffusion on higher order FEIR measurements can also be predicted using a stochastic model.

Chapter Bibliography

(1) Mukamel, S. *Principles of Nonlinear Optical Spectroscopy*; 1995; Vol. 6.

(2) Wagner, W.; Li, C.; Semmlow, J.; Warren, W. Rapid Phase-Cycled Two-Dimensional Optical Spectroscopy in Fluorescence and Transmission Mode. *Opt. Express* **2005**, *13* (10), 3697–3706.

(3) Li, C.; Wagner, W.; Ciocca, M.; Warren, W. S. Multiphoton Femtosecond Phase-Coherent Two-Dimensional Electronic Spectroscopy. *J. Chem. Phys.* **2007**, *126* (16).

(4) Tekavec, P. F.; Lott, G. A.; Marcus, A. H. Fluorescence-Detected Two-Dimensional Electronic Coherence Spectroscopy by Acousto-Optic Phase Modulation. *J. Chem. Phys.* **2007**, *127* (21).

(5) Perdomo-Ortiz, A.; Widom, J. R.; Lott, G. A.; Aspuru-Guzik, A.; Marcus, A. H. Conformation and Electronic Population Transfer in Membrane-Supported Self-Assembled Porphyrin Dimers by 2D Fluorescence Spectroscopy. *J. Phys. Chem. B* **2012**, *116* (35), 10757–10770.

(6) De, A. K.; Monahan, D.; Dawlaty, J. M.; Fleming, G. R.; De, A. K.; Monahan, D.; Dawlaty, J. M.; Fleming, G. R. Two-Dimensional Fluorescence-Detected Coherent Spectroscopy with Absolute Phasing by Confocal Imaging of a Dynamic Grating and 27-Step Phase-Cycling Two-Dimensional Fluorescence-Detected Coherent Spectroscopy with Absolute Phasing by Confocal Imaging of a. *J. Chem. Phys.* **2014**, *140*.

(7) Karki, K. J.; Kringle, L.; Marcus, A. H.; Pullerits, T. Phase-Synchronous Detection of Coherent and Incoherent Nonlinear Signals. *J. Opt.* **2016**, *18* (1), 15504.

(8) Grégoire, P.; Kandada, A. R. S.; Vella, E.; Leonelli, R.; Silva, C. Incoherent Population Mixing Contributions to Phase-Modulation Two-Dimensional Coherent Excitation Spectra. *J. Chem. Phys.* **2017**, *147* (114201).

(9) Tiwari, V.; Matutes, Y. A.; Gardiner, A. T.; Jansen, T. L. C.; Cogdell, R. J.; Ogilvie, J. P. Spatially-Resolved Fluorescence-Detected Two-Dimensional Electronic Spectroscopy Probes Varying Excitonic Structure in Photosynthetic Bacteria. *Nat Comm* **2018**, *9* (4219).

(10) Bhattacharyya, K. Quantum Decay and the Mandelstam-Tamm- Energy Inequality. *J. Phys. A Math. Gen.* **1983**, *16*, 2993–2996.

(11) Hilgevoord, J. The Uncertainty Principle for Energy and Time. *Am. J. Phys.* **1996**, *64* (12), 1451–1456.

(12) Bolton, J. R.; Archer, M. D. Calculation of Natural Radiative Lifetimes from the Absorption and Fluorescence. *J. Phys. Chem.* **1991**, *95* (22), 8453–8461.

(13) Tokmakoff, A. Time-Dependent Quantum Mechanics and Spectroscopy.

(14) Milonni, P. W. Why Spontaneous Emission? *Am. J.* **1984**, *52* (4), 340–343.

(15) Göppert-Mayer, M. Uber Elementarakte Mit Zwei Quantensprüngen. *Ann. Phys.* **1931**, *401* (3), 273–294.

(16) Mastron, J. N.; Tokmakoff, A. Two-Photon-Excited Fluorescence-Encoded Infrared Spectroscopy. *J. Phys. Chem. A* **2016**, *120* (46), 9178–9187.

(17) Mastron, J. N.; Tokmakoff, A. Fourier Transform Fluorescence-Encoded Infrared Spectroscopy. *J. Phys. Chem. A* **2018**, *122* (2), 554–562.

(18) Marshall, A. G.; Roe, D. C. Dispersion versus Absorption: Spectral Line Shape Analysis for Radiofrequency and Microwave Spectrometry. *Anal. Chem.* **1978**, *50* (6), 756–763.

Appendix 4

Supplementary Figures to Chapter 7

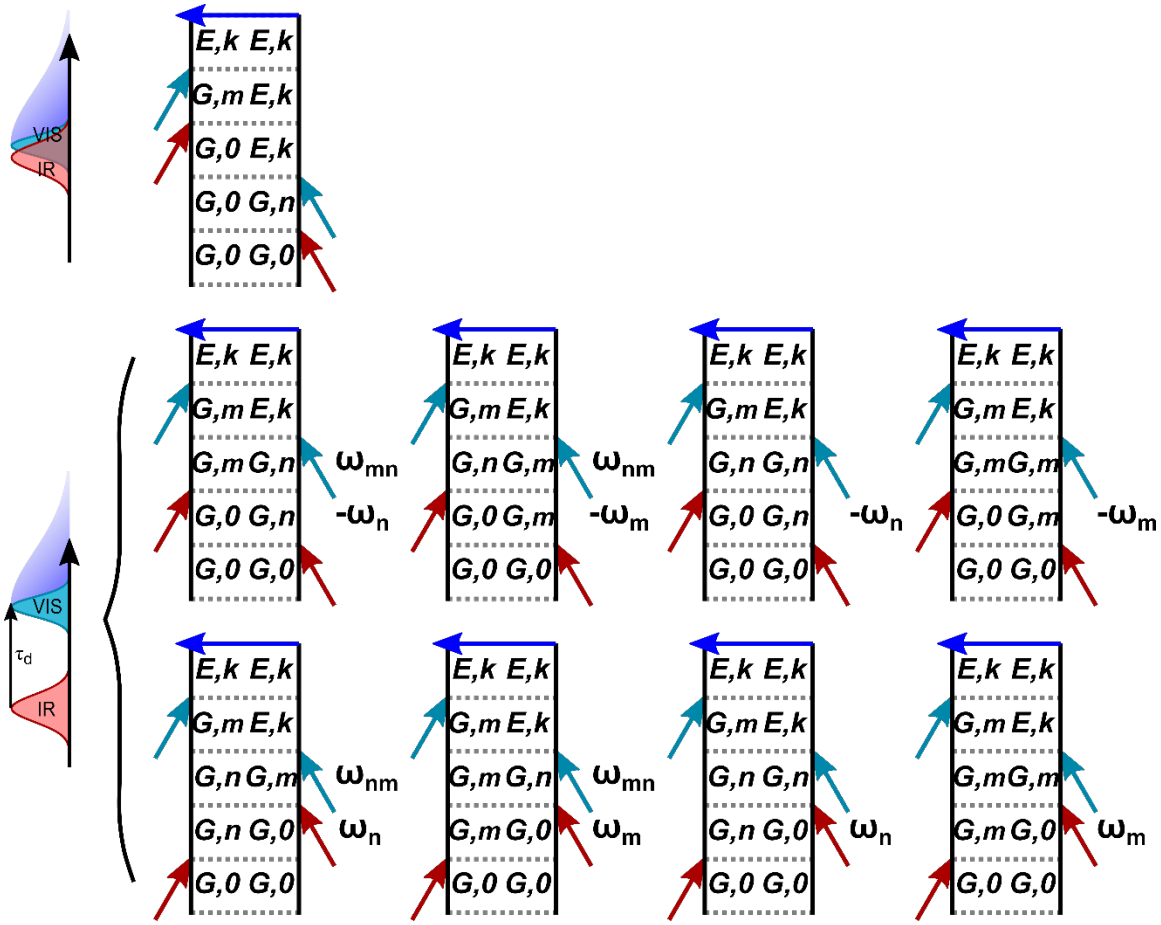

Figure 7.A4.1) Liouville Pathways for FEIR of a three level system. The quasi-linear pathways here share the same sign, as do their complex conjugates. The top pathway will contribute only within the pulse-overlap region. The bottom two rows contribute to the peak quartet feature described previously for FT FEIR measurements.

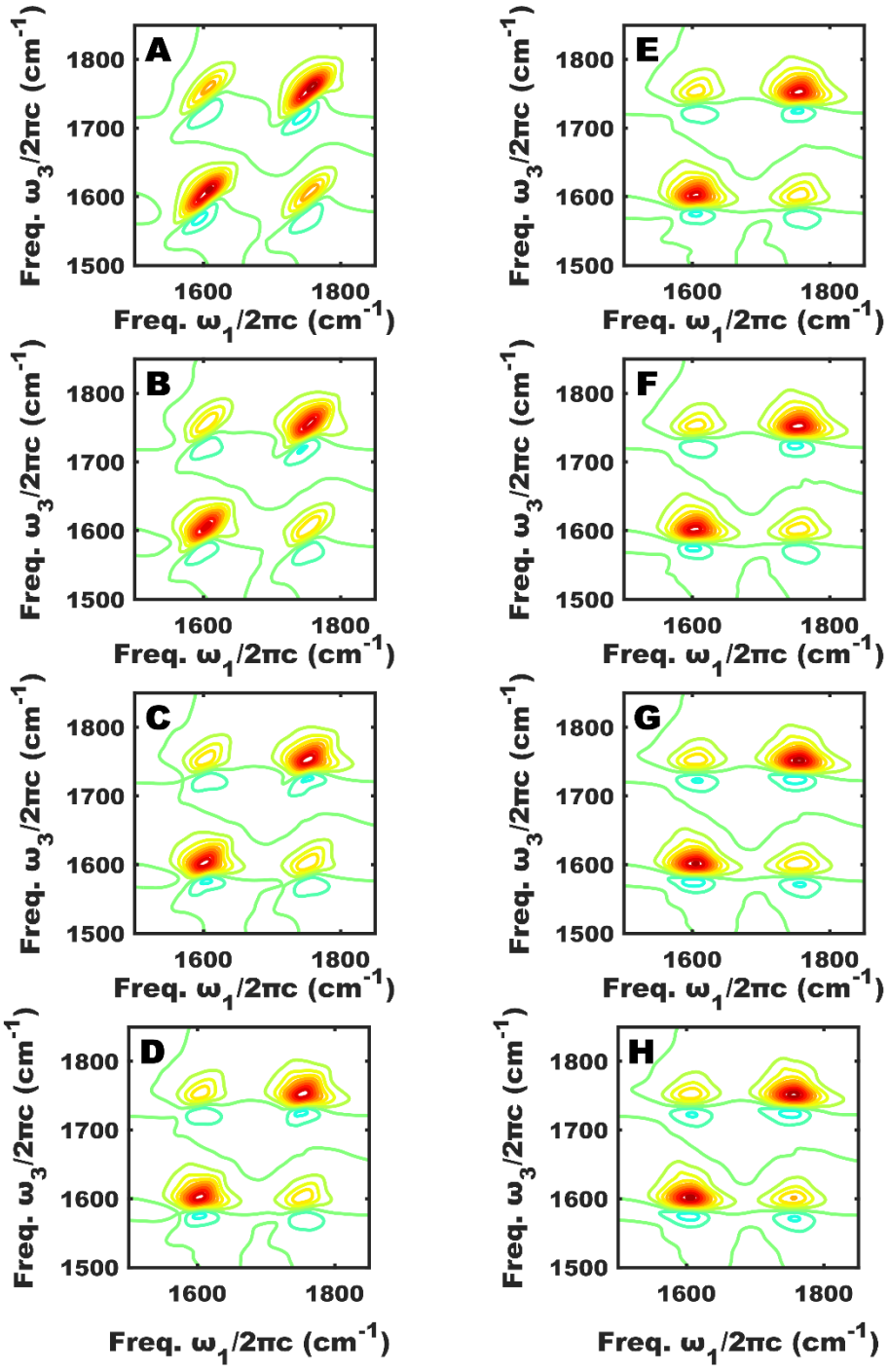

Figure 7.A4.2) CLS Relaxation in Spectral diffusion. This figure corresponds to a time series of spectral diffusion of two correlated modes (in arbitrary time units), from **(A)** to **(H)**. As time progresses, the ensemble loses frequency correlation exponentially due to stochastic switching of the environments local to the components of the ensemble.

Chapter 8
Conclusions

8.1 A Review of the Overarching Topic

In this dissertation, I have presented some of my work toward the development of Fluorescence-Encoded Infrared (IR) Vibrational Spectroscopies. As the primary goal of this project was to increase the sensitivity of IR-driven vibrational measurements to lower concentrations, the clear choice was to develop a mixed-IR-Visible technique that retains the structural sensitivity of an ultrafast IR measurement with added detection efficiency of an optical observable. Fluorescence-Encoded IR spectroscopies fulfill these requirements and allow for interferometric detection of vibrational modes in the solution phase in concentrations at least two orders of magnitude lower than can be measured in a reasonable time-frame with 2D IR or FT IR. The principles described here could be implemented with ultra-low-concentration fluorescence detection to measure structural dynamics using vibrational signatures at unprecedentedly-low concentrations.

8.2 DFT Results for an Aminocoumarin Model System

DFT calculations of the vibrational normal modes and electronic excited state transitions were used to characterized the behavior of Coumarin 466, an electronically-bright aminocoumarin dye molecule, as a model system. Coumarin 466 has several structural degrees of freedom, and has several strong mid-IR

ring and carbonyl stretch modes. Further, the diethylamino molecular rotor moiety at the 7 position allows a further degree of freedom in rotor orientation.

The results of the DFT calculations can be used to predict the qualitative behaviors of Coumarin 466 as a function of a subset of its structural degrees of freedom. In the equilibrated ground electronic and vibrational states, the molecular rotor moiety should be "locked" from rotating by steric hindrance with the aminocoumarin core, in a racemic mixture of conformational enantiomers due to the chirality of the locked rotor geometry. A potential energy scan in the rotor angle shows that the "locked" orientation is the minimum energy position (although this calculation does not include entropic effects). Thus, it is predicted that the ensemble of aminocoumarin molecular rotors observed in a vibrational measurement should consist mainly of molecules with little rotation in this degree of freedom. Perhaps due to entropic effects not accounted for here, FTIR shows the occurrence of rotor twisting to some extent in the ground state ensemble.

From time-dependent DFT results, the first, second, and fourth electronic singlet transitions can be assigned using Kohn-Sham molecular orbitals as a shift of electron density from the molecular rotor to the aromatic coumarin core, while the third singlet transition can be assigned as an anti-symmetrization of the electron density from a symmetry-broken ground state. A potential energy scan in the displacement along the nuclear coordinates of the strong mid-IR modes, as can be driven with an IR field, will result in a change of electronic transition energies and oscillator strengths. Further, the nature of higher-lying electronic states will be further altered due to predicted avoided crossings in these coordinates. In sum, these results predict that a change in the electronic transition, or an observable proportional to the electronic transition, could be used to report on the structural dynamics of Coumarin 466 upon ultrafast vibrational excitation.

8.3 Linear FEIR Results using a TPEF Encoding Scheme

Building on the predications that can be made from DFT calculation, a simple two-pulse Fluorescence-Encoded IR (FEIR) measurement was developed that fulfills the overarching requirements. An off-resonance electronic transition is brought on-resonance with the encoding pulse by vibrational modes with vibronic coupling to the electronic states. Using a two-photon-encoded fluorescence signal as the experimental observable, the TPE-FEIR response to a vibrational excitation results in encoding-time dependent traces of aminocoumarin dyes in solution. This experiment reports on the relaxation of the vibrational populations and coherences prepared by the IR pump field, however the information content differs from the corresponding IR pump–probe experiments. Coherences appear much more strongly in FEIR than in 2D IR, which can possibly be explained by the difference in observable: the amount of population projected onto the electronic excited state by the two-photon interaction contrasted with the electric field generated by the nonlinear nuclear polarization. The obvious next step for this experiment is the expansion of FEIR to a linear Fourier-Transform experiment using two IR pulses from an interferometer followed by the encoding pulse to resolve the signal as a function of both the interferometric and encoding time delays.

8.4 Linear FT FEIR Results in Two Time Delays

The two-IR-pulse experiment should provide interferometric control over the populations and coherences prepared before the encoding process and thus more directly resolve which vibrational states participate in the final signal. The signal in the interferometric IR delay τ_1 oscillates at fundamental

frequencies in a manner similar to a free induction decay. This axis can be transformed to its Fourier-conjugate to reveal a frequency-domain ground-state IR spectrum of the vibrational modes that participate in the FEIR process (as projected onto the electronic excited state). In this chapter, Fourier Transform FEIR (FT FEIR) is demonstrated to report on coupled vibrational modes. This data can be then mapped to similar frequency axes as conventional 2D IR measurements. This FT FEIR signal can be described using a response function formalism, and I have modelled the spectral features. While the mapped data appears to contain some of the same information content as 2D IR, it does not arise through the same Liouville pathways. While the coherence cross peaks arise from coherent superpositions of coupled vibrational modes and thus report on the relative probability of observing a molecule where these modes are coupled in the ensemble, the quasi-third-order terms that contribute to FT FEIR do not report on the strength of this coupling as the cross peak anharmonicities in 2D IR can. The presence of coupling in FT FEIR suggests that it can be used to distinguish different spectroscopic species in a way that FTIR cannot. With the heightened sensitivity of fluorescence detection methods, FEIR could be used to distinguish species concentrations orders of magnitude lower than accessible with 2D IR or reported here. Further, by analogy to other fluorescence-detected 2D electronic methods, it may be possible to expand FT FEIR to a higher order experiment with the addition of two more IR interactions to measure nonlinear vibrational line shapes similar to 2D IR. If FEIR is to be a generally applicable technique, it will prove important to demonstrate how the FEIR spectrum reports on its local environment.

8.5 Solvent Influences on FT FEIR of Coumarin 466

As a technique that is linear in IR intensity, and nonlinear overall, FT FEIR occupies a unique niche, and could be used in principle in the same ways as FTIR to report on the interaction between the system and the local environment, but extending the accessible concentration range to much more dilute systems. In this chapter, I have demonstrated that FEIR is indeed applicable to a number of studies on how the structure of the coumarin probe is affected by the local environment. The solvent proticity, or ability to donate a hydrogen bond, polarity, and viscosity all affect the FEIR spectra of Coumarin 466 in different ways. The spectrum of hydrogen-bonded C466 can be extracted using an SVD analysis as a function of hydrogen bond donor concentration in a binary solvent mixture, and used to extract hydrogen-bonded Coumarin concentrations in each mixture. The ratio between free and hydrogen-bonded C466 increases sub-linearly with donor concentration, possibly indicating the presence of local domains in the binary solvent mixture at low hydrogen-bond-donor concentrations.

As can be observed in FTIR measurements at high concentrations, the coumarin carbonyl mode is sensitive to the solvent polarity, and a Stark shifting can be observed with FEIR. Thus, FEIR Stark shift measurements of the local electric field should be possible at low concentrations for FEIR active modes. The increase in local inhomogeneity in polar solvents can be modeled with a simple line shape model that accounts for a distribution of peak center frequencies.

Perhaps most interestingly, vibrational relaxation or population and coherence transfer between different vibrational modes can be observed in FEIR as modes that are dark at an encoding time delay of zero can appear to grow in at later encoding times. This can be described with a solvent-bath-coupled kinetic state model that qualitatively matches the experimental results. Deviations from this behavior in

more viscous solvents suggest that a higher solvent viscosity that hinders the molecular rotor will interfere with vibrational equilibration. This suggests that the orientation of the molecular rotor can act as a bath state for the coumarin vibrational modes in this transfer process.

With these findings, it is clear that FT FEIR should be at least applicable to similar linear studies as FTIR but at the lower concentrations that fluorescence excitation makes accessible. Particularly, the hydrogen-bonding series provides some insight that could lend value to applications of the FEIR technique to more generalized molecular binding problems at low dye concentrations. However, in highly-inhomogeneous systems, there is a tradeoff as some information on the prepared vibrational superpositions is lost as inhomogeneity washes out the coherence cross peaks. Given the right experimental conditions, higher order expansions of the FEIR technique could provide value as incoherently-detected analogues to full 2D IR measurements.

8.6 Challenges of the Expansion of FEIR To Higher Orders

Measurement of a higher-order FEIR signal proved experimentally challenging. With an increased number of IR pulses, the signal separation strategy that worked well for FT FEIR required expanding upon. Starting with a more theoretical description of optical chopping, I have generalized the commonly-used dual-chopping scheme to a higher order, and related the observed signal modulation to the terms of a response function. The resulting quadruple-chopped data can be processed by Fourier transform to separate individual "pathways" with 18 unique signal contributions, but requires a significant increase in data collection time. To reduce collection time, a 2D frequency-domain surface can be collected using an Inverse Radon Transform method. By measuring angular slices in the time-

domain and Fourier transforming them into the frequency-domain, one obtains projections that can then be reconstructed into a 2D frequency-domain surface with an Inverse-Radon-Transform back projection identical to that used in computer-aided tomography measurements. These strategies were implemented to collect comparable 2D frequency-domain data using both stage-stepped, quadruple-chopped and stage-scanned, dual-chopped methods. While various properly-phased FT FEIR signal components were measured, a higher order signal could not be conclusively resolved from the noise, perhaps due to a combination of low IR fluence, reduced duty cycle of higher-order chopping methods, and the reduced averaging time in stage-scanning methods. However, the signal separation and data acquisition methods I have developed for FEIR measurements can conceivably also be applied to 2D IR measurements.

8.7 Formalism for Incoherently-Detected Spectroscopies

The FEIR response can be described as a process that is arbitrarily proportional to an electronic excited state population. However, the incoherent detection of an electronic excited state population can be described with a response function formalism, and combined with the previous Liouville pathways that end in an electronic population, incoherent spectroscopies such as FEIR and 2D FS can be described explicitly. I have described response functions for incoherently-detected linear FEIR measurements as in Chapters 3, 4, and 5; and predicted the form of nonlinear response functions that will contribute to a 4-IR-pulse higher-order FEIR measurement. The frequency-domain line shape model was used with the various higher-order FEIR terms of the quasi-seventh-order response function to predict the form that that should be taken by nonlinear FEIR spectra. A stochastic-switching spectral model predicts that both

the initial environmental inhomogeneity and spectral diffusion should contribute in higher order FEIR measurements.

8.8 Overarching Conclusions and Future Directions

While not every measurement proved successful, the body of my work culminates in success. As intended, I have achieved my primary goal of developing a Fluorescence-Encoded Infrared Spectroscopy that combines the structural sensitivity of vibrational spectroscopies with the detection efficiency of an optical observable. This technique promises to extend the interferometric detection of vibrational modes in the solution phase to much lower concentrations – with my experimental setup that is not particularly optimized for low-light detection, I have still been able to measure an FEIR signal on samples at a concentration that is two orders of magnitude lower than accessible to FTIR with a similar amount of averaging.

As fluorescence-detection measurements are possible on the scale of single-molecule concentrations, a study of the sensitivity limits of the FEIR class of techniques will prove to be important in the future. While I used a two-photon-excited fluorescence process as the experimental observable to increase the experimental contrast between the off-resonance encoding field and the emitted Stokes' shifted field, with optimized resonance conditions, a one-photon-excited fluorescence observable and high-repetition rate photon counting should provide the sensitivity necessary to observe the FEIR signal in low concentration samples (or higher-concentration samples with lower fluorescence yields than my model system). Based on the groundwork presented here, this experiment is currently under development by other members of this research group – I will be excited to see the results of this extended effort!